UNIVERSITY OF SOUTHAMPTON

SCHOOL OF ENGINEERING SCIENCES

MATERIALS RESEARCH GROUP

MICROMECHANICAL ASSESSMENT OF FATIGUE IN AIRFRAME FUSION WELDS

by

Fabien Lefebvre

Doctor of Philosophy

December 2003

UNIVERSITY OF SOUTHAMPTON

ABSTRACT

SCHOOL OF ENGINEERING SCIENCES

MATERIALS RESEARCH GROUP

Doctor of Philosophy

MICROMECHANICAL ASSESSMENT OF FATIGUE IN AIRFRAME FUSION WELDS

By Fabien Lefebvre

The present study concentrates on micro-mechanical aspects of fatigue performance in a fusion welded airframe alloy, 2024-T351. Within the overall program the initiation and growth of short fatigue cracks was studied for two forms of welding: Metal Inert Gas (MIG) and Variable Polarity Plasma Arc (VPPA). Fatigue testing has been carried out on relatively small samples in 3-point bending at constant amplitude and at a R-ratio equal to 0.1. During the tests, replication techniques were used to determine crack initiation points and crack length as a function of the number of fatigue cycles. Secondary electron and back-scattered imaging observations, in association with electron back-scattered diffraction mapping, were carried out on failed samples to determine the crack initiation sites and assess the associated microstructural interactions. Optical microscopy, differential scanning calorimetry and transmission electron microscopy studies have also been carried out to elucidate the local microstructural conditions of the different elements of the welds. Thereby a balance between aging, overaging, re-solutionising and re-precipitation has been identified across the heat affected zone.

It is concluded that several fatigue crack initiation processes may occur within the welds, each with its own implications for performance/lifing. Fatigue life of the MIG welds is controlled in the fusion zone by the combined effects of interdendritic defect sizes, crack coalescence, and, to a lesser degree, residual stresses. In the VPPA case, the fusion zone presents a much finer, lower density of crack initiating defects, and although crack initiation is indeed clearly seen in the fusion zone, fatigue life then becomes limited by the high peak residual stress levels of the VPPA heat-affected zone (HAZ) and the 'naturally occurring' defect population of the parent material. In the context of multiple crack interactions, an *engineering* micromechanical modelling has been successfully developed to predict the fatigue life of the MIG fusion zone and autogeneous VPPA HAZ (1mm crack length) as a function of the probability of initiation and the density/distribution of pores (or intermetallic particles). Semi-empirical crack growth rate approximation and a microstructural crack growth rate approach are used. First order estimates of short crack closure behaviour are used to introduce a residual stress influence on crack growth rates model.

Acknowledgements

Firstly, I would like to thank my supervisor, Dr. Ian Sinclair, for giving me the opportunity to work on this project, and for his constant guidance throughout its duration. His optimism and continuous encouragement provided me constant inspiration to overcome the challenges.

The financial support of the Engineering and Physical Sciences Research Council (EPSRC) and Airbus are gratefully acknowledged.

I wish to thank all the members of the DARP "WELDES" project from Cranfield University and The Open University particularly Prof. Phil Irwin, Prof. Lyndon Edwards and Dr. Mike Fitzpatrick for their stimulating questions and warm discussions during my several presentations. My thanks are extended to Gabriel Serrano from Cranfield University for the supply of the welded plates and Supriyo Ganguly from The Open University for measuring the residual stress fields of my materials.

A special thank is reserved for Eric Bonner, Dave Beckett and Erik Roszkowiak for their valuable help in the specimen preparation, rig manufacture and interesting discussions during the tea break.

There are numerous others that I would like to show my appreciation of. These are the other PhD students, post doctoral researchers and staff of the Engineering Materials group.

Je voudrais également remercier pour leurs supports, leurs amitiés, leurs joies de vivre, les soirées passées au pub, tous mes amis d'Angleterre, de France et de Navarre: Anne, Rachael, Anthony, Jo, Gus, Martin, Suresh, Leo, Nicolas, Sandrine, Etienne, Marie, Fabrice, Elouan, Dominique, Yann, Tit, Tom, Xav, David, Seb, Mel, Jf, Gilles…

Finally I would like to thank my family, who has always been encouraging and supportive in my choice to stay three more years in England after my Erasmus exchange program.

Contents

Nomenclature

α	–	Constant
β	–	Constant defined for the CTOD
λ	–	Distance between the crack tip and the next grain boundary
δ_t	–	Crack tip opening displacement (CTOD)
$\frac{\delta_R}{2}$	–	Plastic stretch to be appended to the crack surfaces
ϕ	–	Angle for calculating surface strain
ϕ^*	–	Fitting parameter
ψ	–	Angle for calculating surface strain
θ	–	Diffraction angle
ε	–	Strain
σ	–	Applied stress
σ_0^*	–	Tensile stress
σ_1	–	Stress acting on the crack surfaces
σ_2	–	Flow stress at the plastic zone
σ_3	–	Stress at the barrier zone
σ_A	–	Stress at the crack tip
σ_c	–	Critical stress
σ_e	–	Endurance limit
σ_f	–	Friction stress
σ_{ef}	–	Equivalent friction stress
σ_{equi}	–	Equivalent stress
σ_{ij}	–	Stress component in Cartesian coordinates
σ_{max}	–	Maximum stress

σ_{min}	–	Minimum stress
σ_y	–	Yield stress
σ'_y	–	Cyclic yield strength
σ_{res}	–	Residual stress
τ	–	Shear stress
τ_0	–	Internal/intrinsic friction stress
τ_0^*	–	Equivalent internal/intrinsic friction stress
ν	–	Poisson's ratio
$\Delta\delta_t$	–	Cyclic crack tip opening displacement
$\Delta\varepsilon_T$	–	Applied total strain
$\Delta\varepsilon_p$	–	Plastic strain
$\Delta\varepsilon_e$	–	Elastic strain
ΔK	–	Stress intensity factor range
ΔK_{eff}	–	Effective stress intensity factor range
ΔK_t	–	Transition stress intensity factor range
ΔK_{th}	–	Threshold stress intensity factor range
$\Delta\sigma$	–	Stress range
ΔP	–	Load range
a	–	Crack length
A	–	Dislocation factor
b^*	–	Burgers vector
c	–	Half surface crack
c'	–	Ellipse major axis
c_1	–	Fitting parameter
C	–	Constant depended on material and load conditions

C_1	–	Constant depended on material and load conditions
d_0	–	Maximum excess oxide thickness
d	–	Inter-planar spacing
D	–	Grain size
E	–	Young's modulus
E'	–	Young's modulus in plane strain
$\mathcal{G}$	–	Strain energy release rate for crack extension
h	–	Ellipse minor axis
$f(x)$	-	Dislocation density
K	–	Stress intensity factor
K_I	–	Stress intensity factor in mode I loading
K_{II}	–	Stress intensity factor in mode II loading
K_{III}	–	Stress intensity factor in mode III loading
K_c	–	Critical stress intensity factor, fracture toughness of the material
K_{cl}	–	Closure stress intensity factor
$K_{\max}$	–	Maximum stress intensity factor
$K_{\min}$	–	Minimum stress intensity factor
$K^*_{\max}$	–	Maximum stress intensity factor with residual stress influence
$K^*_{\min}$	–	Minimum stress intensity factor with residual stress influence
K_{op}	–	Opening stress intensity factor
K_{res}	–	Stress intensity factor with residual stress
$2l$	–	Location of the thickest oxide formation behind the tip
l^*	–	Critical microstructural size scale
m	–	Constant depended on material and load conditions.
m_1	–	Constants dependent on material and load conditions
m^*	–	Orientation factor

n	–	Number of grains spacing the crack
P	–	Applied load
(r,θ)	–	Polar coordinates
r_0^*	–	Grain boundary width
r_0	–	Distance between the grain boundary and a dislocation source
r_c	–	Cyclic plastic zone
r_p	–	Radius of the (assumed circular) plastic zone
r_x	–	Plastic zone in the crack direction
r_y	–	Plastic zone perpendicular to the crack direction
R	–	Load ratio
R_e	–	Yield stress
S	–	The upper limit of the stress acting on a dislocation source
T_{ij}	–	'T-term'
U	–	Proportional factor between ΔK_{eff} and ΔK
W	–	Specimen width
x	–	Distance from the crack tip
Y	–	Dimensionless parameter

Chapter 1

Introduction

Research into weight saving and high performance materials has long been a theme of aerospace engineering (Hou *et al.*, 1996; Woodward *et al.*, 2000). In recent years, reduction in manufacturing costs has become an increasingly significant additional factor within the aircraft industry. To this end, researchers are exploring the use of welding as a cost effective alternative to mechanical fastening of metallic aircraft parts and components. Various research programs have focused on process development to achieve high quality welds in high strength 2xxx and 7xxx heat treatable alloys used in aircraft construction (Norman *et al.*, 1997; Woodward *et al*, 2000; Booth, 2003). Application of these process developments may demand radical changes in aircraft design and construction techniques with important implications for fatigue durability and damage tolerance. From a materials perspective, the use of welded structure leads to a number of effects, such as: (i) change in local material microstructure, with different grain structures and precipitate distributions, (ii) formation of new distributions of crack initiating defects not present in conventional wrought alloy, (iii) formation of soft and hard heat-affected zone regions adjacent to the welds, and (iv) formation of local and global residual stress fields.

An important factor in fatigue life in many situations is the development of cracks of less than 0.5 to 1 mm, that is to say the "short crack regime". The majority of fatigue life may be spent in this regime where processes may be especially susceptible to microstructural influences. Whilst substantial research has been carried out on short fatigue crack growth rates in wrought airframe aluminium alloys, and on the associated influences of crack size, crack tip plasticity and development of crack closure (Navarro & de los Rios, 1992; Zhang & Edwards, 1992; Newman *et al.*, 1999; Lee & Song, 2000), the influences of weld microstructure on such crack growth rates are essentially unknown.

The present study concentrates on micro-mechanical aspects of fatigue performance in a fusion welded 2xxx-series airframe alloy, specifically damage tolerant 2024-T351 material. Two welding techniques have been selected: Metal Inert Gas (MIG) and Variable Polarity Plasma Arc (VPPA). The aim of this work is to develop a micro-mechanical understanding of crack initiation and early growth behaviour, with a view to develop appropriate *engineering* modelling approaches to predict short crack growth life in a welded structure. This work has been carried out in close collaboration with Cranfield University which supplied the material and studied the long crack fatigue regime (specifically cracks longer than 1mm), and The Open University, which carried out residual stress measurements on the fusion welded material. This collaborative effort was particularly directed towards the use of welds in wing skin-stringer structures (Davies, 2000). A further joint project at Cranfield University designed a demonstrator skin-stringer structure (specifically, a two-bay structure), which has now been manufactured using the VPPA method, with fatigue testing due to be carried out after the completion of the present thesis.

A complete understanding of weld microstructure development and associated micro- and macro-mechanical aspects of fatigue crack initiation and short crack growth is clearly beyond the scope of any one PhD thesis, even for one weld type. As such, the present work has taken a focused approach to assessing short crack behaviour in the welds of interest: whilst there are clear bounds on the scope of the work, it is anticipated that achieving a sound mechanistic understanding within those bounds may still provide useful generic understanding. In particular the project has concentrated on fatigue behaviour up to crack lengths of ~1mm (as noted above), as a complement to the long crack work carried out at Cranfield University. Freely initiating crack behaviour is considered within longitudinal test coupons (loading parallel to the weld line) that have been skimmed (machined) to a depth of several millimetres from the as-welded surfaces, representative of the condition of the welds in the proposed skin-stringer structure, but not considering the various surface treatments that may be carried out in aircraft manufacture (e.g pickling, peening, anodising, etc.). Tests have all been carried out under simple constant amplitude load conditions, at low R-ratio. A relatively small, three-point bend test coupon geometry was particularly used to

facilitate detailed study of small crack behaviour, and to make effective use of limited material supplies (particularly for the VPPA welds).

Chapter two of the thesis presents a literature survey relevant to the research objectives. Fatigue behaviour and materials science background are considered in two separate parts. Micro- and macro-mechanisms of fatigue crack behaviour (initiation and growth) are presented. Small fatigue crack phenomena, including the definition of small cracks and general features of small crack growth are then introduced. Models describing small fatigue crack propagation are reviewed. Crack closure phenomenon and residual stress effects in fatigue are also considered. Details on high strength heat-treatable aluminium alloys (in particular the 2xxx series) are reported, and background on fusion welding techniques is then presented. Chapter three reports the materials used, fatigue testing methods and experimental techniques employed in this study. Principal microstructural features of the MIG and VPPA welds, including optical and electron microscopy, hardness mapping, DSC and TEM assessments are discussed in chapter four along with results of residual stress analyses. Chapter five presents and discusses the experimental results of short crack fatigue tests carried out on the MIG weld. Based on the fatigue behaviour and microstructural features of the MIG weld, fatigue life predictions have been developed using a crack-crack interaction model with semi-empirical and microstructural crack growth rate approximations. Chapter six similarly describes and discusses the short crack behaviour of filled and autogeneous VPPA welds in relation to the previous chapter, and applies modelling approaches from the former chapter. Finally, the results are summarized and suggestions for future research work are given in chapter seven.

References

Booth, D. P. P. (2003). Fatigue of friction stir welded AA2024-T351 plate (PhD Thesis). Materials Research group, School of Engineering Sciences. Southampton (UK), Southampton.

Davies, H. (2000). Private communication, Airbus, Filton (UK).

Hou, R., D. M. Evans, J. C. McClure, A. C. Nunes and G. Garcia (1996). "Shielding gas and heat transfer efficiency in plasma are welding." Welding Journal 75(10): S305-S310.

Lee, S. Y. and J. H. Song (2000). "Crack closure and growth behavior of physically short fatigue cracks under random loading." Engineering Fracture Mechanics 66: 321-346.

Navarro, A. and E. R. de los Rios (1992). "Fatigue crack growth modelling by successive blocking of dislocations." Proc. Roy. Soc. 437: 375-390.

Newman, J. C. J., E. P. Phillips and M. H. Swain (1999). "Fatigue-life prediction methodology using small crack theory." International Journal of Fatigue 21: 109-119.

Norman, A. F., K. E. Jakielski, G. Scott and P. B. Prangnell (1997). Process Control of Weld Microstructures in a 2024 (Al-Cu-Mg) Alloy. 4th Decennial International Conference on Solidification Processing, Sheffield, 670-674.

Woodward, N. J., I. M. Richardson and A. Thomas (2000). "Variable polarity plasma arc welding of 6.35 mm aluminium alloys: parameter development and preliminary analysis." Science and Technology of Welding and Joining 5(1): 21-25.

Zhang, Y. H. and L. Edwards (1992). "The effect of grain-boundaries on the development of plastic deformation ahead of small fatigue cracks." Scripta Metallurgica et Materialia 26: 1901-1906.

Chapter 2

Literature review

2.1 Fatigue:

In the last 100 years or so numerous papers have been published on fatigue failure behaviour in structural materials. In industry it has been estimated that ~80% of all services failures in structural materials result from fatigue at some point (Bathias & Baïlon, 1997). The nucleation of micro-defects and the rate of advance of cracks under cyclic loading have been shown to be influenced by a wide range of mechanical, microstructural and environmental factors. In understanding these effects it is important to understand how to define the processes of fatigue. In this section, experimental observations, basic fracture mechanics concepts and micro- and macro-mechanics models theories available to describe fatigue crack growth behaviour in aluminium alloys are particularly summarised.

2.1.1 Cyclic stress-strain relationships:

(σ-ε curve and S-N curve)

If a metal is cycled to produce plastic deformation of a pre-determined strain, a hysteresis loop such as that shown in Figure 2.1 is typically obtained. The applied total strain $\Delta\varepsilon_T$ is divided in two parts: one as a plastic term ($\Delta\varepsilon_p$) and one as an elastic component term ($\Delta\varepsilon_e$). The elastic behaviour is linear with a slope equal to the Young's modulus. The behaviour of the hysteresis loop with ongoing cycling is distinctly dependant upon the load levels and alloy microstructure, with the underaged Al-Cu-Mg alloy, 2024-T351 for example being known to have a much greater capacity for cyclic hardening than equivalent peak aged material (Lemaignan, 2000). This point will be considered in Section 2.2.2. Overall, the cyclic σ-ε curve will be a function of

dislocation multiplication/sub-structure formation and interrelated dislocation-precipitate interactions.

In 1860, Wöhler introduced the stress-life approach to assess fatigue failure resistance, and particularly characterised fatigue behaviour in terms of stress amplitude-life curves (S-N curves) (François *et al.*, 1995). These curves are obtained from nominally defect free, smooth samples. The stress amplitude is plotted against the number of fatigue cycles to cause failure (see Figure 2.2). Generally beyond about 10^7 fatigue cycles, these curves exhibit a plateau (particularly for strain hardening materials), below which the specimen may be cycled indefinitely without causing failure. The associated stress level is commonly identified as the fatigue limit. In materials with a less distinct plateau in the S-N curve, an endurance limit (σ_e) may be defined in terms of stress levels to sustain a nominal high number of load reversals (e.g. 10^7 or 10^8).

2.1.2 Crack initiation:

Generally, fatigue crack initiation appears on the surface of residual stress free fatigue test samples. Forsyth (Forsyth, 1972) identified 3 reasons for such behaviour:

(i) Dislocations are more mobile at the surface of material than inside the material bulk due to less mechanical constraint.

(ii) The surface is a preferential site for the nucleation of dislocations.

(iii) The surface is subjected to the environment.

In relatively pure metals and alloys, fatigue microcracks may arise from slip bands exhibiting intrusion-extrusion behaviour. The mechanism due to Cottrell and Hull (Cottrell & Hull, 1957) for forming an intrusion-extrusion on the surface is based on the simple movement of dislocations, where two slip bands intersect and create intrusions and extrusions during semi-cycles of traction and compression. Mulhvihill and Beevers (Mulvihill & Beevers, 1986) have for example reported that in a high purity Al 4%Cu alloy in the solution treated and quenched condition, slip band formation was indeed a primary cause of cracking. In relation to most engineering metals, atmospheric species may react with fresh surfaces of slip bands, potentially augmenting any intrinsic irreversibility of dislocation notion. In addition, when there

is the formation of deformation bands, it may occur that cracks may nucleate preferentially along their intersections with grain and twin boundaries (Rabbe & Anquez, 1997). During slip band crack initiation, it has been seen that the larger grains may crack more easily due to enhanced strain localisation capacity (Kung & Fine, 1979).

In commercial alloys and corresponding components, principal sites of fatigue crack initiation are often voids, slag or gas entrapment, inclusions, dents, scratches, forging laps and folds, macroscopic stress concentration regions, and regions of microstructural and chemical inhomogeneity. The presence of coarse inclusions (of the order of tens of micrometers or larger) and pores in particular may decrease fatigue life and fatigue strength. Wanhill and Schra (Wanhill & Schra, 1992) found for 2024-T3, tested using single edge notch tension specimens, that crack initiation was from the interfaces between inclusions and the aluminium alloy matrix. Another type of crack nucleation involves cracking along the slip band emanating from, or terminating at, coarse inclusions.

In terms of inclusion initiation of cracks, Lankford and Kusenberger (Lankford & Kusenberger, 1973) have for example described in further detail the mechanism of initiation via debonding of the inclusion-matrix interface, leading to the formation of a micropore which then causes crack nucleation. This process is illustrated in Figure 2.3 in terms of: (a) initial state, (b) debonding (decohesion) at a pole, (c) widening of this decohesion and debonding at the other pole, (d) increasing debonding with nucleation of initial flaws in the matrix, (e) flaws grow and coalescence to form a microcrack, (f) crack propagation and new flaws nucleate.

Other mechanisms of particle nucleation have been identified, such as preferential slip band formation within the strain concentration that occurs at stiff, well bonded particles (Suresh, 1998). Particle cracking may also appear as crack initiation sites (Zabett & Plumtree, 1995). In terms of crack initiation from pores, such defects may be seen as obvious stress/strain concentration sites. (Gerard & Koss, 1990; Buffiere *et al.*, 2001). In Al-Si casting alloys, Buffiere et al. have highlighted the significance of pores size and shape (as stress concentrators) and grain boundaries in the initiation process (Buffiere *et al*, 2001) concluding that microstructural effects (such as co-

location of pores at boundaries) may have a distinct influence on crack initiation beyond simple mechanical influences. Gerard and Koss, (Gerard & Koss, 1990), in considering powder-processed titanium containing rounded pores at levels ranging from 0.4 to 6 vol.% have shown the acceleration of microcrack intiation may be linked to pore-induced plastic zones which create locally high regions of plastic strain at/or very near specimen surface adjacent to the pore. They also suggest that microcrack initiation process is further enhanced if the pores tend to be more elongated due to increased stress/strain concentration effects.

2.1.3 Crack growth:

In order to understand crack propagation subsequent to initiation, it is conventional to employ linear elastic fracture mechanics principles, as summarised in the following section.

2.1.3.1 Linear Elastic Fracture Mechanics:

The loading of a crack can be described by three basic independent modes of opening, see Figure 2.4. Mode I is the tensile opening mode, which is a normal traction to the plane of a crack. Mode II is the in-plane sliding mode, where a shear load is applied to the crack plane, perpendicular to the crack front. Mode III is the tearing or anti-plane shear mode, where a shear load acts on the crack plane, but parallel to the crack front.

In practice, mode I loading is principally studied as the most critical to failure performance. With different boundary conditions (Suresh, 1998) and elasticity equations, it is possible to describe the near-tip stresses at a crack. For a plane stress problem, as illustrated in Figure 2.5, the leading singular terms for mode I stress fields in Cartesian coordinates may be shown to be of the form:

$$\sigma_{xx} = \frac{K_I}{\sqrt{2\pi.r}} \cos\left(\frac{\theta}{2}\right)\left(1 - \sin\left(\frac{\theta}{2}\right)\sin\left(\frac{3\theta}{2}\right)\right) \quad (2.1)$$

$$\sigma_{yy} = \frac{K_I}{\sqrt{2\pi.r}} \cos\left(\frac{\theta}{2}\right)\left(1 + \sin\left(\frac{\theta}{2}\right)\sin\left(\frac{3\theta}{2}\right)\right) \quad (2.2)$$

$$\sigma_{xy} = \frac{K_I}{\sqrt{2\pi.r}} \cos\left(\frac{\theta}{2}\right)\left(\sin\left(\frac{\theta}{2}\right)\sin\left(\frac{3\theta}{2}\right)\right) \quad (2.3)$$

$$\sigma_{zz} = \nu\left(\sigma_{xx} + \sigma_{yy}\right) \text{ plane strain} \quad (2.4)$$

$$\sigma_{zz} = 0 \text{ plane stress} \quad (2.5)$$

$$\sigma_{ij} = \frac{K_I}{\sqrt{2\pi.r}}.f_{ij}(\theta) \quad (2.6)$$

For these equations it is seen that $\frac{1}{\sqrt{2\pi.r}}.f_{ij}(\theta)$ represents all local scales in the near-tip region. K_I (or K_{II} and K_{III} for mode II and mode III loading respectively) is termed the stress intensity factor, which incorporates the boundary conditions of the cracked body and is a function of loading, crack length and geometry. K essentially represents the stress distribution around a flaw (as a scaling factor applied to the $\frac{1}{\sqrt{r}}$ singularity). The unit of K is $Pa.\sqrt{m}$, or, more generally, $MPa.\sqrt{m}$. It is possible to obtain similar near-tip fields for mode II and mode III loading (specifically the angular dependencies of the stress fields for each load case) (Suresh, 1998).

To characterise a linear elastic crack in the near-tip region, it is then only necessary to know the stress intensity factor. It may be shown that the stress intensity factor K is related to the applied stress and the crack length by:

$$K = Y.\sigma.\sqrt{\pi.a} \quad (2.7)$$

$$Y = f\left(\frac{a}{W}\right) \quad (2.8)$$

where a is the crack length, σ the applied stress, Y is a dimensionless parameter which depends on the geometries of specimen and crack and W is the specimen width.

In a thin body, the stress through the thickness (σ_z) cannot vary appreciably due to the thin section because there can be no stresses normal to a free surface: σ_z is equal

to zero throughout the section and a biaxial state of stress results. This is termed a *plane stress condition* (see Figure 2.6(a)). In a thick body, the material is constrained in the z direction due to the thickness of the cross section and ε_z is equal to zero, resulting in a *plane strain condition.* Due to Poisson's effect in elastic deformation, a stress, σ_z, is developed in the z direction (see Figure 2.6(b)).

It is possible to relate the above elastic stress field approach to an energy balance approach to elastic cracks and fracture. Specifically, it may be shown that $\mathcal{G}$ (the strain energy release rate for crack extension) and K (the stress intensity factor) are related via:

$$\mathcal{G} = \frac{K^2}{E} \text{ for plane stress} \qquad (2.9)$$

$$\text{or } \mathcal{G} = \frac{K^2}{E}\left(1-\nu^2\right) \text{ for plane strain} \qquad (2.10)$$

Analytically, the state of stress around a crack in the elastic case may be given by the singular stress components (expressed as stress intensity factors) defined in equation (6) and by non-singular stress terms, (often identified with a 'T-term'), such that one may write (for mode I loading at least):

$$\sigma_{ij} = \frac{K_I}{(2\pi r)^{1/2}} f_{ij}(\theta) + \left[T_{ij0} + T_{ij\infty}(r)\right] \qquad (2.11)$$

As described by Larsson and Carlsson (1973), by separating the non-singular stress components into two parts, it is possible to choose these so that T_{ij0} is constant over a large distance in front of and behind the crack tip, whereas $T_{ij\infty}(r)$ is non-zero only close to the outer boundaries of the specimen and $\lim_{r\to 0} T_{ij\infty}(r) = 0$. Of the T_{ij0}-components, only the normal stress parallel to the crack plane, the x-direction stress, is different from zero, and this component may be denoted by T_x (Larson & Carlsson, 1973).

2.1.3.2 LEFM in ductile metals

Considering equation (2.1), in plane stress, σ_{zz} is equal to zero, σ_{xx} is active and, for $\theta = 0$, is equal to:

$$\sigma_{xx} = \frac{K_I}{\sqrt{2\pi.r}} \quad (2.12)$$

During loading, the stress σ_{xx} must locally reach the elastic limit σ_y for a given ductile metallic material, and, as such a plastic zone appears ahead the crack. For the practical use of LEFM in ductile materials it has been generally assumed that when the extent of crack tip plasticity is small in relation to the K-dominated (elastic) region around the crack tip, then the non-linear behaviour may be directly characterised by the (elastic) stress intensity factor.

Based on the elastic stress distribution and simple stress redistribution, various calculations of crack tip plastic zone have been presented in the literature (Dugdale, 1960; Bilby *et al.*, 1963; Irwin, 1964; Levy *et al.*, 1971; Knott, 1973; Rice, 1974; Tracey, 1976). These calculations vary from first order approximation to involved finite element solutions; Irwin (Irwin, 1964) provides a simple estimate of plastic zone size from equation (2.1) under plane stress conditions as:

$$r_p = \frac{1}{2\pi}\frac{K_I^2}{\sigma_y^2} \quad (2.13)$$

Where r_p is the radius of the (assumed circular) plastic zone directly ahead of the crack tip, and σ_y is the yield stress.

The size of the plastic zone depends strongly on the stress state. In plane strain, the Irwin equation may be modified by increasing the yield stress by a factor of $3^{1/2}$ to account for the constraint of the crack tip based on non-linear elastic analysis (Knott, 1973). Rice and co-workers (Levy *et al*, 1971; Rice, 1974) show that the plastic zone in plane strain is formed of two wings defined in Figure 2.7 by the coordinates r_x and r_y, where r_x is the size in the crack direction and r_y the perpendicular direction. Rice and co-workers (Levy *et al*, 1971; Rice, 1974) find in plane strain, monotonic loading

$$r_y \simeq \frac{1}{2\pi}\frac{K_I^2}{\sigma_y^2} \quad (2.14)$$

and

$$r_x \simeq \frac{1}{9\pi}\frac{K_I^{\,2}}{\sigma_y^{\,2}} \quad (2.15)$$

When considering a cyclic loading, it is commonly assumed that during the tensile load stroke, there is deformation equivalent to simple monotonic loading. During unloading, a new reverse plastic zone is formed inside the first plastic zone which Rice suggests may be characterised in terms of crack tip material having an effectively doubled yield strength due to the tensile stresses that are present at the load maximum (i.e. the reverse zone is then ¼ the size of the forward plastic zone) (Suresh, 1998). Figure 2.8 shows a schematic representation of the development of cyclic plastic zone upon unloading (Suresh, 1998). Hence the radius of the cyclic plastic to equation (2.13) but with the yield stress doubled.

The crack tip opening displacement (CTOD) concept is another way to characterise the behaviour of cracks in ductile material. Due to plastic deformation, an "initially" sharp crack opens up; consequently the crack tip blunts under the applied load. So this blunting effects may provide a critical value of this separation of crack flanks at the crack tip, quantified by the crack tip opening displacement (CTOD), δ_t.

Under small scale yielding/LEFM conditions, a relationship exists between CTOD and stress intensity factor as:

$$\delta_t = \beta\frac{K^2}{E.\sigma_y} \quad (2.16)$$

where E is Young's modulus, σ_y the yield strength and β is a constant. In physical terms CTOD may be particularly significant in defining the scale of the high plastic strain region at a crack tip where micromechanisms of failure are specifically active. Various calculations of β in the literature suggest a value between 0.4 and 0.5 for plane strain conditions and a value near unity under plane stress conditions (Rice & Rosengren, 1968; Rice & Johnson, 1970; Levy *et al*, 1971; Tracey, 1976; Mc Meeking, 1977).

Under cyclic loading, Rice's model of reversed plastic flow may be used to show that the change in CTOD on going from K_{max} to K_{min} is given as:

$$\delta_t = \beta \frac{K^2}{2.E.\sigma_y} \quad (2.17)$$

where β is a constant defined previously (Rice & Rosengren, 1968; Rice & Johnson, 1970; Levy *et al*, 1971; Tracey, 1976; Mc Meeking, 1977).

2.1.3.3 Fracture mechanics assessment of fatigue:

Fatigue crack propagation is generally expressed in terms of the crack length increment per cycle ($\frac{da}{dN}$) in mm per cycle. Figure 2.9 represents schematically crack length as a function of number of fatigue cycles for different loading conditions.

For a constant applied stress range, stress intensities experienced at a crack will increase as the crack size increases.

When cyclic stresses are applied, the stress range and the stress intensity factor range are defined respectively:

$$\Delta\sigma = \sigma_{max} - \sigma_{min} \quad (2.18)$$

$$\text{and } \Delta K = K_{max} - K_{min} \quad (2.19)$$

The typical fatigue crack growth rate behaviour of metallic materials is generally represented as the log of crack growth rate, $\frac{da}{dN}$, versus the log of the stress intensity, ΔK, see Figure 2.10(Paris *et al.*, 1961; Paris & Erdogan, 1963)

This curve is commonly divided into 3 regimes:

In **regime I**, a threshold value ΔK_{th} can generally be defined. This is the value below which cracks do not apparently propagate. Above this value, crack growth rate increases relatively rapidly with ΔK.

In **regime II**, commonly known as the Paris Regime, there is often a linear relationship (approximate at least) between $log\,(\Delta K)$ and $log\,(\frac{da}{dN})$ (Paris *et al*, 1961; Paris & Erdogan, 1963).

In **regime III**, the curve rises to an asymptote where K_{max} (the maximum stress intensity factor) approaches K_c, the critical stress intensity factor for monotonic failure.

2.1.3.4 Microscopic stages of fatigue crack growth:

Before describing the three regions of Figure 2.10 in further detail, it is valuable to comment on the microscopic stages of fatigue crack growth as illustrated in Figure 2.11 and Figure 2.12 (Suresh, 1998), (Forsyth, 1972):

Stage I fatigue crack growth (see Figure 2.11) typically exhibits a serrated or faceted profile. Forsyth (1962) identified Stage I crack growth as a single slip mechanism, leading to a zigzag crack path. Such growth may be attributed to the zone of plastic deformation surrounding a crack tip being confined to within a few grain diameters, with crack tip deformation occurring predominantly by single shear in the direction of the primary slip system.

Stage II crack growth (see Figure 2.12) is often linked to the formation of fatigue "striations" in many engineering alloys (Forsyth, 1972). With higher stress intensity range values, the plastic zone at the crack tip may encompass several grains. The attendant crack growth process involves simultaneous or alternating flow on two or more slip systems (i.e. a duplex slip mechanism). Such duplex slip mechanism results in a planar (mode I) crack path normal to the tensile axis.

2.1.3.5 Different regimes of fatigue crack growth:

Regime I:

Crack propagation rates in regime I, as shown in Figure 2.10, are seen to fall off rapidly with decreasing the ΔK, tending towards a minimum or threshold stress intensity range ΔK_{th}, below which crack can no longer propagate. Due to problems in establishing experimental threshold values, ΔK_{th} is conventionally defined as the stress intensity range at which da/dN falls below a specific value, often taken to be 10^{-8}mm per cycle.

The regime I is commonly seen as sensitive to the microstructure, load conditions, and environment. McCllntock in 1963 (McClintock, 1963) was the first to identify the

crack growth threshold. He assumed that the crack is stopped when the extent of near tip plasticity becomes comparable to some characteristic microstructural size scale (hence producing a primary influence of microstructure). In 1972, Donahue *et al.* (Donahue *et al.*, 1972) based a model on the notion that the threshold for the onset of crack growth occurs when the crack tip opening displacement attains a value comparable to a critical microstructural dimension, leading to the expression:

$$\Delta K_0 \propto \sqrt{\sigma_y E' l^*} \quad (2.20)$$

where σ_y is the yield strength, E' is the Young's modulus in plane strain and l^* is the critical microstructural size scale. The transition from the near-threshold regime to the intermediate stage of fatigue crack growth may also be associated with microstructural scale, with the transition in fatigue failure modes from region I to region II occurring when the size of the cyclic plastic zone r_c becomes comparable to a given microstructural dimension such as the grain size (Yoder *et al.*, 1983; Suresh, 1998). If the stress intensity factor range corresponding to this transition is termed ΔK_T, then

$$r_{c\,(critical)} \approx l^* \quad (2.21)$$

$$\text{and} \quad r_{c\,(critical)} = \alpha \left(\frac{\Delta K_T}{\sigma'_y} \right)^2 \quad (2.22)$$

where σ'_y is the cyclic yield strength and α is a constant. (Suresh, 1998)

$$\text{So } \Delta K_T \propto \sigma'_y \sqrt{l^*} \quad (2.23)$$

Other models of fatigue crack threshold condition have been based on a diverse range of crack arrest concepts, for example, concepts such as: (i) the dynamics of dislocation activity at the crack tip (Sadananda & Shahinian, 1977; Mura & Weertman, 1984) (ii) critical crack tip opening levels (Donahue *et al*, 1972) (iii) critical crack tip stress or strain conditions (Weiss & Lal, 1974), (iv) energy/plastic work considerations (Taylor, 1988).

Regime II:

Regime II crack growth is generally considered to be more weakly influenced by microstructure, and stress ratio. Generally, this part is defined by the Paris law as noted earlier.

$$\frac{da}{dN}=C.(\Delta K)^m \quad (2.24)$$

where C and m are constants depended on material and load conditions.

For most engineering alloys, m is between 2 and 4. Different models of crack growth have been proposed based on this simple relationship (Knott, 1973). Geometrical models for example exist, based on a notional relationship between the crack tip opening displacement and the crack length increment per cycle in the Paris regime. Assuming that $\Delta\delta_t$ is the cyclic crack tip opening displacement there may be, for geometrical reasons, proportionality between da/dN and $\Delta\delta_t$. Laird and Lardner (Laird, 1967; Lardner, 1967) then suggest:

$$\frac{da}{dN} \approx \Delta\delta_t = \beta\frac{\Delta K^2}{\sigma_y'.E} \quad (2.25)$$

where β is a function of stress state as defined previously. Note that this equation predicts a Paris exponent of 2, which is then reasonable for some alloys. Models that invoke criteria for fatigue fracture based on critical values of accumulated strains or plastic work at the crack tip may be used to explain higher m-values, with such models commonly producing m exponents of 4 (McClintock, 1963).

Regime III:

This region may be strongly influenced by microstructure, load ratio and stress state. The crack growth rates are generally too rapid to be affected by environment. In this region, da/dN accelerates due to an interaction between fatigue and static/monotonic fracture mechanisms (microvoid coalescence, cleavage, etc...) (Sinclair, 1984). The strong influence of load ratio is due to the maximum stress intensity factor value for the fatigue cycle, K_{max} approaching the fracture toughness of the material, K_c. Forman *et al.* (Forman *et al.*, 1967) particularly noted that the Paris law does not take failure at $K_{max}=K_c$ into account and proposed a simple empirical relationship:

$$\frac{da}{dN} = \frac{C_1(\Delta K)^{m_1}}{(1-R)K_c - \Delta K} \quad \text{(Forman's equation)} \quad (2.26)$$

where C_1 and m_1 are constants dependent on material and load conditions This equation describes regions II and III (with $R = \frac{\sigma_{min}}{\sigma_{max}} = \frac{K_{min}}{K_{max}}$) and has been assessed for various cases in aluminium alloys, but does not describe fatigue behaviour of various steels where the influence of stress ratio R may be less pronounced (Masounave *et al.*, 1997).

2.1.3.6 Short crack fatigue:

A fatigue crack may be defined as being "short" when it satisfies one or more of the following criteria (Suresh, 1998):

(1) The crack size is comparable to microstructural features such as grain size or precipitate/reinforcement interparticle spacing. Such a crack may be defined as a microstructurally small crack.

(2) Crack tip plasticity is comparable in scale to the crack size or the crack is surrounded by the plastic strain field of a notch. The crack may then be defined as a mechanically small crack.

(3) Cracks are significantly larger than the scale of local plasticity and microstructure but are not macroscopic (i.e. <1-2mm). These cracks may be defined as physically short.

(4) Crack growth shows a length dependence of environmental influence. Such cracks can be defined as chemically short.

When compared to conventional "long" fatigue crack growth (as illustrated in Figure 2.10), short or small fatigue cracks commonly exhibit a number of anomalies. Short cracks may exhibit higher growth rates (Pearson, 1975) than would be predicted from the long crack curve at the same nominal cyclic driving force (ΔK). Crack growth may be observed at lower ΔK than the long crack threshold (ΔK_{th}) with individual short crack curves often exhibiting highly variable growth rates. It has been noted that the concept of linear elastic fracture mechanics (LEFM) used to describe long

cracks cannot be strictly applied for short cracks, as the small scale yielding condition is broken.

Retardations in short fatigue crack growth have particularly been observed when a crack tip encounters grain boundaries. This is in opposition to LEFM predictions for long cracks where the nominal driving force for crack advance (ΔK) is expected to increase with increasing crack length. There is a general agreement in observing grain boundaries slowing or even arresting of short crack growth (Morris, 1979; Lankford, 1982; Zabett & Plumtree, 1995) (see Figure 2.13). A number of different assumptions have been put forward for this retardation. These include arrest of crack growth at the grain boundary until a sizeable plastic zone has developed in the adjacent grain (Morris *et al.*, 1981; Tanaka & Nakai, 1983; Navarro & de los Rios, 1992; de los Rios *et al.*, 1994; Edwards & Zhang, 1994a; Suresh, 1998). Size and orientation of grains also appear to be important factors associated with such growth (Lankford, 1982; Navarro & de los Rios, 1992; de los Rios *et al*, 1994; Edwards & Zhang, 1994a); for example, Lankford has suggested that the relative crystallographic misorientation between neighbouring grains represents the primary factor in such crack retardation events (Lankford, 1982).

2.1.3.7 Micromechanical modelling of short crack fatigue behaviour:

It is known that the propagation of small cracks is strongly influenced by the microstructure, with crack arrests being observed when the crack tip reaches a microstructural barrier such as a grain boundary. Different short crack growth models exist and are based on a variety of physical, semi-empirical or empirical approaches. In this section, a semi-empirical approach based on the Hobson model (Hobson, 1982) is described, followed by a more detailed physical model developed by Navarro and de los Rios (Navarro & de los Rios, 1992; de los Rios *et al*, 1994).

- Semi-empirical modelling:

Hobson (Hobson, 1982) presents a simple model in which crack growth rate is assumed to be proportional to the distance between the crack tip and the grain boundary. So the propagation rate is described by the following equation:

$$\frac{da}{dN} = C_1(\frac{n}{2}D - a)^{1-\alpha} a^{\alpha} \quad (2.27)$$

where D is the grain size, n the number of grain spacings along the crack, a the crack length, and C_1 and α are constants.

Figure 2.14(a) shows a schematic illustration of a grain structure with a crack propagating through the grains. The previous equation assumes that crack retardation will occur at the grain boundary. To obtain the constants C_1 and α, some fitting with experimental data may then be carried out. This approach has been developed by others, such as Grabowski *et al.* (Grabowski & Yates, 1992) and Bomas *et al.* (Bomas *et al.*, 1996). Based on experimental data for the material in question, they define the boundary conditions of the model in terms of the spread of maximum and minimum growth rates.

With the boundary conditions being defined by experimental observations, crack growth may be assumed to vary in a linear manner between grain boundaries (i.e. $\alpha=0$), see Figure 2.14(b). The main difference between Grabowski's model and other models is that it takes into account growth rate perturbations within grains. Perturbation may occur when slip band orientation changes, resulting in intermediate growth rate fluctuations (Grabowski & Yates, 1992).

- Microstructurally sensitive crack propagation model:

Navarro and de los Rios have developed a micromechanical model (identified here as the NR model), which describes microstructurally sensitive short crack propagation. The NR model is based on the concept proposed by Bilby, Cottrell and Swinden in 1963 of simulating the crack and the plastic zone by continuous distributions of infinitesimal dislocations. This concept is used when the plasticity ahead of a crack cannot be neglected; that is to say when the elastic stress distribution is altered by crack plasticity. This is the case for a crack initiating from the surface when the stresses are relatively high (above the fatigue limit) and/or the crack is short.

In the NR model, the crack system is represented by three zones (as shown in Figure 2.15):

(i) the crack itself

(ii) the plastic zone

(iii) the microstructural barrier zone (grain boundary).

In each of these 3 regions, there are resistances reacting to the applied load: (i) the general stress acting on the crack surfaces which may represents a closure stress, (σ_1), (ii) the material resistance to plastic deformation in the plastic zone, (σ_2), and (iii) the barrier strength at the grain boundary, of width r_0^*, (σ_3) which represents a measure of reaction stress developed at the barrier due to the blocking of the slip bands (Navarro & de los Rios, 1992; de los Rios *et al*, 1994).

The equilibrium equation of the system incorporates all the forces (internal and external) acting in the system. The crack tip opening displacement δ_t (CTOD) or the stress at the barrier (σ_3) may be then calculated by solving this equilibrium equation of all the forces acting in the system (Navarro & de los Rios, 1992; de los Rios *et al*, 1994; Rodopoulos & de los Rios, 2002; Wei *et al.*, 2002).

For example, the stress at the end of the slip band (i.e. at the barrier), (σ_3), for an applied load (σ), and the crack tip opening displacement, are given by:

$$\sigma_3 = \frac{1}{\cos^{-1} n_2}\left[(\sigma_2 - \sigma_1)\sin^{-1} n_1 - \sigma_2 \sin^{-1} n_2 + \frac{\pi}{2}\sigma\right] \quad (2.28)$$

$$\delta_t = \frac{2b^* c}{\pi^2 A}\left\{(\sigma_1 - \sigma_2)\left(n_1 \cosh^{-1}\left(\left|\frac{1+n_1^2}{2n_1}\right|\right)\right) + \left(1-n_1^2\right)^{1/2}\left[(\sigma_1 - \sigma_2)\sin^{-1} n_1 + (\sigma - \sigma_2)\frac{\pi}{2}\right]\right\}$$

(2.29)

with $n_1 = \frac{a}{iD/2 + r_0^*}$, $n_2 = \frac{iD/2}{iD/2 + r_0^*}$, b^* = the burgers vector and A = a dislocation factor.

The variables n_1 and n_2 represent the normalised value of crack length and the normalised value of fatigue damage size respectively (Wei *et al*, 2002).

The idea of the model is that the plastic zone (slip band) associated with the crack extends to the grain boundary where it is blocked. So the model assumes the interface of plastic and elastic deformation always coincides with grain boundaries. As the crack grows with the plastic zone still blocked at the grain boundary, the stress (σ_3) at a dislocation source in the barrier zone increases until it attains a value sufficiently high to activate the next dislocation source. So in this case the crack is able to propagate across the barrier because the barrier resistance is overcome, hence the crack tip moves and the elastic-plastic interface advances to the next grain. Crack growth rate is considered to be proportional to the crack tip opening displacement through a Paris type relationship:

$$\frac{da}{dN} = C.(\delta_t)^m \quad (2.30)$$

where the values of the parameters C and m are stress and material dependent. (Navarro & de los Rios, 1992)

Fatigue lives may be calculated by integrating the crack growth rate in each grain then individual partial lives are added to compute total life. The integration in each grain is made by using the initial crack length in each grain interval and the final crack length in each interval. According to this present model, the crack growth rate changes in value in an oscillatory manner every time crack tip plasticity is generated in a new grain. The end of the oscillation appears at the transition point between the short and long crack regimes, that is to say when the crack tip plastic zone and the corresponding crack strain can be predicted by LEFM.

In the NR model, grain orientations may be considered using a yielding orientation factor. After crack initiation and during early growth, the crack will propagate within just one grain (probably the best orientated grain in relation to the applied stress for plastic deformation). In this case the orientation factor should be low. As the crack grows the orientation factor corresponding to other successive grains should increase in magnitude until a value representative of truly polycrystalline behaviour is reached (via the Taylor value of 3.07 for face centred cubic materials)(de los Rios *et al*, 1994; Rodopoulos & de los Rios, 2002).

Similar models have been developed by other researchers, as for example, Edwards *et al.* (Edwards & Zhang, 1994b) and Tanaka *et al.* (Tanaka & Nakai, 1983).

2.1.3.8 Microstructure and fatigue crack growth resistance in Al-alloys:

The influence of microstructure in real commercial alloys on fatigue crack propagation may be complex and has been investigated by many researchers over the years. For example, tests in Al-alloys of varying aged condition have shown a high threshold levels and high crack growth resistance for underaged structures containing shearable precipitates when compared to overaged structures with non-shearable precipitates. The effects of inhomogeneous planar slip deformation (enhanced by shearable precipitates in underaged alloys) may be twofold. Planar slip may decrease fatigue crack growth rate by enhancing sllp reversibility, which results in less cyclic "damage" in the crack tip plastic zone (Grosskreutz, 1972; Starke & Staley, 1996). Furthermore, the more facetted, stage I-type growth that is promoted may enhance crack closure effects (see section 2.1.4). Many commercial alloys have dispersoids that inhibit grain growth during high temperature processing and subsequent heat treatment. Bucci *et al.* and Sanders and Staley (Sanders & Staley, 1979; Bucci *et al.*, 1980) have reported that dispersoids decrease the energy required to propagate monotonically loaded cracks by initiating microvoids that coalesce in void sheets and link cracks initiated at constituent particles. As such, dispersoids may influence static mode contributions to growth at high K_{max} levels. The presence of dispersoids may also reduce fracture surface roughness by their retardation effect on grain growth and their direct slip homogenisation effects. These effects may decrease fatigue crack growth resistance by reducing crack closure.

Coarse, secondary intermetallic particles are brittle and provide preferential monotonic crack paths ahead of a crack. Some studies show that the effect of the volume fraction of secondary particles (coarse intermetallic particles) on fracture toughness and fatigue crack growth rate under constant-amplitude loading depends on temper as well as on level of stress intensity factor range with greater influence tending to be seen at high ΔK levels (Xu, 2000). In 2024 under constant amplitude loading (Truckner *et al.*, 1976), at a stress intensity range of ~18MPa$\sqrt{m}$, the fatigue

crack growth resistance of 2024-sheet in the higher strength T86 temper is approximately doubled if the volume fraction of intermetallic constituents decreases from 2.2 to 1.4 %, whilst the lower strength T31 temper is not affected. On the other hand, at ΔK near 7MPa√m, the crack resistance is not influenced in either temper.

Coarse secondary particles are widely reported to have a direct effect on fatigue crack initiation in commercial alloys at low stress to intermediate levels (Halliday & Beevers, 1992). When stress levels are high, fatigue crack initiation may however be favoured at slip bands that are not associated with intermetallic particles (Sanders & Staley, 1979). Fatigue crack growth resistance of 2024 in T3 and T8 tempers under intermediate stress intensity range levels progressively decreases as monotonic yield strength increases either by artificial ageing or by stretching up to about 5% (Truckner *et al*, 1976). The effect of aluminium copper magnesium (Al_2CuMg) precipitates on fatigue crack growth rate may be attributed to their influence on cyclic strain hardening and softening as well as to their influence on ductility or toughness. The improved fatigue resistance of 2024 in a T3 at compared to a T8 temper has been accredited to the ability of GP zones to promote a high degree of cyclic hardening and planar slip (Truckner *et al*, 1976).

2.1.4 Crack Closure:

The phenomenon of crack closure is widely thought to exert a strong influence on fatigue crack growth. Closure ideas have been cited to explain, at least in a qualitative manner, a great many crack propagation effects, especially concerning the near-threshold region and variable amplitude fatigue.

In 1970, Elber (Elber, 1970) particularly highlighted the phenomenon of crack closure: specifically, he noted that a fatigue crack could close even at a far field tensile load. This observation indicated that the crack growth rate is not only influenced by the conditions ahead of the crack tip, but also by the nature of the crack face contact behind the crack tip. This premature contact may be generally termed "crack closure". Based on the incidence of closure, it was suggested that fatigue crack growth rates cannot be determined by the nominal stress intensity factor range, ΔK, but rather by an effective value ΔK_{eff} which accounts for fracture surface contact in

the wake of the fatigue crack tip. Thus the effective stress intensity factor range, ΔK_{eff}, at the crack tip is less than the applied ΔK. ΔK_{eff} may be defined as:

$$\Delta K_{eff} = K_{\max} - K_{cl} \quad (2.31)$$

where K_{cl}, larger than $K_{\min}$, is the stress intensity factor at which the fracture surfaces first come into contact during the unloading portion of the stress cycle (Elber, 1970).

Elber's work focused on the influence of prior plastic deformation on crack closure during fatigue fracture. This work represented just one closure mechanism: that is to say plasticity-induced closure. However, other sources of closure have been identified: corrosion layers can form within a fatigue crack (oxide-induced crack closure), surface asperities between crack surfaces can also form and interact (roughness-induced crack closure), viscous fluids can penetrate inside cracks, and stress or strain induced phase transformation can occur at the crack tip (Elber, 1970). Whilst the concept of closure is well established in the fatigue research community, controversy remains. For example, Vasudevan and Sadananda (Vasudevan *et al.*, 1994) have suggested that for a wide range of alloys closure effects may have an order of magnitude less effect on crack growth than is commonly supposed. It may be noted however that very many other authors have produced quite detailed experimental and theoretical evidences for a central role of crack closure in many aspects of fatigue crack behaviour (Dugdale, 1960; Beck *et al.*, 1967; Elber, 1970; Endo *et al.*, 1972; Budiansky & Hutchinson, 1978; Newman, 1981; Suresh *et al.*, 1981; Suresh *et al.*, 1982; Suresh & Ritchie, 1983; Newman, 1998; Sinclair & Gregson, 1998; Parry, 2001).

2.1.4.1 Plasticity induced crack closure:

As a fatigue crack grows through a succession of plastic zones, a plastic wake is of necessity left behind the crack (see Figure 2.16). During one cycle of crack growth, a residual plastic stretch is obtained due to the limited extent of reversed plasticity (the bulk of the material responds elastically on unloading, so the constraint of the surrounding elastic bulk results in "excess" plastic wake material being pushed back into the crack, and the crack flanks make contact behind the crack tip).

Elber argued that a fatigue crack could not propagate when the crack faces are closed and concluded that we would make be mistaken if we consider the total cyclic stress intensity amplitude to establish the Paris' relation: i.e.

$$\frac{da}{dN} = f(\Delta K) \quad (2.32).$$

The *effective* stress range $\Delta\sigma_{eff}$ and the corresponding effective stress intensity factor range ΔK_{eff} are then identified as:

$$\Delta\sigma_{eff} = \sigma_{\max} - \sigma_{cl} \quad (2.33)$$

$$\text{and } \Delta K_{eff} = K_{\max} - K_{cl} = U.\Delta K \quad (2.34)$$

U is then a proportional factor between ΔK_{eff} and ΔK. The corresponding characterisation of fatigue crack growth based on linear elastic fracture mechanics then becomes:

$$\frac{da}{dN} = C(\Delta K_{eff})^m = C(U.\Delta K)^m \quad (2.35)$$

Based on experimental compliance measurements from fatigue tests conducted in 2024-T3 aluminium alloy under plane stress conditions over a ΔK range of 13 to 40 MPa $m^{1/2}$ (at test frequencies of 1 Hz to 30 Hz and for R-ratio of -0.1 to 0.7), Elber (Elber, 1971) proposed the following relationship between the ratio of the closure stress intensity factor to maximum stress intensity and the R-ratio:

$$\frac{K_{cl}}{K_{\max}} = 0.5 + 0.1R + 0.4R^2 \quad (2.36)$$

It is now recognised that this relationship between R and the ratio of ΔK is strongly influenced by the stress state, alloy, the stress intensity factor range and environment. Many empirical relationships between opening stress intensity factor and the load ratio have been established by many investigators for different materials and loading conditions. (Budiansky & Hutchinson, 1978; Newman, 1981; Newman, 1998).

In 1978, Budiansky and Hutchison (Budiansky & Hutchinson, 1978) developed the first physically-based analytical model to understand the influence of plasticity induced crack closure on crack propagation. In this model, the assumptions must be made of steady state crack growth under plane stress conditions. The Dugdale model

(Dugdale, 1960) was used to estimate crack opening displacements. Upon unloading, the residual plastic stretch in the crack wake was seen to generate contact over the entire length of the crack for a load ratio equal to zero.

Budiansky and Hutchison's model may be shown to lead to:

$$\frac{K_{op}}{K_{\max}} = 1 - \left[\frac{1.37 \times E \times \sigma_y \times (\delta_t - \delta_R)}{K_{\max}}\right]^{\frac{1}{2}}, \quad (2.37)$$

where δ_t is the crack tip opening displacement at $K=K_{max}$, $\frac{\delta_R}{2}$ is the plastic stretch to be appended to the upper and lower crack faces by prior plasticity and K_{op} the opening stress intensity factor necessary to open fully the crack faces. They found that during unloading (i.e crack closing) at R=0, $K_{op}/K_{\max}$ is equal to 0.48, and during the reloading (i.e. crack opening) $K_{op}/K_{\max}$ is equal to 0.56 (Budiansky & Hutchinson, 1978). This model has a number of strengths and limitations: it provides a theoretical justification for the use of ΔK_{eff}, and rationalises reasonably well the effect of load ratio R on crack closure as reported by Elber. Limitations exist for example in that the model only "works" in plane stress; it does not invoke any mechanism of fatigue crack growth and it considers only one aspect of fatigue crack closure; other crack closure mechanisms such as oxide-induced and roughness-induced closure are not addressed (see below).

2.1.4.2 Oxide induced crack closure:

It has been realised that corrosion products formed within a growing crack can influence subsequent crack extension rates (see Figure 2.17). Endo *et al.* (Endo *et al*, 1972) showed the first indication that fatigue crack growth in steels may in fact be slower in aqueous environment than in air, and attributed the effect to the presence of oxide layers formed between the fracture surfaces in the aqueous tests. Suresh *et al.* (Suresh *et al*, 1981) suggested the possibility of crack closure due to corrosion debris influencing near-threshold growth rates and threshold values in certain aluminium alloys using secondary ion mass microscopy to measure the oxide layer thickness.

The presence of a moist atmosphere may particularly lead to the formation of oxide layers within a crack, which are thickened at a low R-ratio by "fretting oxidation", i.e., a continual breaking and reforming of surface oxide. The formation of corrosion deposits and the processes of oxide-induced crack closure are influenced by microstructure, environment, ΔK level and load ratio (Beck *et al*, 1967; Vasudevan & Suresh, 1982). At high load ratios ($R \geq 0.5$), the possibility of crack closure is minimised because increased crack tip opening displacements may effectively prevent oxide fretting. Assuming only a mechanical closure phenomenon arising from the presence of excess oxide debris on the crack faces and ignoring plasticity and hysteresis effects, the closure stress intensity factor at the crack tip (Suresh *et al*, 1982) (Suresh & Ritchie, 1983) may be obtained for the plane strain condition as:

$$K_{cl} = \frac{d_0 E}{4\sqrt{\pi l}\left(1-\upsilon^2\right)} \quad (2.38)$$

Where d_0 is the maximum excess oxide thickness, $2l$ the location behind the tip corresponding to the thickest oxide formation and $E/(1-\upsilon^2)$ the effective Young's modulus under plane strain conditions.

2.1.4.3 Roughness-induced closure:

Roughness induced crack closure has been identified as a major source of closure that can arise at near-threshold stress intensities due to the rough nature of the fracture surface, especially when crack tip opening displacements become comparable to the scale of fracture surface asperities (see Figure 2.18). The deflected nature of the crack leads to propping open of the crack if asperities contact prematurely on unloading.

Deflected crack paths and a degree of shear irreversibility are required for the mechanisms to operate. Overall it is suggested that roughness induced crack closure is enhanced by low stress intensity factor levels, underaged microstructures, large grain size and by environmental interactions (may enhance shear irreversibility at the crack tip), with stage I type crack growth being particularly conducive to the surface roughness and shear offsets that may give rise to roughness-induced closure. Several quantitative and semi-quantitative models of roughness induced crack closure exist in

the literature; for example Parry has developed finite element and analytical models to investigate crack closure processes arising from crack deflection, under both constant and variable amplitude loading conditions. (Parry, 2001).

2.1.5 Residual stresses & fatigue:

Residual stresses can be defined as stresses (tension or compression) that remain in a material or body after manufacture and processing, in the absence of external forces or thermal gradients. Residual stress measurement techniques invariably measure strains rather than stresses, and the residual stresses are deduced using the appropriate material parameters such as Young's modulus and Poisson's ratio. Residual stresses develop during manufacturing processes involving material deformation, heat treatment, machining or processing operation that transform the shape or change the microstructural properties of a material. The residual stresses may be sufficiently large to cause local yielding and plastic deformation, and can severely affect component performance. For this reason, it is vital that some knowledge of the internal stress state can be deduced either from measurements or modelling predictions

2.1.5.1 Residual stress generation and assessment:

Residual stresses may be generated or modified at every stage in a component life cycle, from original material production to final disposal. Most manufacturing processes (such as welding, brazing, forming or founding) and surface treatments produce residual stresses. Residual stresses can be beneficial for the structure or give unexpected failure or behaviour.

Welding is one of the most significant causes of residual stresses and typically produces large tensile stresses whose maximum value may be of the order of the yield strength of the materials being joined, balanced by lower compressive residual stresses elsewhere in a component (Masubuchi, 1980). The welding generates a highly localised thermal transient, which causes the weld area to be heated up sharply relative to the surrounding material. The main source of residual stress is produced by the shrinkage of the weld. Figure 2.19(a) shows a simple illustration of residual stresses formed by shrinkage in a butt weld. The main orthogonal stresses are

designated by σ_{xx} and σ_{yy}: stresses that are parallel to the weld direction and transverse to it respectively. A typical distribution of the longitudinal residual stress, σ_{xx}, is shown in Figure 2.19(b). Tensile stresses of high magnitude are produced in the region near the weld. These decrease rapidly and become compressive after a distance several times the width of the weld metal. Figure 2.19(c) shows the distribution of the transverse residual stress, σ_{yy}. Tensile stresses of relatively low magnitude are produced in the middle part of the joint whilst compressive stress exists at the ends of the weld.

A second important source of residual stress may be related to volume expansion arising from phase transformation in the weld and surrounding material occurring during the welding process and cooling period. If the yield stress of the material is significant during the time of the phase change, compressive residual stress can be generated in the weld area.

Figure 2.20 presents a schematic illustration of typical longitudinal stress distribution for three different welded materials. Figure 2.20(a) shows the longitudinal stress distribution for mild and low alloy steels where the shrinkage is a dominant component, resulting in a tensile zone in the fusion zone with a magnitude close to the yield limit. Small compressive stresses due to phase transformations may be found in Al-alloys whilst high compressive stress due to phase transformation may be present in high alloy steels (see Figure 2.20(b) & (c)). The peak value in the tensile region may then be reduced as shown in Figure 2.20(b). The stress distribution given in Figure 2.20(c) is for high alloy steels where significant phase transformation gives compressive stresses in the weld centre (Radaj, 1992).

Various quantitative and qualitative methods have been developed to assess residual stresses over the last few decades. In general, a distinction is made between *destructive* and *non-destructive* techniques. The first series of methods is based on destruction of the state of equilibrium of the residual stress after sectioning of the mechanical component, machining or layer removal. The redistribution of the internal forces leads to local strains, which are measured to evaluate the residual stress field. The residual stress is deduced from the measured strain using elasticity theory (analytical approaches or finite element calculations). The most usual methods are:

- *Hole drilling:* Hole drilling is one of the most widely used techniques for measuring residual stresses. It is relatively simple, cheap, quick and may be used in laboratory or field work. The principle of the technique involves drilling a small hole into a component containing residual stresses. The relieved surface strains can be measured by a special residual stress strain gauge rosette, allowing a back-calculation of residual stress to be made. Whilst hole drilling technique can be applied to a wide range of materials, components, and weld materials, drilling may cause plastic strain at the periphery of the hole, which may displace the measured results. This method is not valid for residual stresses greater than 50% of yield stress and for depths more than ~10mm. Another major problem with the hole drilling technique is the interpretation of the data (Flewitt *et al.*, 2002).

- *Deep Hole drilling:* Deep hole drilling technique is a variation of the previous technique, which has been developed for measuring residual stresses in thick-sections. The basic procedure involves drilling a small reference hole through the specimen. The internal diameter of the hole is accurately measured. Using a trepan cylinder, a new hole containing the reference hole is drilled up to a certain depth. A new measurement of the diameter of the reference hole at the same location as before is carried out; the change in diameter and height is then converted into stresses. This technique may measure residual stresses to very large depth (~100mm), however the technique is technically challenging and time consuming (~10 days to measure one hole) (Flewitt *et al*, 2002).

- *Plate sectioning using resistance strain gauges*: Strain gauges are attached on the plate on which the residual stress measurements have to be carried out. Parts of specimen are sequentially cut and strain relaxations are then measured. This method may achieve a high accuracy. It gives average stresses over the area of the piece removed from the specimen. This method is not suitable for measuring locally concentrated stresses (Flewitt *et al*, 2002).

The second series of methods (non-destructive techniques) is based on the relationship between the physical and crystallographic parameters, and residual stress. The most developed methods are:

- *Laboratory X-ray, synchrotron X-ray and neutron diffraction:* These methods are based on the use of the lattice material spacing as a strain gauge. Synchrotron X-ray measurements reveal high resolution and stress field reproducibility (Flewitt *et al*, 2002). Details of how diffraction data may be used to determine residual stress levels are described further in Appendix 1.

- *Ultrasonic techniques:* These techniques are based on variations in the velocity of ultrasonic waves, which can then be related to the residual stresses.

- *Magnetic methods* rely on the interaction between magnetization and elastic strain in ferromagnetic materials. Different magnetic properties can be studied: permeability, magnetostriction, and hysteresis.

Prediction of residual stresses by numerical modelling of welding and other manufacturing processes has increased rapidly in recent years. Modelling of welding is technically and computationally demanding, and simplification and idealisation of the material behaviour, process parameters and geometry are inevitable. Numerical modelling is a powerful tool for residual stress prediction, but validation with reference to experimental results is clearly essential (Flewitt *et al*, 2002).

2.1.5.2 Residual stresses in fatigue:

As presented earlier, the behaviour of components during cycling loading is influenced by the materials properties based on the microstructure, however it may be also influenced in many cases by the magnitude and distribution of residual stresses. (El-Soudani & Pelloux, 1975; Miyazaki *et al.*, 1999; Bussu & Irving, 2000). The fatigue analysis of as-welded structure is often complicated by the presence of high tensile residual stresses in the weld region. Compressive residual stresses effects are generally beneficial on the fatigue life, but may cause a decrease in buckling loads. Tensile stress on the contrary often reduces the mechanical performance of materials (El-Soudani & Pelloux, 1975; Kang *et al.*, 1989; Kang *et al.*, 1990; Peyre *et al.*, 1992; Miyazaki *et al*, 1999; Bussu & Irving, 2000; Mochizuki *et al.*, 2000).

Different investigations have been reported to evaluate the influence of residual stress fields on fatigue crack propagation. For example, it is possible to use the principle of stress superposition leading to stress ratio changes and sometimes to redistribution of the residual stresses caused by crack propagation (El-Soudani &

Pelloux, 1975; Glinka, 1979; Miyazaki *et al*, 1999; Bussu & Irving, 2000; Mochizuki *et al*, 2000). In an elastic regime, residual stresses may just be added to the applied stress as a static load. This may for example lead to an apparent increase in fatigue limits. When the total stress (applied and residual stress) exceeds the yield strength, the material plastically deforms. This leads in changes of the residual stress field: an adaptation of the structure to the applied load takes place. In the case of cyclic loading, cracks can initiate and propagate at stress levels much lower than the yield strength leading to a redistribution (relaxation) of the residual stress.

The effect of residual stress on fatigue has been evaluated by considering the effect of crack opening and closing (Kang *et al*, 1989; Beghini & Bertini, 1990; Kang *et al*, 1990; Beghini *et al.*, 1994), as such fatigue crack growth through a tensile residual stress field may be thought to be governed by the crack closure phenomenon. Tensile residual stress may then act to increase the effective stress intensity factor range ΔK_{eff}, and then accelerate the crack propagation. Compressive residual stress fields may conversely reduce the effective stress intensity factor range, with corresponding reduction in crack propagation rates.

Depending on the residual stress field across a welded material, crack propagation behaviour may vary through the weld and heat affected zone. It may also be noticed that residual stress relaxation, due to fatigue, or annealing, and surface layer removal (machining) produce dimensional changes in industrial components. High tensile stresses generated by machining of work hardening alloys, hard turning of steels, grinding, welding, and many forming operations can be highly deleterious to fatigue performance. The effect may be most significant in the high cycle fatigue regime where the applied stress magnitude may not be sufficient to significantly relax the residual stresses produced during manufacturing.

2.2 Materials background:

Commercial wrought aluminium alloys are commonly classed into two categories: non-heat treatable and heat treatable. The non-heat treatable alloys are commonly Al-Mn and Al-Mg-based, with their properties being controlled by solid solution strengthening and cold deformation. Typical applications include automotive frames

and panels. The wrought heat treatable alloys of interest in airframe structures, such as Al-Cu (2xxx), Al-Mg-Si (6xxx) and Al-Zn-Mg (7xxx), develop significantly higher strengths via precipitation hardening.

2.2.1 High Strength Heat Treatable Aluminium Alloys:

The 2xxx series of alloys is often used in fuselage and lower wing structures of civil aircraft due to their good damage tolerance (cyclic and static crack growth resistance), whereas the 7xxx series is commonly used in upper wing structures due to their high strength: whilst the exact tempers used for commercial applications vary between the two alloy groups, the heat treatment principles are the same.

During the heat treatment (see Figure 2.21), the key successive steps are:

1- Solution heat treatment:

At high temperature, there is annealing within the single-phase region to dissolve the alloying element(s).

2- Quenching:

A rapid cooling is applied to obtain a supersaturated solid solution of the alloying elements and vacancies in the aluminium matrix.

3- Ageing:

At room temperature (natural ageing) or an intermediate temperature (artificial ageing), there is decomposition of the supersaturated solid solution, which produces precipitate particles: Guinier-Preston (GP) zones, intermediate meta-stable precipitates, and equilibrium precipitates.

GP zones are typically small, ordered, and coherent with the matrix, and very finely dispersed within the matrix. Zones are commonly identified as clusters of solute atoms with significant controversy still surrounding their exact structure (Gao *et al.*, 2002). The density of GP zones may be of the order of 10^{17} and 10^{18} cm^{-3} (Polmear, 1995), producing a significant strengthening effect despite their relative shearability. GP zones are usually, but not always, followed by the formation of semi-coherent intermediate particles of meta-stable phases. Intermediate precipitates either nucleate homogeneously within the aluminium matrix or heterogeneously at lattice defects such as dislocations or sub-boundaries (Buhl, 1992). Equilibrium precipitates are

generally larger and more widely spaced than the intermediate particles. They can form directly from supersaturated solid solution or by transformation of intermediate precipitates and are commonly incoherent with the matrix. Grain boundaries and sub-grain boundaries, or the interface between other particles and the matrix may be particularly effective sites for the nucleation of equilibrium precipitates.

Two further categories of particles are generally present in commercial high strength age hardenable aluminium alloys. These are coarse intermetallic (or "constituent") particles, and dispersoid particles. Coarse intermetallic particles are, in most cases, compounds of impurity elements (specifically Fe and Si). They form inter-dentrically during solidification. During subsequent working of the ingots, the largest of the remaining particles (after homogenisation) are fractured, which reduces their size to the range of 1-10μm and causes them to become aligned as stringers in the working direction. Dispersoid particles in aerospace Al-alloys generally contain Mn, Cr or Zr. They control the grain structure by preventing recrystallisation and grain growth. Their distribution in the matrix is often inhomogeneous (due to casting segregation) and is not influenced by age hardening treatments. They contribute only slightly directly to the strength of the alloys but they influence it indirectly via the grain structure. The Cr and Mn containing dispersoids (e.g. $Al_{12}Mg_2Cr$ and $Al_{20}Mn_3Cr$) are typically incoherent and relatively large (up to 0.5 μm in the longest dimension), whilst Zr containing generally contain smaller, coherent Al_3Zr particles (Buhl, 1992).

All alloys in which precipitation occurs may exhibit distinct precipitate free zones (PFZ) along grain boundaries. PFZs may be due to solute depletion or/and vacancy depletion. For solute depletion, there is a narrow region near grain boundaries where solute elements are depleted due to the ready diffusion of solute atoms into the large particles of equilibrium phase which may have formed there. For vacancy depletion, vacancies are reduced to levels below those needed to assist with the formation of precipitates (boundaries act as an effective sink for the vacancies) (Polmear, 1995).

2.2.2 2xxx Aluminium alloys:

2.2.2.1 General characteristics:

The International Alloy Designation System (IADS) designates 2xxx series aluminium alloys having copper as the main alloying element although most commercial variants also containing significant magnesium additions. The ageing sequence for simple binary Al-Cu alloys during artificial ageing can be described as:

SS_α (Supersaturated solid solution α) → GP zones →θ" →θ' → θ (Al_2Cu) (1)

And for alloys which additionally contain magnesium (At% Mg ≈ At% Cu):

SS_α (Supersaturated solid solution α) → GP (B) zones → S' → S (Al_2CuMg) (2)

Details of these phases and zones are summarised in Table 2.1 (Gregson, 1996).

Precipitates	*Crystallography*
Al-Cu(-Mg) with high Cu/Mg	
GP zones	Cu-rich zones (thin plates)
θ"	Fully coherent intermediate precipitates probably nucleated at GP zones
θ' – $CuAl_2$	Semi-coherent plates on $(100)_\alpha$ generally nucleated at dislocations Tetragonal: a = 0.404 nm, c=0.580 nm
θ - $CuAl_2$	Incoherent equilibrium phase which may nucleate at the surface of θ' Body centred tetragonal: a= 0.607 nm, c= 0.487 nm
Al-Cu-Mg with low Cu/Mg	
GP zones	Cu- and Mg- rich zones as thin rods along $<100>_\alpha$
S' – Al_2CuMg	Semi-coherent laths on <210> along >100> nucleated at dislocations. Orthorhombic: a= 0.404 nm, b= 0.925 nm, c= 0.718 nm
S - Al_2CuMg	Incoherent equilibrium phase of similar morphology to S' Orthorhombic: a=0.400nm, b=0.923nm, c= 0.717nm

Table 2.1 Crystallography of precipitates commonly seen in 2xxx alloys (Gregson, 1996).

2.2.2.2 2024-T351:

2024-T3 is one of the most popular of the 2xxx alloys for aerospace applications and was introduced in the 1930s. 2024 is an Al-Cu-Mg alloy, following closely the ageing behaviour in equation (40). Mn is particularly used as the dispersoid forming element to control grain structure. In the nomenclature of heat treatable aluminium alloys, T3 indicates the alloy has been solution treated and then allowed to naturally age; additional digits can be added to give a more detailed description of the alloy condition: 2024-Tx51 is an alloy that has been stress relieved by stretching to 0.5-3% prior to ageing. In the naturally aged condition, 2024 has a high ductility, excellent fatigue crack propagation resistance and high fracture toughness. In general, the fuselage skin and the lower wing skins of commercial aircraft such as those of Boeing or Airbus are manufactured from 2024-T3 (or closely related variants). Their associated rates of fatigue crack growth may be close to one third those observed in the 7xxx series alloys (Gregson, 1996).

2.2.2.3 Strength development:

Generally, the interaction of mobile dislocations with precipitates control the strength of heat-treatable alloys. The strength increase due to precipitate formation (i.e. on ageing) is essentially a function of the particle radii and separation distances. In the first stage of age hardening, the precipitates (GP zones and metastable precipitates) are small and coherent with the matrix and may be sheared by dislocations during plastic flow. As such strength increases with the particle size as the shear strength of the precipitates increases (see Figure 2.22) up to the critical radius r_c shown on the x-axis.

As age hardening progresses, the particles grow and lose their coherency with the matrix and can no longer be cut by moving dislocations. The particle-dislocation interaction then changes from shearing to looping (Orowan strengthening). The strength is then inversely proportional to particle size (for a fixed volume fraction of precipitate) as particle spacing becomes the controlling strength parameter (beyond r_c in Figure 2.22). The intersection point between shearing and looping of precipitates broadly represents the maximum strength that can be developed in the alloy.

Complex interactions occur among GP (GPB) zones, solute atoms and vacancies during natural ageing in 2xxx series aluminium alloys. Although the extent and the rate of natural ageing vary from one alloy to another, most of the strengthening occurs during the first day and is stable after four days. For 2024 type alloys, cold work after the quench from the solution heat treatment increases strength by increasing dislocation density in natural aged materials and by refining the size of S' (Al_2CuMg) produced during subsequent artificial ageing (Truckner *et al*, 1976). While the maximum strength cannot normally be realised during natural ageing, many 2xxx alloys are used in naturally aged tempers such as T3 and T4 due to their balance of strength, ductility, fracture toughness and fatigue crack growth resistance. It is well established that in 2xxx alloys (and indeed most conventional metallic materials), the increased strength is associated with artificial aged tempers.

2.3 Fusion Welding:

Significant interest has been shown in the use of advanced welding techniques for aircraft structure, particularly in relation to the design opportunities that they afford over established mechanical joining methods. Whilst different processes of welding exist and continue to be improved, *Metal Inert Gas (MIG) welding* and *Variable Polarity Plasma Arc (VPPA) welding* are two techniques of fusion welding under particular consideration for welded airframe structures and are studied in this thesis. They are considered industrially to produce high quality welds and are suitable for automation, which allows an increase in productivity. Other techniques of welding that have been studied for airframe applications include for example:

(i) Gas Tungsten Arc Welding (GTAW) is frequently referred to as TIG welding. TIG welding is a commonly considered as high quality welding process and has become a popular choice of welding processes when high quality, precision welding is required. In TIG welding an arc is formed between a non-consumable tungsten electrode and the metal being welded. Gas as Argon or helium or argon and hydrogen is fed through the torch to shield the electrode and the molten weld pool. If filler wire is used, it is added to the weld pool separately. Helium is generally added to increase heat input

(increase welding speed or weld penetration). Hydrogen will result in cleaner looking welds and also increase heat input; however, Hydrogen may promote porosity or Hydrogen cracking.

(ii) Friction Stir Welding is distinctive in being a low energy, solid-state process. In the Friction Stir Welding process (process invented and patented by TWI), a welding tool moves along the area to be joined while rotating at a high speed. The action between the tool and the aluminium creates frictional heat, which softens the aluminium but does not melt it. The plasticized material is then, in essence, consolidated to create one piece of metal where there were originally two. The weld is left in a fine-grained, hot worked condition with no entrapped oxides or gas porosity.

(iii) Electron Beam welding that in its most simple form, is carried out by translating the beam, with respect to the parts to be joined, and locally melting the material. No filler addition or consumable is necessary and welding is achieved in a single pass almost irrespective of the material thickness. Consequently the weld quality and properties achievable are controlled by the composition of the material alone.

(iv) Laser Welding is the joining of two metals using a high power laser to melt portions of both metals so they mix and solidify as one piece to create a desired combination of strength, stiffness and weight savings.

Further aspects of MIG and VPPA welding are considered in section 2.3.2 and 2.3.3

2.3.1 General features of fusion welds in aluminium alloys:

Three main zones can be defined in relation to a typical fusion weld:

- The base (parent) metal, i.e. material essentially unaffected by welding
- The heat affected zone (HAZ), i.e. phases and grain size differ from parent material due to thermal cycling
- The weld metal, i.e. recast base metal with or without filler

The boundary between material that has been recast and that which remains fully solid (the HAZ) is described as the fusion line, transition zone or partial melting zone, see Figure 2.23.

Problems are conventionally considered to exist in the fusion welding of high strength alloys (7xxx, 2xxx). Specifically, such materials may be considered prone to liquation and solidification cracking or porosity problems.

Two categories, based on cracking mechanism and cracking location, may be used to classify weld defects in aluminium alloys. Solidification cracks appear within the weld zone, whilst liquation cracking occurs adjacent to the fusion zone and may or may not be readily apparent. Solidification cracking (or hot tearing) is due to high levels of thermal stress and solidification shrinkage present in the weld zone due to the inability of the liquid to support the strain imposed by this shrinkage (Dowd, 1972; ASM International, 1998). Solidification cracking can be effectively controlled using a selected filler alloy: the associated additives modify the alloy or base metal constituents, which may not always be desirable. The liquation cracking region is associated with a thin boundary layer adjacent to the fusion zone that is referred to as the partially melted region. This region is produced when eutectic phases or constituents (that have low melting points) liquate or melt at grain boundaries during welding (ASM International, 1998). As such, this is may be strongly dependant on the parent alloy composition and condition.

Aluminium alloys are also highly susceptible to hydrogen porosity during welding. Porosity generally is produced when the weld pool absorbs hydrogen. Hydrogen dissolves readily into the molten weld pool and produces gas pores (cavities) upon solidification. Common sources of hydrogen are water in the form of moisture on the metal surface, shield gas leaks. Oil and other lubricants also act as hydrogen sources. Hydrogen porosity can be avoided by using proper gas shielding during welding, keeping the aluminium clean and dry, and avoiding temperature fluctuations that lead to condensation. Also the cooling rate will dramatically affect the formation and growth of porosity. Rapid cooling rates retard growth by eliminating the time available for diffusion of hydrogen.

High strength aluminium alloy weld metal microstructures are reported to exhibit equiaxed-dendritic structures with the edge of the fusion zone often exhibiting a parallel array of columnar α-aluminium dendrites and interdentritic second-phase constituents (Cross & Edwards, 1989; Norman *et al.*, 1997; Norman *et al.*, 1998b;

Norman & Prangnell, 1998). Axial columnar structures have also been noted. For example, it has been noted by Norman *et al.* (Norman *et al*, 1997) that the weld centre line may present at high welding speed an axial dendritic structure parallel to the heat source. It has been also shown that the addition of an Al-Cu filler wire 2319 during the welding process of the 2024 alloys may allow a refinement in the equiaxed region of the weld (Norman *et al*, 1997).

Several papers report relationships between hardness profile and microstructure characterisation in a fusion welded structure, particularly in terms of HAZ region. For example, Norman *et al.* (Norman *et al.*, 1998a) suggested for Al-Cu-Mg autogeneous TIG welds that precipitation reactions occur across the whole weld. A complex hardness profile is identified and a balance between aging, overaging, re-solutionising and re-precipitation is suggested across the heat affected zone, with the near fusion zone hardness being attributable to partial re-solutionising and re-aging and the loss of strength being attributable to over-aging. Such loss in hardness has also been reported for a VPPA welded Al-Cu alloy (Martukanitz *et al.*, 2000) considering the Orowan relationship to describe the loss of strength.

Whilst fatigue in friction stir welding of heat-treatable airframe alloys is becoming relatively well reported in the literature, literature on fatigue of fusion welded heat-treatable airframe alloys is limited. Friction stir welds do not contain a recast fusion zone of course, however aspects of the heat-affected zone might be considered relatively similar, with, for example, a loss of strength being identified with over-aging in fusion welded and friction stir welded materials. Considering the 2024 Al-alloy welded by friction sir welding, it has been reported (Booth, 2003) that fatigue life of a friction stir welded structure is lower than the fatigue life of parent material. Two failure locations were identified: outside the weld nugget region (in the HAZ) where initiation came from S-phase particles and over the nugget region where initiation came from coarse intermetallics or linear defects at/or just below the surface. Bussu and Irving (Bussu & Irving, 2000) suggested that residual stress in 2024-T351 friction stir welds dominates fatigue crack growth rates. In terms of fatigue in fusion welds, Lin *et al.* (Lin *et al.*, 2003) have reported, for MIG welded 2024 and 7150 aluminium

alloys tested in fatigue (long crack regime) with dog-bone coupon samples (1mm crack was placed at the centre of the weld, perpendicular to the weld line), that fatigue crack propagation was influenced by residual stress field, hardness and microstructure variation. They suggested that controlling these factors may optimise the damage tolerance capability in welded safety critical structure. In the fusion zone of both welds, the lowest hardness region was seen to coincide with the smallest growth rates. In the HAZ the residual stress peak was reported to coincide with fast growth rates. Chaturvedi and Chen (Chaturvedi & Chen, 2000) worked on fatigue on weld simulations in the Al-Li alloy (2195), particularly to simulate HAZ behaviour. It was reported that fatigue strength decreased with the weld simulation due to coarsening of grain size and presence of microcracks and voids along grains boundaries.

2.3.2 Metal Inert Gas welding:

Metal Inert Gas (MIG) welding was first patented in the USA in 1949 for welding aluminium. From about 1952 the process became popular in the UK for welding aluminium using argon as the shielding gas, and for carbon steels using CO_2. MIG is an attractive alternative to Manual Metal Arc (MMA), offering high deposition rates and high productivity.

MIG is similar to MMA in that heat for welding is produced by forming an arc between a metal electrode and the workpiece; the electrode melts to form the weld bead. The main difference is that the metal electrode has a small diameter wire fed from a spool. As the wire is continuously fed, the process is often referred to as automatic or semi-automatic welding. MIG welding productivity is typically twice MMA productivity but the equipment is more expensive. A schematic representation of a MIG torch is shown Figure 2.24. The temperature generated at the arc causes melting of both the filler wire and the parent metal, and in order to maintain an arc and a continuous weld, the wire must be supplied to the arc at a speed to match the melting rate. In this process, no deslagging is required. MIG is widely used in many industry sectors and accounts for almost 50% of all weld metal deposited. Compared to MMA, MIG has the advantage in terms of flexibility, deposition rates and suitability for automation. MIG welding of aluminium is commonly performed with

direct current and a positive electrode, using either a constant-voltage or constant-energy power supply. The effect of different gas mixtures on weld bead shape and penetration was discussed by Reichelt *et al.* (Reichelt *et al.*, 1980) who have suggested argon to be the optimal shielding gas. Overall argon shielding gas promotes arc stability and results in a clean weld appearance.

In the MIG welding process, the filler wire serves as a consumable electrode, melting off as a spray of droplets at high welding currents or as discrete drops at lower welding currents. Filler metal composition may be determined by the weldability of the parent metal, minimum mechanical properties of the weld metal, corrosion resistance and anodic coating requirements.

2.3.3 Variable Polarity Plasma Arc welding:

The Variable Polarity Plasma Arc (VPPA) welding concept dates to 1947, but has been relatively poorly developed over the intervening years. In the 80's, the VPPA process was investigated extensively by NASA for high quality welding of aluminium alloys (Hou *et al.*, 1996; Micheli & Pistor, 1998; Micheli & Pilcher, 2000). The VPPA welding technique integrates two features, a plasma arc (PA) and variable polarity (VP).

VPPA welding employs variable current waveforms that enable the welding system to operate for pre-set time increments in either of positive or negative polarity modes. The VPPA welding controls the polarity of the arc by varying the amounts of direct current electrode negative (DCEN or straight polarity or welding current) and direct current electrode positive (DCEP or reverse polarity). Typically for an aluminium of 2xxx series, the VPPA welding process uses a high current, DCEP of around 180Amps for a short time (~3ms) and a welding current of around 150Amps for a longer time (~19ms) (Martikainen, 1995; Hou *et al*, 1996; Micheli & Pilcher, 2000)). Using welding current (DCEN) compared to reverse polarity current gives higher arc efficiencies. Whilst reverse polarity does not transfer as much as heat, it has the advantageous effect of cleaning and etching the weld surface. The cathodic etching of the DCEP enhances the weld pool flow characteristics significantly, making keyhole possible. The cathodic cleaning of the refractory oxide on aluminium

improves the electrode life (Nunes *et al.*, 1984; Martikainen, 1995). Figure 2.25 shows a schematic of the weld torch. The plasma arc is particularly carried by a constricted gas flow (Argon or Helium). Weld pool shielding is provided by a concentric annular flow of helium or argon. By controlling the welding current and plasma gas flow, a powerful plasma beam may be created. The plasma arc blows a hole into the material to be joined, whilst behind the hole the molten metal flows together (due to gravity (if vertical setup), surface tension or gas pressure from the shielding gas) to form the weld.

VPPA welding can be used to weld relatively thick sections: up to 15 mm in a single pass for most aluminium alloys. A filler wire is generally used to ensure a smooth profile without undercut. VPPA welding of aluminium alloys is particularly considered to produce high quality welds in one pass with a low gas/pore content (Hou *et al*, 1996). The use of variable polarity associated to plasma welding provides the power density to produce keyhole welding. In addition, the variable polarity welding provides the oxide layer from the aluminium weld surface to be removed through cathodic cleaning or etching. Removing the oxide layer improves the weldability of the weld pool, forming a higher quality weld and substantially reducing the cost associated with weld preparation.

References

ASM International (1998). Aluminium and Aluminium Alloys. in. A. S. Handbook, Davis, J.R.: 376-420.

Bathias, C. and J.-P. Baïlon (1997). in La fatigue des matériaux et des structures. Paris, Hermes.

Beck, A. F., M. A. Heine, E. J. Caule and M. J. Pryor (1967). "The kinetics of the oxidation of Al in oxygen at high temperature." Corros. Sci. 7(1): 1-22.

Beghini, M. and L. Bertini (1990). "Fatigue crack propagation through residual stress fields with closure phenomena." Engineering Fracture Mechanics 36(3): 379-387.

Beghini, M., L. Bertini and E. Vitale (1994). "Fatigue crack growth in residual stress fields: experimental results and modelling." Fatigue and Fracture of Engineering Materials and Structures 17(12): 1433-1444.

Bilby, B. A., A. H. Cottrell and K. H. Swinden (1963). "The spread of plastic yield from a notch." Proc. Roy. Soc. Lond. 272A: 304-314.

Bomas, H., T. Linkewitz and P. Mayr (1996). "Short cracks and lifetime of a normalized carbon steel under cyclic block loading." Fatigue and Fracture of Engineering Materials and Structures 19(2/3): 299-307.

Booth, D. P. P. (2003). Fatigue of friction stir welded AA2024-T351 plate (PhD Thesis). Materials Research group, School of Engineering Sciences. Southampton (UK), Southampton.

Bucci, R. J., A. B. Thakker, T. H. Sanders, R. R. Sawtell and J. T. Staley (1980). "Effect of Load Spectrum Variables on Fatigue Crack Initiation and Propagation." ASTM STP 714: 41-78.

Budiansky, B. and J. W. Hutchinson (1978). "Analysis of closure in fatigue crack growth." Journal of Applied Mechanics 45: 267-276.

Buffiere, J. Y., S. Savelli, P. H. Jouneau, E. Maire and R. Fougeres (2001). "Experimental study of porosity and its relation to fatigue mechanisms of model Al-Si7-Mg0.3 cast Al alloys." Materials Science and Engineering a-Structural Materials Properties Microstructure and Processing 316(1-2): 115-126.

Buhl, H. (1992). Advanced Materials. in Advanced Aerospace Materials. Springer-Verlag: 20-25.

Bussu, G. and P. E. Irving (2000). "Fatigue performance of Friction Stir Welded 2024-T351 aluminium joints." International Journal of Fatigue 25(1): 77-88.

Chaturvedi, M. C. and D. L. Chen (2000). "Influence of weld simulation on the microstructure and fatigue strength of 2195 Aluminium-Lithium Alloy." Materials Science Forum(331-337): 1769-1774.

Cottrell, A. H. and D. Hull (1957). "Extrusion and intrusion by cyclic slip in copper." Proc. Roy. Soc. Lond. A242: 211-213.

Cross, C. E. and G. R. Edwards (1989). Welding of aluminium alloys. in Aluminum Alloys--Contemporary Research and Applications. A. K. Vasudevan and R. D. Doherty, Elsevier Science & Technology. 31.

de los Rios, E. R., X. J. Xin and A. Navarro (1994). "Modelling microstructurally sensitive fatigue short crack growth." Proc. Roy. Soc. 447: 111-134.

Donahue, R. J., H. M. Clark, P. Atanmo, R. Kumble and A. J. McEvily (1972). "Crack opening displacement and the rate of fatigue crack growth." International Journal of Fracture 8: 209-219.

Dowd, J. D. (1972). "Weld cracking of Aluminium Alloys." Welding Journal 31(10): 448s.

Dugdale, D. S. (1960). "Yielding of stell sheets containing slits." Journal of the mechanics and physics of solids 8: 100-108.

Edwards, L. and Y. H. Zhang (1994a). "Investigation of Small Fatigue Cracks .1. Plastic-Deformation Associated with Small Fatigue Cracks." Acta Metallurgica Et Materialia 42(4): 1413-1421.

Edwards, L. and Y. H. Zhang (1994b). "Investigation of Small Fatigue Cracks .2. A Plasticity Based Model of Small Fatigue-Crack Growth." Acta Metallurgica Et Materialia 42(4): 1423-1431.

Elber, W. (1970). "Fatigue Crack closure under cyclic tension." Engineering Fracture Mechanics 2: 37-45.

Elber, W. (1971). Significance of fatigue crack closure. in Damage Tolerance on Aircraft Structures. Philadelphia, ASTM. STP 486: 230-242.

El-Soudani, S. M. and R. M. Pelloux (1975). "Anisotropy of fatigue crack propagation in aluminium alloy butt welded joints." Welding Journal: 144s-153s.

Endo, K., T. Okada and T. Hariya (1972). "Fatigue Crack Propagation in Bearing Metals Lining on Steel Plates in Lubricating Oil." Bulletin of the Japan Society of Mechanical Engineers 15(82): 439-445.

Flewitt, P., R. Legatt, P. Withers and A. Dowling (2002). Residual stresses: their origin, measurement and application, The Institute of Materials, London, UK Forum for Engineering Structural Integrity,

Forman, R. G., V. E. Kearney and R. M. Engle (1967). "Numerical analysis of crack propagation in cyclic loaded structures." Journal of Basic Engineering 89: 459-464.

Forsyth, P. J. E. (1972). "Fatigue behaviour and its dependance on microstructure." Colloq. Metall. 15: 1-25.

François, D., A. Pineau and A. Zaoui (1995). in Comportement mécanique des matériaux. Paris, Hermes.

Gao, N., L. Davin, S. Wang, A. Cerezo and M. J. Starink (2002). Precipitation in stretched Al-Cu-Mg alloys with reduced alloying content studied by DSC, TEM and atom probe. ICAA8, Cambridge, Trans Tech publications, 2, 923-928.

Gerard, D. A. and D. A. Koss (1990). "Porosity and crack initiation during low cycle fatigue." Materials Science and Engineering a-Structural Materials Properties Microstructure and Processing A(129): 77-85.

Glinka, G. (1979). "Effect of Residual Stresses on Fatigue Crack Growth in Steel Weldments Under Constant and Variable Amplitude Loads." American Society for Testing and Materials: 198-214.

Grabowski, L. and J. R. Yates (1992). "The Effect of Specimen Geometry on Short-Crack Growth-Behavior of a Nickel-Based Superalloy." International Journal of Fatigue 14(4): 227-232.

Gregson, P. J. (1996). Aluminium Alloys. in: 49-84.

Grosskreutz, J. C. (1972). "Strengthening and Fracture in Fatigue (Approaches for Achieving High Fatigue Strength)." Met. Trans. 3(5): 1255-1262.

Halliday, M. D. and C. J. Beevers (1992). Fatigue crack growth on 2024. ICAA3, Norwegian Institute of Technology, Trondheim, Norway, NTH-SINTEF, 3, 526-532.

Hobson, P. D. (1982). "The formulation of a crack growth equation for short cracks." Fatigue of Engineering Materials and Structures 5(4): 323-327.

Hou, R., D. M. Evans, J. C. McClure, A. C. Nunes and G. Garcia (1996). "Shielding gas and heat transfer efficiency in plasma are welding." Welding Journal 75(10): S305-S310.

Irwin, G. R. (1964). "Structural aspects of brittle fracture." Applied mechanics research 3: 65-81.

Kang, K. J., J. H. Song and Y. Y. Earmme (1989). "Fatigue crack growth and closure through a tensile residual stress field under compressive applied loading." Fatigue and Fracture of Engineering Materials and Structures 12(5): 363-376.

Kang, K. J., J. H. Song and Y. Y. Earmme (1990). "Fatigue crack growth and closure behaviour through a compressive residual stress field." Fatigue and Fracture of Engineering Materials and Structures 13(1): 1-13.

Knott, J. F. (1973). in Fundamentals of Fracture Mechanics. London, Butterworths.

Kung, C. Y. and M. E. Fine (1979). "Fatigue Crack Initiation and Microcrack Growth in 2024-T4 and 2124-T4 Aluminium Alloys." Metallurgical Transactions A 10A: 603-610.

Laird, C. (1967). The influence of metallurgical structure on the mechanisms of fatigue crack propagation. in Fatigue crack propagation. ASTM. Special technical publication 415: 131-168.

Lankford, J. (1982). "The Growth of Small Fatigue Cracks in 7075-T6 Aluminum." Fatigue of Engineering Materials and Structures 5(3): 233-248.

Lankford, J. and F. N. K. Kusenberger (1973). "Initiation of fatigue cracks in 4340 steel." Metallurgical Transactions 4(A): 553-559.

Lardner, R. W. (1967). "A dislocation model for fatigue crack growth in metals." Philosophical Magazine 17: 71-82.

Larson, S. G. and A. J. Carlsson (1973). "Influence of non-singular stress terms and specimen geometry on small-scale yielding at crack tips in elastic-plastic materials." Phys. Solids 24: 263-277.

Lemaignan, C. (2000). Manuscript: Mécanique de la rupture.

Levy, N., P. V. Marcal, W. J. Ostergren and J. R. Rice (1971). "Small scale yielding near a crack in plane strain - a finite element analysis." International journal of Fracture Mechanics 7(2): 143-156.

Lin, J., S. Ganguly, L. Edwards and P. E. Irving (2003). The effects of residual stress and HAZ on fatigue crack growth in MIG welded 2024 and 7150 aluminium. Fatigue 2003,

Martikainen, J. K. (1995). Plasma welding of aluminium alloys used in transport industries. Sixth International Conference on Aluminum Weldments (INALCO), Cleveland, Ohio, USA, American Welding Society, 333-341.

Martukanitz, R. P., A. L. Wilson and P. R. Howell (2000). "Loss of strength within heat-affected zone of Al-Cu and Al-Cu-Li alloys." Materials Science Forum 331-337: 1291-1296.

Masounave, J., J.-P. Baïlon and D. J-I (1997). Les lois de fissuration par fatigue. in La fatigue des materiaux et des structures. C. Bathias and J.-P. Baïlon.

Masubuchi, K. (1980). in Analysis of welded Structures, Pergamon Press.

Mc Meeking, R. M. (1977). "Finite deformation analysis of crack tip opening in elastic-plastic materials and implications for fracture initiation." J. Mech. Phys. Solids 25: 357-381.

McClintock, F. A. (1963). On the plasticity of the growth of fatigue cracks. in Fracture of solids, Drucker, D.C., Gillman, J.J. 20: 65-102.

Micheli, J. and C. Pilcher (2000). "Advanced variable polarity plasma arc welding." The Fabricator: 46-48.

Micheli, J. and R. J. Pistor (1998). "Variable polarity plasma arc welding (How the process affects the welding of aluminium)." Practical welding today July/August: 21-24.

Miyazaki, K., M. Mochizuki, S. Kanno, M. Hayashi, M. Shiratori and Q. Yu (1999). "Analysis of stress intensity factor due to surface crack propagation in residual stress fields caused by welding (comparison of influence function method and inherent strain analysis)." Trans. Jpn. Soc. Mech. Eng. 65(636): 1709-1715.

Mochizuki, M., T. Hattori and K. Nakakado (2000). "Residual stress reduction and fatigue strength improvement by controlling welding pass sequences." Transactions of the ASME 12: 108-112.

Morris, W. L. (1979). "The Noncontinuum Crack Tip Deformation Behaviour of Surface Microcracks." Metallurgical Transactions A 11A: 1117-1123.

Morris, W. L., M. N. James and O. Buck (1981). "Growth rate models for short surface cracks in Al 2219-T851." Met. Trans. 12A: 57.

Mulvihill, P. and C. J. Beevers (1986). "The Initiation and Growth of Intergranularly Initiated Short Fatigue Cracks in an Aluminium 4.5 per cent Copper Alloy." The behaviour of Sort Fatigue Cracks 1: 203-213.

Mura, T. and J. Weertman (1984). Dislocation Models for Threshold Fatigue Crack Growth. in Fatigue crack growth threshold concepts. D. L. Davidson and S. Suresh, The Metallurgical Society/AIME: 531-549.

Navarro, A. and E. R. de los Rios (1992). "Fatigue crack growth modelling by successive blocking of dislocations." Proc. Roy. Soc. 437: 375-390.

Newman, J. C. (1981). A crack-closure model for predicting fatigue crack growth under aircraft spectrum loading. in Methods and Models for Predicting Fatigue Crack Growth under Random Loading. Philadelphia, American Society for Testing and Materials. 748: 53-84.

Newman, J. C. (1998). An evaluation of the plasticity-induced crack closure concept and measurement methods. H. NASA Langley Research Center, VA 23681-0001, NASA/TM-1998-208430.

Norman, A. F., V. Drazhner, N. Woodward and P. B. Prangnell (1998a). Effect of welding parameters on the microstructure of Al-Cu-Mg autogeneous TIG welds. 7th International conference on joints in aluminium, Cambridge, 26-37.

Norman, A. F., R. Ducharme, A. Mackwood, P. Kapadia and P. B. Prangnell (1998b). "Application of thermal modelling to laser beam welding of aluminium alloys." Science and Technology of Welding and Joining 3(5): 260-266.

Norman, A. F., K. E. Jakielski, G. Scott and P. B. Prangnell (1997). Process Control of Weld Microstructures in a 2024 (Al-Cu-Mg) Alloy. 4th Decennial International Conference on Solidification Processing, Sheffield, 670-674.

Norman, A. F. and P. B. Prangnell (1998). A study of microsegregation effects in TIG and Laser beam welds of an Al-Cu-Mg alloy. ICAA-6, Toyohashi, The Japan Institute of Light Metals, 3, 1435-1440.

Nunes, A. C., E. O. Bayless, C. S. Jones, P. M. Munafo, A. P. Biddle and W. A. Wilson (1984). "Variable Polarity Plasma-Arc Welding on the Space-Shuttle External Tank." Welding Journal 63(9): 27-35.

Paris, P. C. and F. Erdogan (1963). "A critical analysis of crack propagation laws." Journal of Basic Engineering 85: 528-534.

Paris, P. C., M. P. Gomez and W. P. Anderson (1961). "A rational analytic theory of fatigue." The Trend in Engineering 13: 9-14.

Parry, M. R. (2001). Finite element and analytical modelling of roughness induced fatigue crack closure (PhD Thesis). Faculty of Engineering and Applied Science. Southampton, University of Southampton.

Pearson, S. (1975). "Initiation of fatigue cracks in commercial aluminium alloys and the subsequent propagation of very short cracks." Engineering Fracture Mechanics 7: 235-237.

Peyre, P., P. Merrien, H. P. Lieurade, R. Fabbro and A. Bignonnet (1992). Optimization of the residual stresses induced by laser shock treatment and fatigue life improvement of two cast aluminium alloys. 3rd European Conference on Residual Stresses, DGM Informationsgesellschaft mbH, 881-890.

Polmear, I. J. (1995). in Light Alloys. Chapter 2 & 3, Arnold: 24-168.

Rabbe, P. and L. Anquez (1997). L'amorcage des fissures de fatigue. in La fatigue des materiaux et des structures. C. Bathias and J.-P. Baïlon. Paris, Hermes: 111-154.

Radaj, D. (1992). in Heat effect of welding - Temperature Field, Residual stress, distorsion. Berlin, Springer-Verlag, Heidelberg.

Reichelt, W. R., J. W. Evancho and M. G. Hoy (1980). "Effects of Shielding Gas on Gas Metal Arc Welding Aluminum." Welding Journal 59: 147-155.

Rice, J. R. (1974). "Limitations to the small scale yielding approximation for crack tip plasticity." J. Mech. Phys. Solids 22: 17-26.

Rice, J. R. and M. A. Johnson (1970). in Inelastic Behaviour in Solids. New York, Mc GrawHill.

Rice, J. R. and G. F. Rosengren (1968). "Plane strain deformation near crack tip in a power law hardening material." Journal of the mechanics and physics of solids 16: 1-12.

Rodopoulos, C. A. and E. R. de los Rios (2002). "Theoretical analysis on the behaviour of short fatigue cracks." International Journal of Fatigue 24: 719-724.

Sadananda, K. and P. Shahinian (1977). "Prediction of Threshold Stress Intensity for Fatigue Crack Growth Using a Dislocation Model." International Journal of Fracture 13(5): 585-594.

Sanders, T. H. and J. T. Staley (1979). Review of Fatigue Fracture Research on High-Strength Aluminium Alloys. in Fatigue and Microstructure, American Society for metals: 467-522.

Sinclair, I. (1984). Fatigue Al-SiCp metal matrix composites (PhD). Materials Science and Metallurgy Departments. Cambridge (UK), Cambridge University.

Sinclair, I. and P. J. Gregson (1998). Fatigue optimisation in Aerospace Aluminium Alloys. Oxford-Kobe Materials Seminar on Aerospace Materials,22-25 sept. 1998,

Starke, E. A. and J. T. a. J. Staley (1996). "Application of modern aluminum alloys to aircraft." Progress in Aerospace Sciences (UK) 32(2-3): 131-172.

Suresh, S. (1998). in Fatigue of Materials. (second edition), Cambridge.

Suresh, S., D. M. Park and R. O. Ritchie (1982). Crack tip oxide formation and its influence on fatigue thresholds. in Fatigue threshold. 1: 391-408.

Suresh, S. and R. O. Ritchie (1983). "Some Considerations on the Modelling of Oxide-Induced Fatigue Crack Closure Using Solutions for a Rigid Wedge inside a Linear Elastic Crack." Scripta Metallurgica 17(4): 575-580.

Suresh, S., G. F. Zamiski and R. O. Ritchie (1981). "Oxide-Induced Crack Closure - an Explanation for near-Threshold Corrosion Fatigue Crack Growth-Behavior." Metallurgical Transactions a-Physical Metallurgy and Materials Science 12(8): 1435-1443.

Tanaka, K. and Y. Nakai (1983). "Propagation and non-propagation of short fatigue crack at a sharp notch." Fatigue and Fracture of Engineering Materials and Structures 6: 315-327.

Taylor, D. (1988). "Fatigue Thresholds: Their Applicability to Engineering Situations." International Journal of Fatigue 10(2): 67-79.

Tracey, D. M. (1976). "Finite Element Solutions for Crack-Tip Behavior in Small-Scale Yielding." Journal of Engineering Materials and Technology-Transactions of the ASME 98(2): 146-151.

Truckner, W. G., J. T. Staley, R. J. Bucci and A. B. Thakker (1976). Effects of Microstructure on Fatigue Crack Growth High-Strength Aluminum Alloys, U.S. Air Force Materials Laboratory report.

TWI (2000). World Centre for Materials Joining Technology, www.twi.co.uk.

Vasudevan, A. K., K. Sadananda and N. Louat (1994). "A Review of Crack Closure, Fatigue-Crack Threshold and Related Phenomena." Materials Science and Engineering a-Structural Materials Properties Microstructure and Processing 188(1-2): 1-22.

Vasudevan, A. K. and S. Suresh (1982). "Influence of Corrosion Deposits on near-Threshold Fatigue Crack-Growth Behavior in 2xxx and 7xxx Series Aluminum-Alloys." Metallurgical Transactions a-Physical Metallurgy and Materials Science 13(12): 2271-2280.

Wanhill, R. and L. Schra (1992). Short Cracks and Durability Analysis of the Fokker 100 Wing /Fuselage Structure. in Short Fatigue Cracks, Mechanical Engineering Publications Limited: 3-27.

Wei, L. W., E. R. de los Rios and M. N. James (2002). "Experimental study and modelling of short fatigue crack growth in aluminium alloy Al7010-T7451 under random loading." International Journal of Fatigue 24: 963-975.

Weiss, V. and D. N. Lal (1974). "Note on the Threshold Condition for Fatigue Crack Propagation." Met. Trans. 5A: 1946-1949.

Xu, Y. (2000). Variable Amplitude Loading Effects on damage Tolerant Airframe Materials (PhD Thesis), University of Southampton.

Yoder, G. R., Y. A. Cooley and T. W. Crooker (1983). "A critical analysis of grain size and yield strength dependence of near-threshold fatigue crack growth in steels." Fracture Mechanics STP 791(1): 348-365.

Zabett, A. and A. Plumtree (1995). "Microstructural Effects on the Small Fatigue-Crack Behavior of an Aluminum-Alloy Plate." Fatigue & Fracture of Engineering Materials & Structures 18(7-8): 801-809.

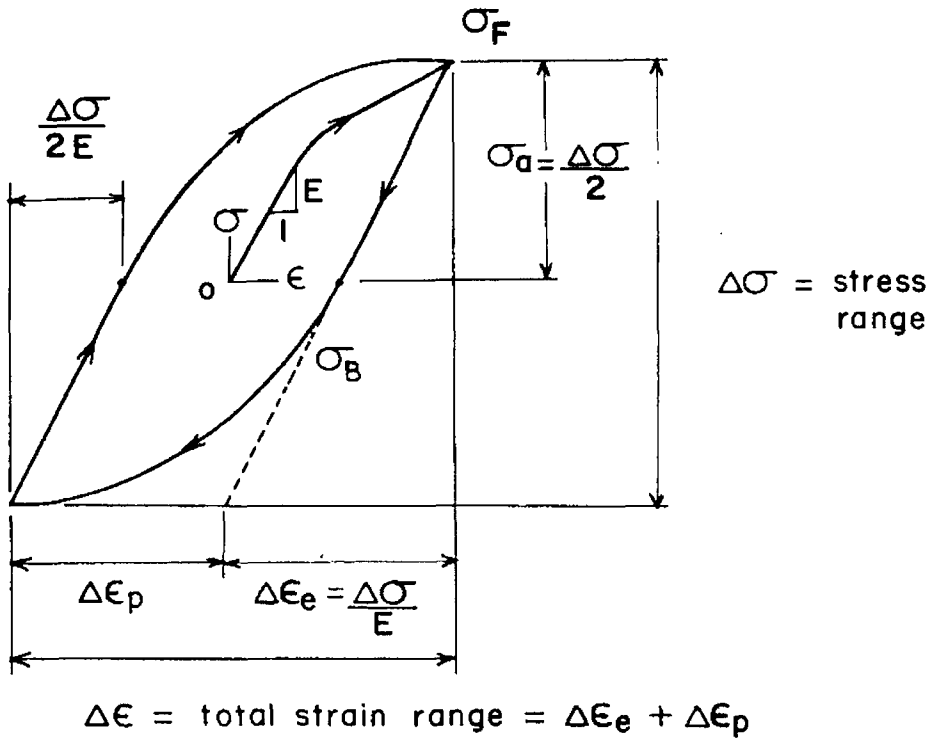

Figure 2.1 Schematic representation of a cyclic stress strain hysteresis loop (Bathias & Baïlon, 1997)

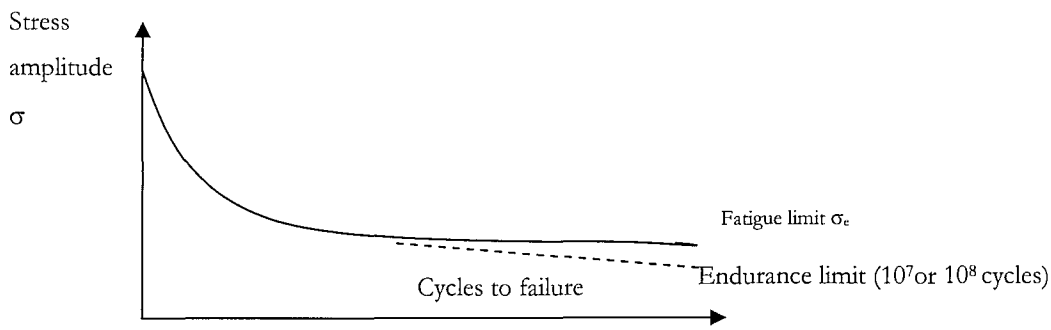

Figure 2.2 Schematic S-N curves based on smooth, polished specimens

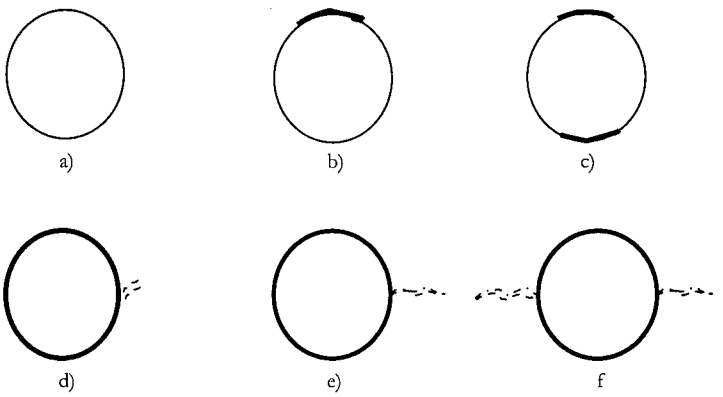

Figure 2.3 Crack initiation mechanism (Lankford & Kusenberger, 1973):
(a) initial state, (b) debonding (decohesion) at a pole,
(c) widening of this decohesion and debonding at the other pole, (d) increasing debonding with nucleation of initial flaws in the matrix, (e) flaws grow and coalescence to form a microcrack, and (f) crack propagation and new flaws nucleate.

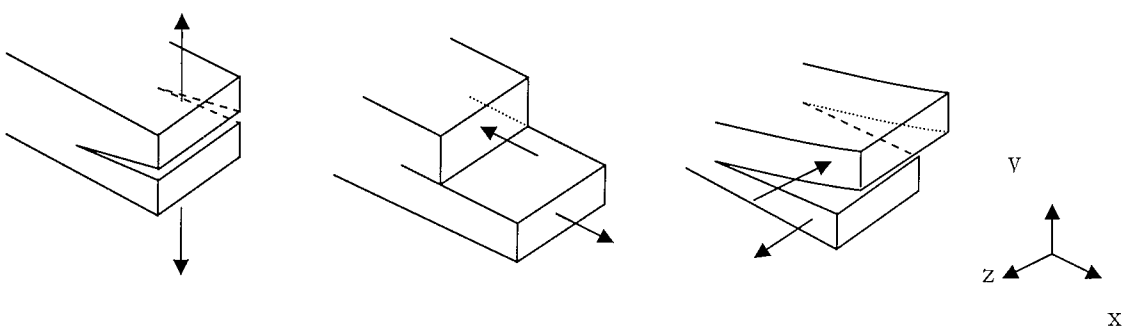

(a) mode I (b) mode II (c) mode III

Figure 2.4 The three modes of fracture: (a) tensile, or mode I, (b) in-plane shear, or mode II, (c) out-of-plane shear, or mode III.

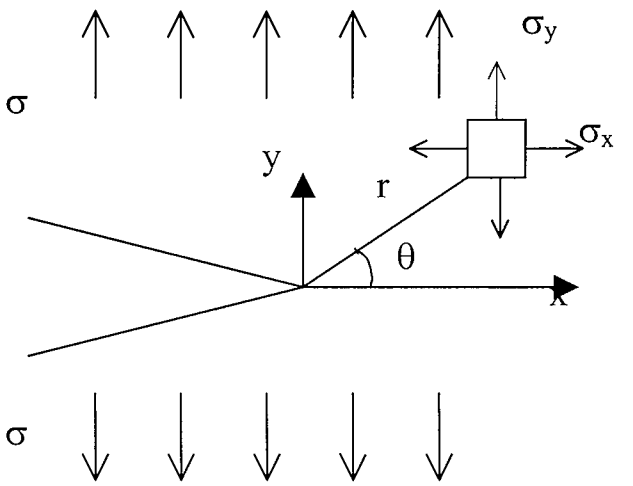

Figure 2.5 Schematic illustration of mode I crack loading and associated nomenclature

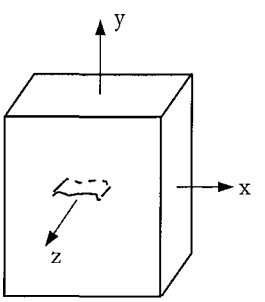

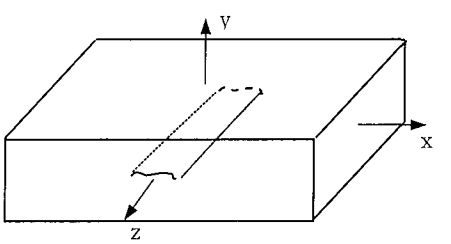

(a) $\sigma_z = 0$, $\varepsilon_z \neq 0$

Plane Stress (thin body)

(b) $\varepsilon_z = 0$, $\sigma_z \neq 0$

Plane Strain (thick body)

Figure 2.6 Plane stress and plane strain conditions (a) Plane Stress (thin body), (b) Plan strain (thick body)

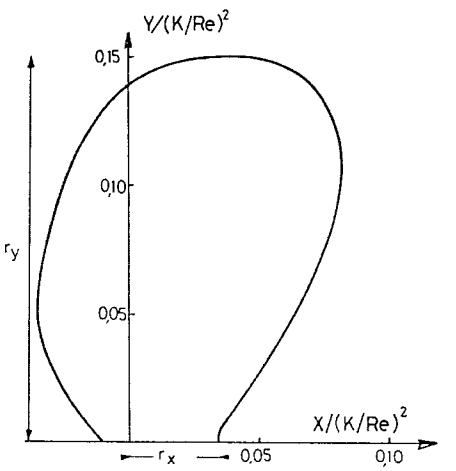

Figure 2.7 Schematic representation of half plastic zone shape ahead of a crack; the crack tip is defined at the origin of the graph with normalised axis ($R_e=\sigma_y$)(Bathias & Baïlon, 1997)

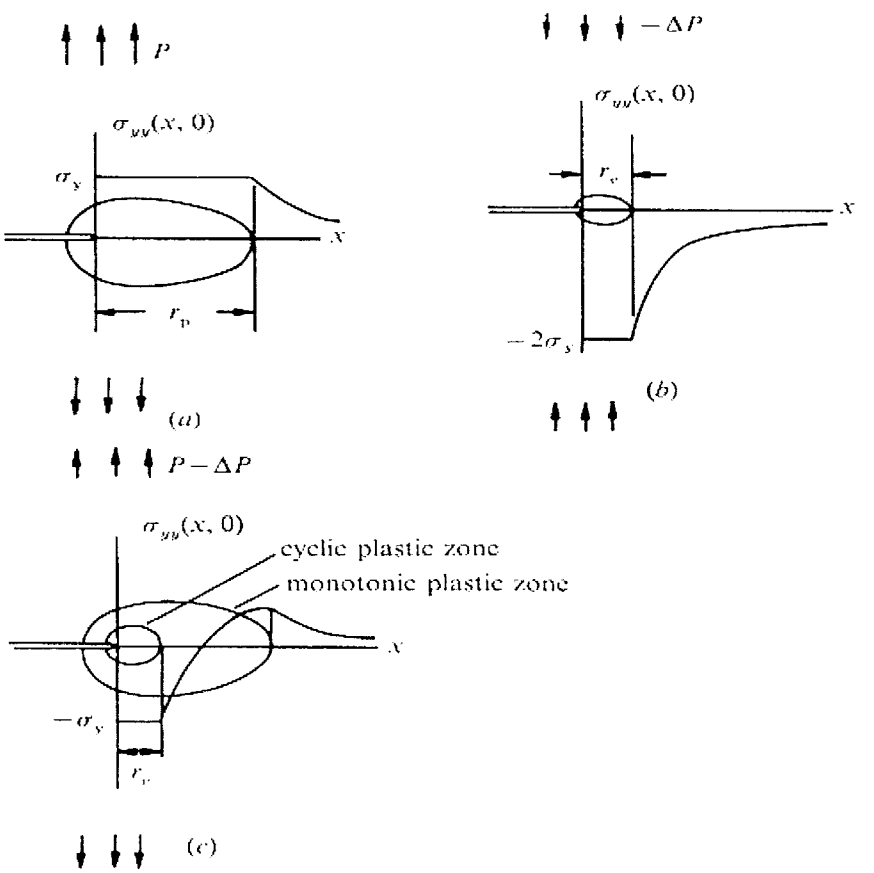

Figure 2.8 Schematic representation of the development of the cyclic plastic zone upon unloading in plane stress:

(a) Monotonic plastic zone created by a far-field load P.

(b) Stress distribution due to the reduction of the load by ΔP which, when superimposed with (a), gives the result in (c). (Suresh, 1998)

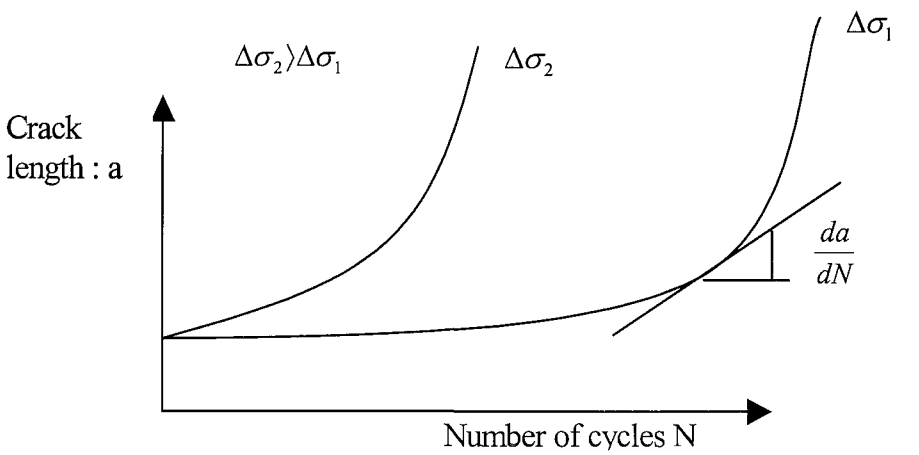

Figure 2.9 Crack length versus Number of cycles in Fatigue

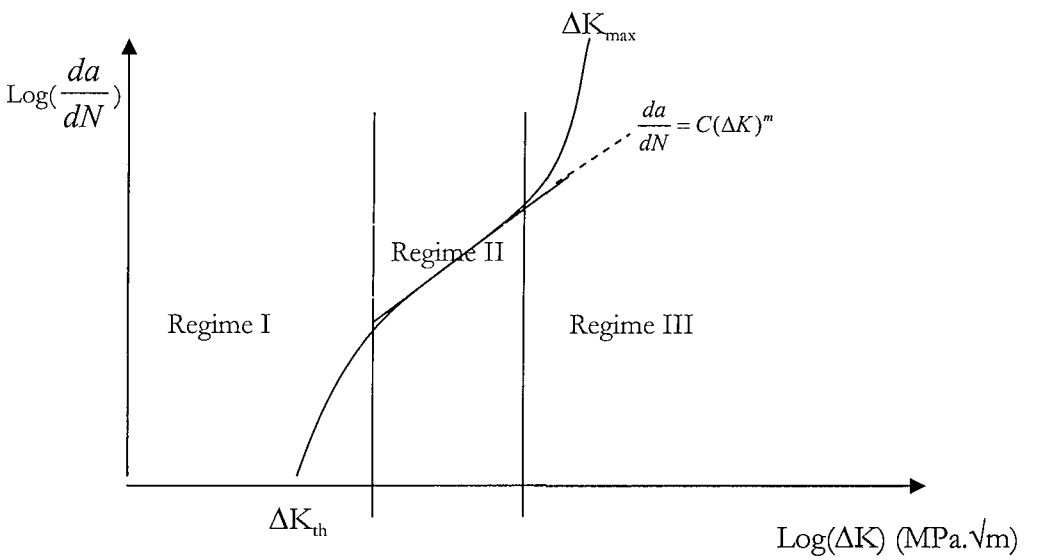

Figure 2.10 Typical fatigue crack growth rate curve

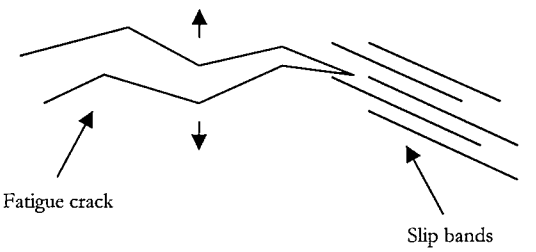

Figure 2.11 Stage I fatigue crack growth

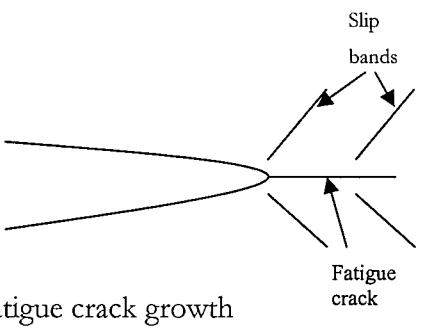

Figure 2.12 Stage II fatigue crack growth

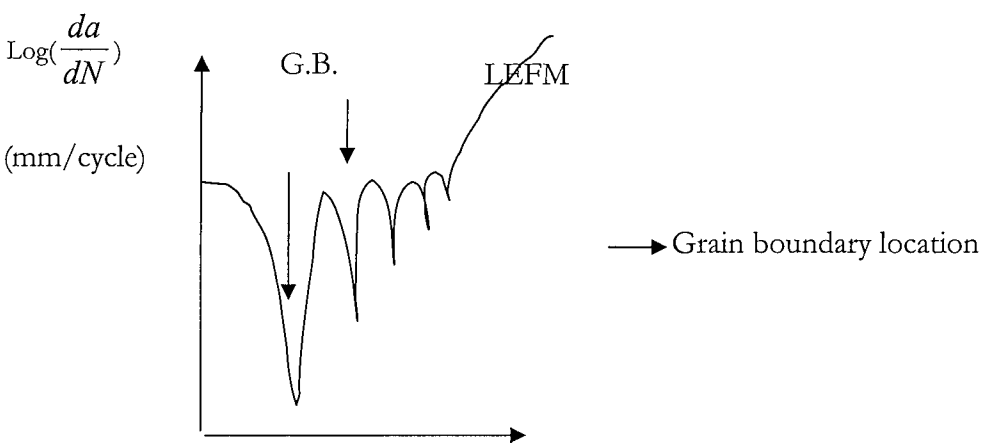

Figure 2.13 Schematic short fatigue crack growth curve.

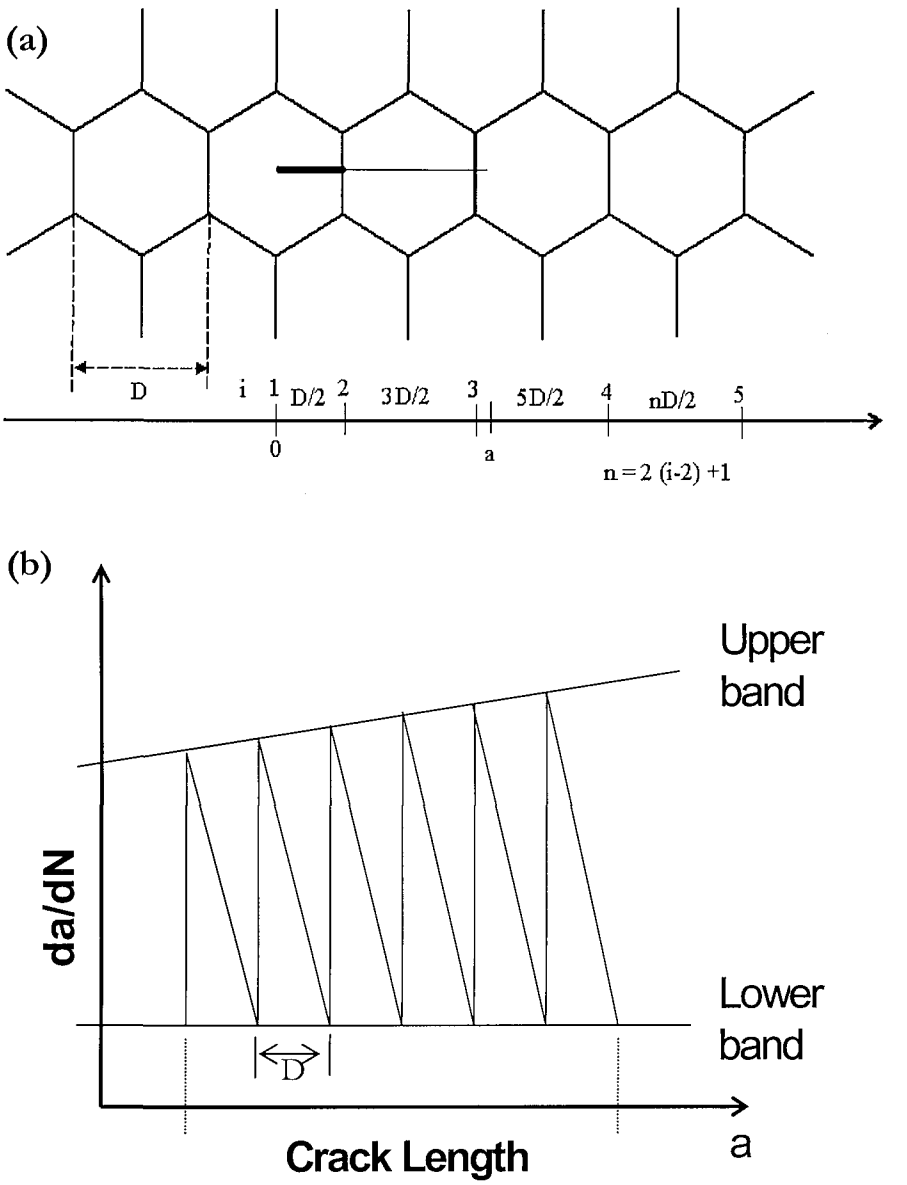

Figure 2.14 Schematic illustration of (a) grain structure with a crack and (b) linear model illustrating the serrated growth process between grain boundaries (Hobson model) (Hobson, 1982)

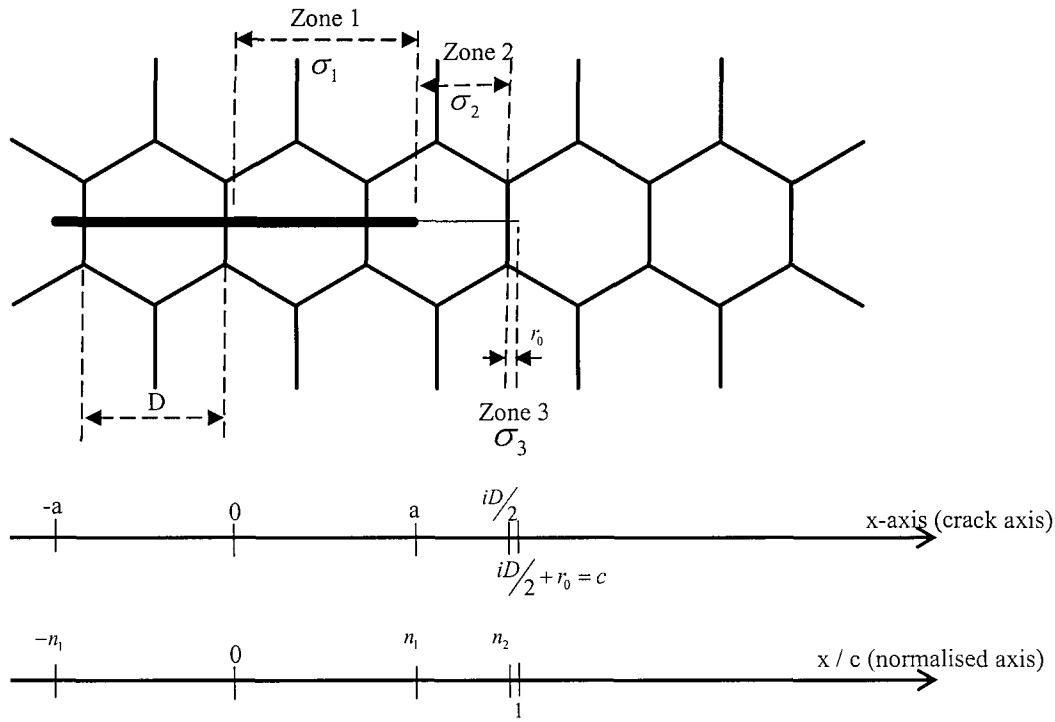

Figure 2.15 Schematic representation of the three zones that constitute the fatigue damage in the Navarro and de los Rios model (the crack, the plastic zone and the barrier zone). (Wei *et al*, 2002)

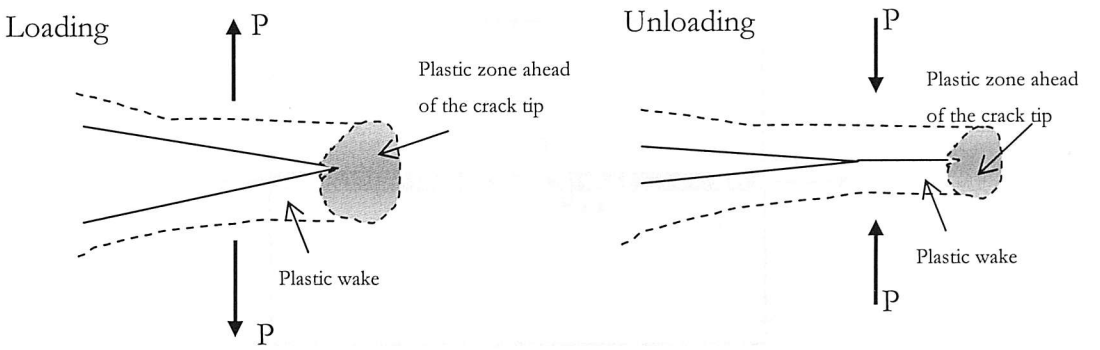

Figure 2.16 Schematic illustration of plasticity induced crack closure, with residual tensile plasticity associated with previous crack growth causing crack flanks to come into contact on unloading.

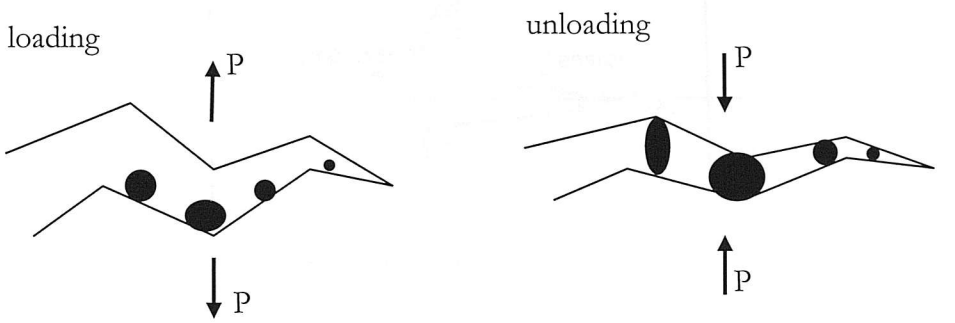

Figure 2.17 Schematic illustration of oxide induced closure, highlighting wedging effect of oxide debris in a crack wake

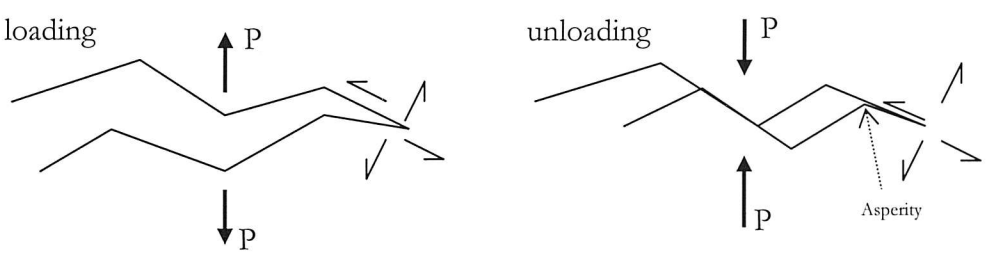

Figure 2.18 Schematic illustration of roughness-induced closure highlighting the role of surface asperities and shear offsets in producing crack face contact.

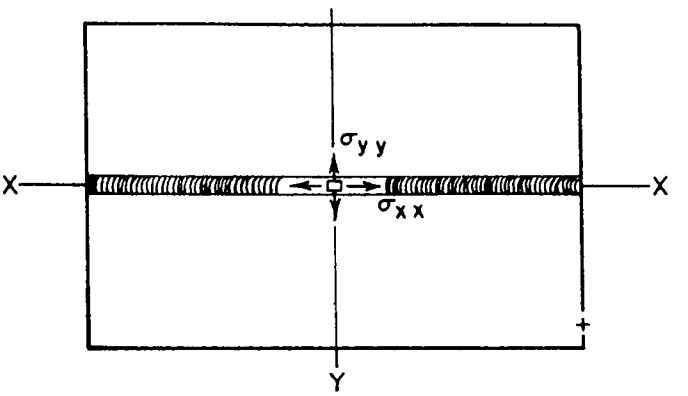

a. Butt Weld

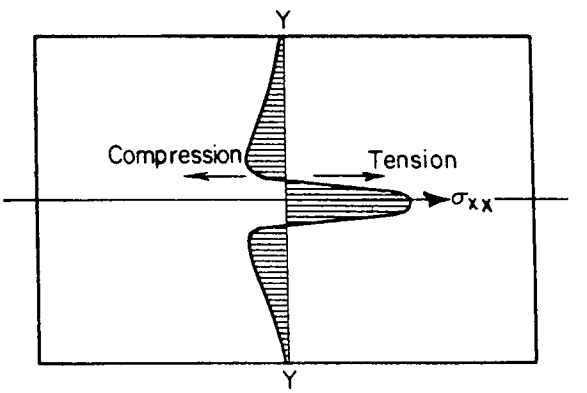

b. Distribution of σ_{xx} Along YY

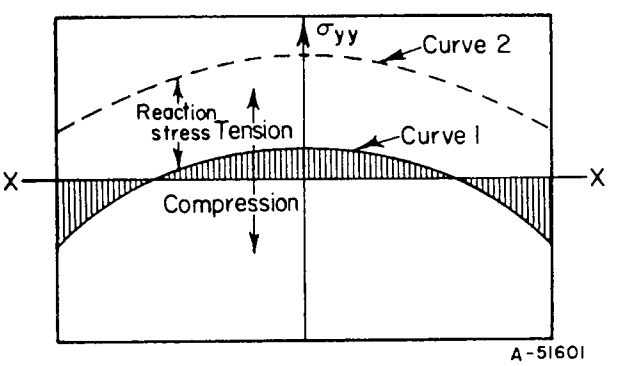

c Distribution of σ_{yy} Along XX

Figure 2.19 Typical distributions of residual stresses in a butt weld.(Masubuchi, 1980)

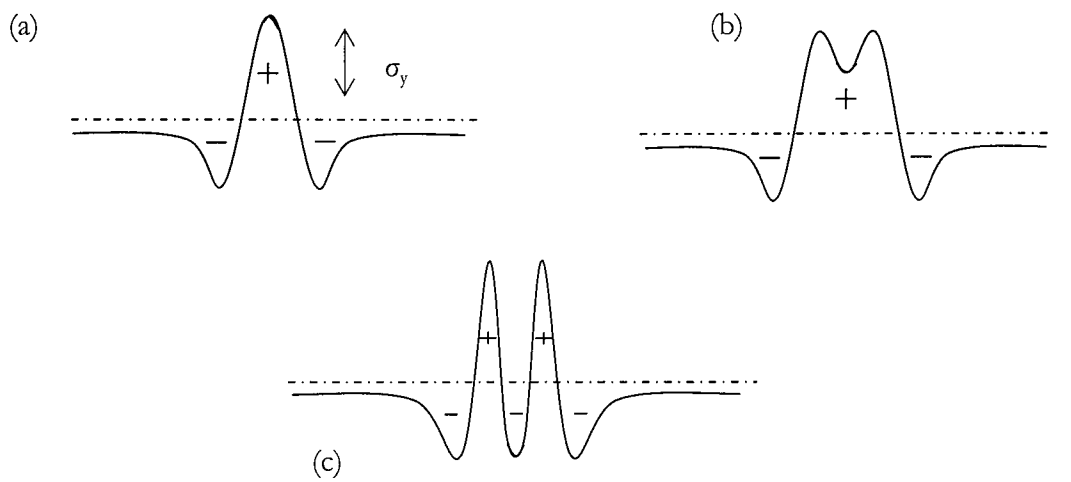

Figure 2.20 Schematic illustration of the longitudinal residual stress distribution for welds in (a) mild steels (b) Aluminium alloys (c) high alloy steels. (Radaj, 1992)

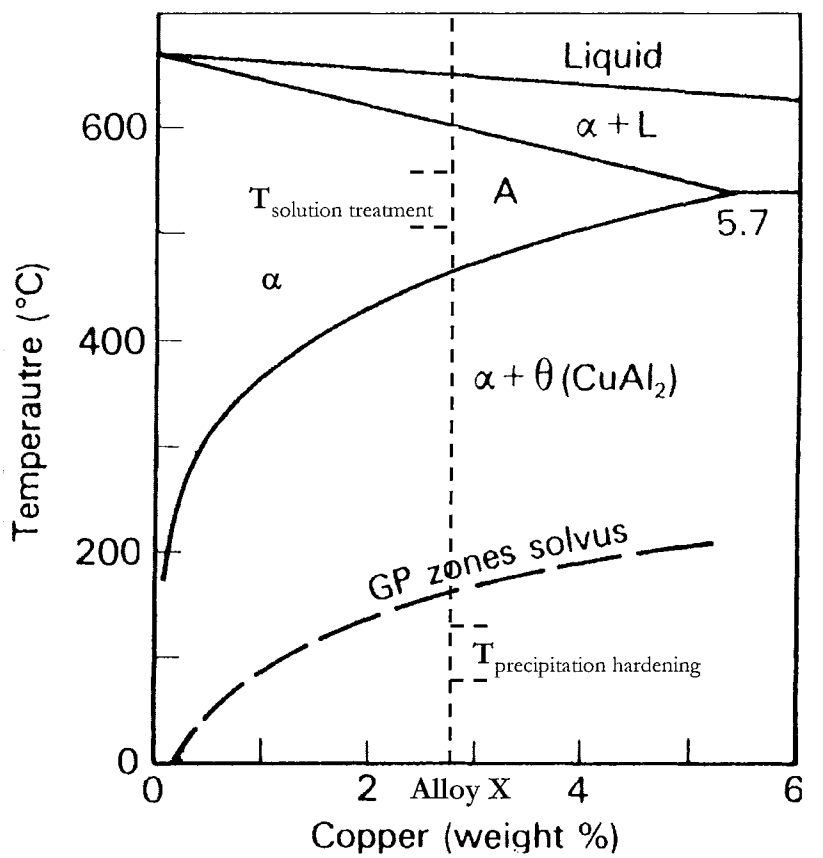

Figure 2.21 Section of Al-Cu eutectic phase diagram. The position of GP zones solvus is shown with heat treatment temperature for an alloy X (Polmear, 1995).

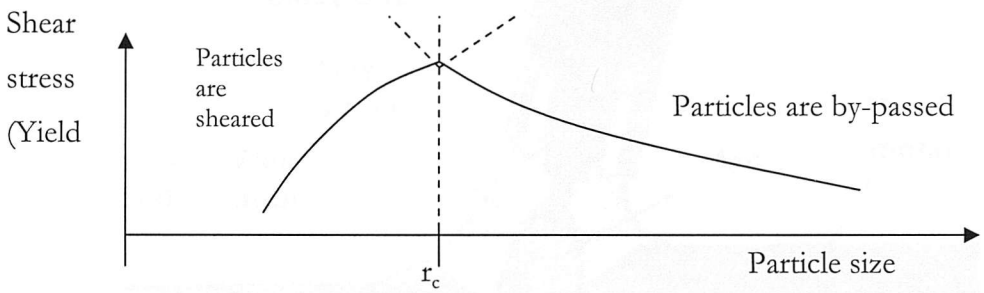

Figure 2.22 Effect of precipitation on mechanical strength at constant particle volume fraction (i.e. precipitate coarsening) (Polmear, 1995).

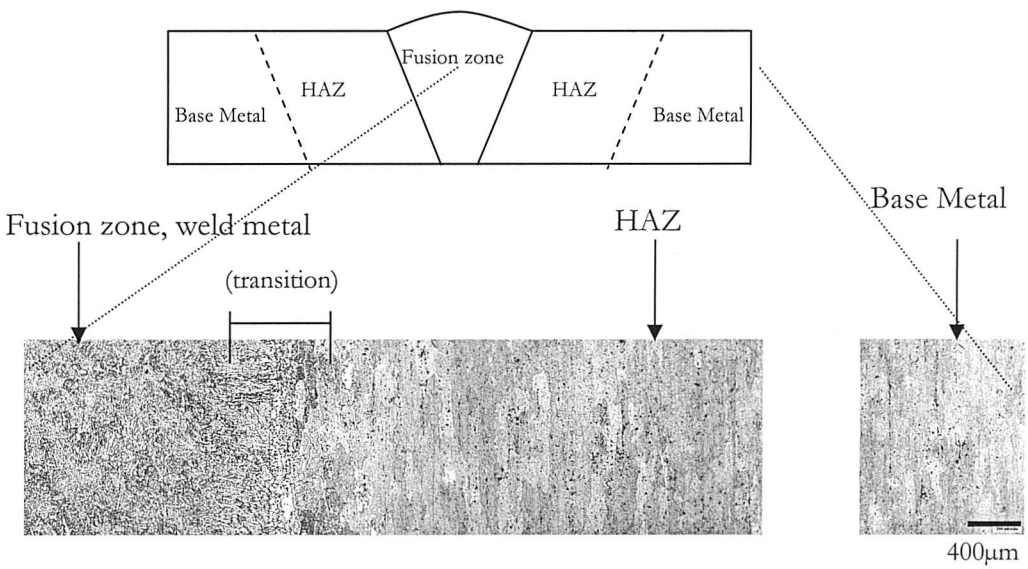

Figure 2.23 Typical macroscopic structure of fusion weld in a wrought Al-alloy (filled VPPA weld of 2024-T351)

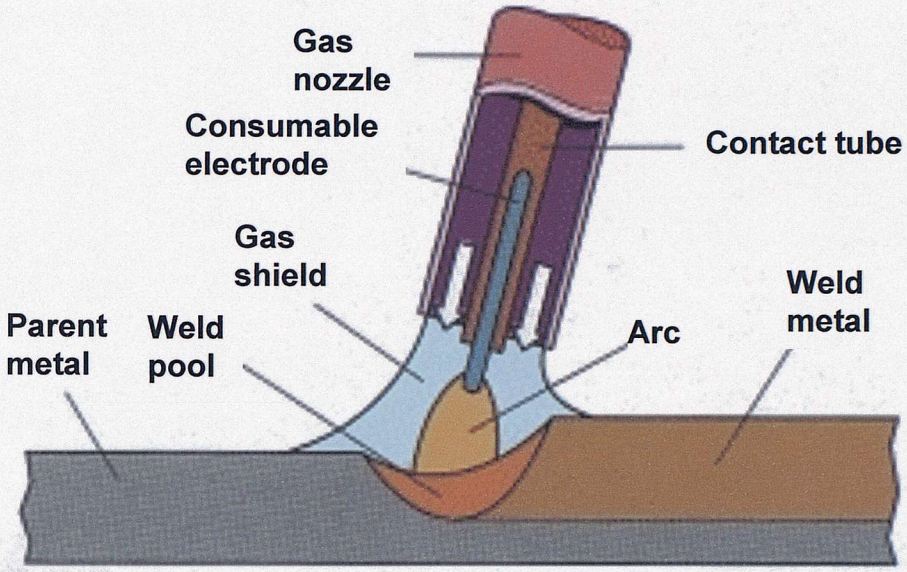

Figure 2.24 MIG torch (copyright TWI) (TWI, 2000)

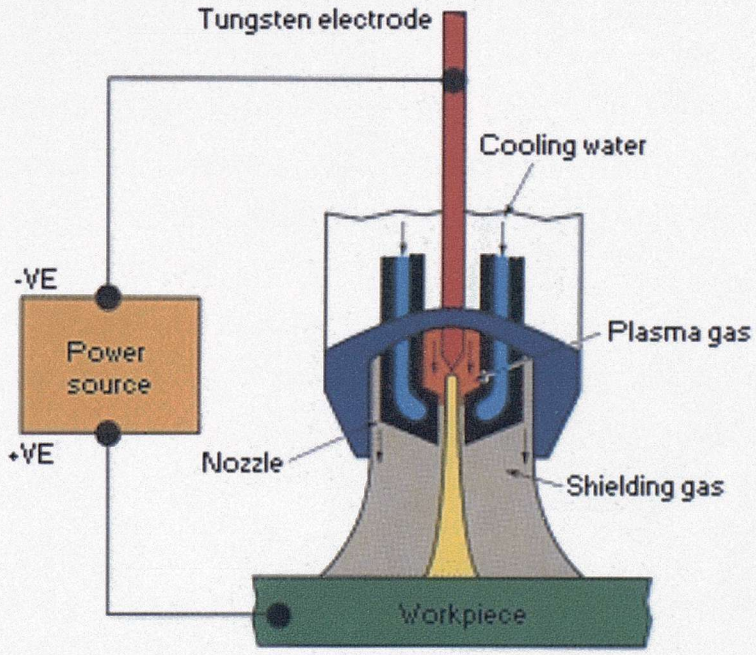

Figure 2.25 VPPA torch (copyright TWI) (TWI, 2000)

Chapter 3

Experimental methods

3.1 Materials

For the present work, weld samples were prepared from commercial 13mm gauge plate of standard commercial 2024. The material was welded in the T351 condition (solutionised, stretched and naturally aged) parallel to the L-direction (i.e. rolling direction) of the material. The nominal chemical compositions of the alloy are shown in Table 3.1. Two forms of welding were studied: Metal Inert Gas (MIG) and Variable Polarity Plasma Arc (VPPA). For the present work simple butt welds were prepared under proprietary conditions using the same filler wire for both welding methods, corresponding to the alloy 2319 (see Table 3.1). The VPPA technique was also studied without using any filler wire addition, i.e. as an autogeneous weld. The VPPA samples were welded in the vertical position whilst MIG samples were welded horizontally. Welds were in single and double pass forms for the VPPA and MIG methods respectively, and no post-weld heat treatments were carried out. All welds were manufactured in Cranfield University . Typical mechanical properties of the parent material 2024-T351 are shown in Table 3.2. Parameters for the welding processes are summarized Table 3.3 and 3.4. The plasma arc is carried by a constricted gas flow of Argon for both processes. It may be noticed in Table 3.4 that there are some differences in the direct current electrode positive (DCEP) values, where for the filled VPPA weld, the current and the time are higher than the autogeneous weld. In comparison the direct current electrode negative (DCEN) values are slightly different but may be considered in the same order of magnitude. The welding speeds of both VPPA welds are broadly similar but much slower than the MIG weld (by a factor 2.5).

Alloy	Cu	Mg	Zn	Mn	Cr	Si	Fe	Zr	V	Al
2024	3.7-4.5	1.2-1.5	<0.25	0.15-0.80	<0.1	<0.15	<0.20	<0.05	-	Bal
2319	5.8-6.8	<0.02	<0.1	0.20-0.40	-	<0.2	<0.3	<0.25	0.1	Bal

Table 3.1 Chemical compositions of 2024 and 2319 (Wt%)(ASM International, 1998).

Alloy	Temper	Yield stress (MPa)	Tensile strength (MPa)	Elongation (%)
2024	T351	350	480	20

Table 3.2 Typical tensile properties in 2024-T351 (Xu, 2000)

Material	Filler wire	Current	Voltage	Welding speed
MIG	2319	268 A	24.3 V	450 mm/min

Table 3.3 Welding parameters for the MIG weld (Serrano, 2003)

Filler wire	Plasma gas and flow rate	DCEN Current and time	DCEP Current and time	Shielding Gas and flow rate	Welding speed
Filled	Ar, 2.4-4l/min	291A, 16ms	291A, 4ms	He, 15l/min	170 mm/min
Autogeneous	Ar, 3.0 l/min	320A, 15ms	170A, 1ms	Ar, 30l/min	165 mm/min

Table 3.4 Welding parameters for the VPPA welds with and without filler wire where DCEN and DCEP are direct current electrode negative (or straight polarity) and direct current electrode positive (or reverse polarity), respectively (Serrano, 2003).

3.2 Experimental procedures

3.2.1 Micro-Hardness

Micro-hardness measurements were carried out across the weld cross-sections using a standard micro-hardness machine. The applied load and time were 1kg and 15seconds respectively. The machine (Matsuzawa MHT-1) was checked before each use on a calibrated test block.

3.2.2 Differential Scanning Calorimetry

To investigate the microstructural conditions in the fusion welded samples, differential scanning calorimetry (DSC) was carried out. The DSC machine was a power-

compensated calorimeter (Perkin Elmer Pyris 1) with all runs being carried out at a heating rate of 10°C/min in nitrogen shielding gas. In power-compensation DSC, the sample and reference materials are each confined to a separate, self-contained calorimeter. The results are then related to the differential in heat provided to keep the sample and the reference at the same temperature. Baselines were obtained before the interpretation of DSC results. Based on the hardness results, key locations from the weld centre to the parent plate were identified for study. Small slices of 0.5mm thickness and ~3mm diameter in the L-S plane were extracted, i.e. sampling small, notionally uniform volumes of material from within the weld/HAZ cross-section. Figure 3.1 shows a typical thermogram for the parent material, 2024-T351. Four main effects may be identified in the thermogram: an endothermic peak, A, between 150°C and 240°C which may be attributed to zone dissolution, an exothermic peak, B, between 240°C and 330°C, which be attributed to the formation of metastable and/or equilibrium precipitates, particularly S'/S (Al_2CuMg), a broad endothermic band, C, above 350°C, identified as a progressive dissolution of previous precipitates, and a sharp endothermic peak, D, above 500°C attributable to incipient melting (Jena *et al.*, 1989; Gao *et al.*, 2002).

3.2.3 Metallography and fractography

All metallographic and fatigue testing specimens were initially ground on 120 grit SiC paper until planar, followed by 600 and 1200 grit, and then 4000 grit. Polishing was then carried out with 3μm diamond spray on DP-Pan† polishing cloth lubricated with DP-Blue† lubricant followed by 1μm diamond polishing and finally OPS† (suspension of alumna in water). Kellers reagent was used to etch the samples (2HF, 3HCl, $5NO_3$, $190H_2O$ in ml). A Struers automatic polishing machine and a suitable designed sample holder were used to ensure good reproducibility and planarity in the grinding and polishing process.

Microstructures of etched and unetched specimens and fracture surfaces were examined by optical microscopy and by secondary electron (SEI) and back-scattered (BEI) microscopy using a Jeol JSM-T300 SEM operating at an accelerating voltage of

† Trade names of Struers LTD

20kV, and a Jeol JSM-8500 FEG-SEM operating at 15kV. Electron diffraction spectroscopy (EDS) analysis were carried out on the Jeol JSM-8500 FEG-SEM operating at 15kV. Slices of material (Electropolished foils - in a 10% nitric acid in methanol solution cooled to -30°C) were also prepared for TEM (transmission electron microscope) study using a JEOL 2000FX instrument operating at 200kV. To characterise the defect populations in the MIG weld in particular, automatic image analysis software Carl Zeiss KS300 was used. Parameters such as area, centre of gravity, feret diameters (X-direction, Y-direction, minimum, maximum), circularity and orientations of pores were measured by binary imaging. Incomplete objects at the edges of the binary images were removed using the image analysis software. The circularity of pores was calculated using the following equation:

$$Circularity = \frac{4\pi(area)}{(perimeter)^2} \quad (3.1)$$

The equation assigns a circularity value of 1 for a circle, and this value will decrease as the object varies to a less circular shape, e.g. an ellipse. The perimeter used by the image analysis software was in fact a perimeter corrected for digitising purposes. The software approximates the perimeter using successive intercepts by discrete summation.

EBSD observations were used to provide crystallographic information on individual grains and associated boundaries. Electron back scattered diffraction (EBSD) specimen were electro-polished: specimen were mechanically polished as described above and then electrolysed ~5s in a 10% nitric acid in methanol solution cooled to -30°C at 30V. The EBSD mapping was carried out using a Jeol JSM-8500 FEG-SEM with an accelerative voltage of 20KeV and a probe current setting of 17-18, and with a HKL Channel 5 EBSD system fitted. The specimen was tilted to 60° with a working distance of 30mm and step size of 1 to 6μm depending on use for overall mapping or specific local analysis (e.g. defect locations). All quoted results achieve successful indexing rates of more than 75%.

3.2.4 Fatigue testing

Short crack fatigue testing was carried out on an Instron 8501 (capacity ± 100kN) servohydraulic testing machine. Fatigue tests were performed parallel to the weld line using three point bend coupons: samples were approximately 100mm long (i.e. parallel to the weld), and 90mm wide (perpendicular to the weld), see Figure 3.2. Given the fusion zone width of ~12mm, the central test gauge of the weld (i.e. directly over the central roller) may be seen to be approximately 3 times this distance from the cut edges of the sample. Top and bottom surfaces of the samples were skimmed by ~2.5mm from the parent plate surfaces. Loading was applied to the top (welding side) of the VPPA welds, whilst the surface of the second weld pass was loaded in the MIG samples. Constant amplitude sinusoidal cycling was used at a frequency of 15Hz and an R-ratio of 0.1. The top surface (the surface to be fatigue loaded) of all specimens was polished to a 0.02μm finish (using OPS†, alumina suspension). Crack growth behaviour was monitored by taking acetate replicas of the specimen surfaces at frequent intervals at the maximum applied stress level (cracks being held open to assist identification/measurement). Acetate was softened using acetone before being pressed onto the specimen surface. The acetate was held until it was firmly stuck on the specimen surface: the replicas were then allowed to dry for 3-4 minutes before being removed from the samples. Care was taken to ensure no bubbles were trapped when taking replicas as this might cause loss of surface and crack details. Growth behaviour of individual cracks was then considered by backtracking through the replica record. The analysis of Scott and Thorpe (Scott & Thorpe, 1981) was used to calculate the nominal stress intensities levels assuming a semi-circular crack profile. Given the unusual format of the test geometry (i.e. relatively wide), care was taken to ensure good rig alignment. In equivalent testing of parent material coupons, it was found that cracks appeared quite uniformly across the sample widths, implying that good sample/rig alignment was in fact being achieved. Comparison of such parent material coupon tests with more conventionally sized bend bars (52x10x6mm) of parent material showed entirely comparable cycles to failure results.

To elucidate microstructural contributions to fatigue characteristics of fusion welded 2024 plates, fatigue tests were carried out on small scale ("or sub-sized") samples with a view to characterise intrinsic properties of individual regions of the welds in samples that are essentially residual stress free due to being cut to a scale smaller than the wave-length of the stress variations in the weld. The study has been carried out on filled VPPA weld and used specifically to estimate different material parameters considered in the development of the crack growth modelling. Location of these samples is considered in more detail in Chapter 6. Sub-sized samples were approximately 25mm long (parallel to the weld line), 1.5mm wide (perpendicular to the weld line) and 3mm high (perpendicular to parent plate plane) (see Figure 3.3). Sub-sized specimens were polished to 1μm diamond + OPS finish, and tested in 3-pt. bend (top surface (25x1.5mm) being in tension). All tests were carried out on a specified designed servo-hydraulic machine with a 1kN load cell. A special rig was designed and manufactured to allow the self-alignment of the specimens (see Figure 3.4). The two axes of rotation in the load chain are highlighted in Figure 3.4(b) by the two arrows.

3.2.5 Residual stress measurements:

Residual stress measurements have been carried out by laboratory X-ray and synchrotron X-ray diffraction techniques. Laboratory X-ray stress analysis is particularly used for the determination of surface stresses since the applicable X-ray sources have a relatively short penetration depth (typically 5-40μm). This method of measurement can be applied to small surface elements and in notches or areas close to a crack tip. Synchrotron X-ray diffraction can be used for determination of internal stresses. Synchrotron sources provide very intense (million times more flux than a laboratory source) high energy beams. With energies of the order of 40 to 80keV, penetrations of many millimetres may be reached. Specialist facilities are of course necessary to carry out Synchrotron measurements (e.g. The European Synchrotron Research Facility in Grenoble (ESRF), France). Whilst both methods are used for different conditions, X-ray and synchrotron stress evaluation methods are based on the same principle; the use of the lattice spacing as a strain gauge (see Appendix 1 for details on the stress evaluation method).

In the present work, residual stresses measurements have been carried out on machined and electro-polished fatigue specimen surfaces (to remove potential artefacts of mechanical preparation). Measurements have been carried out by The open University on fatigue test specimens before loading, and after a single load cycle (to a stress level of 270MPa) to assess relaxation effects associated with any initial deformation. Two laboratory X-ray machines have been used: (i) a "Bruker" machine using the (331) reflecting plane and (ii) a "Stresstech" machine using the (311) plane. In the Bruker machine X-rays are generated from a *Cu* tube giving a penetration depth of about 40μm, whereas the Stresstech machine uses a *Cr* tube offering a penetration depth of about 12μm. The (331) reflection plane (diffraction angle of 110°) was used in the Bruker machine due to the Cu-Ka radiation available. With a (311) reflection plane, the diffraction angle is less important (~78°) which means high errors during the strain calculation. In the stresstech machine the diffraction angle available is between 130-160° and in this range with Cr-ka only (311) or (222) reflection plane can be measured and the (311) plane was a better choice. Synchrotron diffraction measurements were also carried out by The Open University at the ESRF. The effective gauge volume of these measurements covered a depth of ~500μm, centred at the depth of about 650μm from the surface.

References

ASM International (1998). Aluminium and Aluminium Alloys. in. A. S. Handbook, Davis, J.R.: 20-21.

Gao, N., L. Davin, S. Wang, A. Cerezo and M. J. Starink (2002). Precipitation in stretched Al-Cu-Mg alloys with reduced alloying content studied by DSC, TEM and atom probe. ICAA8, Cambridge, Trans Tech publications, 2, 923-928.

Jena, A. K., A. K. Gupta and M. C. Chaturvedi (1989). "A differential scanning calorimetric investigation of precipitation kinetics in the Al-1.53wt%Cu-0.79wt%Mg alloy." Act. Metall. Mater. 37(3): 885-895.

Scott, P. M. and T. W. Thorpe (1981). "A critical review of crack tip stress Intensity factors for semi-elliptic cracks." Fatigue of Engineering Materials and Structures 4(4): 291-309.

Serrano, G. (2003). Personal communication: Welding conditions for MIG & VPPA welds. Cranfield.

Xu, Y. (2000). Variable Amplitude Loading Effects on damage Tolerant Airframe Materials (PhD Thesis), University of Southampton.

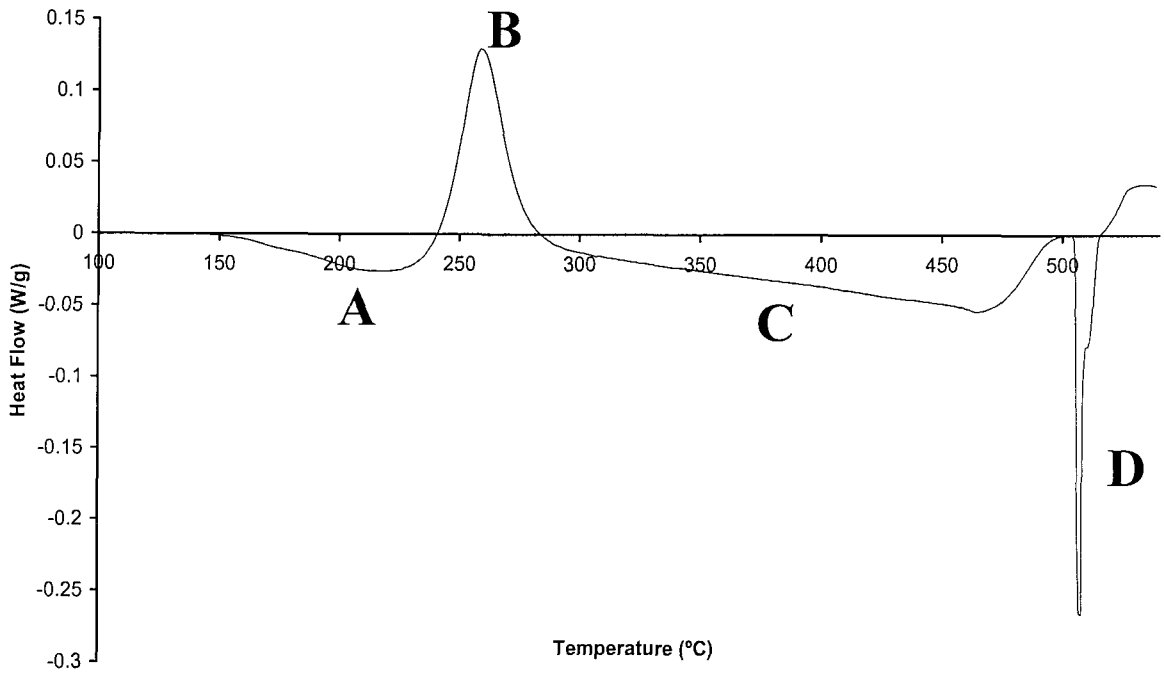

Figure 3.1 Typical DSC thermogram of the parent material (2024)

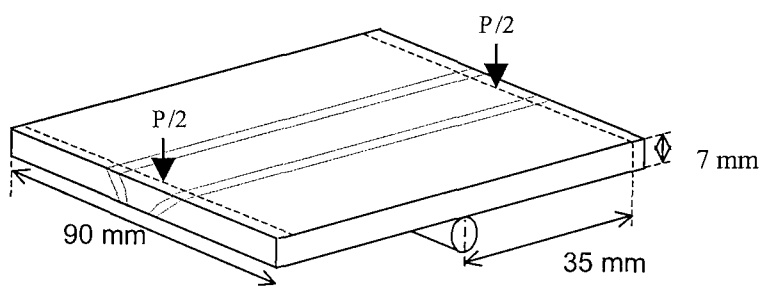

Figure 3.2 Schematic illustration of 3-pt. bend test configuration

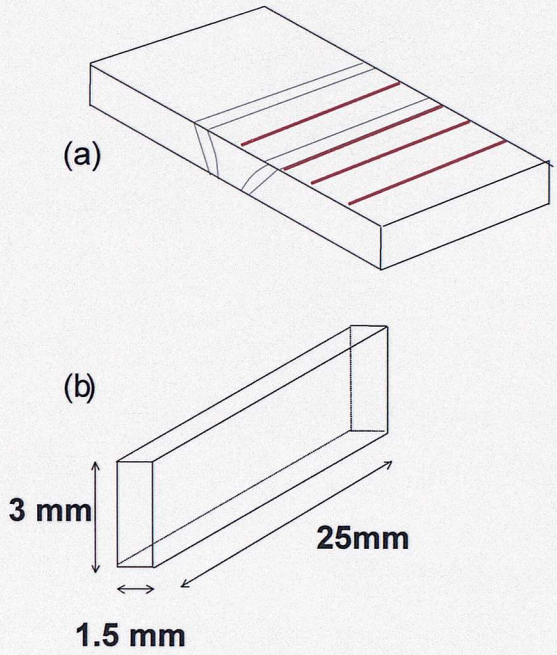

Figure 3.3 Schematic illustration of the sub-sized samples:

(a) locations in relation to the weld

(b) specimen geometry

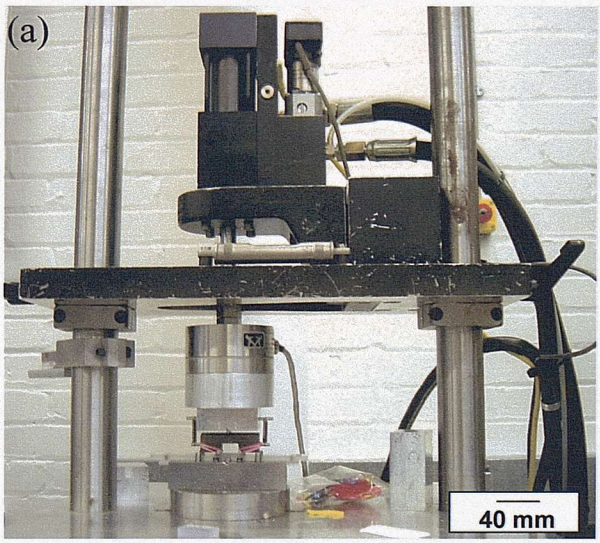

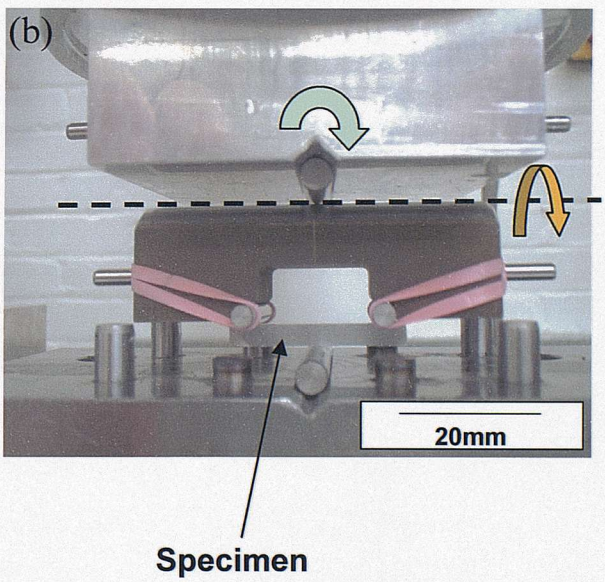

Figure 3.4 Sub-sized sample testing:

(a) servo-hydraulic machine

(b) self-alignment rig with arrows indicating the two axes of rotation in the upper loading block.

Chapter 4

Microstructural characterisation Results and discussion

4.1 MIG welds

4.1.1 Weld microstructure: SEM/EBSD/Optical observations

Optical and back scanning electron observations have been carried out on the MIG weld top surfaces exposed in the fatigue test coupons corresponding to the second weld pass surface (i.e. skimmed by ~2.5mm from the top surface of the parent material), see Figure 4.1. In keeping with the literature review (2.3.1), the weld structure may be broken down in different zones: fusion, transition, heat-affected and parent plate. In Figure 4.1, it may be seen that a reasonably fine dendritic network is evident in the fusion zone. The central region of the fusion zone consists of an equiaxed-dendritic structure. The edge of the fusion zone microstructure exhibits a more columnar structure growing in from the weld edge. The BSI images particularly highlight the columnar dendritic structure of the fusion zones edge and the associated interdendritic phases. Dendrites arm spacings are measured as around 6μm in the centre of the fusion whilst they are of the order of 12μm at the edge of the fusion zone. In the heat-affected zone, grain boundary decoration and large intermetallic particles may be seen. Intragranular precipitation is also particularly evident in the transition region between heat-affected zone (HAZ) and fusion zone (white spots within the HAZ grains, see Figure 4.1).

Electron diffraction spectroscopy (EDS) analysis was carried out on the welds and associated parent plate. The parent plate showed evidence of Cu and Mg rich particles (close to Al_2CuMg), as well as more Mn and Fe rich particles. A small number of Si rich intermetallics were also identified. Within the fusion zone, coarse interdendritic particles were clearly identified with a preponderance of Cu rich phases (with Mg also,

but significantly lower proportion than in Al_2CuMg, with Cu:Mg ratios between 5:1 and 10:1 in atomic proportions) being indicated by EDS measurement.

In terms of grain structures, Figure 4.2 presents an EBSD map, along with some BEI macrographs indicating different regions of the fusion zone (especially the transition zone). From the EBSD map, it may be considered that the grain structure is fairly uniform and equiaxed: for at least 80% of the fusion zone width the grain size is of the order of 50 to 100μm (based on equivalent area circle sizes). A finer grained region of a few hundreds micrometers width from the edge of the fusion zone may be identified.

In the first instance the generally fine fusion zone structure may of course be attributed to fast cooling rates in the associated weld (Bussu & Irving, 2000). Norman *et al.* have noted that for TIG 2024 welds (process similar to the MIG welding), dendrite arm spacings between 3 and 6μm were measured in the centre of the weld with the corresponding weld speeds being in the range of 420 to 1500 mm min^{-1} (Norman & Prangnell, 1998). It is reported by a number of researchers that equiaxed dendritic grains may form along the weld centreline, whereas columnar structures grow in from the weld edge(Cross & Edwards, 1989; ASM International, 1998).

In the transition zone between HAZ and fusion zone, heavy grain boundary decorations, large intermetallic particles and intragranular precipitations have been seen. Liquation and phase transformations may be expected to take place in the transition zone as reported by the literature (Norman *et al.*, 1998; Prangnell & Norman, 1998; Huang & Kou, 2000). The large intermetallics in the near HAZ region may be produced by a combination of heterogeneous precipitation on original particles and a degree of liquation. Huang and Kou have reported liquation occurring at large precipitates of Al_2Cu (θ) phase along grain boundaries and at isolated points within a gas metal arc weld of 2219-T851 alloy (Huang & Kou, 2000). They identified liquation taking place before the equilibrium (solid+liquid) region of the phase diagram (see Figure 2.21) if the heating rate is sufficiently fast to prevent the Al_2Cu (θ) particles from dissolving. Incipient melting of grain boundaries has been identified by Norman and co-workers on 2024 TIG welds and linked to the formation of precipitate free zones and coarse spherical precipitates of the Al_2CuMg (S) phase due to the wide freezing range of the 2024 alloy (~140°C) and the melting and resolutionising of the eutectic

phase at the grain boundaries (Norman *et al*, 1998; Prangnell & Norman, 1998). EDS of the transition region in the present welds confirms the presence of S phase. Figure 4.3 shows the partial melting zone where distinctive eutectic phase may be observed at grain boundaries and a number of larger intragranular particles. Within the weld, the intermetallic distribution is, as expected, dominated by the dendritic structure, with such phases tending to form interdendritically due to solute rejection during solidification (ASM International, 1998). A high Cu content in the phases may of course be attributed to the use of an essentially binary Al-Cu filler alloy.

4.1.2 Micro-Hardness

In terms of micro-hardness, Figure 4.4 (a) and Figure 4.4 (b) shows a two dimensional hardness map across the MIG weld along with a single hardness trace from the top surface of the skimmed specimens (i.e. ~2.5mm below the parent surface). The double pass nature of the MIG weld in Figure 4.4(a) is evident with the central soft region of the weld exhibiting a waisted hourglass shape. It is clear that the hardness presents a minimum at the centre: i.e. in the fusion zone. The fusion zone flow strength may be evaluated as approximately 70% of the parent plate (based on hardness levels). Two main hardness peaks in the HAZ may be noticed: one is close to the fusion line with a hardness level somewhat lower than the parent plate, whilst another is remote from the fusion line with a hardness level higher than the parent metal (see arrows in Figure 4.4(b)).

4.1.3 DSC assessment of MIG welds

To elucidate basic microstructural conditions of the different regions of the MIG weld, DSC measurements have been carried out in relation with the hardness distribution. Figure 4.5 shows the hardness trace for the depth at which DSC samples were extracted from the weld (key positions are highlighted). Figure 4.6 shows the corresponding DSC results. A general description of the results is as follows:

(i) Between position 6 and 5, the hardness increases (after an initial shallow "dip" in hardness). The DSC thermogram in Figure 4.6 for position 5 shows that the endothermic peak A related to cluster/zone dissolution

(Jena *et al.*, 1989; Gao *et al.*, 2002) is reduced in relation to position 6 and exothermic peak B is also reduced. As such, it may be expected that during the welding process, some zone content was lost to S precipitation with the material experiencing a degree of age-hardening (for the purposes of this work, no distinction is draw between S and S'). The dip in hardness seen between position 6 and 5 is then attributable to a slight degree of reversion seen at the earliest stages of low temperature ageing (ASM International, 1998).

(ii) From position 5 to position 4, a significant drop in hardness is identified. The corresponding DSC curve in position 4 presents a marked reduction in peak A heat content, consistent with limited zone/cluster strengthening at this location. The total energy of peak B is also reduced at position 4. The reduced heat content of this peak is then consistent with extensive S formation, i.e. overaging of the material. The reduced temperature of peak B is a distinctive feature of this location, not seen in other MIG weld thermograms. Such an effect may be influenced by changes in the effective overlap of the peaks associated with A and B, although microstructural contribution from changes in the S-phase nucleation/growth may also be noted, with changes in the extent of dislocation, sub-boundary and grain boundary formation. The details of such effects have not been established as part of this project.

(iii) From position 4 to position 3, DSC results show higher zone content consistent with increasing hardness. Given the increase in zone content it may be noted that a degree of effective re-solutionising occurred at this position. Re-solutionising must indeed be partial, with the hardness increase over location 4 being limited.

(iv) From position 3, care should be taken in the interpretation of the results as filler wire was employed in the weld altering the composition of the material (increasing the Cu:Mg ratio). A distinct double peak may be

identified in the zone / cluster dissolution of this material. Significant zone content could appear to be present, however limited strengthening clearly results.

In general terms the strengthening condition in the MIG weld/HAZ is clearly associated with a balance of aging, overaging, resolutionising and reprecipitation across the heat affected zone, see Figure 4.5(a). Strength levels close to the weld (low strength peak at this location) are influenced by the zone/cluster content available for reprecipitation.

4.1.4 Pore characterisation

Two predominant forms of defect appear in the MIG welds: interdendritic defects of the order of 10 to 50μm in length, and gas porosity of the order of 50-200μm in diameter (see Figure 4.7 and Figure 4.8). Optical observations have been carried out on parts of the fatigue test samples for image analysis to provide a statistical description of the pore distribution. Considerable care was taken to prepare samples to minimise scratches, comet tails, edge rounding, etc, to obtain reproducible results in the image analysis (see Figure 4.8). From this preparation, a general distribution of pores across the MIG welds has been obtained. Figure 4.9 (a) shows an optical image of a typical section of weld, running from the fusion zone centre to its edge. For the graph (Figure 4.9(b)), results have been grouped into three bands (of 2mm width) from the centre of the fusion zone. The graph shows pore densities, binned in different sizes ranges for the three regions. Variations from section to section may be seen across the fusion zone; larges bubbles are clearly more concentrated towards the FZ edge, and smaller interdendritic defects are more prevalent towards the centre. Figure 4.10 presents the relationship between size and shape of the defect population. Size is represented by area on the y-axis. Shape is represented by circularity (see section 3.2.4), with decreasing values for more elongated or irregular objects. The two populations of pores may be identified: large pores are clearly tending to circles, being gas bubbles. The smallest pores show some tendency back towards circularity, which is consistent with them being less elongated along interdendritic regions, however for areas less than

25 μm^2, objects are picked up by 10 pixels or less, so shapes may be less accurately defined in the image processing.

4.1.5 Residual stress

Plots of longitudinal residual stresses across the weld line of a representative fatigue test sample before and after a single fatigue load cycle at 270MPa are shown in Figure 4.11, 4.12 and 4.13 in relation to the corresponding weld hardness trace. Figure 4.11 presents the residual stress data for the MIG using the (331) reflection lab X-ray, Figure 4.12 using (311) reflection lab X-ray whilst synchrotron x-ray data are shown in Figure 4.13(a). Figure 4.13 (b) and (c) show the three types of X-ray results before and after loading respectively. In order to reduce scatter, most of the data have been binned and folded (averaged by: (a) assuming symmetry about the weld centre-line and (b) taking 3 point moving averages of individual X-ray measurements that are 1mm apart). Only one set of data has not been binned ((331) reflection, before loading, see figure 4.12) as these residual stress measurements were made with a wide aperture (3mm, as opposed to 1mm for the other lab X-ray data). As noted in chapter 3, X-ray measurements using the (331) reflecting plane offer a penetration depth of about 40μm, whereas the (311) reflecting plane results correspond to a penetration depth of the order of 12μm. In the case of synchrotron X-rays, measurements correspond to a depth of ~400 - 900μm. Similar general stress profiles outside the fusion zone (tensile peaks) may be identified for the three sets of data. For the lab X-ray measurements, the peak stresses are of the order of 150-180MPa before loading, whilst the peak stresses after loading are of the order of 80 to 120MPa for the (331) and (311) reflections respectively. For the synchrotron X-ray measurement, a peak stress may be seen of the order 180MPa before loading whilst after loading clear double tensile peaks may be seen around 75MPa and 100MPa. The residual stress drops to ~25MPa between these tensile peaks. A stress gradient may be seen in the fusion zone for the (331) reflection plane results, whilst a more uniform residual stress is seen in the fusion zone for the (311) reflection plane. No data have been obtained within the fusion zone for the synchrotron measurement due to the associated grain structure.

In the three graphs, it may be seen that the tensile peak before loading corresponds approximately to the location of the minimum strength observed on the hardness trace. For the (331) reflection plane, double stress peaks could be seen in the HAZ but may be considered a single tensile peak being given the typical error bars (±25MPa). Distinct relaxation of residual stresses is seen after the first loading of the sample, with the peak tensile stress moving from ~±12mm from the weld line, to ~±7mm. After loading the residual tensile stress peaks correspond approximately to the hardness peak location close to the fusion zone. The minimum residual stress for the synchrotron data corresponds to the minimum of hardness. Underlying differences between the results may in the first instance be linked to the different penetration depths of the measurements, with the Synchrotron and (331) reflection lab X-rays addressing a larger material volume than the (311) lab X-rays. As such it may be seen that the reasonable consistency of the (331) lab X-ray and synchrotron results highlight the following key points regarding residual stresses to a depth of ~900μm in the MIG weld:

(a) Peak residual stresses of the order of 170 MPa are present around +/- 10mm from the weld line in the unloaded weld samples.

(b) After initial loading, peak stress relaxation occurs, reducing maximum stress levels to approximately 100 MPa, with the peak location moving towards the weld centre line. This stress level is closely co-located with the minor hardness peak at the inner edge of the HAZ (approximately +/- 8mm from the centre), whilst stresses across the remaining majority of the HAZ fall below this value.

4.2 VPPA filled and autogeneous welds

4.2.1 Weld microstructure: SEM/EBSD/Optical observations

Optical observations of both VPPA welds are presented in Figure 4.14 and 4.15 for typical weld top surfaces subjected to fatigue loading (i.e. skimmed by 2mm from the parent surfaces). It may be seen from Figure 4.14 that similar columnar structures exist at the edge of the fusion zone for both VPPA welds showing a degree of alignment/columnar growth, analogous to observations made for the MIG weld. Grain boundary decoration and intragranular precipitation may also be observed just outside the fusion zone in the heat affected zone of both VPPA welds. The dendrite arm

spacings at the edge of the fusion zone have been measured as around 18μm for the filled weld and 21μm for the autogeneous weld, whilst they were around 12μm for the MIG weld, i.e. suggesting faster solidification in the MIG weld. Figure 4.15 presents the fusion zone centres of both welds where significant differences in microstructure may be distinguished. For the filled VPPA weld the central region of the fusion zone consists of an equiaxed-dendritic structure, similar to that seen in the MIG weld, whilst the autogeneous VPPA weld presents an axial columnar interdendritic structure. Norman and co-workers. (Norman *et al.*, 1997; Norman *et al.*, 1999) report both microstructures in their studies of TIG weld microstructures in a 2024 alloy. A schematic diagram summarises their results in Figure 4.16. They note that for autogeneous welds, a slow welding process speed favours a columnar dendritic growth mode in the weld centre, whilst an equiaxed dendritic structure is favoured at higher speeds (see Figure 4.16(a)). They also suggested that the addition of the filler alloy 2319, having a high solute content (6.6 wt.% Cu with the presence of Zr and Ti acting as nucleation sites for the solidifying liquid) promotes the formation of equiaxed-dendritic grains in the centre of welds at relatively low welding speed (see Figure 4.16(b)). As such it may be considered in the present study that knowing the welding speed do not vary significantly between the two VPPA welding techniques (165mm/min for the autogeneous weld compared to 170mm/min for the filled weld), the microstructure difference in the centre of the fusion zone may be simply due to the presence or not of the filler wire 2319. In the centre of the fusion zone, the dendrite arm spacings were measured as around 18 μm for the filled weld and of the order of ~25μm for the autogeneous weld (the coarse grain structure of the autogeneous weld showed significant variability in dentrite arm spacings, presumably linked to local orientation effects), whilst for the MIG weld they were around 6μm (welding speed of 450mm/min). So in terms of dendrite arm spacings, the MIG fusion zone presents the finest structure of all three welds consistent with a high solidification rate, and the coarsest fusion zone structure may be attributable to the autogeneous VPPA weld. The band of intragranular precipitation in the HAZ/transition was also seen to be narrower in the MIG weld (~250μm for both VPPA welds and ~100μm for the MIG weld).

Using the EBSD technique, the grain structure corresponding to each weld has been studied. The EBSD maps and associated BEI images for different regions of the fusion weld are presented Figure 4.17 and 4.18 for the filled VPPA weld and the autogeneous VPPA weld respectively. From the EBSD mapping for the filled VPPA weld, it may be seen that the grain structure is indeed predominantly equiaxed. A gradual decrease in grain size may be observed from the centre towards the edge going from approximately 60μm to 30μm (again expressed as equivalent circle grain diameter). A coarser columnar region may be seen just at the edge of the fusion zone with a grain size of approximately 60μm. For the autogeneous VPPA weld, Figure 4.18 clearly presents a distinctive grain structure in comparison with the filled weld. A particularly coarse columnar grain structure may be identified from the edge to the centre of the fusion zone. In the fusion zone centre, an axial columnar grain structure is confirmed by the EBSD results, but it is interesting to note a consistent boundary relationship between dendrites: many of boundaries in the centre of fusion zone are twin related (<111>/60deg) (see Pole Figure in Figure 4.18 (b)). It has been reported in the literature that annealing twins are rarely (if ever) found in cast metals because grain boundary migration is negligible during casting (Smallman & Bishop, 1999). Whilst an interesting feature of the autogeneous VPPA weld has been pointed out, the origins of this unusual crystallographic structure is beyond the remit of the present thesis.

4.2.2 Micro-Hardness

Figure 4.19 presents hardness maps of both VPPA welds. Figure 4.20 presents the hardness profiles on the top surfaces of the skimmed fatigue specimens for both welds. As presented for the MIG weld, the hardness presents a broad minimum at the centre (i.e. across the fusion zone) and several peaks in the HAZs. For the filled weld, two strong peaks are identified in the HAZ that are harder than the parent plate. For the autogeneous weld, only the outer HAZ peak is harder than the parent plate, and may be seen to be wider than the equivalent peak in the filled weld. The peak close to the fusion zone exhibits approximately the same strength level than the parent material. In comparison to the MIG weld, the hardness peak close to the fusion zone is clearly more pronounced. The minimum HAZ hardness for the autogeneous weld is

approximately the same level as the fusion zone hardness. For the filled weld, the minimum HAZ hardness is above the fusion zone level, with the filled weld showing a generally harder but narrower HAZ hardness profile than the autogeneous weld. The spacing of hardness peaks in the HAZ region is seen to be slightly greater in the VPPA welds than in the MIG.

4.2.3 DSC & TEM assessment of VPPA welds

4.2.3.1 DSC & TEM assessment of VPPA filled welds

As presented for the MIG weld, DSC has been carried out to investigate influences of aging, re-solutionising and re-precipitation across the HAZ for the filled VPPA welds. TEM observation was also performed for this weld. From the hardness trace, six different locations (from the weld centre to the parent plate) were identified for DSC and TEM assessment, again broadly following the minima and maxima of the hardness data (see Figure 4.21). Figure 4.22 presents the corresponding thermograms.

Figure 4.23 shows typical TEM micrographs at three of the positions studied (numbers 2, 3 and 4 in Figure 4.21); insets show the corresponding [001] Al diffraction patterns. Figure 4.23 (b),(d) and (f) show schematic diffraction patterns, based on the formation of S (Al_2CuMg) and Ω (Al_2Cu) phases. At position 4, extensive S formation dominates the structure, showing much stronger reflection contrast than the Ω phase. In position 3 large, but sparse Ω precipitates are seen (dark field image in top-left insert of Figure 4.23(c)), but no other aging precipitate could be resolved by the conventional imaging used here. The diffraction pattern (top-right insert), however shows weak streaks at S reflection positions, as well as some unknown spots (represented by squares in Figure 4.23(d)). These unknown reflections have been reported by Ratchev *et al.* (Ratchev *et al.*, 1998) who attributed them to S" phase. However, simulations made for this work (Wang *et al.*, 2003) indicated that the proposed structures for S" by Cuisiat *et al.* (Cuisiat *et al.*, 1984) could not elucidate such diffraction effects. In fact, such spots have been also observed in Al-Cu (Phillips, 1975) and Al-Zn-Mg-Cu (Park & Ardell, 1983), suggesting they are not exclusive to Al-Cu-Mg system. In the first instance these spots are believed to be from oxidation (Al_2O_3) during sample preparation as suggested by

Phillips and Park *et al.* (Phillips, 1975; Park & Ardell, 1983). At position 2 (closer to the fusion zone), only coarse Ω precipitates are observed (Figure 4.23 (e) and (f)) in the TEM.

Age hardening in 2x24-type alloys is generally identified with reactions from Al-Al_2CuMg pseudo-binary sequence. It has however been noted by a few authors that the Ω phase may in fact form in Al-Cu-Mg materials, even in the absence of the Ag micro-alloying additions that are widely linked to Ω precipitation in high Cu:Mg ratio alloys (Muddle & Polmear, 1989; Garg *et al.*, 1990; Wang *et al.*, 1999). Beyond the well known influence of silver on Ω formation, factors reported to influence the proportions of Ω as opposed and other Cu containing phases (i.e. θ (Al_2Cu) and S) include: (a) increased post-solutionising stretch levels tending to inhibit Ω precipitation – a process attributed to reduced vacancy concentrations in stretched materials restricting the formation of zone-type precursors to Ω (Cassada & Bartholomeusz, 1996) and enhances competitive heterogeneous θ and S nucleation, (b) slow cooling from solutionising temperature enhancing heterogeneous high temperature formation of Ω, with large particles (of the order of 200nm) being seen to form at Mn containing dispersoids at temperatures in excess of 300°C (Wang *et al*, 1999), and (c) direct quenching from solutionising temperature to intermediate aging temperatures, favouring Ω over S phase formation due to the absence of low temperature precipitation in conventionally heat treated materials (Wang *et al*, 1999).

In terms of the overall relationships between the hardness, DSC and TEM results in the filled VPPA welded materials, the results may then be described as follows:

(i) Between position 6 and 5 in Figure 4.21, hardness increases: the DSC thermogram in Figure 4.22 for position 5 shows that the endothermic peak A related to zone dissolution and the exothermic peak B related to the S precipitation are reduced in relation to position 6 (corresponding to the parent plate) (Jena *et al*, 1989; Gao *et al*, 2002). It may then be expected that at this outer edge of the HAZ, zones were lost to S precipitation in an essentially 'normal' artificial aging of the original naturally aged material (temperatures of the order of 220°C being required to age 2024 over periods of the order of

minutes (Polmear, 1995)). As noted for the MIG welds, It may be noted from the DSC curves for position 5 and 6 that the sharp, symmetrical form of the exothermic peak at ~210°C indicates that only one intermediate precipitate forms at these locations (i.e. S, with little or no Ω), as generally expected for 2024.

(ii) From position 5 to position 4 a significant drop in hardness is identified. The corresponding DSC curve in position 4 presents a broad exothermic peak B, which, in comparison to position 5 and 6, is shifted to higher temperature and has a lower heat content. The change in exothermic peak is consistent with further S formation of having occurred during welding. The TEM results show Ω formation due to the weld heat cycle. The apparent broadening and upward shift in temperature of exotherm B in the DSC results may then be consistent with Ω formation during the DSC run, with Ω formation being a higher temperature reaction that overlaps with the S formation peak. Overall, the DSC results show the material to be in an overaged condition at position 4, with the relatively sharp S phase diffraction spots indicating the precipitates have grown appreciably.

(iii) TEM and DSC results associated with the hardness peak at position 3 indicate a reasonably high zone content, with very fine S formation and relatively large, sparse Ω. The exothermic peak at 250-320°C now exhibits two clear shoulders, with the lower and higher temperature sides of the exotherm attributable to S and Ω respectively. Given the higher temperatures achieved at this location compared to position 4, the increased zone content and fine S phase distribution are attributable to reasonably effective re-solutionising at this location. This being the case, the formation of Ω is then consistent with the slow cooling effect reported by Wang *et al.* (Wang *et al*, 1999) for conventional 2x24 material. In terms of strength/hardness levels at position 3, the high zone content and fine S precipitation are consistent with a significant degree of low temperature/natural aging taking place post-welding. In terms of the measurements from position 2, some caution must be exercised in interpretation given the slope of the hardness curve at this point, the spatial

uncertainty in extracting the DSC and TEM samples (of the order of ±1mm), and the potential incidence of liquation and diffusion interactions with the fusion zone (Rading *et al.*, 1998). However, it is still significant to note the prevalence of coarse Ω at this location (with the DSC results also indicating a high zone content).

4.2.3.2 DSC assessment of VPPA autogeneous welds:

As presented for the MIG and VPPA-filled welds, key locations linked to the hardness profile have been identified for DSC measurements (see Figure 4.24) although TEM observation was not performed for these samples. Figure 4.25 presents the corresponding DSC thermograms which may be described in relation to the hardness trace as follow:

(i) In figure 4.24, the hardness increase between position 6 and position 5. The DSC thermogram for position 5 shows in Figure 4.25 a reduction of the endothermic A and exothermic B peaks compared to position 6. It may be also noticed that these peaks are shifted at lower temperature. Less zone content and less S phase formation may be seen , so it may be expected 'normal artificial aging' of the material at this position which is consistent with the maximum hardness.

(ii) From position 5 to position 4, the hardness drops. A clear difference occurs for the exothermic peak B which has low heat content and is shifted to higher temperature. The low heat content of the peak related to the S formation implies the extensive prior S formation which may be interpreted as an overaging of the material at this position.

(iii) Between position 4 and 3, the hardness increases again. In DSC thermograms, higher zone content may be noticed in position 3 compared to position 4. Two clear exothermic peaks shifted at higher temperature may be distinguished in the DSC curve for position 3. In keeping with earlier discussion, the material appears to be re-solutionised at this position

whilst no TEM observation has been made to investigate the microstructure at this position, it may be noted that similar double exothermic peaks have been observed in the DSC thermograms at intermediate temperatures. As such it is presumed that the high temperature peak corresponds to Ω phase formation. Re-solutionsing may hold for position 2.

Whilst the hardness distributions of both VPPA welds present similar general profiles but with a wider outer HAZ hardness peak and generally lower hardness in the autogeneous weld, it may be seen that the DSC thermograms also present similar profiles with broadly similar interaction of aging, overaging, and resolutionising apparent across both welds.

4.2.3.3 Observations on DSC assessment for the MIG and VPPA welds

It may be identified that complex and spatially varying influences of ageing (coarsening), resolutionising and reprecipitation (during cooling, or on standing of the weld) occur within the HAZ for the three welds studied. DSC provides evidence of these conditions (as discussed above). Although it must be recognized that DSC is indirect evidence of matrix precipitation condition, it is possible to be fairly confident of the assessment given since the alloy system is well known, and TEM analyses confirm a number of the observations. The overall DSC thermograms presented in this study for the three welds (MIG, filled VPPA and autogeneous VPPA welds) show similar profiles and suggest similar conclusions in relation with the hardness traces, however a major difference (in terms of DSC results) exists between the MIG weld and the VPPA welds (filled and autogeneous) in the presence of Ω phase in the VPPA welds, presumably due to slow heating/cooling effects. The MIG weld has a much higher welding speed (~ x2.6) than both VPPA welds, consistent with slow cooling being a determining effect in Ω formation in the HAZ close to the fusion zone for the VPPA welds. However further quantitative analysis of thermal histories for the various processes would clearly be valuable for further quantitative microstructural understanding, particularly given the evidence of more effective re-solutionising and re-aging of material in the VPPA HAZs close to the fusion zone, suggesting rapid

effective cooling. To summarise the DSC and TEM study, Figure 4.26 illustrates schematically the overall sequence of events thought to occur in the various region of the weld microstructure in relation to the associated thermal cycle.

4.2.4 Pore characterisation

In terms of defect population in both VPPA welds, a semi-quantitative study has been carried out. BEI micrographs are presented in Figure 4.27. In the filled VPPA weld, fine interdentritic defects may be detected of the order of 10 to 20μm. Occasional gas porosity up to 50μm may also be identified (around 1 or 2 per mm^2). In the autogeneous VPPA weld, very few gas bubbles (less than 1 per mm^2) are seen in comparison with the large population identified in the MIG (see Figure 4.8). Interdendritic defects of the order of 5 to 10μm are identified in the centre of the fusion zone. At the edge of the fusion zone, the defects are seen to be somewhat larger: of the order of 20 to 40μm. These longer defects may be considered as more damaging in longitudinal loading of the welds due to the grain orientation at the edge of the fusion zone which would then be approximately perpendicular to the loading direction.

4.2.5 Residual stress

Figure 4.28 presents the longitudinal residual stress data obtained from a representative fatigue test sample of the autogeneous VPPA weld before and after a single fatigue load cycle at 270MPa, using (lab) X-ray diffraction measurements ((331) reflection plane) and X-ray synchrotron diffraction measurements. The residual stress data are plotted in conjunction with a corresponding hardness trace. As presented for the MIG weld, all data have been binned and folded (i.e. averaged by: (a) assuming symmetry about the weld centre line and (b) taking 3 point moving averages of measurements that are 1mm apart). Complex stress profiles may be identified in Figure 4.28: prior to loading, similar stress profiles may be seen for the lab X-rays and Synchrotron X-rays. Starting from the outer HAZ edge, the residual stress rises from compressive to tensile levels until a maximum tensile stress of ~100MPa is reached at a distance of the order of ±15mm from the centre-line, dropping to ~75MPa at the transition between HAZ and fusion zone. After loading, stress redistribution and relaxation occur, as seen in the

MIG weld. Clear double tensile residual stress peaks may now be seen in the HAZ for both X-ray methods. From the outer HAZ edge, the synchrotron residual stress increases up to ~90MPa (~80MPa by lab X-ray) and then drops to a low/compressive residual stress of the order of -11MPa (~-40MPa by lab X-ray). This minimum is located in the soft and overaged region of the HAZ (minimum in hardness trace). Moving closer again to the fusion zone, the residual stress increases again to a tensile peak value of 60MPa (~25MPa by lab X-ray), located near the re-solutionised and re-aged part of the HAZ (hardness peak close to the fusion zone). Whilst the typical error bars are significantly different (factor of 3 between the lab X-rays and Synchrotron X-rays), the overall residual stress trendlines are reasonably consistent.

4.3 Conclusion

Weld structures have been observed by optical and SEM microscopy. Columnar dendritic structures at the edge of the fusion zone may be seen for the MIG and VPPA welds, with equiaxed dendritic structure in the centre only for the MIG and filled VPPA welds. In the autogeneous VPPA weld, axial columnar dendritic structure is seen in the centre of the fusion zone. The finest dendritic arm spacings may be seen for the MIG welds. In the transition between fusion zone and HAZ, grain boundary decoration and intragranular precipitation may be observed in all three welds. In terms of grain structure, fairly uniform and equiaxed grain structure of the order of 50μm may be seen in the MIG weld for 80% of the fusion zone width. In the filled VPPA weld, a similar predominantly equiaxed grain structure with a gradual decrease in grain size may be seen from the centre towards the edge of the fusion zone, with some larger grains being seen at the transition region between HAZ and fusion zone. In the autogeneous VPPA weld, a central coarse columnar grain structure may be identified with a twin boundary relationship between dendrites. In terms of hardness, the fusion zone strengths are of the order of 70 % of the parent material strength. Double hardness peaks in the HAZ may be observed in all three welds but are most distinct in the VPPA welds. A balance between aging, overaging, re-solutionising and re-precipitation has been identified across the heat affected zone, with the near fusion zone hardness peak being attributable to partial re-solutionising and re-aging. A

consistent feature of the HAZ in both VPPA welds is the apparent presence of Ω (Al_2Cu), attributable to slow cooling rates (competitive formation with S/S′). It may also be noted that HAZ hardness profiles reported for TIG welded 2024 (Norman *et al*, 1998) are similar in form to those reported in this study. Similar conclusions were reached regarding thermal effects across the heat-affected zone, although DSC assessment of the material conditions was not reported and the presence of Ω phase was not identified. In terms of weld defect population, quantitative and semi-quantitative studies have been carried out. In the MIG welds, large, circular gas porosities and more acicular interdendritic defects have been identified. The finer interdendritic defects have been observed in the VPPA welds with few gas bubble defects. Two interdendritic defect populations have been observed in the autogeneous VPPA weld, with larger defects towards the edge of the fusion zone. In terms of residual stress, residual stress fields have been measured on fatigue samples for two welds by laboratory X-ray or synchrotron methods prior to and after, a single fatigue loading cycle. It is clear that stress relaxation and stress redistribution occur when the fatigue samples are loaded for one cycle. In the MIG weld, it has been noticed that the fusion zone presents a tensile residual stress field, especially at the edge of the fusion zone. For the autogeneous VPPA weld, complex residual stress profiles in the HAZ have been identified and linked to the hardness traces. Double tensile peaks have been observed in the loaded sample where the minimum residual stress is located in the soft over-aged region of the HAZ: somewhat higher residual stress levels are noted in regions of the HAZ further from the weld line in the loaded autogeneous VPPA weld compared to the MIG weld, particularly for the region outside of the HAZ hardness minimum.

References

ASM International (1998). Aluminium and Aluminium Alloys. in. A. S. Handbook, Davis, J.R.: 376-420.

Bussu, G. and P. E. Irving (2000). "Fatigue performance of Friction Stir Welded 2024-T351 aluminium joints." International Journal of Fatigue 25(1): 77-88.

Cassada, W. A. and M. F. Bartholomeusz (1996). "The effect of Cu and Mg content on mechanical properties of Al- Cu-Mg alloys with and without Ag additions." Aluminium Alloys: Their Physical and Mechanical Properties, Pts 1-3 217: 1765-1770.

Cross, C. E. and G. R. Edwards (1989). Welding of aluminium alloys. in Aluminum Alloys--Contemporary Research and Applications. A. K. Vasudevan and R. D. Doherty, Elsevier Science & Technology. 31.

Cuisiat, F., P. Duval and R. Graf (1984). "Study of Primary Stages of Decomposition of an Al-Cu-Mg Alloy." Scripta Materialia 18: 1051-1056.

Gao, N., L. Davin, S. Wang, A. Cerezo and M. J. Starink (2002). Precipitation in stretched Al-Cu-Mg alloys with reduced alloying content studied by DSC, TEM and atom probe. ICAA8, Cambridge, Trans Tech publications, 2, 923-928.

Garg, A., Y. C. Chang and J. M. Howe (1990). "Precipitation of the Omega-Phase in an Al-4.0cu-0.5mg Alloy." Scripta Metallurgica Et Materialia 24(4): 677-680.

Huang, C. and S. Kou (2000). "Partially melted zone in Aluminium welds - Liquation mechanism and directional solidification." Welding Journal Supplement: 113s-120s.

Jena, A. K., A. K. Gupta and M. C. Chaturvedi (1989). "A differential scanning calorimetric investigation of precipitation kinetics in the Al-1.53wt%Cu-0.79wt%Mg alloy." Act. Metall. Mater. 37(3): 885-895.

Muddle, B. C. and I. J. Polmear (1989). "The Precipitate Omega-Phase in Al-Cu-Mg-Ag Alloys." Acta Metallurgica 37(3): 777-789.

Norman, A. F., V. Drazhner and P. B. Prangnell (1999). "Effect of welding parameters on the solidification microstructure of autogenous TIG welds in an Al-Cu-Mg-Mn alloy." Materials Science and Engineering a-Structural Materials Properties Microstructure and Processing 259(1): 53-64.

Norman, A. F., V. Drazhner, N. Woodward and P. B. Prangnell (1998). Effect of welding parameters on the microstructure of Al-Cu-Mg autogeneous TIG welds. 7th International conference on joints in aluminium, Cambridge, 26-37.

Norman, A. F., K. E. Jakielski, G. Scott and P. B. Prangnell (1997). Process Control of Weld Microstructures in a 2024 (Al-Cu-Mg) Alloy. 4th Decennial International Conference on Solidification Processing, Sheffield, 670-674.

Norman, A. F. and P. B. Prangnell (1998). A study of microsegregation effects in TIG and Laser beam welds of an Al-Cu-Mg alloy. ICAA-6, Toyohashi, The Japan Institute of Light Metals, 3, 1435-1440.

Park, J. K. and A. J. Ardell (1983). "Microstructures of the Commercial 7075 Al Alloy in the T651 and T7 Tempers." Metallurgical Transactions A 14(10): 1957-1965.

Phillips, V. A. (1975). "High Resolution Electron Microscope Observations on Precipitation in Al-3.0per cent Cu Alloy." Act. Metall. Mater. 23(6): 751-767.

Polmear, I. J. (1995). in Light Alloys. Chapter 2 & 3, Arnold: 24-168.

Prangnell, P. B. and A. F. Norman (1998). Grain boundary melting in Al-Cu-Mg alloy welds. ICAA6, Toyohashi, The Japan Institute of Light Metals, 3, 1501-1506.

Rading, G. O., M. Shamsuzzoha and J. T. Berry (1998). "A model for HAZ Hardness Profiles in Al-Li-X alloys: Application to the Al-Li-Cu Alloy 2095." Welding Journal Research Supplement.

Ratchev, P., B. Verlinden, P. De Smet and P. Van Houtte (1998). "Precipitation hardening of an Al-4.2 wt% Mg-0.6wt%Cu Alloy." Acta Materialia 46: 3523-33.

Smallman, R. E. and R. J. Bishop (1999). in Modern Physical Metallurgy & Materials Engineering, BH.

Wang, L. M., H. M. Flower and T. C. Lindley (1999). "Precipitation of the Omega phase in 2024 and 2124 aluminium alloys." Scripta Materialia 41(4): 391-396.

Wang, S., F. Lefebvre, I. Sinclair and M. J. Starink (2003). "Microstructure of VPPA welding of 2024 alloys with 2319 filler." in preparation Southampton, UK.

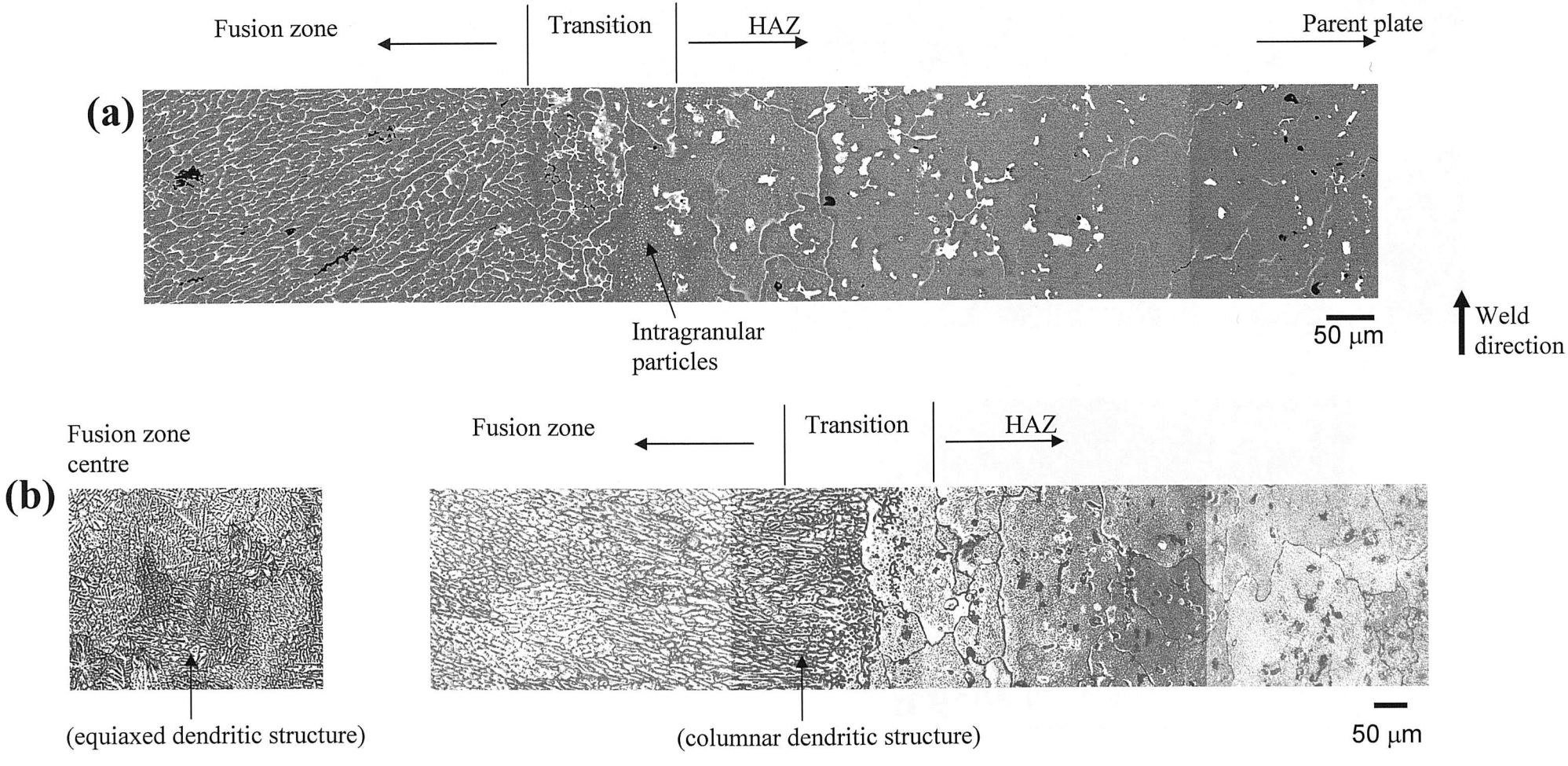

Figure 4.1 MIG weld microstructure corresponding to the fatigue coupon top surfaces: (a) back scattered electron image, (b) optical image

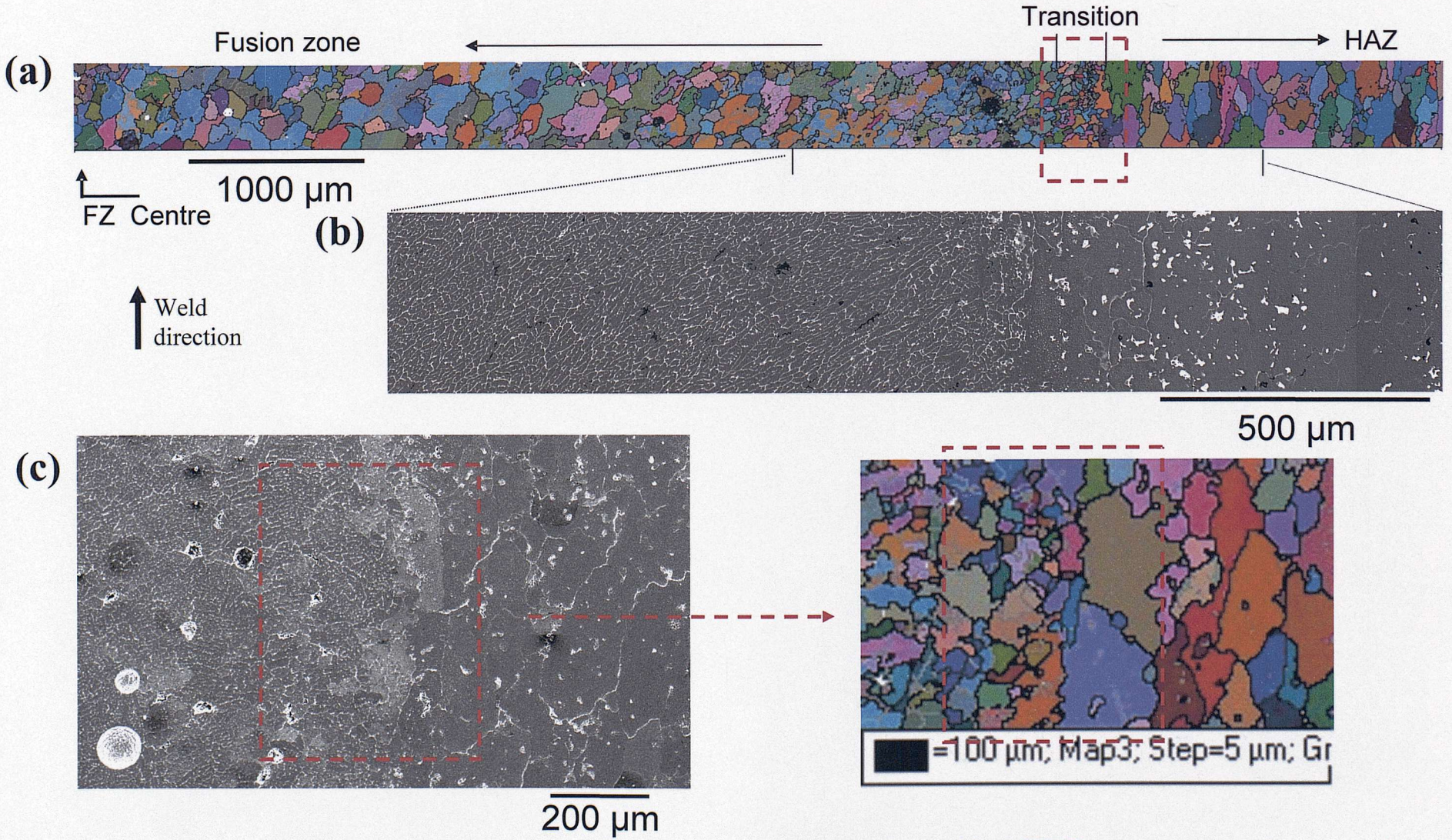

Figure 4.2 Microstructure of the MIG weld corresponding to fatigue sample top surfaces with (a) EBSD orientation map, (b) associated SEI macrograph of the edge of the fusion zone and (c) highlights of the transition zone with EBSD and SEI macrographs

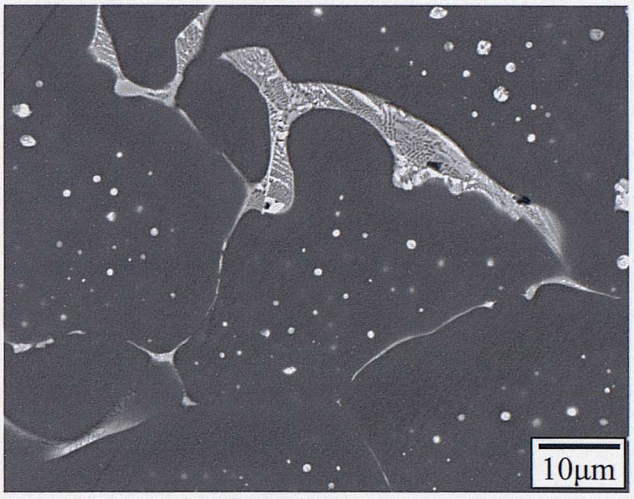

Figure 4.3 BEI micrograph of partial melting zone (transition zone) with eutectic phase, grain boundary decorations and intragranular precipitates

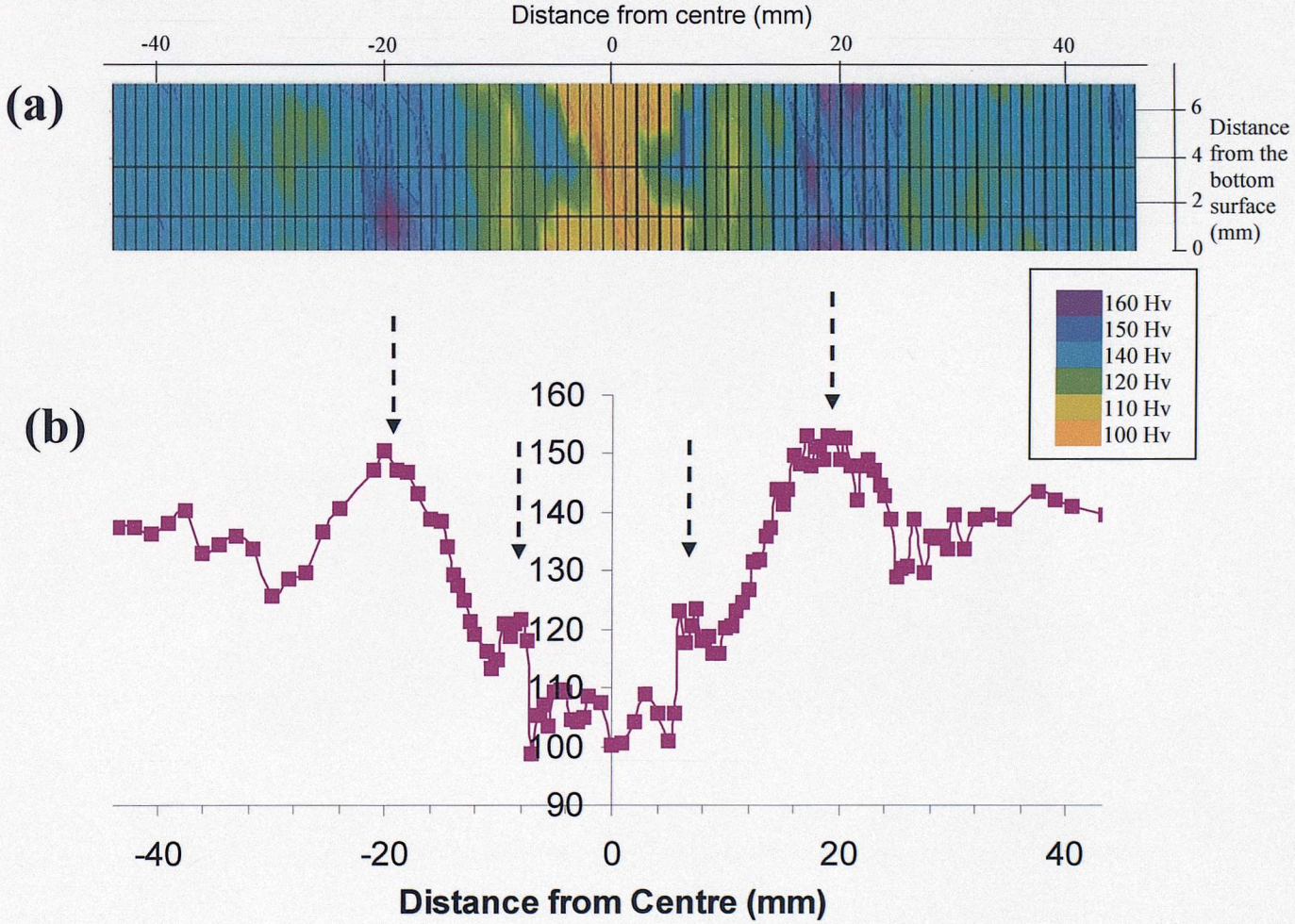

Figure 4.4 (a) Two dimensional hardness map of the MIG weld (b) Hardness trace of the weld on the top surface of typical skimmed fatigue sample. Arrows indicate hardness peaks.

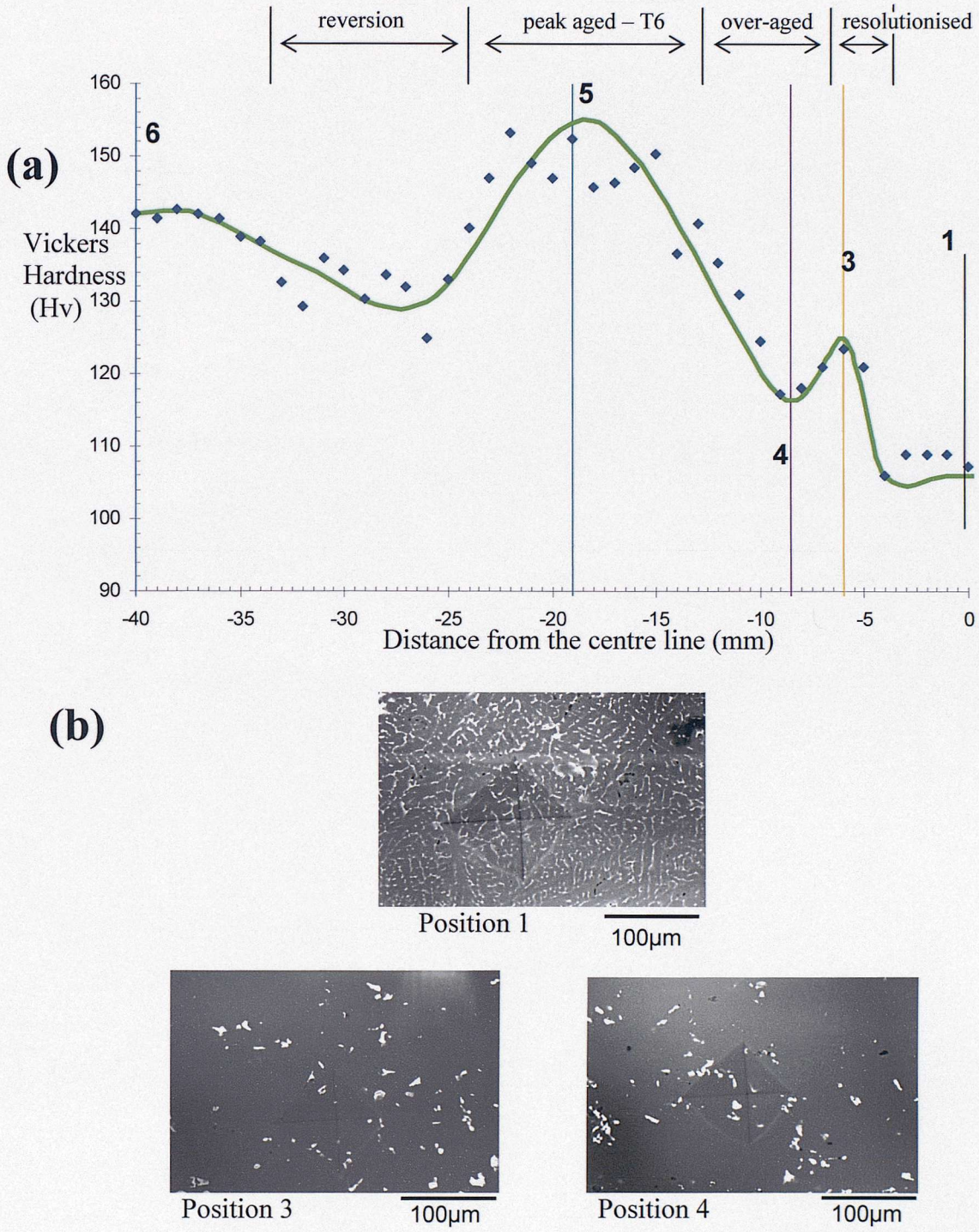

Figure 4.5 (a) Hardness trace for the skimmed MIG weld highlighting the locations of DSC/TEM sample extraction and (b) back-scattered electron images of locations 1, 3 and 4.

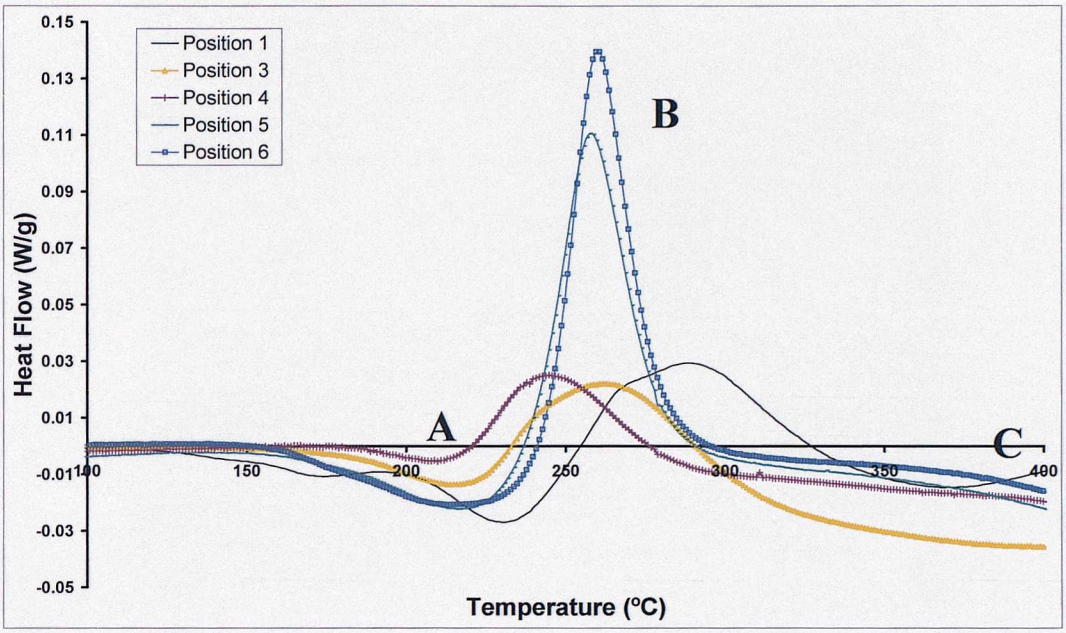

Figure 4.6 DSC thermograms for the MIG weld between 100°C and 400°C.

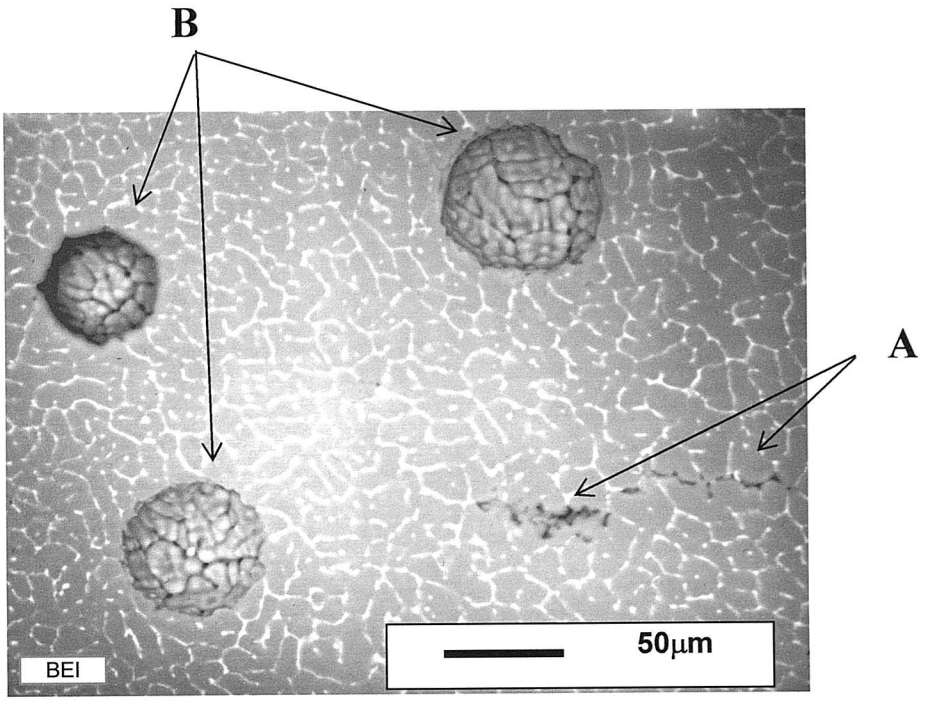

Figure 4.7 Pore characterisation in MIG fusion zone (SEI micrograph): interdendritic defects (A) and gas porosity (B).

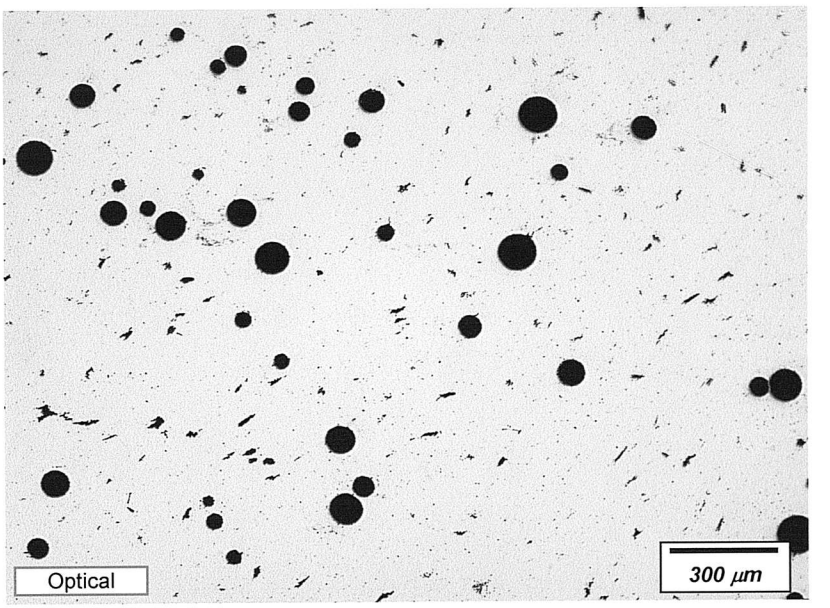

Figure 4.8 Optical macrograph of MIG fusion zone defect distribution.

(a)

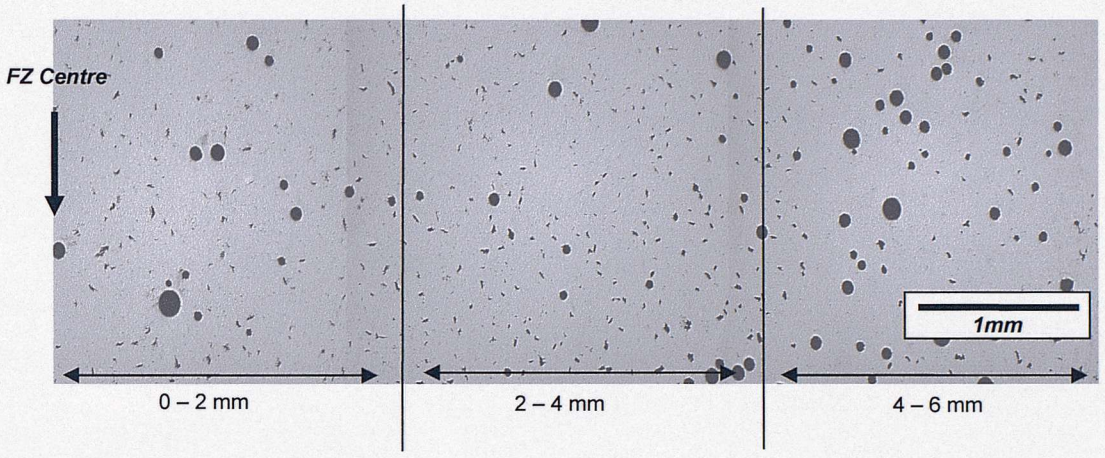

(b)

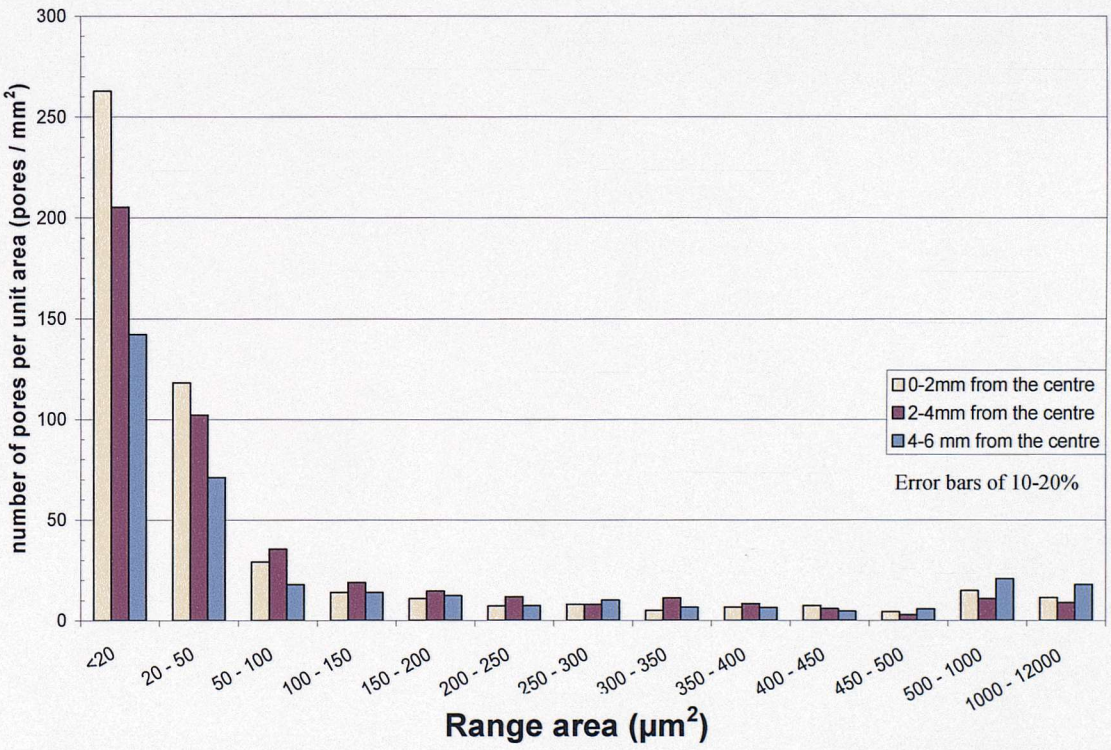

Figure 4.9 Pore characterisation across the MIG fusion zone – (a) typical optical section of the MIG weld (b) histogram of pore density vs pore size for 3 bands across the fusion zone.

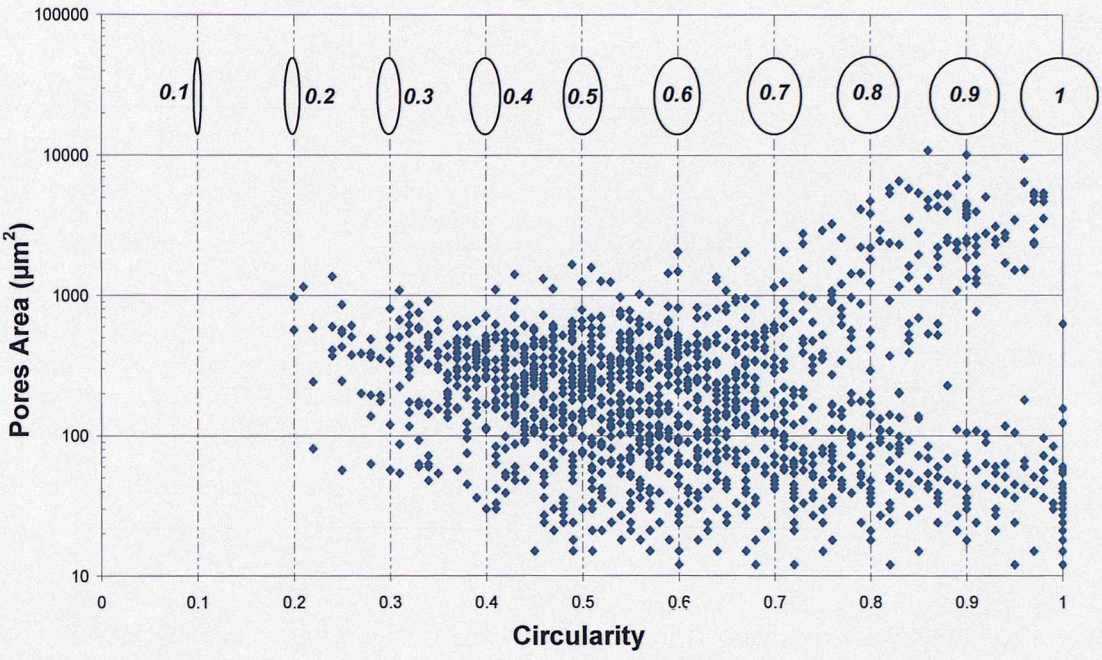

Figure 4.10 Size and shape relationship for the MIG fusion zone pore population

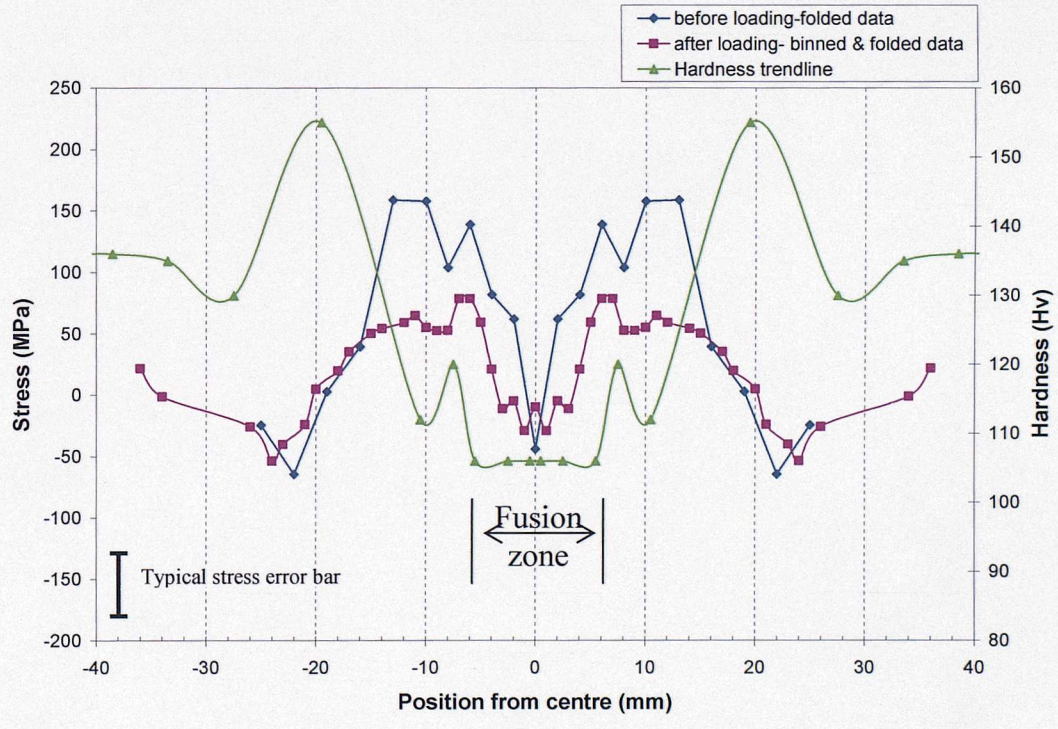

Figure 4.11 Residual stress and hardness traces for the MIG weld using (331) laboratory X-ray reflections.

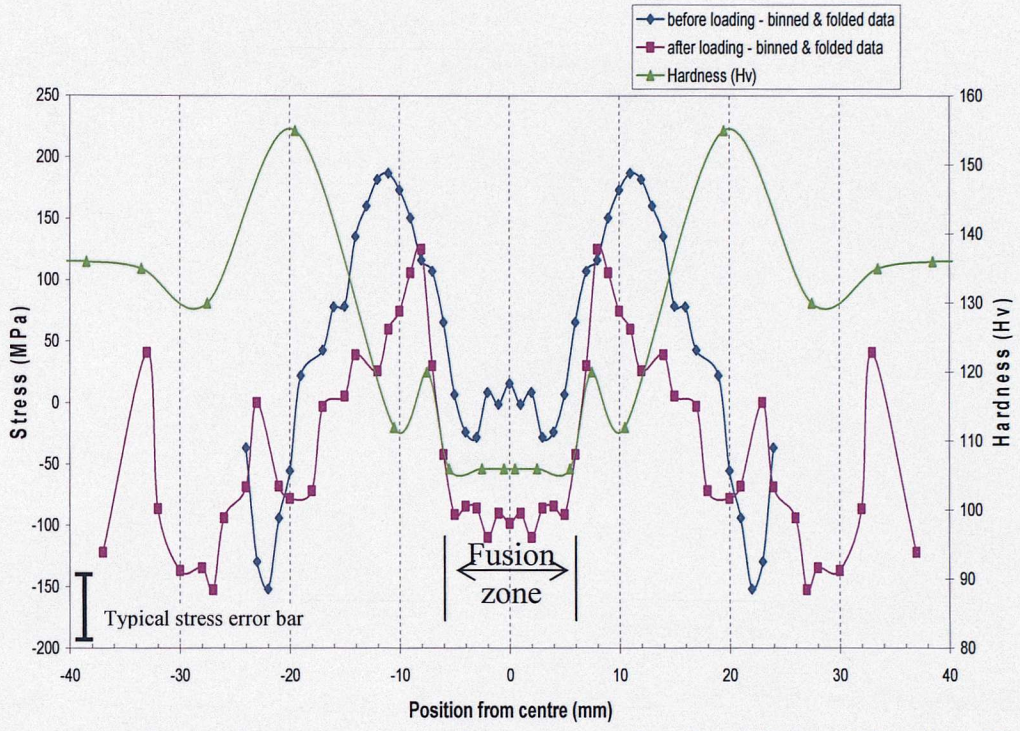

Figure 4.12 Residual stress and hardness traces for the MIG weld using (311) laboratory X-ray reflections.

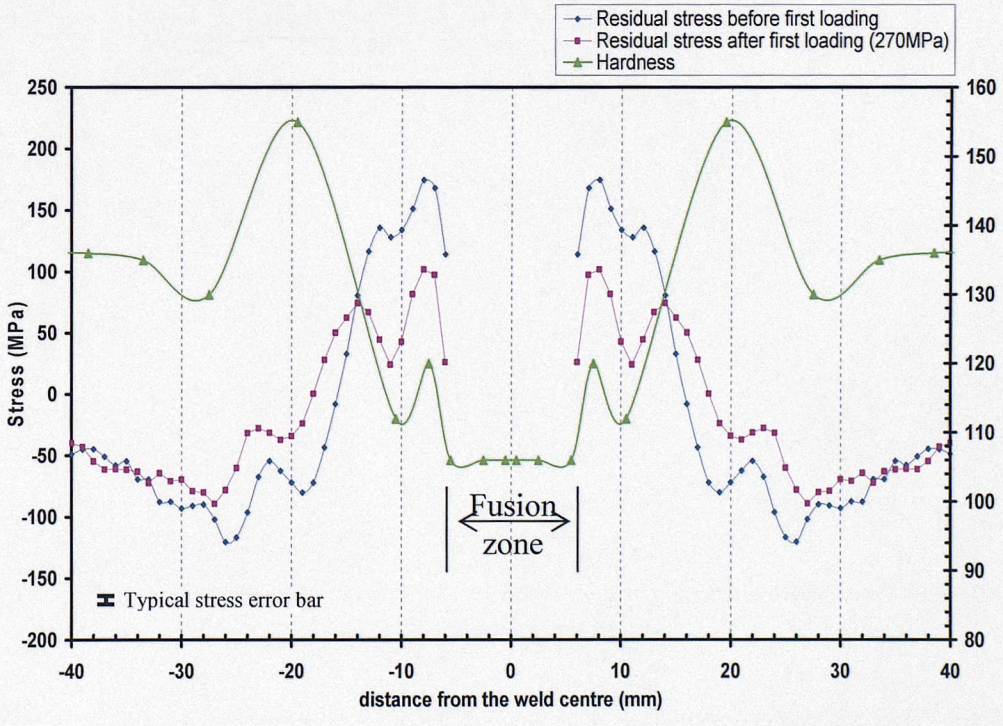

Figure 4.13 (a) Synchrotron residual stress and hardness traces for the MIG weld

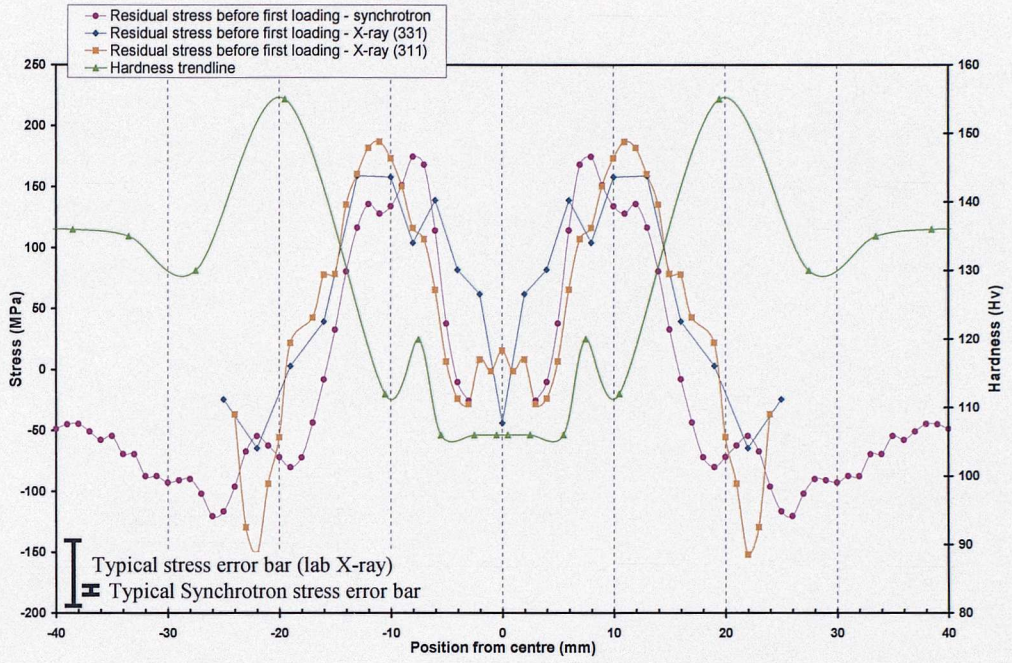

Figure 4.13 (b) Residual stress and hardness traces for the MIG weld before first loading for (331) and (311) laboratory X-ray reflections and Synchrotron X-ray.

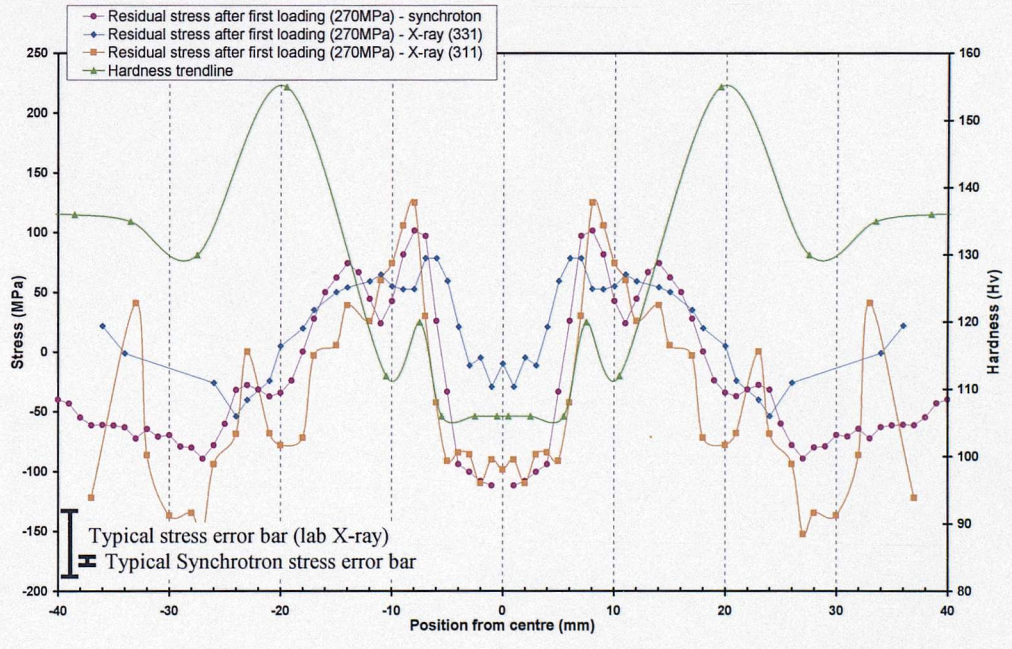

Figure 4.13 (c) Synchrotron residual stress and hardness traces for the MIG weld after first loading (270MPa) for (331) and (311) laboratory X-ray reflections and Synchrotron X-ray.

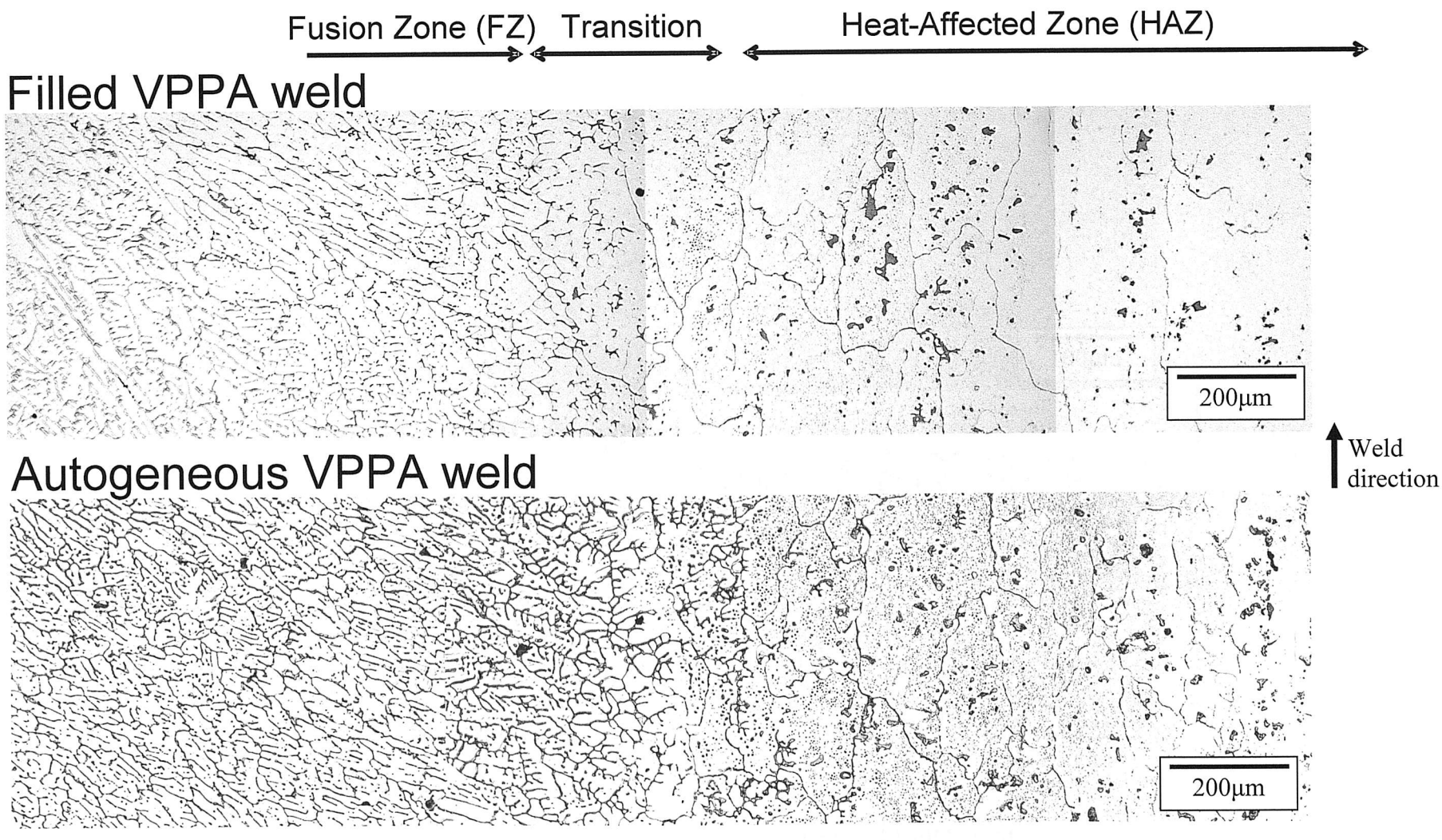

Figure 4.14 Columnar interdendritic structures at the edge of the fusion zone for the filled and autogeneous VPPA welds

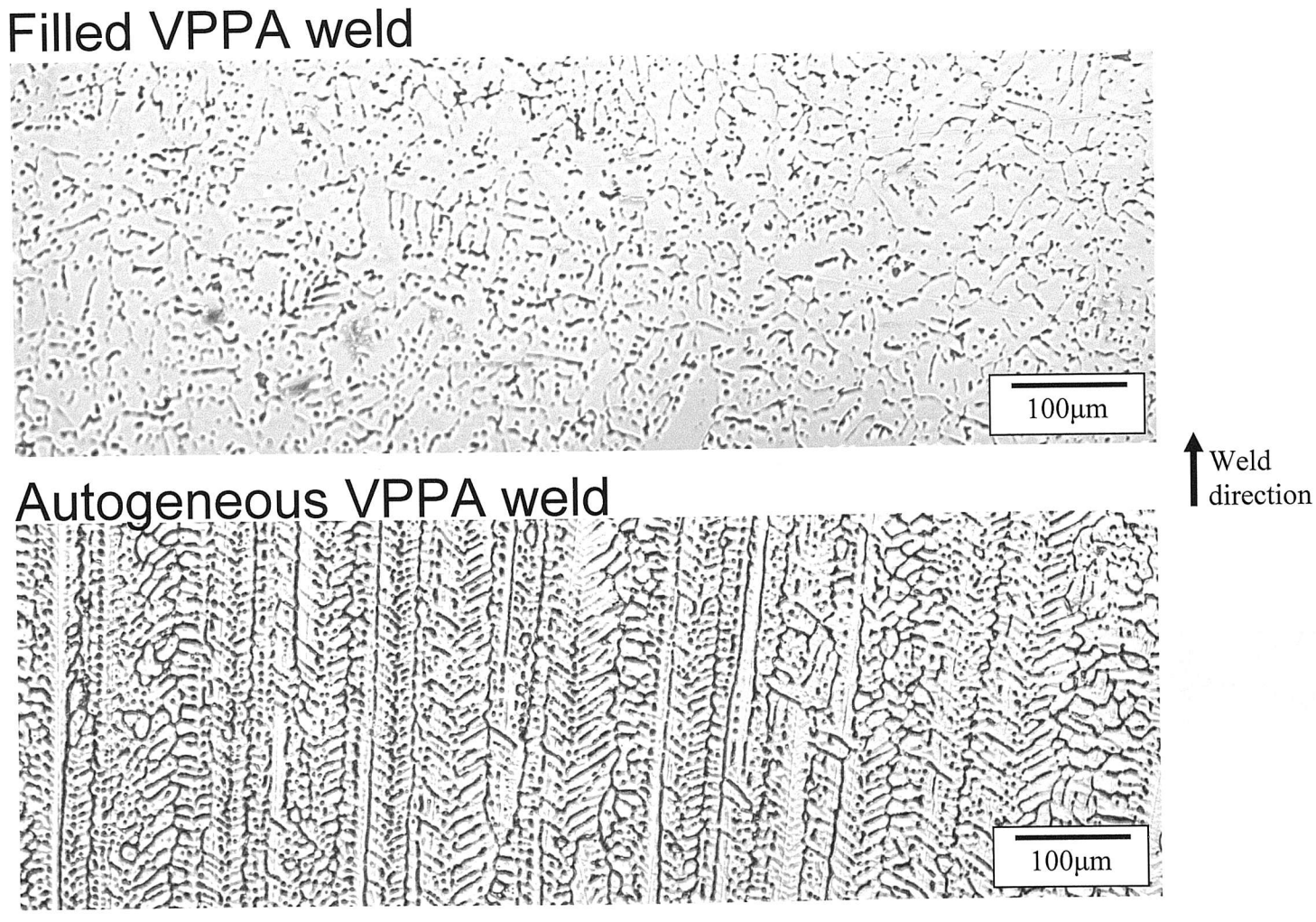

Figure 4.15 Variation of the microstructure in the centre of the fusion zone for the filled VPPA weld (equiaxed structure) and autogeneous VPPA weld (axial columnar)

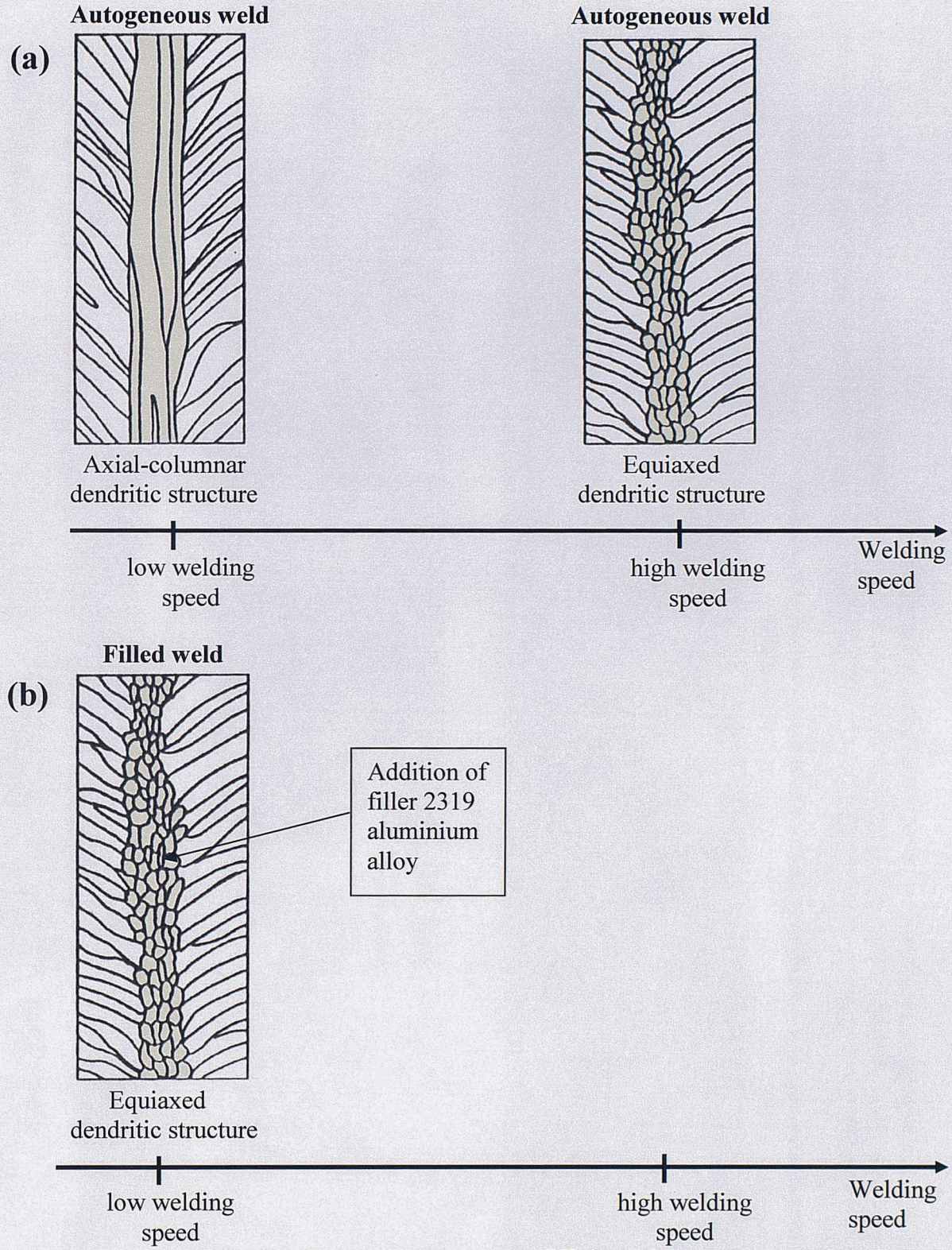

Figure 4.16 Schematic diagram illustrating the different microstructures in the centre of the fusion zone found in the TIG 2024 depending on (a) the welding speed and (b) with the addition of filler material (Norman *et al.*, 1997; Norman *et al.*, 1999)

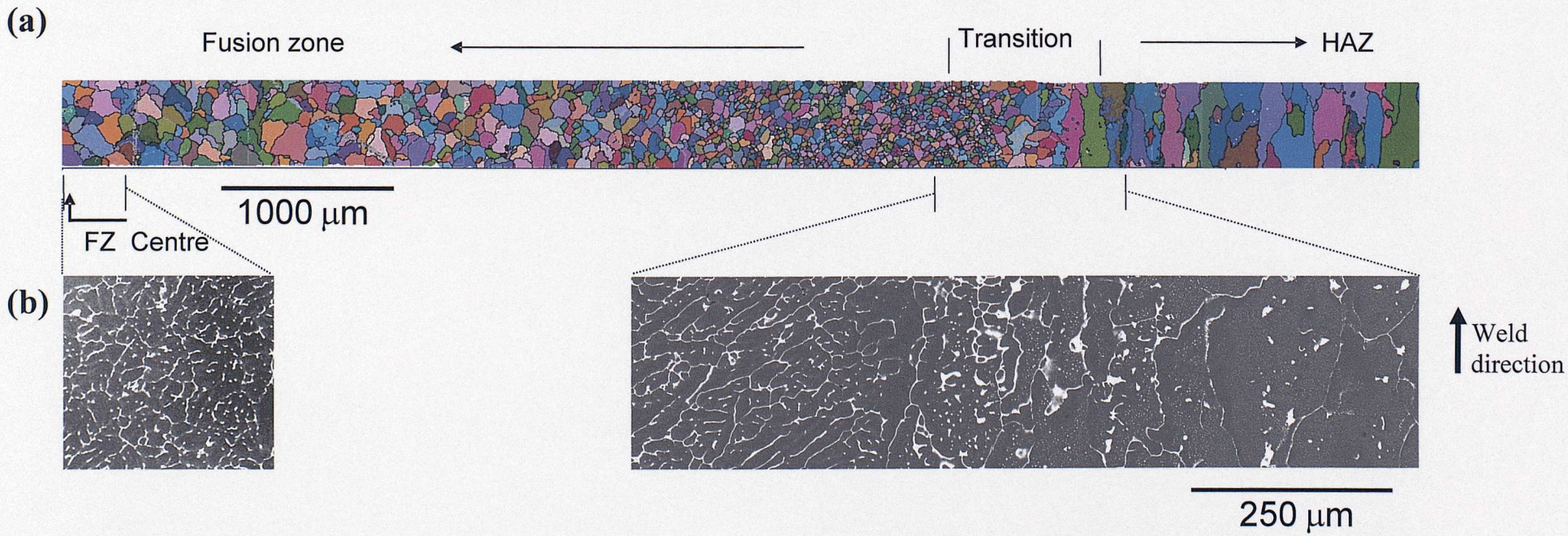

Figure 4.17 Weld microstructure of the filled VPPA weld with (a) EBSD maps associated and (b) associated BEI macrographs of the different parts of the fusion zone.

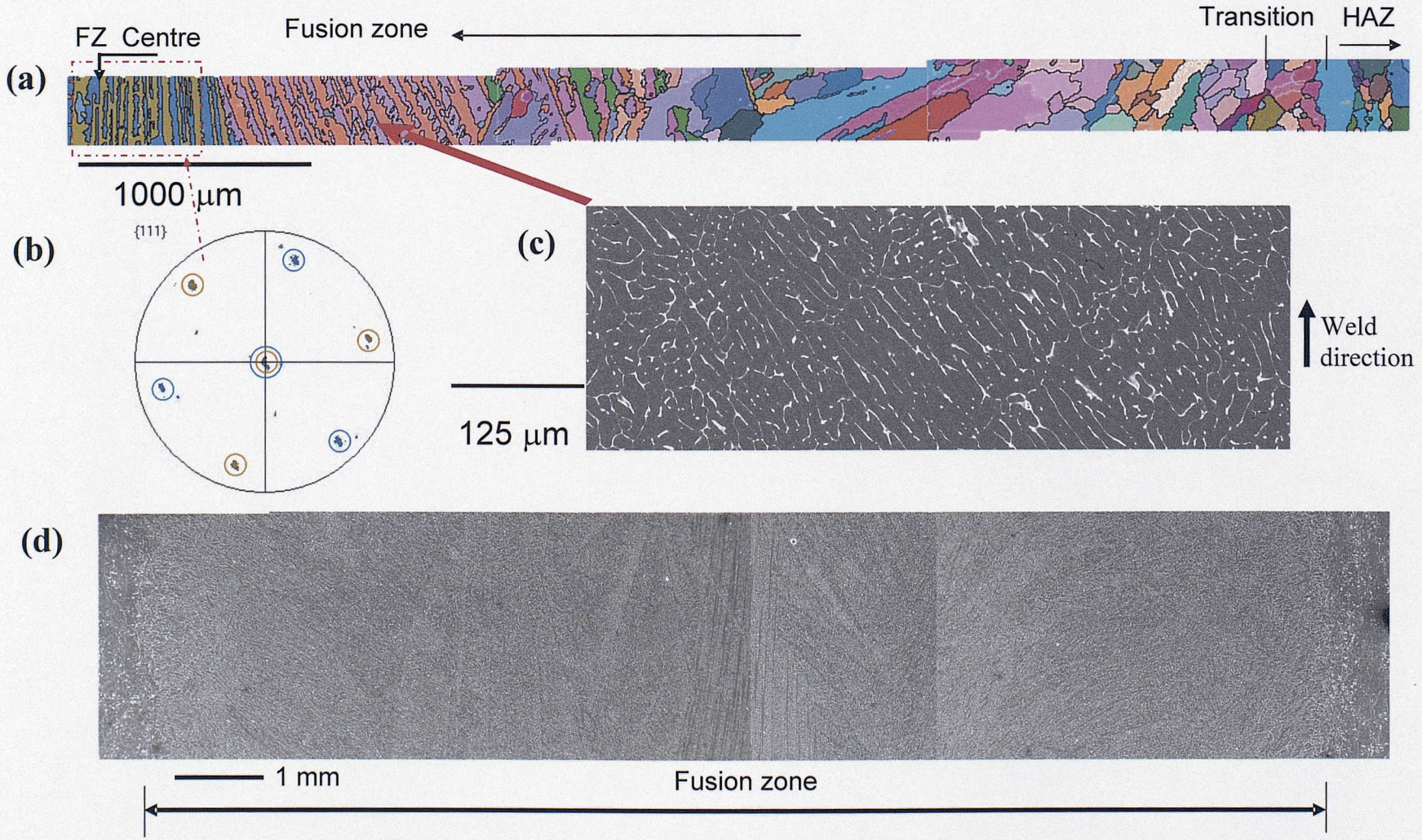

Figure 4.18 Weld microstructure of the autogeneous VPPA weld with (a) EBSD maps, (b) Pole figure in plane {111}associated with the centre of the fusion zone, coloured circles highlight poles associated with the two grain orientations in the far left hand region of (a), and (c) & (d) associated BEI macrographs of the different parts of the fusion zone

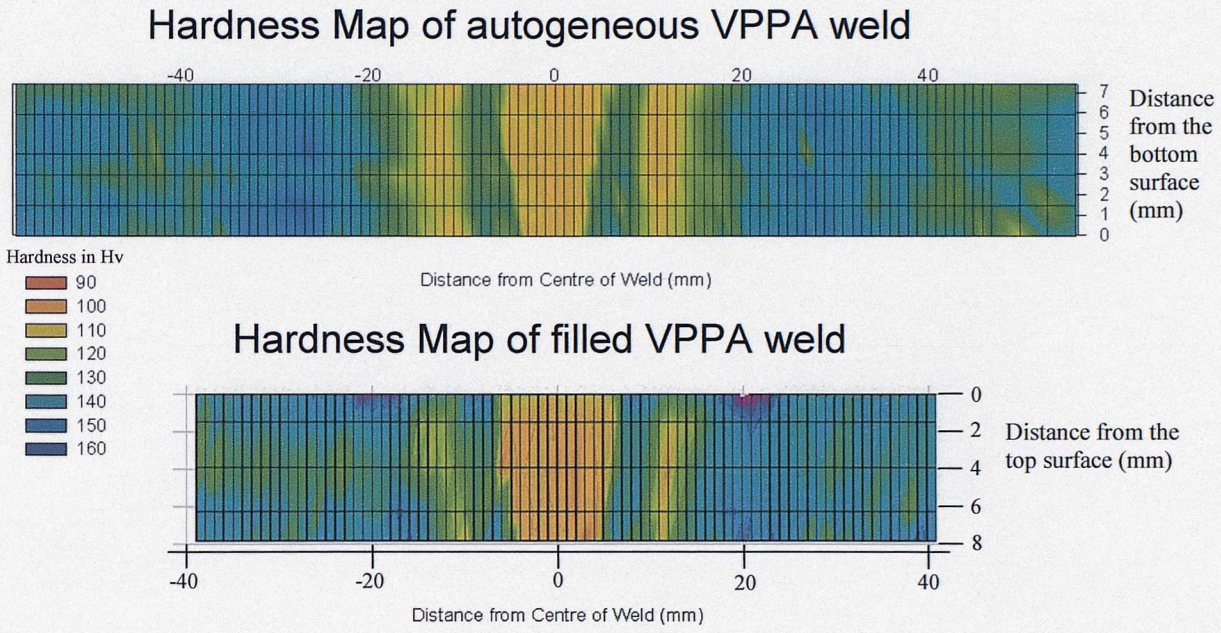

Figure 4.19 Hardness map from (a) autogeneous VPPA and (b) filled VPPA welds

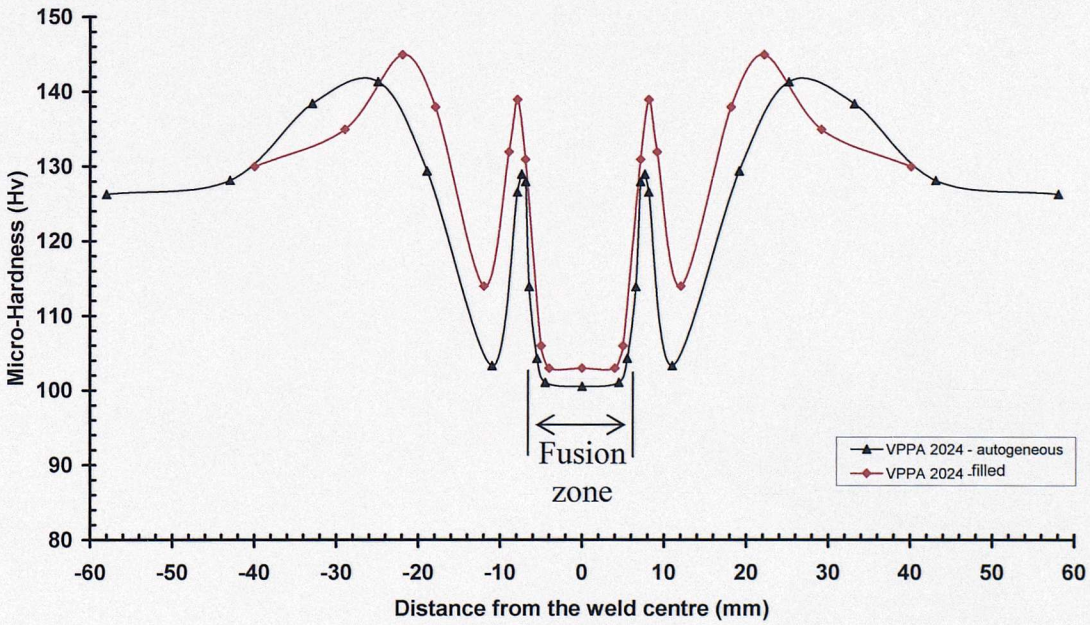

Figure 4.20 Representative hardness traces from the top surface of the autogeneous VPPA and filled VPPA welds.

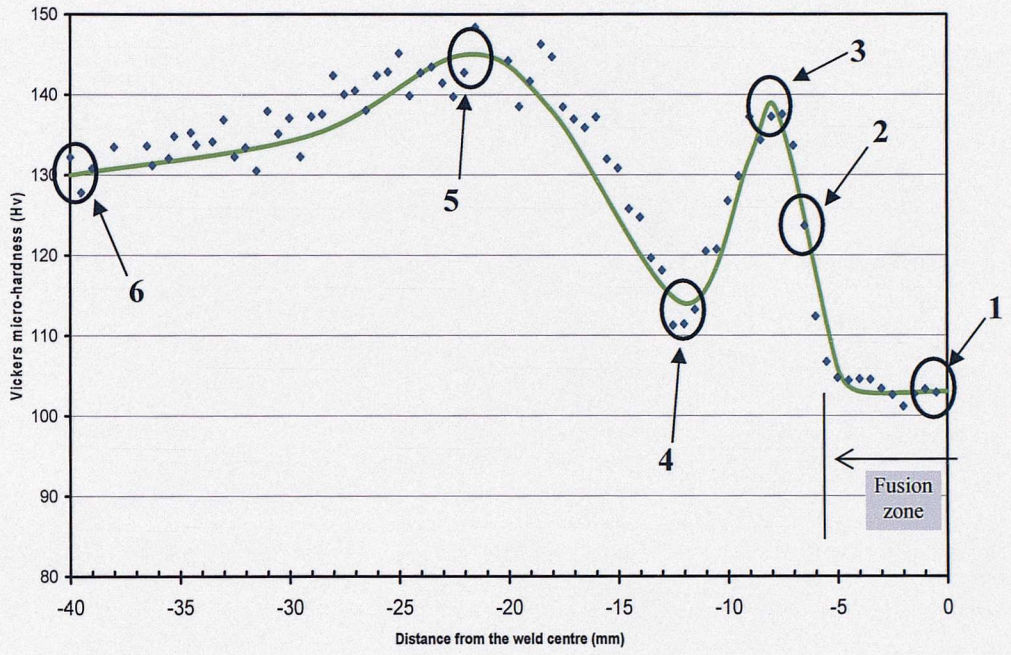

Figure 4.21 Hardness trace for the skimmed filled VPPA weld: numbered circles highlight the locations where DSC & TEM samples were extracted

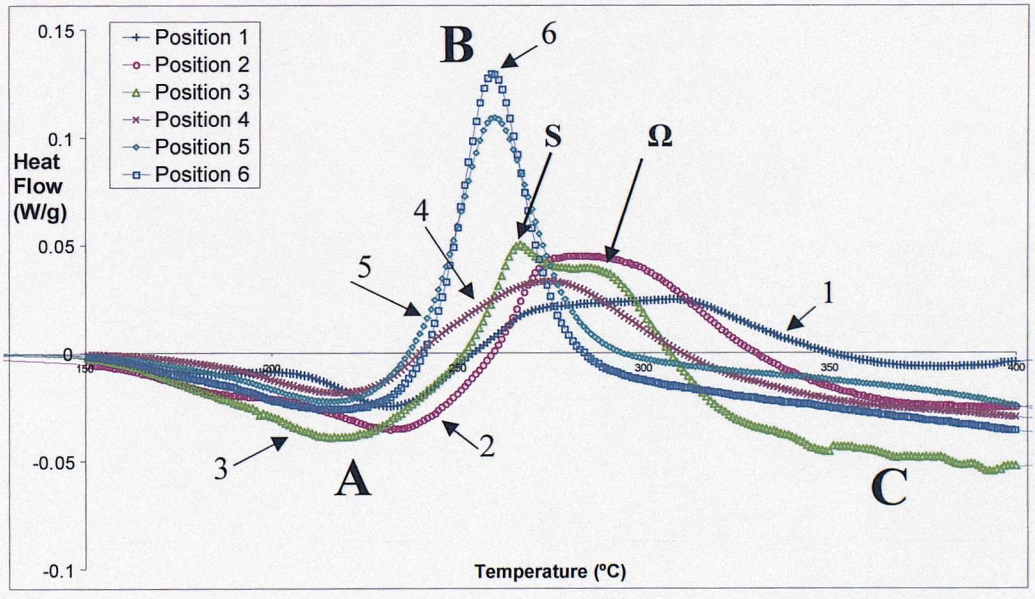

Figure 4.22 DSC thermograms for the various curve locations highlighted in Figure4.21.

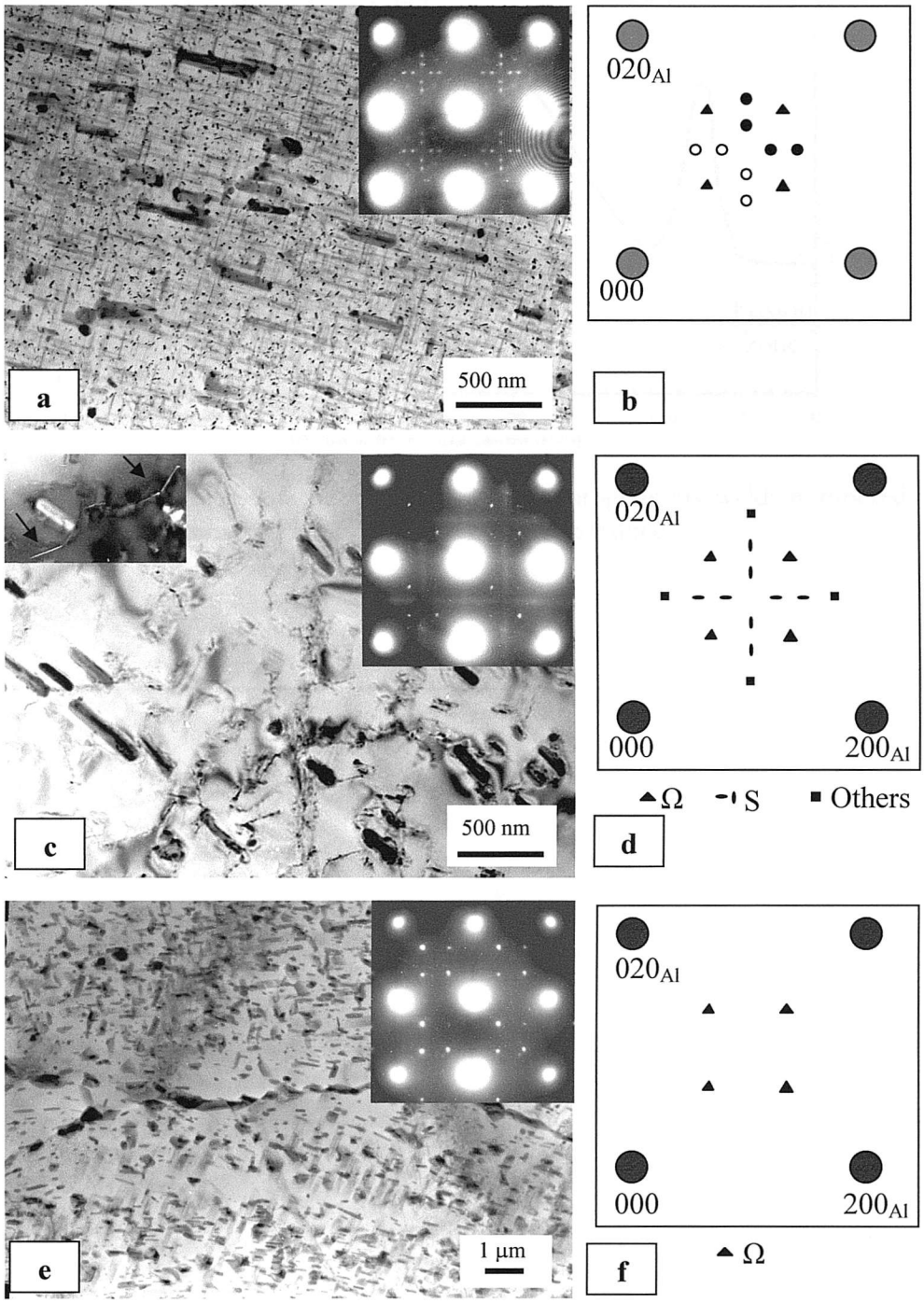

Figure 4.23 TEM micrographs and corresponding $[001]_{Al}$ selected area diffraction patterns showing the formation of S (Al_2CuMg) and Ω (Al_2Cu) precipitates at different locations (refer to Figure 4.18): (a) & (b) Position 4, S (+Ω), (c) & (d) Position 3, S+Ω, (and some unknown spots), and (e) & (f) Position 2, GP+Ω.

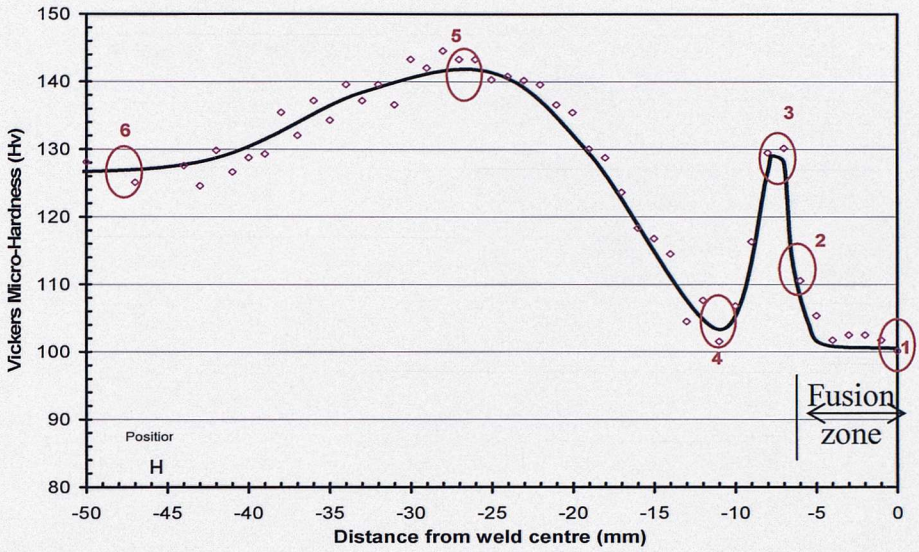

Figure 4.24 Hardness trace for the skimmed VPPA autogeneous weld: numbered circles highlight the locations where DSC samples were extracted

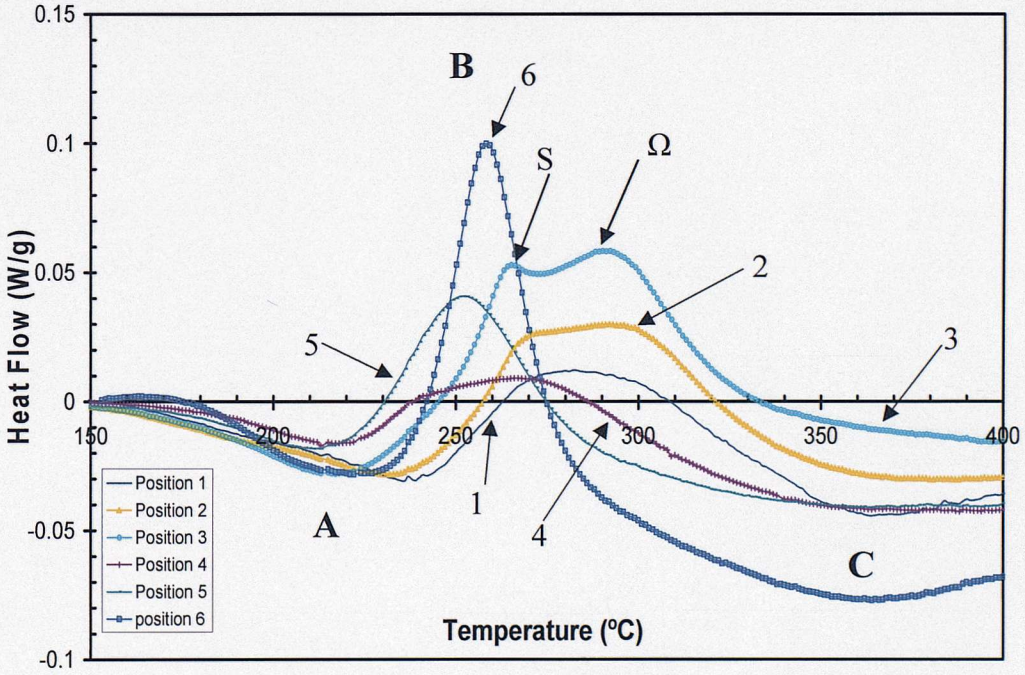

Figure 4.25 DSC thermograms for the various curve locations highlighted in Figure 4.24.

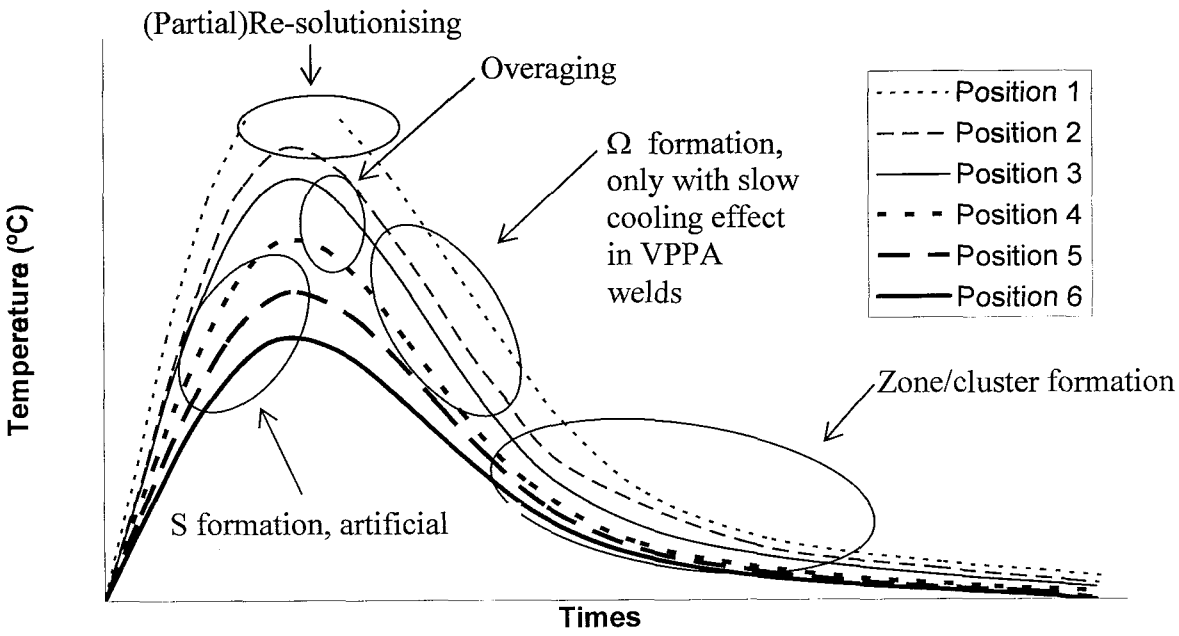

Figure 4.26 Time versus temperature diagram schematically depicting the different transformations that occur in the areas close to the HAZ during welding (position numbers related to Figure 4.4(a), 4.21 and 4.24)

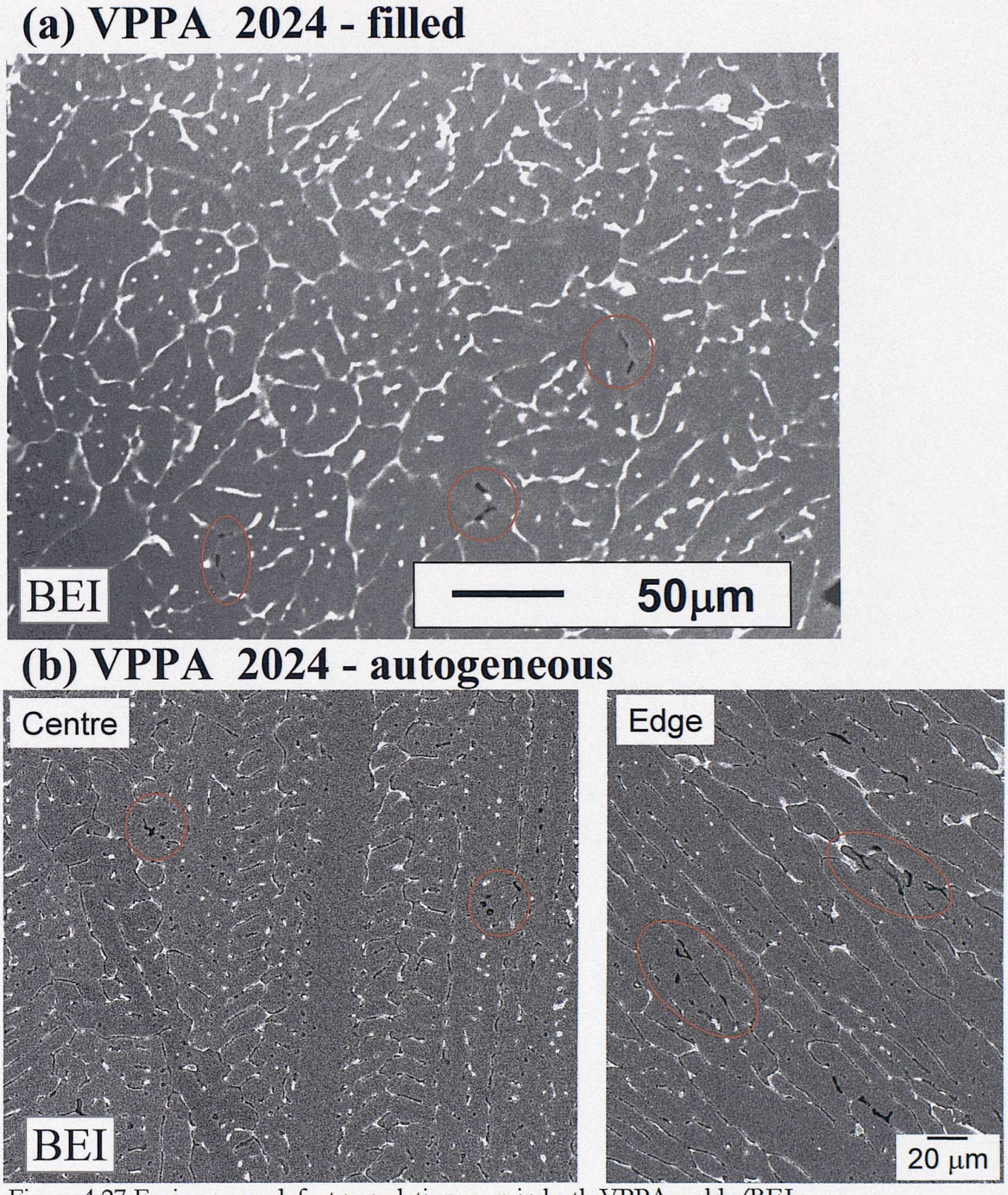

Figure 4.27 Fusion zone defect population seen in both VPPA welds (BEI micrographs):

(a) Filled VPPA weld:
- Fine Interdentritic defects ~ 10-20 μm
- Occasional gas porosity up to 50 μm, ~ 1-2 per/mm2

(b) Autogeneous VPPA weld:
- Primarily small interdendritic defects (few gas bubbles c.f. MIG)
- 5-10 μm defects at centre
- 20-40 μm defects at edge

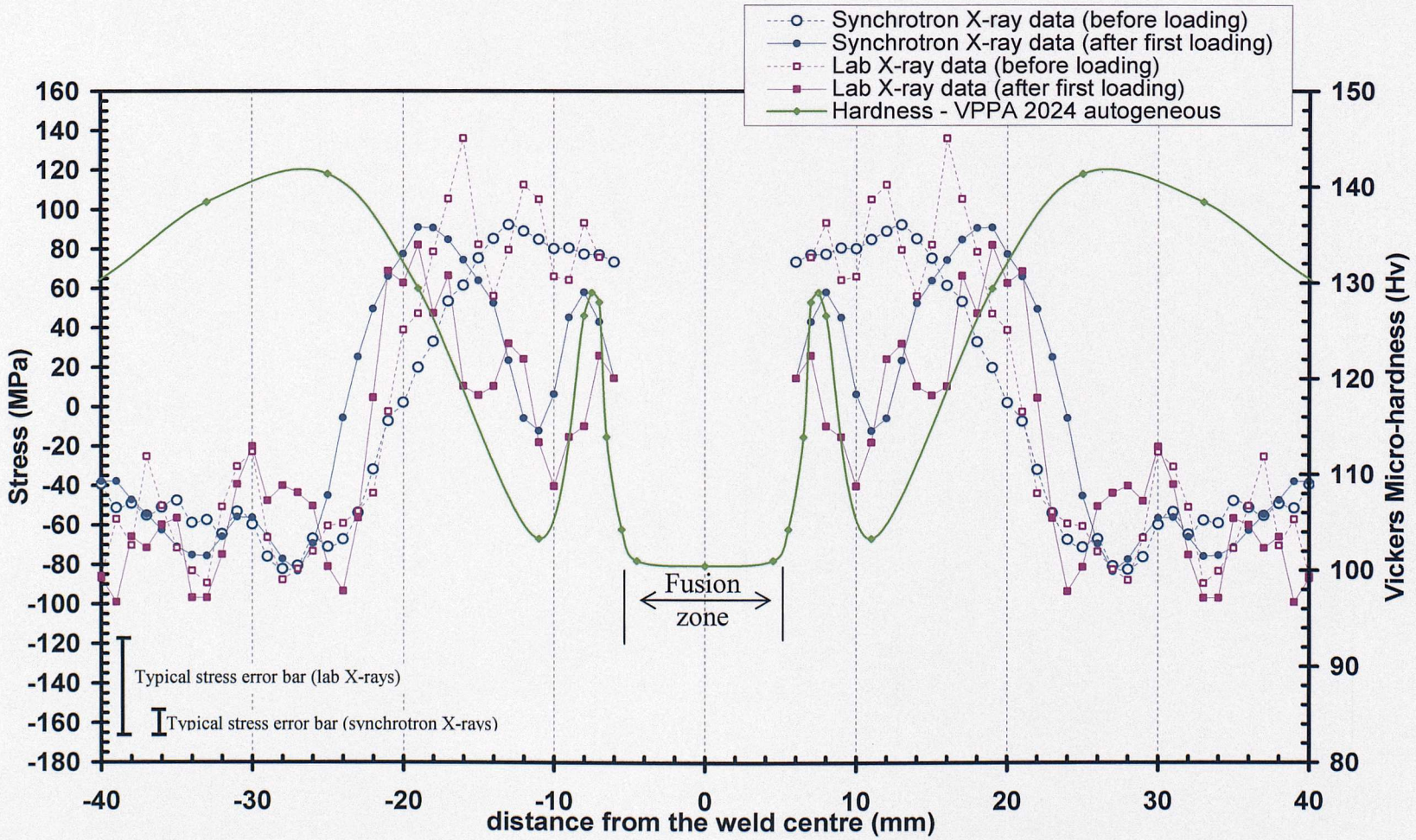

Figure 4.28 Residual stress data with the corresponding hardness trace for the autogeneous VPPA weld (Synchrotron X-ray measurements and lab X-ray measurements).

Chapter 5

Fatigue behaviour of the MIG welds: Results and discussion

5.1 Fatigue life results : S-N curves

As presented in chapter 3, fatigue tests were performed on the MIG weld material by loading parallel to the weld line using three point bend coupons. Overall fatigue performance of the MIG welds is illustrated in Figure 5.1 in terms of stress amplitude-life curves (S-N curves), along with results for the parent plate tested with the same surface preparation and load geometry. A broad scatter band is also shown for a variety of sources on 2024-T351 & T4 sheet and plate also tested at an R-ratio equal to 0.1 (Parry, 2001). In terms of the present results it may be seen that whilst the weld results fall below those of the present parent plate tests (by a factor of ~4 in fatigue life), MIG weld performance is just within the range bounded by the literature data. It may be noted that relative performance of the welds falls off significantly at lower stress levels, with the weld results showing a distinctive linear (in logarithmic scale) performance curve.

5.2 Crack initiation

A high density of crack initiation was identified to occur right across the fusion zone. Secondary cracks were also identified in the heat-affected zone but they did not contribute significantly to failure, growing to no more than 100μm by the end of the fatigue life. In the fusion zone multiple crack initiation was seen early in the fatigue life. Figure 5.2 shows a further optical micrographs of a typical multiple crack distribution in the middle of the MIG fusion zone at $N/N_f = 0.3$. To identify if cracks continue to initiate after the few first cycles, an optical survey of cracks was carried out on replicas at different stages of the fatigue life (see Table 5.1). For a stress level of 270MPa a survey was carried out at $N/N_f = 0.03$ (i.e. after relatively few cycles) and

$N/N_f = 0.2$. As such it was noted that at 20% of life, the number of cracks had only increased by ~14% over the number of cracks initiated at 3% of life. For a higher stress level (330MPa), it was noted that between 20% and 25% of the total life, a less than 2% increase in the number of cracks occurred. The overall crack density was seen to increase by a factor of the order of 1.6 between 270MPa and 330MPa (crack density of the order of 8-9 cracks per mm^2 at 270MPa) at 20% of the total life.

As noted in chapter 4, the general stereology of the surface pore population of the MIG welds has been characterised. It has been seen that two forms of defect predominate in the fusion zone: interdendritic defects of the order of 10 to 50μm, and gas porosity up to hundred's micrometers in diameter. Crack initiation has been seen to occur from defects located at the surface of the material or just beneath it. Figure 5.4 shows a typical SEM micrograph of an interdendritic defect initiating cracks on the top surface of a fatigue specimen. Qualitative observation suggested a strong preference for crack initiation at the interdendritic sites, with relatively few cracks forming from the large bubbles (see figure 5.2). To confirm which defects are the most damaging, a survey of the initiating pore population have been carried out. Figure 5.4 shows a typical crack initiating pore population measured over an area of ~1.5x12mm (i.e. covering a full fusion zone width) in a sample tested at a stress level of 307MPa, super-imposed over the general pore population presented Section 4.1. It may indeed be seen that relatively few large pores initiate cracks. Practical issues in obtaining these results should be noted: inspection of the fatigue sample replicas indicated that obtaining accurate measurements of the whole pore population was going to be difficult in a tested sample. It was however still considered reasonable to spend time picking out the crack initiating pores and measuring them essentially individually. As discussed previously, the background has been characterised from sections within the original fatigue samples, re-polished to a high standard: by counting number densities, the interdendritic and bubble defect populations are found to be reasonably consistent between the background and cracked regions (to within ±10%). Using the available background population information as at least a first order reference, an indication of initiation probabilities as a function of pore size may be defined (see Figure 5.5). On

this graph, initiating pores densities have been binned by size and divided by corresponding overall pore density. It may be seen there is a skew distribution with a maximum of initiation probability at intermediate pore sizes of the order of 50 to 200μm^2. Overall it would appear that interdendritic pores (predominant in the 50-200μm^2 range) are indeed statistically more damaging than the larger gas bubbles.

In terms of the MIG interdendritic defects being more damaging than the large bubbles, it may be considered that initiation is not a simple function of defect size but micromechanical factors such as interdendritic defects tending to be sharper/more crack-like. The sharp 'points' of the small interdendritic pores will also of necessity occur at intermetallic bands, as illustrated in Figure 5.6, which may also be seen as deleterious feature of these defects. Further potential differentiating features of the two defect types may include: (i) different microstructure-scale tessellated stresses (i.e. stresses surrounding individual defects, as opposed to the long wavelength residual stress variations measured in Chapter 4) and (ii) different local surrounding microstructural features, such as varying dendrite arm spacings and/or interdendritic particles distributions. Semi-quantitative assessment shows no obvious evidence of point (ii) above, whilst (i) is unfortunately difficult to assess experimentally.

Recent work on Al-Si casting alloys, by Buffiere *et al.*, has highlighted the significance of grain boundaries in fatigue failure from casting defects (Buffiere *et al.*, 2001). They suggest from fatigue specimen surface observations that crack initiation occurs preferentially by decohesion of Si particles close to the convex parts of pores. By EBSD image analysis, they found that cracks initiate on the sides of pores co-located at grain boundaries that are approximately perpendicular to the applied stress direction. As such they identified initiation to be dependant on a combination of stress concentrating effect of sharp pore "corners", elastic and plastic incompatibility which exists between Si particles and surrounding matrix, and grain boundary induced strain mismatch (elastic and plastic incompatibility) in the material. The present MIG fusion zone microstructures may of course be seen as similar, with defect corners being co-located with coarse Cu & Mg containing phases as opposed to Si particles. In this context a statistical survey has been carried out on pores, cracks and grain boundary

relationships in the present welds. In the first instance observations have been carried out on cracked defect extremities in relation to the grain boundaries via local EBSD assessment. It was seen that cracked interdendritic defects occurred both on and off grain boundaries in approximately 1:1 proportion† based on a random sample of some 20 defects, see Figure 5.7 and Figure 5.8. Figure 5.7 presents an SEI macrograph and the associated EBSD orientation map where a pore and associated cracks may be seen in the interdendritic structure. The shape of the pores is clearly strongly defined by the dendrites (particularly the re-entrant points). Two initiated cracks from grain boundaries may be clearly identified in Figure 5.7. In this picture, crack growth is clearly not strongly influenced by grain boundaries: viz. cracks *start* from grain boundaries, but rapidly become transgranular. Figure 5.9 highlights crack initiation both on and off grain boundaries from the same defect. To discern any strong statistical relationship between crack initiation and grain boundary location at defects a semi-quantitative assessment has been carried out to estimate the preponderance of pore location at grain boundaries. In the background fusion zone microstructure, a random population of non-cracked interdendritic pores (~20) was examined, with the presence of grain boundaries at extremities perpendicular to the load axis being identified in ~50% of cases, i.e. showing no significant variation from the crack initiating defects. Looking at the larger gas pores, these were seen as statistically less favourable to crack initiation but are not "free" of grain boundaries, typically being intercepted by several grains each (see Figure 5.10). As such it may be seen that whilst crack initiating pores may still have some minor damaging co-location with grain boundaries, grain boundaries are not a primary factor in crack initiation from a given pore. It is also interesting to note that on observation of many cracked defects in the MIG fusion zone, no particular evidence of cracks actually initiating from particles *ahead* of pore apices was seen (as proposed by Buffiere *et al.*), although such a process cannot be entirely ruled out if coalescence of particle cracks with the associated defect is rapid.

† Here it must be recognised that orientation accuracy of EBSD measurements is of the order of 2-3°, so small misorientations that may arise between individual dendrite arms are effectively ignored

In terms of the simple mechanics of defects of different shape, the stress concentration effects of elliptical holes may be investigated by well known mechanics calculations. A sheet containing an elliptical hole, of major axis length, 2c' and minor axis length, 2h (see Figure 5.11) subjected to a uniform uniaxial tensile stress, σ_0^*, remote from the hole, in a direction perpendicular to the major axis of the ellipse. Stress at the tip, σ_A of the major axis is defined in first approximation as (Anderson, 1995):

$$\sigma_A = \sigma_0^* \left(1 + \frac{2c'}{h} \right)$$

When a large gas bubble is considered, a circular hole may be assumed with $h/c' = 1$ and then the stress at the tip is equal to $\sigma_A = 3\sigma_0^*$. When an interdendritic defect is considered, an elliptical hole may be assumed with h/c' between ½ and ¼ (as suggested by figure 5.5), so the nominal stress at the tip is equal to $\sigma_A = 5\sigma_0^*$ and $\sigma_A = 7\sigma_0^*$ respectively. It is clear that the stress at the ellipse is much higher than the circle which may then of course be more susceptible to initiate cracks as suggested by the experimental observations. It is also interesting to consider nominal stress intensity factors associated with the earliest stages of crack growth from the different defect types. Based on available solutions in the literature (Rooke & Cartwright, 1976) it is possible to calculate stress intensities for 1, 5 and 10μm cracks appearing symmetrically from : (a) a small elliptical defect of 20x5μm, and (b) a circular pore 200μm (the elliptical defect then being approximately representative of what was the most favourable crack initiation site). Table 5.2 shows that even for the very smallest crack length the greater size of the circular defect (i.e. gas pore) dominates stress intensity levels. Whilst such calculations are clearly simple (considering only elastic behaviour in two dimensions), there is an implication that it must be processes in the very earliest stages of crack formation that determine the damaging effect of the smaller interdendritic defects.

5.3 Crack propagation

In terms of crack propagation, complex and multiple crack failure has been seen in the fusion zone region, see Figure 5.12. Crack-crack interactions were clearly prevalent from the earliest stages of crack evolution (crack lengths of the order of hundreds micrometers) with crack-crack separation distances less than individual crack lengths and coalescence being seen directly: cracks circled in red in Figure 5.12(a) particularly identify a group that coalesce later in the life of the sample. No dominant crack was in fact identifiable in the fusion zone until multiple microcrack coalescence occurred to form a crack crossing the whole fusion zone (length of the order of 8 to 10mm) in the final 40-30% of the fatigue life. Figure 5.12 illustrates multiple crack behaviour occurring within the fusion zone at different stages of crack evolution: (a) $N/N_f = 0.3$, (b) $N/N_f = 0.6$, (c) $N/N_f = 0.99$ with (a) and (b) both showing distinct multiple crack character.

Figures 5.13 (a) and (b) show growth rates for multiple small cracks (<1mm) in the parent plate 2024 tests and the MIG fusion zone respectively. Both graphs exhibit scatter as acceleration and deceleration in growth rates occur, i.e. classical short crack behaviour. For the MIG weld, extended scatter may be particularly seen which may in the first instance be identified with crack-crack interactions. Such behaviour has been pointed out by Kamaya and Totsuka (Kamaya & Totsuka, 2002), and Soboyejo and Knott (Soboyejo & Knott, 1991) noting that high local crack growth rates particularly occur during crack coalescence. For the sake of clarity and comparison with the results obtained for the VPPA welds presented in the next chapter, and the modelling presented in the next section, schematic bands may be defined for both crack growth data sets, as shown together in Figure 5.14. The particular extension of the upper bound growth rates for the MIG weld fusion zone may then be identified with coalescence events.

To investigate further crack-crack interactions, individual cracks from the overall crack population may be studied. Figure 5.15 shows a graph representing crack lengths as a function of the percentage of fatigue life for two cracks highlighted in Figure 5.16.

Figure 5.16 presents a sequence of images from $N/N_f = 0.06$ to $N/N_f = 0.34$ (i.e. optical micrographs of replicas at different cycle counts). Crack 1 and crack 2 are labelled on Figure 5.16 ($N/N_f = 0.06$): for each crack, two tips are defined as "A" and "B", as highlighted for $N/N_f = 0.13$. The crack evolution sequence in Figure 5.16 may then be described as follows: considering crack 2, crack 2/tip B grows slowly initially (between $N/N_f = 0.06$ and $N/N_f = 0.09$ in Figure 5.15): however as crack 1 begins to approach (off axis) crack 2 (i.e. when the two crack tips get to within 40μm), rapid acceleration is seen in crack 2/tip B, taking the 2 tips into an "overlap" configuration. Growth rates of crack1/tip A and crack2/tip B then stay low (see Figure 5.15), consistent with the crack tips effectively shielding each other. At the other end of crack 2 (crack2/tip A), growth is initially gradual, until a secondary crack that is essentially co-linear (highlighted by a yellow dash circle in Figure 5.16 $N/N_f = 0.29$) falls within a tip separation of 25μm, and a rapid acceleration is seen until coalescence occurs (see Figures 5.15 and 5.16).

From the above assessment of crack initiation to ~40% of the total fatigue life, it would appear that crack-crack interaction behaviour (shielding and coalescence events) are occurring, although it must be recognised that some crack acceleration and arrest events are likely to be attributable to grain boundary influence (viz. the growth rate scatter in parent plate). Multiple crack interaction has been treated in more detail in the next section.

In terms of residual stress influence on crack propagation, it has been noted in Chapter 2 that several researchers have suggested that compressive residual stress effects are generally beneficial to the fatigue life, whilst tensile stress on the contrary reduce fatigue performance. Considering the principle of elastic stress superposition, residual stress may then influences the effective fatigue stress ratio. Lee & Song particularly show that growth rates of short cracks in 2024 aluminium alloys are significantly influenced by stress ratio; if the stress ratio increases, the crack propagation rate for a given stress intensity factor increases (Lee & Song, 2000). In the present work on the MIG fusion zone, much of the region of interest appears to be relaxed to a low residual stress

condition after the first loading (see chapter 4). As noted earlier however, a difference in longitudinal residual stress exists between the edge and the centre of the fusion zone after loading, approximately equal to +50MPa; as such a tensile residual stress is still present at the fusion zone edge and may be expected to influence crack propagation. For the present tests, superimposed stress of 50MPa may be expected to raise R-ratios to values of the order of 0.2-0.3 (depending on applied stress levels), which may be considered appreciable (ASM International, 1998; Lee & Song, 2000). Whilst crack lengths at any given number of cycles in the present MIG fusion zones are clearly not a simple function of propagation rates (being influenced by crack coalescence and shielding processes), it may be noted that crack lengths in the 2-3mm closest to the fusion zone/HAZ interface were generally larger than those in the fusion zone centre (~ by a factor 2), see Figure 5.17, i.e. over a distance somewhat larger than may be attributable to the grain size refinement and columnar structure seen at the fusion edge.

5.4 Micromechanical modelling

Any complete numerical description of the present weld failures clearly represents an ambitious synthesis of several processes or phenomena, particularly: (i) multiple crack initiation as a function of defect size/shape, (ii) classical short crack growth phenomena, (iii) crack coalescence, (iv) crack shielding and (v) residual stress superposition. Theses issues are further complicated by spatial variations in a number of undetermined 'input' features (such as pore distribution, residual stress and grain sizes). As such, a significant level of simplification is clearly valuable in initial model formulation. In terms of the literature relevant to this work, Chapter 2 has clearly addressed a number of the relevant reports, although additional consideration of crack-crack interaction processes is clearly of value to the present MIG welds. Various models have been noted in the literature, particularly Joyce (2000), Kamaya and Totsuka (2002), Soboyejo *et al.* (1989), Chen and co-workers (1995) and Hünecke and co-workers (2001).

Joyce (Joyce, 2000) has for example investigated, via finite element analysis, crack deflection, coalescence and bifurcation during crack growth in Al-based bearing alloys. Two interacting cracks of the order of 200 to 2000μm have been modelled in a simple

two dimensional manner for different configurations, such as co-linear cracks, parallel cracks or oblique arrangements where crack midpoints are displaced along an axis inclined at an arbitrary angle to the applied stress (see Figure 5.18).

In this work, one crack was held at a fixed length (1000μm) and referred to as a "free crack", the other crack was then identified as the "growing crack" (could be grown incrementally by 200μm). The J-integral was used to assess and monitor both crack tip driving force and the directional propensity of crack growth. Considering co-linear cracks, Joyce has reported that initially no crack interaction occurs when the crack tip plastic zones are small and a large elastic region exists between them (see Figure 5.19(a)). As the crack tip spacing is reduced, the plastic zones may overlap, forming an annular plastic region between the converging tips (see Figure 5.19(b)). If the growing crack length continues to increase, the region between the two cracks becomes entirely plastic and coalescence occurs. As the length of the growing crack is increased, it has been noticed that when plastic zones of both cracks appear to merge, crack tip driving force increases significantly beyond the predicted values for a corresponding single isolated crack. This considerable increase in crack tip driving force has then been linked to experimentally observed crack growth rate acceleration immediately prior to coalescence. For parallel cracks models, it has been reported that a long crack is capable of shielding a smaller neighbouring crack considering a crack spacing distance of the order of the length of the smaller crack. In the oblique crack case, the crack spacing distance was fixed at 500μm and the initial projected crack tip spacing was of the order of 1500μm. The length of the "growing crack" was increased from 1000μm to 5000μm. It has been shown that crack tip driving force may increase until an overlap of 500μm is established between cracks. If growth continues (i.e. generating further overlap), the two cracks begin to shield each other, and their plastic zones overlap.

Kamaya and Totsuka (Kamaya & Totsuka, 2002) have developed a crack growth simulation to analytically evaluate the effect of multiple cracks on growth behaviour considering their relative positions and relative lengths in relation to stress corrosion cracking (SCC) experiments performed in a Nickel based alloy in high temperature environments. Modelling in two dimensions, pairs of cracks of ~100μm length were separated by set distances in the stress axis direction, and perpendicular stress direction.

Changing these distances and allowing cracks to change their growth directions according to a maximum tensile stress criteria, different crack configurations were studied to highlight shielding and coalescence events. In order to take into account the effect of crack interaction, the stress intensity factor was calculated using the body force method and the crack growth as a function of the stress intensity factor. Kamaya and Totsuka suggested that if the crack spacing of two equal cracks (~100μm) is short enough (of the order of the crack length), the growth rates of the two cracks would be almost similar than the growth rate if the cracks were combined. When two cracks are co-linear, even if they are of different length, they might be seen accelerated by the interaction, however when the crack spacing becomes larger, the interaction tends to become limited, depending on the length of the cracks. Kamaya and Totsuka have then concluded that in addition to the relative position of cracks, their relative lengths are also very important in the interaction between multiple cracks on crack growth behaviour. In most cases, approaching cracks tend to be accelerated due to interactions.

Soboyejo et al. (Soboyejo *et al.*, 1989) have performed experimental and numerical work on interaction and coalescence of pairs of co-planar semi-elliptical cracks. A general finite element model was used to calculate elastic stress intensity factors at various points along the crack front. Local advance was predicted as a function of stress intensity factor using a Paris equation. They found that co-planar semi-elliptical cracks grow almost independently before "contact" (i.e. until their plastic zones come into contact with each other). Fatigue crack interaction therefore appears to be limited to a very small portion of crack growth prior to coalescence. When "contact" occurs, the stress intensity factor increases to a maximum value during coalescence which results in high crack growth acceleration. During coalescence, a rapid transition to a single semi-elliptical crack occurs. Finite element growth predictions were reported to be in good agreement with the experimental fatigue crack growth data.

Chen and co-workers (Chen *et al.*, 1995b; Chen *et al.*, 1995a) have studied the effect of microcracks on rapid catastrophic failure in a 2124 aluminium alloy reinforced with silicon carbide wiskers. Experimentally, they observed microcrack initiation and

propagation to total failure. They characterised distribution and orientation of microcracks with particular interest in coalescence events leading to failure. They showed that growth rates typically increase during coalescence. Chen *et al.* further developed a micro-mechanical simulation to predict the arrest and coalescence behaviour of a field of microcracks using statistical approaches (Monte-Carlo-type) based on experimental probabilistic results (Chen *et al*, 1995a). As such probabilities, such as probability of crack growth, crack arrest or crack coalescence, have been defined. The model may be summarised as follow: for a given cycle, crack initiation occurs to a specific crack length of 2μm. At this stage, the crack population may be divided in different parts: initiated cracks, arrested cracks, non-arrested cracks, and "escaped" cracks. "Escaped" cracks are defined as arrested cracks with the potential to grow again. Initiated, non-arrested and "escaped" cracks encounter different sets of condition (arrest, individual growth and coalescence) which needed to be satisfied in order to grow. The probability of individual growth is defined as a function such as Paris equation type. If the growth condition is satisfied, the crack grows of a pre-determined length (~2μm). The probability of arrest is a function based on microcrack lengths and hence depends on the corresponding stress intensity factor. The probability of coalescence is defined as stereological geometric probability as a function of crack length, cumulative cracks length in the studied region and area of the region of interest. It may be noted that if two cracks coalesce, the resulting crack is taken to be a geometrically average length instead of the sum of the two cracks since linkage of the two cracks is possible in all direction (i.e. coalescence does not necessary occur from crack tip to crack tip). Considering crack growth, crack arrest and crack coalescence, the Monte-Carlo simulation developed by Chen and co-workers gave a reasonably good prediction of the microcrack length distributions observed experimentally in a 2124 Al-SiC_w composite.

Hünecke and co-workers (Hünecke *et al.*, 2001; Hünecke & Schöne, 2002c; Hünecke & Schöne, 2002a; Hünecke & Schöne, 2002b) have developed a simulation of multiple short crack behaviour under constant amplitude fatigue loading. Their model predicts fatigue life via a simple geometrical approximation of coalescence and shielding processes. Experimental investigations on low carbon steel were performed to identify

large numbers of short cracks, which coalesce to form a main long crack. In this context, the microstructure of the material was modelled by generating ferrite and pearlite grains as a representative specimen area. From experimental observations, crack initiation was restricted to the ferrite grains only. The number of cycles to initiate cracks was predicted with regards to grain size, grain orientation, applied load and material constants. The simulated crack initiation rates were calibrated to the experimental data. Crack growth rates were calculated using the continuous dislocation methods with regards to grain size and distance between crack tip and grain boundaries. The interaction between neighbouring cracks was considered by simple geometrical approximations discussed further later in this section. The short crack simulation model was reported to be reasonably well supported by experimental investigations (at least in terms of fatigue life data).

As presented above, several researchers have performed finite element analysis, analytical modelling, and experimental observations to understand and predict the fatigue behaviour in multiple crack fields. Criteria for plastic zone size, crack positioning, and crack driving forces have been used in the different models and reported to be important in considering crack-crack interaction.

As noted earlier, the present MIG welds represent a complex modelling problem requiring a variety of simplifications to be tractable within the scope of the present thesis. In the first instance, the following modelling approach identified:

1- Initial pore distributions may be identified either directly from microstructural imaging or from computer generated simulations of predefined pore population types (varying distribution in size, shape and clustering levels), as shown in Figure 5.20. Pores may be considered as ellipses of different angles and sizes (major and minor axis). Ellipse extremities are identified as key crack initiation sites. Whilst software tools are available to provide wide ranging control of "artificial" pore distributions (Yang *et al.*, 2001) (in terms of pore size, shape distribution and spatial arrangements), the modelling work presented in this chapter is all derived from "real" microstructure images, with

ellipses of equivalent area and aspect ratio being used to represent each individual defect of representative weld microstructure images.

2- Cracks are initiated from the pore distribution using a Monte-Carlo method, based on the probability of initiation from each individual pore as a function of its size and shape, as derived from the experimental observations defined in Section 5.1 (see Figure 5.21). This approach may be considered similar to some extent to the approach developed by Chen *et al.* (Chen *et al*, 1995a). In keeping with experimental observations in Section 5.1.2, it has been assumed that most initiation occurs early in the fatigue life (influences of progressive initiation are ignored). When a pore is considered as a crack initiator, one crack comes from each pore extremity. A total crack length may then be identified with the distance between the crack tips considered in two dimensional Cartesian coordinates.

3- Initiated cracks are allowed to grow by a defined number of cycles according to some short crack growth rate model as a function of the current stress intensity level. Surface crack stress intensity factor levels may be calculated using the Scott and Thorpe relationships (Scott & Thorpe, 1981) (as identified in the experimental section to describe the crack propagation) and initial pore shape effects are ignored.

4- Crack-crack interactions are considered with different conditions to define the incidence of crack shielding or crack coalescence. As suggested in the description of the different models in the literature, crack-crack interaction depends on relative crack positions and lengths (Soboyejo *et al*, 1989; Chen *et al*, 1995b; Joyce, 2000; Hünecke *et al*, 2001; Kamaya & Totsuka, 2002). To illustrate the crack-crack interaction used in the present modelling a schematic diagram is presented Figure 5.22: as suggested by Hünecke and Schöne (Hünecke & Schöne, 2002a), it has been assumed in this study that shielding leads to simple crack tip arrest: when a crack is arrested, it does not have the possibility to grow further again (c.f. the model developed by Chen *et al.* where

a crack can grow again after having been arrested (Chen *et al*, 1995a)). Shielding interactions are treated as a severe "brick-wall" effect: a notional "shielding area" associated with a crack is considered as a circle of diameter equal to the crack length. The red circles in Figure 5.22 illustrate different shielding areas. For a given crack, if the shielding area intercepts one or both crack tips of another crack, then the corresponding tips are considered to be shielded from any further growth. In terms of coalescence, a "coalescence area" is defined as a circle of radius equal to the nominal plastic zone size of the associated crack based on the Irwin approximation of the plane stress plastic zone size (Hünecke & Schöne, 2002c). In Figure 5.22, the green circles at the crack tips represent different coalescence areas. For a given crack, if the coalescence area intercepts a coalescence area of another crack, the cracks are considered to spontaneously coalesce (i.e. zero cycles to cross the separation distance associates with the plastic zone dimensions). A new crack is then considered with a length given by the distance between the two other crack tips.

5- Step 4 & 5 are repeated until one of the cracks (or coalesced group of cracks) achieves a pre-determined length of 1 mm corresponding to a notional short crack regime limit as identified in Chapter 1. In the actual MIG weld tests, the time to form 1mm cracks (or 1mm coalesced groups of cracks) was seen to correspond to approximately 50% of total fatigue life.

As such it may be seen that a combination of empirical and micromechanical/physical analysis methods is to be considered in the present simulations. In this context two versions on the modelling approach may be identified in the choice of short crack growth modelling method (step 3 in the previous description). Two methods have been specifically adopted here: (a) the essentially empirical approach of Hobson, and (b) the more micromechanical methods of Edwards and Zhang (Edwards & Zhang, 1994b).

5.4.1 Models based on Hobson-type short crack simulation

As presented section 2.1.3.7, Hobson has developed a simple model in which crack growth rate is assumed to be proportional to the distance between crack tip and an approaching grain boundary (Hobson, 1982); with the growth rate boundary conditions being defined by experimental observation, crack growth is assumed to vary in a linear manner between boundaries. Based on EBSD observations and grain size measurements reported in Section 4.1, nominal grain size in the MIG fusion zone region has been defined as 50μm. For the da/dN bounds, it is clearly ideal to have growth data for MIG fusion zone material in a residual stress free condition, and a number of individual cracks that can be monitored without crack-crack interactions. In terms of the latter condition, it may be noted that the MIG fusion zone material is problematic in its high intrinsic susceptibility to multiple crack initiation. As such, it may be noted that a number of "sub-sized" samples of fusion zone material from the filled VPPA weld have been tested (see Chapter 6). Given the small size of these samples (3x1.5mm cross section) and the fact that only a few cracks form in each test, it may be assumed the growth rate data are reasonably representative of residual stress free, individual crack growth processes. This data was therefore been used as the best available approximation to intrinsic short crack growth behaviour in the MIG fusion zone, bearing in mind: (a) similar filler wire was used, specifically 2319, (b) an equiaxed grain structure is present in each, (c) hardness levels are similar, and (d) similar DSC traces are evident. It may be pointed out however that dendrite arm spacing are different, but grain sizes are of the same order (see Chapter 4). Figure 5.23 shows typical da/dN behaviour obtained from the sub-size fusion zone tests for the simulation of short crack growth. The upper band is defined by the points A and B, and the lower band by the points B, C and D. The growth rate bounds of the parent plate 2024-T351 are also drawn in Figure 5.23 for reference. After the short crack regime, linear (Paris law) growth is assumed to occur. It may be noted that crack growth rate predictions are dependent on the applied stress, so for each stress level considered, a da/dN simulation is obtained as different K levels are reached at successive grain boundaries. Figure 5.24 shows short crack growth rates for two applied stress ranges, corresponding to 200 and 270MPa. It may be noted that an

individual growth curve based on the schematic crack/grain boundary structure geometry is generated for each crack (i.e. each crack starts from the centre of a regular hexagonal boundary structure). As such there is no single or "global" grain structure defined for the multiple crack simulations: rather, the model incorporates a representative periodicity of crack-grain boundary interactions for the cracks that are present. Given the rapid accelerations and decelerations associated with early short crack fatigue behaviour, it should be noted that a convergence study was carried out to identify the optimum number of cycles used in each model step (small numbers increase model time, whilst large numbers may effectively obliterate crack acceleration/deceleration events). A cycle increment of 1000 was found to reasonably represent short crack growth in the present work.

Figure 5.25 presents an example of a simulated weld area with the associated crack initiation and growth for a stress level of 270MPa after 79000 cycles. Crack interactions may be seen: i.e. crack shielding and crack coalescence. As the crack initiation simulation is based on probabilities, modelling results shown here are all based on 10 repeat calculations for identical load conditions. Average and error range (standard deviation in the mean) values of fatigue life predictions are then calculated, as summarised in Table A.1 and Table A.2 in Appendix 2 for different considered simulations: for the sake of clarity, average fatigue lives without error bars are represented on the following SN-curve predictions, although a general indication of scatter is highlighted in each diagram. Figure 5.26 shows predictions of fatigue life based on two versions of the current model for a final total crack length of 1mm based on:

a. A representative 'real' pore population of MIG fusion zone, i.e. derived from an optical micrograph (~1.2mm x 1.4mm area as Figure 5.25), from the fusion zone edge.

b. a notional single crack growing from a pre-defined defect of 20μm length.

It can be noted that all SN curves presented in this section include the real fatigue life results from the MIG weld (both total life and life to ~1mm crack length), results from the parent plate material and the broad band for 2024 plate and sheet from the literature. In Figure 5.26, it may be seen that the MIG weld simulation actually provides an over estimate of life in the real MIG welds, but does follow the slope of the experimental SN curve quite well. The model results for the single crack situation clearly give an indication of the net accelerative effect the weld initiation sites. It is interesting to note that the single crack model gives a reasonable approximation of the parent alloy behaviour at high stress levels, which may be seen as consistent with the typical initiating defect size in parent plate (i.e. intermetallics of 10-20μm) and the similarity of residual stress free growth rate bands in parent and fusion zone material (Figure 5.23). The divergence of the parent plate SN data at low stress may in the first instance be attributed to increasing initiation life in the parent material at low stress (Edwards & Zhang, 1994a; Suresh, 1998) which is not addressed in the present modelling (cracks initiate immediately on first loading). The steep SN curve slope for the weld tests would therefore appear consistent with the rich population of initiating defects in the weld fusion zone and a negligible initiation life even, at low stress levels. The error range in predicted weld lives may be seen to be small, with different patterns of crack initiation associated with each model run having a limited effect on overall multiple crack behaviour.

It is of course valuable to consider a parametric study of the present model framework to identify first order influences and possibly gain mechanistic insight. For discussion purposes the results presented (Figure 5.26) above for multiple crack/weld behaviour in an area of 1.2x1.4mm weld will be considered as original/reference model results.

In the first instance, the microstructure area simulated may be varied. Firstly a region of 1.2x1.4mm containing representative real pore population as presented previously was considered as the original/reference area. Considering the direction perpendicular to the applied stress (i.e. direction across the fusion zone) the original/reference simulated area has been extended by different factors: x2, x3, x4, x6 and x12: as such the microstructure area labelled areax12 represents the full MIG fusion zone. As an

alternative to specifically extending the area sampled across the weld, an area corresponding to 2.4x2.8mm (area-FZ-x2*2) has been considered, i.e. extending both perpendicular and parallel to the load direction when compared to the original 1.2x1.4mm model. Sizes, shapes and locations of pores have been defined from the real pore population of the MIG fusion zone for the x2, x3, x4, x2*2, and x6 areas (x6 area representing half of a typical fusion zone image). The x12 area was obtained by symmetrical transformation of the x4 area, so no longer strictly represents a real microstructure. Figure 5.27 presents the fatigue life predictions obtained for the original/reference simulated area (i.e. 1.2x1.4mm) and those for the various larger areas (x2, x3, x4, x6, x12 and 2x2). Appreciable changes in fatigue life predictions may be seen (maximum range varying from a factor of 2.5 at high stresses to 1.5 at low stresses. From the original/reference microstructure area (1.2x1.4mm) to the double microstructure area size (i.e. x2, 2.4x1.4mm), an accelerative effect may be seen. For the x3 and x4 areas (again extending the microstructural sample area across the weld/perpendicular to the load axis), fatigue life may be seen to decrease further. Life results for the 2x2 area are seen to increase in relation to the x4 area result (i.e. equivalent microstructural sample sizes, but extending the sample parallel to the load direction as opposed to the perpendicular direction). Life results for the x4, x6 and x12 areas are seen to be essentially indistinguishable, whilst predictions for the x3, x4, 2x2, x6 and x12 areas are in fact all within a factor of 1.6 of each other.

In considering area sampling effects on model results, a number of factors are identified:

(i) Achieving a statistically representative number of defects for initiation to occur from.

(ii) Achieving a statistically representative number/variety of crack-crack interactions.

(iii) Ensuring cracks achieving the final length condition (i.e. 1mm) are contained within the microstructural simulation area (i.e. do not grow out into 'defect-free' material).

Examination of the x1, x2, x3 and 2x2 simulations shows that final 1mm cracks in these cases do in fact extend significantly beyond the microstructural simulation area, whilst final cracks in the majority of the x4, x6 and x12 models (remembering that 10

repeat runs are performed for each case) are contained within the simulation area. As such, some unrepresentative contributions of factor (iii) above may be expected in the x1, x2, x3 and 2x2 area results. Apparent extension of fatigue life for these smaller sample areas may then be identified with insufficient crack-crack interactions to the model results. In terms of achieving a statistically representative sample of potential crack-crack interactions, it may be noted that each model run for each sample area generates a different set of crack-crack geometries. The limited scatter between model runs then suggests that achieving different crack 'patterns' is not a major influence on the failure condition considered here (i.e. a total crack length of 1mm being achieved). In terms of having achieved a statistically representative number of defects for initiation to occur, behaviour of the experimental coupons is of interest. Experimental tests were performed in a three point bend configuration where the peak stress region is of course a line (as opposed to an area) across the weld width. In practice, cracks contributing to final failure in these coupons were seen to lie within an approximately ±1mm band about the centre roller position, i.e. similar to the spread of the present model areas in the loading direction. It may be seen from Figure 5.1 that the scatter in fatigue behaviour of the different MIG coupons tests is in some senses remarkably narrow given the clear dependence of failure on local defect populations along the weld line. Given the close consistency in the present x4, x6 and x12 area modelling results, and the limited difference in modelling the x3 and 2x2 areas, it may be presumed that the x6 area represents a reasonable microstructural sample size for the present modelling purposes, although it is recognised that further re-sampling and simulation of the weld microstructures may be valuable to fully quantify longer range/wavelength weld variability effects.

Having identified a simplistic representation of crack interactions (i.e. coalescence and shielding) in this modelling framework, it is valuable to consider the impact of varying the length scales attributed to these processes to gain some impression of the errors the simplifications may involve. In Figure 5.28 model results are shown for the x6 area sample, varying the crack shielding zone diameter for individual cracks between 0.25, 0.5, 1, 1.5 and 2 times the associated total crack length, where 1 times the associated crack length is the original/reference model condition. It may be seen that the wide

range in shielding area size shown Figure 5.28 (i.e. covering a factor of 8) actually has a limited impact on predicted fatigue lives (within a factor of 2), with only the too largest shielding area dimensions (1.5 and 2 times crack length) appreciably extending fatigue performance. Figure 5.29 alternatively shows a more pronounced effect of model parameters on predictions, with increasing crack coalescence area size between 0.25 and 2 times the nominal plastic zone size giving a factor of 8 reduction in fatigue lives at high stresses, and a factor of 2 reduction at low stresses. The effect may be seen to be particularly strong for increasing the coalescence area size from 1 to 2 times the nominal plastic zone size.

The relative impact of crack shielding and coalescence parameters on the original model formulation (i.e. shielding and coalescence area diameters equal the crack length and plastic zone size respectively) is further highlighted in Figure 5.30, where model predictions with no shielding area, or no coalescence area, are shown. It may be seen that results for models with no shielding area are not significantly different to those for the original model formulation, whilst removing the coalescence effect increases predicted fatigue lives by a factor of approximately 2. The results for the model with no crack coalescence bears further consideration, particularly in relation to the single crack model. It may be noted that the fact a multiple crack model having no coalescence effect, but allowing crack shielding, shows shorter fatigue lives than a single crack model is as little surprising on first inspection (i.e. as the only multiple crack consideration is a shielding effect). What must be noted is that the original defect sizes in the weld simulation are larger than the 20μm size used in the single crack model. The influence of increasing initial defect size in the single crack case is shown in Figure 5.31, where it may be seen that initial defect sizes of the order of the critical defects in the weld microstructure have a clear effect on life, and may in fact account for some 30-40% of the predicted decrease in fatigue life for the original x6 area weld predictions in relation to the single crack/20μm defect predictions. It may be emphasised that a 100μm defect represents a distinct upper bound dimension of interdendritic defects present in the welds, highlighting the fact that single critical defect growth cannot explain the present weld behaviour (i.e. a crack interaction model is required to predict weld performance, as demonstrated by Fig 5.30 also).

It is clear that clarification of effective errors in defining the coalescence condition is most significant to the present simulations. Support within the literature for the original crack coalescence condition assumptions may be particularly seen in the FE predictions and the experimental results of Joyce (Joyce, 2000) or Soboyejo *et al.* (Soboyejo *et al*, 1989) presented previously. The crack growth observations associated with Figure 5.15 and 5.16 may also be interpreted in terms of nominal plastic zone sizes. The early acceleration identified in growth for crack 2 was caused by interactions between crack2/tipB and crack1/tipA. The nominal plastic zone size of crack 2 may be estimated of the order of 11μm for a crack length of 60μm whilst crack 1 has a nominal plastic zone of 34μm for a crack length of 195μm. The tip separation distance was approximately 40μm. The coalescence event associated with crack2/tipA was associated with a tip separation distance of 25μm. Crack 2 had a crack length of 154μm and a nominal plastic zone of 27μm whilst the secondary crack length was 21μm with a nominal plastic zone of 3.7μm. For these particular crack-crack events, the point were growth rate acceleration was seen in each case is roughly consistent with the present modelling approximation, although it may be seen that only one of the interactions actually gave coalescence (but the crack shielding that appeared to occur was within the proposed shielding area of the model). As such further optimisation of the crack-crack assumption may be suggested for future investigation.

Whilst the present modelling may be improved by including, for example, angle and stress influences in the crack initiation probability and further verification of variabilities in pore distribution , it may be concluded that the simulation of the MIG weld fusion zone considering the probability of initiation as a function of pore size and shape, the Hobson approach for crack growth rate depending of the applied stress, the crack-crack interaction having the original shielding area and coalescence area definitions, gives a reasonably good first approximation of weld fatigue life to 1mm crack length. Keeping in mind these previous results, it is interesting to incorporate into this model a more microstructural sensitive approach. In this context the next section considers the small fatigue crack modelling approach of Edwards and Zhang (Edwards & Zhang, 1994b).

5.4.2 Microstructural crack growth rate approach:

Whilst various researchers, as such Navarro, de los Rios and Tanaka have developed models of short crack growth by calculating crack tip opening displacements (CTOD) and effects of grain boundaries, Zhang & Edwards have experimentally found for 7000 series aluminium alloys that plastic zone size ahead the crack tip is a key important factor that may be used to characterise small crack growth rates. They note that the relatively large plastic deformation zone associated with small fatigue cracks may explain their fast growth rates compared to long cracks. As such the intrinsic decelerations and accelerations of small cracks are considered in terms of the effect of grain boundaries on plastic deformation ahead the crack tip.

In the case of a small crack, the crack and its plastic zone may be initially considered to be contained within a single grain. Figure 5.32 presents a schematic illustration of a crack within a grain structure as considered in the present model. $2c$ is the surface crack length, D is the grain diameter, so $iD/2$ is the distance of each subsequent grain boundary from the crack origin (take to be at the grain centre). r_p is defined as the plastic zone size ahead the crack tip and $b = r_p + c$. The distance between the crack tip and the next grain boundary is λ.

Following from the approach of Bilby, Cottrell and Swinden (Bilby *et al.*, 1963), for continuous distributions of infinitesimal dislocations with a uniform applied stress, the dislocation density, $f(x)$, is obtained by solving the equilibrium equation defined for locked dislocations across the grain boundary (bounded condition) (see Chapter 2):

$$f(x) = \frac{\sigma_f}{\pi^2 A}\left(\cosh^{-1}\left(\left|\frac{M}{(c-x)} + n\right|\right) - \cosh^{-1}\left(\left|\frac{M}{(c+x)} + n\right|\right)\right) \quad (5.1)$$

where all variables are defined as follow:

c is the half surface crack, $M = \dfrac{\left(b^2 - c^2\right)}{c}$, $n = \dfrac{c}{b}$, x is the distance from the crack tip, A is a constant depending on the type of dislocation considered (screw or edge),

σ_f is the friction stress opposing the movement of dislocations in the plastic zone. It may be noted that Navarro and de los Rios have solved the dislocation density function for both bounded and unbounded conditions (Navarro & de los Rios, 1988).

The yield stress, σ_y, of the material may be divided into two parts: one is the internal or intrinsic friction stress, which opposes the movement of dislocations and the other is the grain boundary strength, which blocks the lead dislocation of a slip band from moving into the next grain. A Hall-Petch type equation may be derived to express, in the first grain, the stress concentration on the lead dislocation and the stress requirement to attain the critical stress to operate a dislocation source in the next grain. This equation is presented as follow:

$$\sigma_y = \frac{1}{2} m^* \tau_0 + m^* \sigma_c \sqrt{\frac{r_0}{D}} \quad (5.2)$$

where τ_0 is defined as the internal/intrinsic stress, m^* is an orientation factor defined below, r_0 is the distance between the grain boundary and a dislocation source in the next grain and σ_c is the critical stress to operate a dislocation source. To take into account the consecutive microstructural grain boundaries and their associated strengths, Sun *et al.* (Sun *et al.*, 1991) proposed a concept of equivalent friction stress replacing the internal friction stress in equation (2) by an equivalent internal stress for grains at a distance $iD/2$ from the crack origin: as such equation (5.2) becomes:

$$\sigma_y = \frac{1}{2} m^* \tau_0^* + m^* \sigma_c \sqrt{\frac{r_0}{iD}} \quad (5.3)$$

where τ_0^* is the equivalent internal/intrinsic friction stress, and $iD/2$ is the distance of each subsequent grain boundary from the crack origin.

From equation (5.3), the equivalent friction stress σ_{ef} may be defined as follow:

$$\sigma_{ef} = \frac{1}{2} m^* \tau_0^* = \sigma_y - m^* \sigma_c \sqrt{\frac{r_0}{iD}} \quad (5.4)$$

The effect of grain orientation is defined by a factor m^*/m_1^* where m_1^* is the orientation factor related to the first grain and m^* is the factor corresponding to successive grains. From experimental data, De los Rios and Navarro identified that crack growth must "of necessity" start in grains of lowest (most favourable) orientation factor with surrounding grains having higher grain orientation factors. m^* is then set to increase with crack length. Edwards and Zhang proposed that this orientation factor should vary between 2 ($m_1^* = 2$), where for the first grain the crystal is favourably oriented so the resolved shear stress is at its maximum, and 3.07 where many grains are covered by a long crack (polycrystalline behaviour) (Edwards & Zhang, 1994b). Navarro and De los Rios (Navarro & de los Rios, 1988) have developed an empirical formula defined as:

$$m^*/m_1^* = 1 + c_1 \ln(i) \quad (5.5)$$

where c_1 is defined by Edwards and Zhang as a fitting parameter equal to *0.25*.

Equation (4) suggests that whilst the yield stress is constant and dependent on a given material, the equivalent friction stress varies as the crack grows (and then i increases). When $i = 1$ (first grain), the equivalent friction stress has a minimum value corresponding to the friction stress but when *i* approaches infinity (i.e. the long crack case), the equivalent friction stress achieves its maximum value and equals the yield stress. By replacing the friction stress, σ_f, with the equivalent friction stress, σ_{ef}, in equation (1), the plastic zone size can be calculated from the condition of vanishing dislocation density at the extremity of the plastic zone (at $x = \pm b$ in equation (1))

$$n = \frac{c}{b} = \cos\left(\frac{\pi\sigma_{\max}}{2\sigma_{ef}}\right) \quad (5.6)$$

$$\frac{r_p}{c} = \frac{1 - \cos\left(\frac{\pi\sigma_{\max}}{2\sigma_{ef}}\right)}{\cos\left(\frac{\pi\sigma_{\max}}{2\sigma_{ef}}\right)} \quad (5.7)$$

where $r_p = b - c$ and $\sigma_{\max}$ is the maximum applied stress.

A fitting parameter, ϕ^*, has been used in equation (5.4) by Edwards and Zhang to correlate the simulated plastic zone with those measured experimentally. Equation (5.4) becomes:

$$n = \frac{c}{b} = \phi^* \cos\left(\frac{\pi\sigma_{\max}}{2\sigma_{ef}}\right) \quad (5.8)$$

It may be noted from equation (5.8) that the plastic zone size is assumed to be large at crack initiation and decreases with initial crack extension; this observation agrees with the selected area channelling pattern observations (Zhang & Edwards, 1992).

Having a formulation of the plastic zone size ahead the crack tip, crack growth retardation behaviour observed in experimental results (Zhang & Edwards, 1992) may then be considered in terms of grain boundary influence. Typically cracks decelerate and may temporarily stop at grain boundaries and further propagation occurs after the development of plastic deformation in the next grain. In the next grain it may be considered that the stress on the first available dislocation source increases until a critical value is achieved.

The upper limit of the stress acting on a dislocation source in the next grain ahead of a slip band can be defined as:

$$S(\zeta_0) = \frac{\sigma}{\sqrt{2}\sqrt{\zeta_0 - 1}}\left(1 - \frac{2\tau_0 \cos^{-1} n}{\pi\sigma}\right) + \tau_0 \quad (5.9)$$

where $\zeta_0 = \dfrac{(b + r_0)}{c}$ and σ is the applied stress. The stress, S, increases as the parameter ζ_0 decreases, which occurs as the crack tip approaches the grain boundary.

The critical stress allowing the crack to overcome the barrier is defined as follow:

$$S(m^*) = \frac{1}{2} m^* \sigma_c \quad (5.10)$$

where σ_c is the critical stress to operate a dislocation source as defined earlier.

Having all the equations necessary to calculate the plastic zone size in all the conditions, it may be valuable to summarise the principles of the model through an analysis of a schematic diagram of plastic zone size as a function of tip position (on the x-axis) and relative proximity to a grain boundary, as shown in Figure 5.33.

When the plastic zone ahead of a crack tip is not blocked by the forthcoming grain boundary (that is to say when $r_p \leq \lambda$), r_p is calculated by equation (5.8).

If the plastic deformation is blocked, and if the stress S at the dislocation source in the next grain is not superior to the critical stress (equation (5.9) and (5.10)), the plastic zone size is assumed to be λ, the distance between the crack tip and the next grain boundary. Once the barrier is overcome, the plastic zone is calculated according to equation (8) with the index i increasing to $i+2$.

It is then assumed that small crack growth rates were proportional to the plastic zone size ahead of the crack tip, so the crack growth rate is defined as follow:

$$\frac{da}{dN} = Cr_p^m \quad (5.11)$$

where C and m are material constants.

To use the above model it is obviously necessary to define the various materials parameters. Navarro and de los Rios (Navarro & de los Rios, 1988) have defined the values of r_0 between $0.1-1\mu m$, σ/τ_0 between $5-20$ and σ_c is the critical stress proportional to the yield stress. In this work, these parameters have been chosen as identical to those defined by Edwards and Zhang in work on 7xxx aluminium alloys. So r_0, σ/τ_0, σ_c are equal to $0.1\mu m$, 10 and $0.96\times\sigma_y$ respectively. ϕ^* is 0.5 and c_1 is equal to 0.25 as defined previously. The material constants C and m have been determined by visual comparison with experimental crack growth data from the fusion zone sub-sized samples at a stress level of 270MPa. They are respectively 2.5×10^{-7} and 2.41 respectively. Figure 5.34 shows the da/dN behaviour used for the simulation at a stress level of 270MPa. It may be noticed the crack growth rate predictions are indeed close to the bounds of the crack growth data from the fusion zone sub-sized

samples. Given the mathematical formulation, a 'perfect' fit is not possible. Given the particular dependence of fatigue lives on the earliest/slowest stages of crack growth, care has been taken in achieving a good fit at the lower end of the experimental data range.

Figure 5.35 presents predictions of fatigue life of a single crack based on both models. As with the Hobson model, the single crack model using Zhang and Edwards' da/dN model gives a reasonable approximation of the parent alloy behaviour, especially at high stress levels. Divergence from the parent plate SN data again occurs at low stress: however a sign of a modelled microstructural influence may be seen in more extended life predictions using the Zhang and Edwards model.

Figure 5.36 presents the fatigue life simulations of the multiple crack models for two pore simulated areas. As shown in Figure 5.35 for the single crack simulation, the results for the original/reference simulated area (1.2x1.4mm) at high stress levels do not show significant differences between the two crack growth models, with both providing an over estimate of the real 1mm crack fatigue lives in the MIG weld. However a "microstructural" effect is seen again at low stress where larger fatigue lives are predicted in comparison with the Hobson-based results. For a large simulated area (x6 area as identify previously), the modelling results present a slight over estimate of the weld life. Overall it may be seen that more microstructurally based crack growth performs in an essentially equivalent manner to the Hobson-based simulations, although it may be recognised that the Zhang and Edwards growth model represents a more mechanistically approach, but is 'fitted' to the same experimental reference data.

As presented in section 4.1, and discussed in section 5.1.3, the fusion zone of the MIG weld is not residual stress free. Any complete treatment of residual stress effects on crack growth in the present samples would have to take into account a number of factors, such as: (a) interactions between crack extension and the overall residual stress field due to stress redistribution, and (b) positional variations in residual stress (moving laterally from the weld line and into the depth of the specimens), and associated interactions with thumbnail cracks emanating from the specimen surfaces. However,

as crack sizes get smaller it may be expected that in-plane and through-thickness residual stress variation effects will become limited (crack becomes smaller than the wavelength of the residual stress variations), as indeed will the effects of crack extension on stress redistribution. Residual stress variations with depth are not particularly considered within the present modelling, however, measurements of residual stresses carried out as a function of depth in equivalent welds have revealed limited through-thickness gradients - at least in terms of the half millimetre depth of concern here (Edwards, 2003). As such, the single surface residual stress measurements used for the crack growth calculations are considered reasonable in the first instance. Given the present interest in cracks up to 1mm in length, an initial estimate of (local) residual stress effects on crack growth may then be gained through superposition of fixed, uniform stresses on the life calculations.

In first instance, a first and very simple estimate of the residual stress influence in the present models may be taken from an increase of effective stress range by the amount of residual stress. Residual stresses are therefore not being considered to simply increase local load R-ratio, but to fully contribute to fatigue failure, i.e. providing an upper bound estimate for adverse effects on crack growth. Based on experimental residual stress of the order of 50MPa measured at the MIG fusion zone edge, modelling results for the x6 area microstructural sample using the Zhang and Edwards growth model are shown in Figure 5.37. It may be seen that this estimate of residual stress influence leads to slightly conservative specimen life prediction (life to 1mm crack length).

Adopting a more physically based approach, several researchers (Kang *et al.*, 1989; Beghini & Bertini, 1990; Kang *et al.*, 1990; Beghini *et al.*, 1994) have suggested that crack closure may be used to characterise fatigue crack growth in residual stress fields. Whilst it may be considered that crack closure occurs in the present tests, crack closure effects in small cracks are difficult to assess and no measurement has been carried out during the present experiments. So in this context a first order estimate of closure influences may be built up. From experimental short crack growth data from the fusion zone sub-sized samples, a transition between "short crack regime" and "long crack regime" may be clearly identified in terms of stress intensity factor. Various

authors have noted that rapid initial short crack growth rates may at least in part be attributable to an absence of crack closure as crack wake length becomes small (Newman *et al.*, 1999). In the present work, cracks initially developing from pores may then be attributed a closure level of zero. At large crack lengths, growth conditions will converge with those of conventional long crack growth, with short and long crack growth rate trends converging. Inspection of the fusion zone sub-sized specimen growth data in Chapter 6 (and summarised Figure 5.23) suggests a transition to essentially long crack behaviour at stress intensities of the order of $7MPa\sqrt{m}$. Whilst obtaining crack closure data even for conventional long crack tests may be problematic and controversial (Xu *et al.*, 2000), closure levels for conventional Al-based materials for such K levels and an R-ratio of 0.1 are variously reported to be of the order of $K_{cl}/K_{\max} = 0.5$ (Xu, 2000), excepting various 'exotic' materials such as Powder Metallurgy alloys and Al-Li materials. In the absence of accurate experimental data, a linear rise in closure levels as $K_{cl}/K_{\max}$, may be then assumed between the initial stress intensity factor range, $\Delta K_{initial}$, and the transition point, $\Delta K_{transition}$, where the closure level achieves 0.5 (Xu, 2000). The closure stress level as a function of crack growth for residual stress free conditions is then defined by equation (5.12):

$$K_{cl}/K_{\max} = 0.5\frac{(\Delta K_{applied} - \Delta K_{transition})}{(\Delta K_{final} - \Delta K_{transition})} \quad (5.12)$$

where $\Delta K_{applied}$ is the applied stress intensity factor range for a given crack length. When residual stress effects on crack growth are considered, it is then assumed that closure levels also follow equation (5.12), with elastic superposition of residual stress effects and applied load then causing an increase in effective crack driving forces.

Now having an estimate of closure level occurring in stress free material, the crack growth simulation needs to be modified to take into account the closure effect and then the residual stress influence. Equation (5.8), defined earlier as the simulated plastic

zone, is modified in replacing the maximum applied stress, σ_{max}, by an equivalent stress, σ_{equi}:

$$n = \frac{c}{b} = \phi \cos\left(\frac{\pi\sigma_{equi}}{2\sigma_{ef}}\right) \quad (5.13)$$

The equivalent stress, σ_{equi}, is then defined by

$$\sigma_{equi} = \sigma_{max} \times U \quad (5.14)$$

The effective stress intensity ratio, U, is defined as:

$$U = \frac{\Delta K_{eff}}{\Delta K_{applied}} \quad (5.15)$$

and the effective stress intensity factor range, ΔK_{eff} is given by

$$\Delta K_{eff} = K_{max} - K_{cl} \quad (5.16)$$

The closure effect is then integrated in the model as follows:

- A small crack is considered closure free just after the initiation and until $K_{cl} \leq K_{min}$ (where K_{min} is the minimum stress intensity factor for a given crack length) , so

$$U = 1 \quad (5.17)$$

$$\text{and so } \sigma_{equi} = \sigma_{max} \quad (5.18)$$

- When $K_{cl} > K_{min}$ and until the transition short-long crack growth regime, a closure effect is considered present and the equivalent stress varies linearly as a function of the effective stress intensity factor range (as noted in equations (5.12) and (5.14).

- At the transition point of the short-long crack growth regime, closure effect is at a maximum, so

$$\sigma_{equi} = 0.5 \times \sigma_{max} \quad (5.19)$$

Secondly the residual effect is integrated in the model:

- A small crack is still considered closure free just after the initiation and until $K_{cl} \leq K^*_{\min}$ (where $K^*_{\min}$ is the minimum stress intensity factor for a given crack length considering the residual stress) , so

$$K^*_{\min} = K_{\min} + K_{res} = K_{\min} \times \left(\frac{\sigma_{\min} + \sigma_{res}}{\sigma_{\min}} \right) \quad (5.20)$$

$$\text{and } U = 1 \quad (5.21)$$

- When $K_{cl} > K^*_{\min}$ and until the transition short-long crack growth regime, a closure effect is considered present and the equivalent stress varies linearly as a function of the effective stress intensity factor range but with the influence of the residual stress.

$$U = \frac{\Delta K^*_{eff}}{\Delta K_{applied}} \quad (5.22)$$

$$\text{and so } \sigma_{equi} = \sigma_{\max} \times U \quad (5.23)$$

The new effective stress intensity factor range, ΔK^*_{eff} is given by

$$\Delta K^*_{eff} = K^*_{\max} - K_{cl} \quad (5.24)$$

where $K^*_{\max}$ is the maximum stress intensity factor for a given crack length considering the influence of residual stress.

$$K^*_{\max} = K_{\max} + K_{res} = K_{\max} \times \left(\frac{\sigma_{\max} + \sigma_{res}}{\sigma_{\max}} \right) \quad (5.25)$$

Figure 5.38 shows the equivalent stress evolution as a function of stress intensity factor ranges between $\Delta K_{initial}$ and $\Delta K_{transition}$. Figure 5.39 shows a schematic diagram of stress intensity factor evolution with and without a residual stress field, with closure effects.

Given a change to considering effective stress intensity influence in growth rates, material constants C and m have been determined again by visual comparison with experimental crack growth data from the fusion zone sub-sized samples at a stress level of 270MPa expressed in terms of effective stress intensity factor ranges and considering the new crack growth simulation with closure effect but no residual stress: as such C was set equal to $6x10^{-7}$ and m to 2.39.

Adopting the various assumptions above, results for fusion zone life predictions (to 1mm crack length) for the x6 area model (i.e. half a fusion zone), with multiple crack interactions, and crack closure effects, are shown in Figure 5.40, both with and without the influence of a 50MPa residual stress. It may be seen that a close approximation of the corresponding weld data is in fact obtained, with the residual stress affected life predictions in this diagram falling somewhat above those for the first order residual stress effect suggested in Figure 5.37.

5.5. Conclusion

2024-T351-based material was studied in conjunction with the metal inert gas (MIG) welding process. This welding technique is considered industrially to produce high quality welds and is suitable for automation. It has been seen that crack initiation and early growth were dominated by the fusion zone. It has been also found that two kinds of weld defect were present and linked to the crack initiation process: interdendritic defects of the order of 10 to 50 microns and gas porosity of the order of hundred's of microns. The more acicular but smaller interdendritic pores were seen to be most damaging in terms of crack initiation. EBSD observations have been carried out to highlight the general microstructure and to investigate if crack initiating pores may have damaging co-location with grain boundaries, although no evidence of additional microstructural contribution to crack initiation behaviour was noted. Multiple crack initiations have been observed in the fusion zone leading to crack-crack interactions. In the context of multiple crack interactions, a model has been developed to predict the fatigue life of the MIG fusion zone based on measured defect distributions. To initiate cracks, a Monte-Carlo method has been used based on the probability of initiation

derived from the experimental observations. The probability of initiation is then a function of pore size, shape. Based on experimental observations it has been considered reasonable to initiate cracks only at the start (in the first cycle) of the fatigue simulations. In first instance, crack propagation models based on a linear Hobson approach, and on a microstructure sensitive approach based on continuous dislocation distribution methods have been used. Different geometrical conditions to define crack shielding or crack coalescence have been considered. Taking further account of influences of measured residual stresses within the welds, it is shown that although a significant number of simplifications and estimates have been used, fatigue behaviour of the present MIG welds is well represented by the current modelling approach.

References

Anderson, T. L. (1995). in Fracture mechanics - Fundamentals and applications, CRC press: 34-35.

ASM International (1998). Aluminium and Aluminium Alloys. in. A. S. Handbook, Davis, J.R.: 654-661.

Beghini, M. and L. Bertini (1990). "Fatigue crack propagation through residual stress fields with closure phenomena." Engineering Fracture Mechanics 36(3): 379-387.

Beghini, M., L. Bertini and E. Vitale (1994). "Fatigue crack growth in residual stress fields: experimental results and modelling." Fatigue and Fracture of Engineering Materials and Structures 17(12): 1433-1444.

Bilby, B. A., A. H. Cottrell and K. H. Swinden (1963). "The spread of plastic yield from a notch." Proc. Roy. Soc. Lond. 272A: 304-314.

Buffiere, J. Y., S. Savelli, P. H. Jouneau, E. Maire and R. Fougeres (2001). "Experimental study of porosity and its relation to fatigue mechanisms of model Al-Si7-Mg0.3 cast Al alloys." Materials Science and Engineering a-Structural Materials Properties Microstructure and Processing 316(1-2): 115-126.

Chen, E. Y., L. Lawson and M. Meshii (1995a). "Comparison of the growth of individual and average microcracks in the fatigue of Al-SiC composites." Metallurgical and Materials Transactions A 26A(December): 3163-3176.

Chen, E. Y., L. Lawson and M. Meshii (1995b). "The effect of fatigue microcracks on rapid catastrophic failure in Al-SiC composites." Materials Science and Engineering A 200: 196-206.

Edwards, L. (2003). WELDES review meeting - 16th September - The Open University. Milton Keynes.

Edwards, L. and Y. H. Zhang (1994a). "Investigation of Small Fatigue Cracks .1. Plastic-Deformation Associated with Small Fatigue Cracks." Acta Metallurgica Et Materialia 42(4): 1413-1421.

Edwards, L. and Y. H. Zhang (1994b). "Investigation of Small Fatigue Cracks .2. A Plasticity Based Model of Small Fatigue-Crack Growth." Acta Metallurgica Et Materialia 42(4): 1423-1431.

Hobson, P. D. (1982). "The formulation of a crack growth equation for short cracks." Fatigue of Engineering Materials and Structures 5(4): 323-327.

Hünecke, J., H. Bomas, S. Laue and D. Schöne (2001). Observation and simulation of short crack behaviour in a low Carbon Stell under constant amplitude loading. Conference Materials week, Munich,

Hünecke, J. and D. Schöne (2002a). Life prediction by observation and Simulation of short crack behaviour in a low carbon steel. Symposium of fatigue testing and analysis under variable amplitude loading, Tour (France), ASTM, 34, 1-3.

Hünecke, J. and D. Schöne (2002b). Short crack behaviour in a low carbon stell under fatigue loading. Fatigue 2002, Stockholm, 3, 2021-2028.

Hünecke, J. and D. Schöne (2002c). Simulation of the short crack behaviour of the low carbon steel SAE1017 under fatigue loading. Conference Materials week, Munich,

Joyce, M. R. (2000). Fatigue of aluminium linings in plain automative bearings (PhD Thesis). School of engineering sciences, Materials Research Group. Southampton, University of Southampton: 243.

Kamaya, M. and N. Totsuka (2002). "Influence of interaction between multiple cracks on stress corrosion crack propagation." Corros. Sci. 44: 2333-2352.

Kang, K. J., J. H. Song and Y. Y. Earmme (1989). "Fatigue crack growth and closure through a tensile residual stress field under compressive applied loading." Fatigue and Fracture of Engineering Materials and Structures 12(5): 363-376.

Kang, K. J., J. H. Song and Y. Y. Earmme (1990). "Fatigue crack growth and closure behaviour through a compressive residual stress field." Fatigue and Fracture of Engineering Materials and Structures 13(1): 1-13.

Lee, S. Y. and J. H. Song (2000). "Crack closure and growth behavior of physically short fatigue cracks under random loading." Engineering Fracture Mechanics 66: 321-346.

Navarro, A. and E. R. de los Rios (1988). "Short and long fatigue crack-growth - a unified model." Philosophical magazine A - Physics of condensed matter structure defects and mechanical properties 57: 15-36.

Newman, J. C. J., E. P. Phillips and M. H. Swain (1999). "Fatigue-life prediction methodology using small crack theory." International Journal of Fatigue 21: 109-119.

Parry, M. R. (2001). Private communication, Plain specimen S-N data for 2024-T3-T4 Aluminium alloy, Airbus, Filton, UK.

Rooke, D. P. and D. J. Cartwright (1976). in Compendium of stress intensity factors, Hillington Press.

Scott, P. M. and T. W. Thorpe (1981). "A critical review of crack tip stress Intensity factors for semi-elliptic cracks." Fatigue of Engineering Materials and Structures 4(4): 291-309.

Soboyejo, W. O., K. Kishimoto, S. R.A. and J. F. Knott (1989). "A study of the interaction and coalescence of two coplanar fatigue cracks in bending." Fatigue and Fracture of Engineering Materials and Structures 12(3): 167-174.

Soboyejo, W. O. and J. F. Knott (1991). "The propagation of non-coplanar semi-elliptical fatigue cracks." Fatigue and Fracture of Engineering Materials and Structures 14(1): 37-49.

Sun, Z. Y., E. R. de los Rios and K. J. Miller (1991). "Modelling small fatigue cracks interacting with grain boundaries." Fatigue and Fracture of Engineering Materials and Structures 14: 277-291.

Suresh, S. (1998). in Fatigue of Materials. (second edition), Cambridge:132-164.

Xu, Y. (2000). Variable Amplitude Loading Effects on damage Tolerant Airframe Materials (PhD Thesis), University of Southampton.

Xu, Y. G., P. J. Gregson and I. Sinclair (2000). "Systematic assessment and validation of compliance-based crack closure measurements in fatigue." Materials Science and Engineering A A(284): 114-125.

Yang, N., J. Boselli and I. Sinclair (2001). "Simulation and quantitative assessment of homogeneous and inhomogeneous particle distributions in particulate metal matrix composites." Journal of Microscopy - Oxford 201(Part 2): 189-200.

Zhang, Y. H. and L. Edwards (1992). "The effect of grain-boundaries on the development of plastic deformation ahead of small fatigue cracks." Scripta Metallurgica et Materialia 26: 1901-1906.

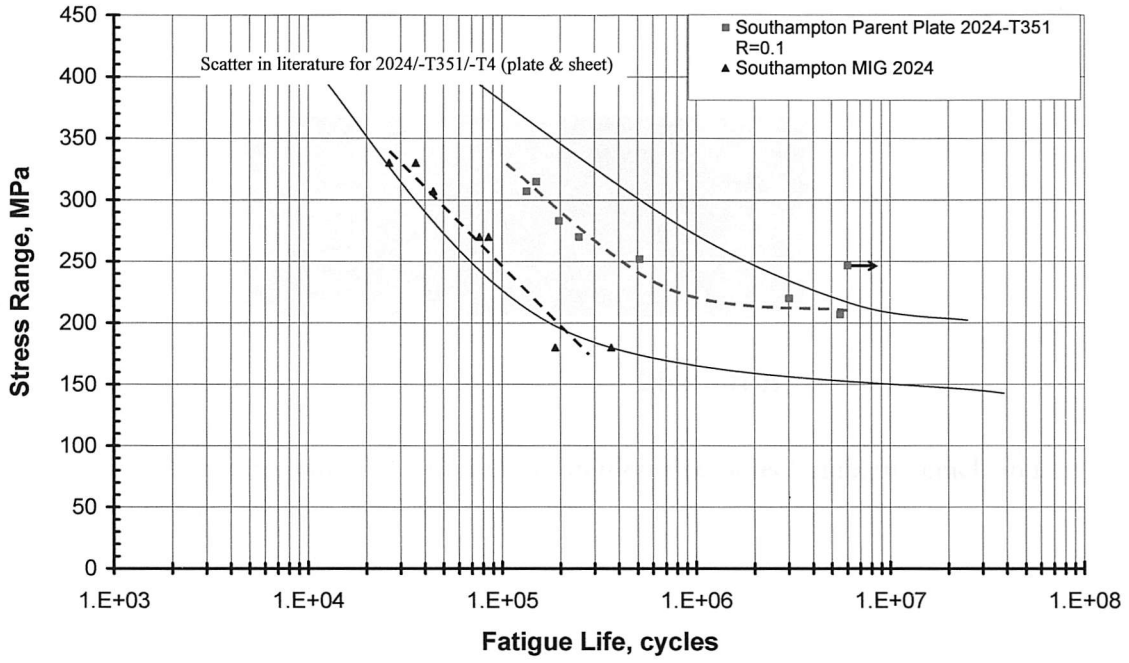

Figure 5.1 Fatigue life data for the MIG weld and the parent plate 2024. Scatter in literature for 2024/-T351/-T4 (plate & sheet) (Parry, 2001)

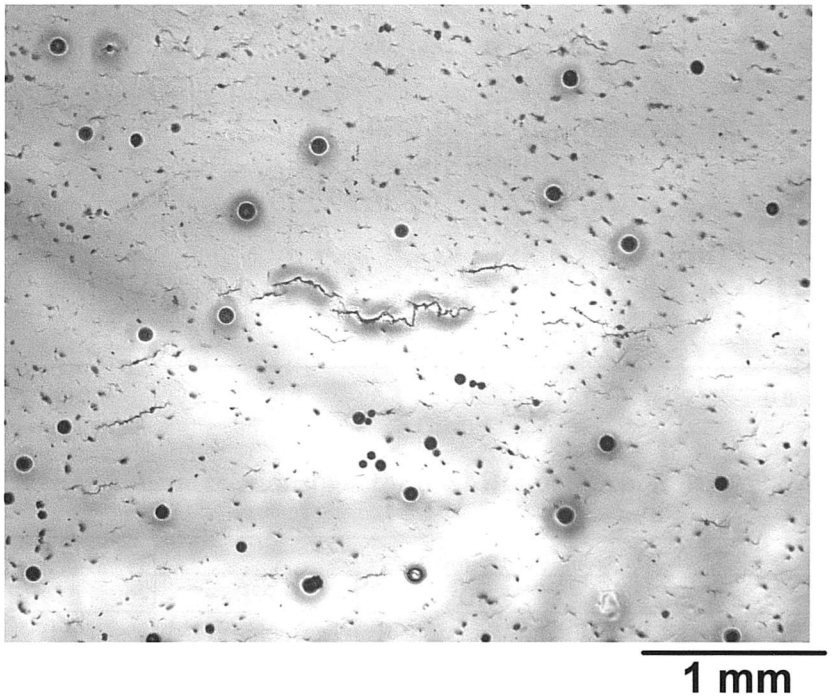

Figure 5.2 Multiple crack initiation observed in the MIG fusion zone at $N/N_f = 0.3$, $\Delta\sigma = 270\ MPa$.

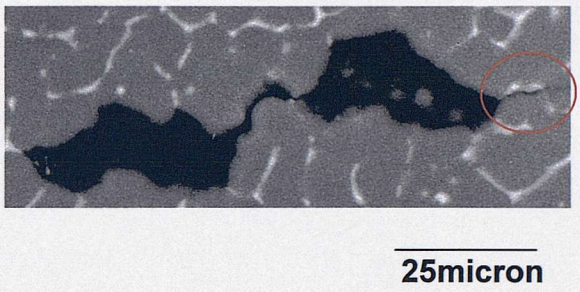

Figure 5.3 SEM macrograph (BEI mode) of interdentritic defect initiating crack and co-location of intermetallic particles.

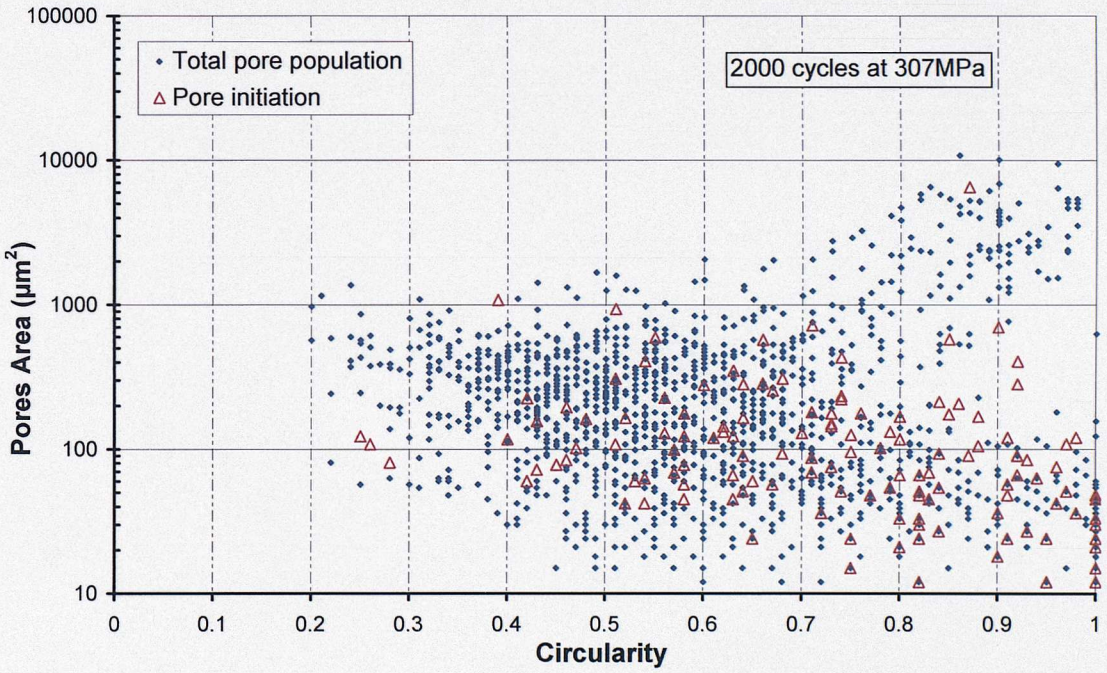

Figure 5.4 Size and shape relationships for the MIG defect population

	Fatigue life		
Stress level	3%	20%	25%
270 MPa	7-8 cracks/mm^2	8-9 cracks/mm^2	-
330 MPa	-	13-14 cracks/mm^2	13-14 cracks/mm^2

Table 5.1 Overall crack density for two stress level and three fatigue life

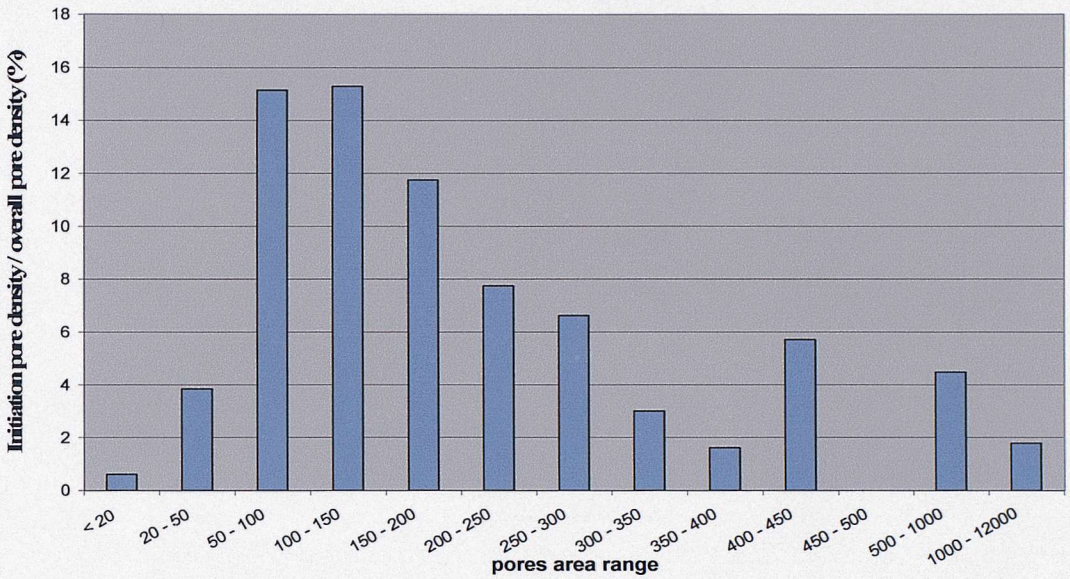

Figure 5.5 Probability of initiation versus pore size after 2000 cycles at stress level of 307MPa.

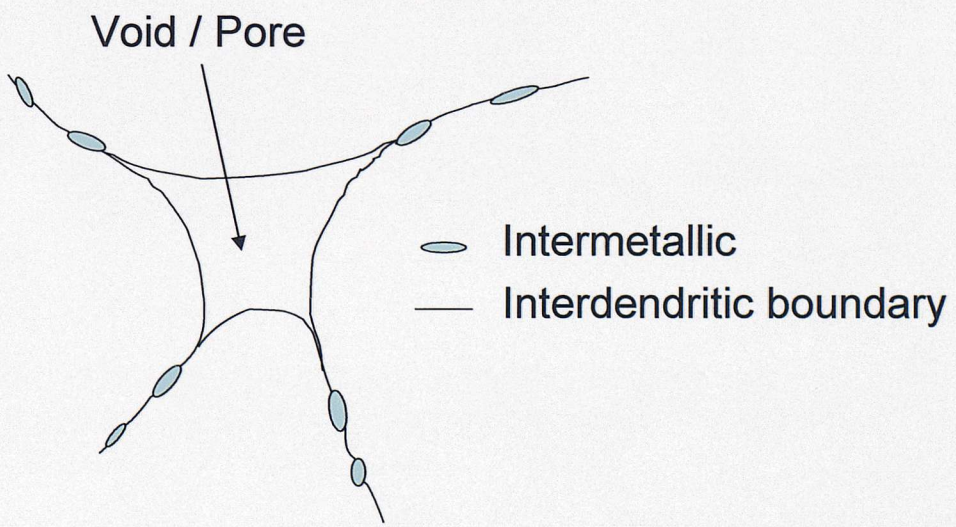

Figure 5.6 Schematic illustration of interdendritic pore morphologies and associated co-location of intermetallics at apices.

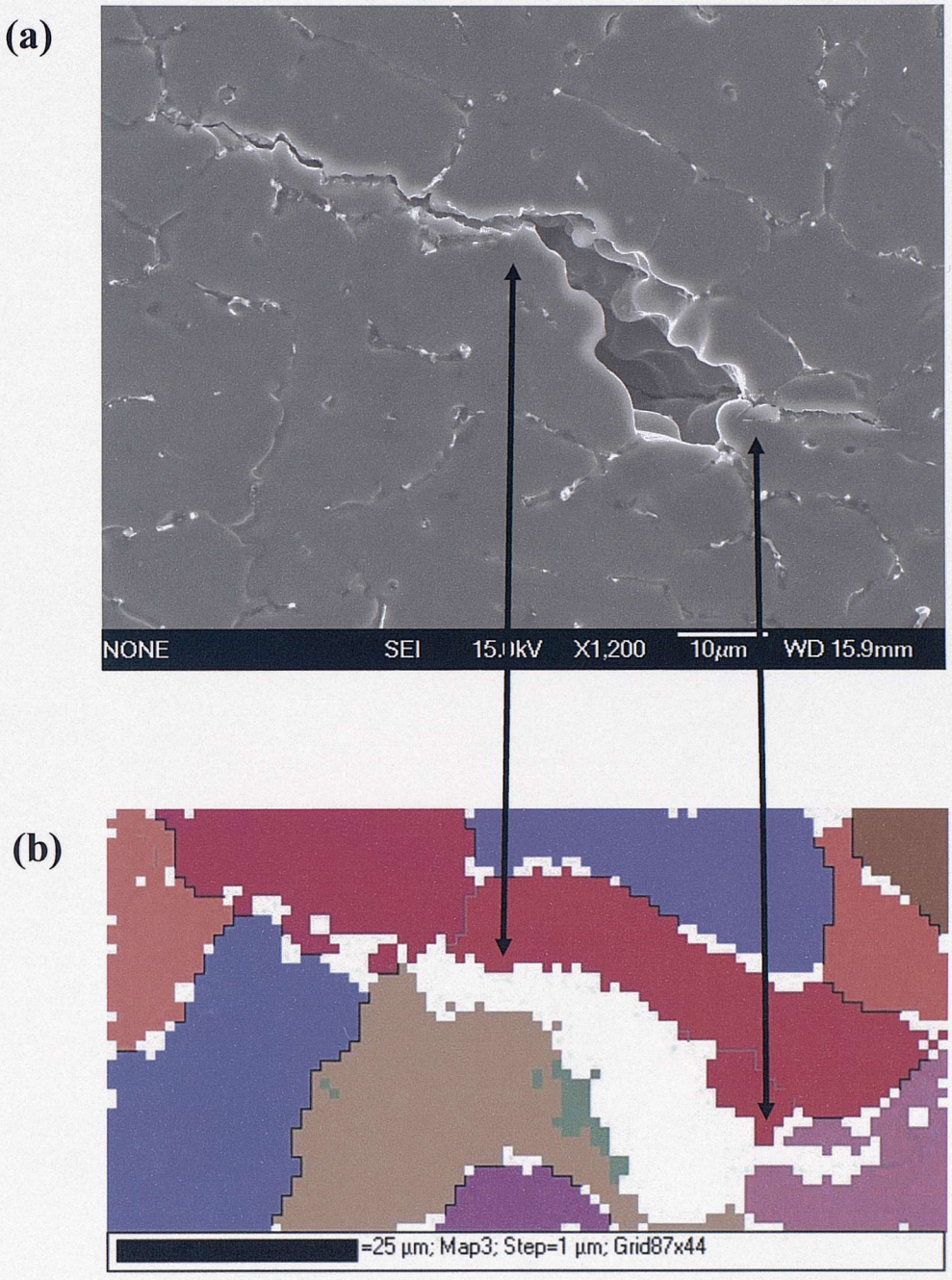

Figure 5.7 SEI macrograph and associated EBSD orientation map of an interdendritic pore and associated cracks initiated from grain boundaries.

(a)

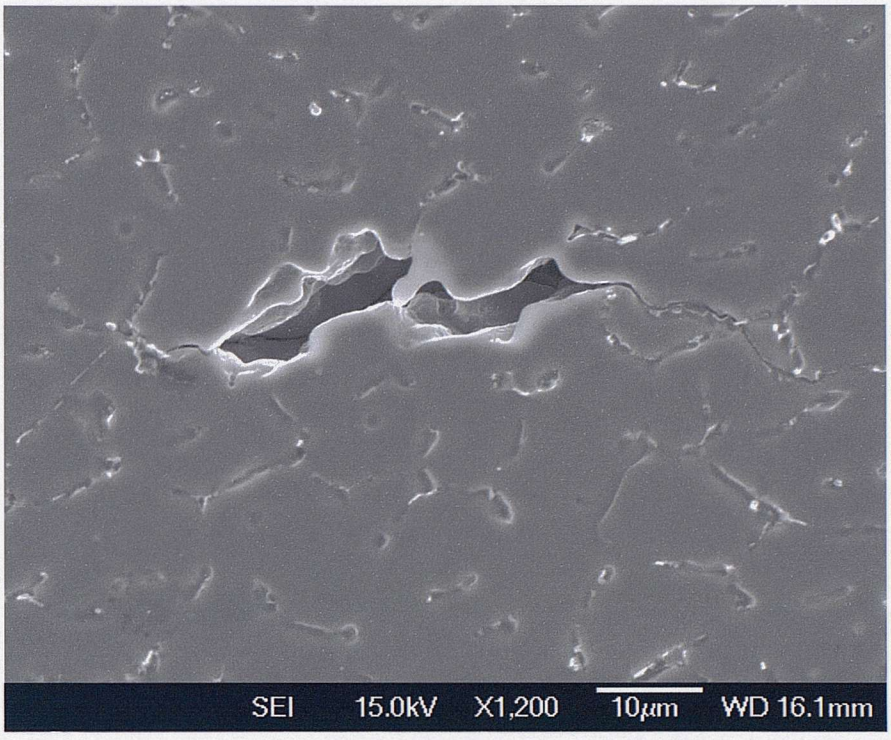

(b)

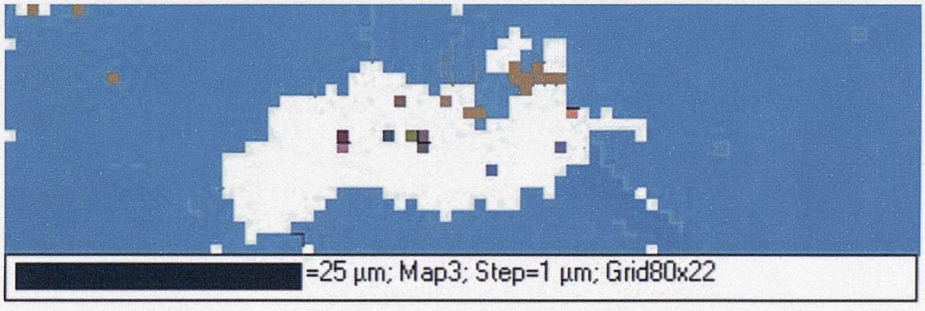

Figure 5.8 SEI macrograph and associated EBSD orientation map of an interdendritic pore and associated cracks not initiated from grain boundaries.

(a)

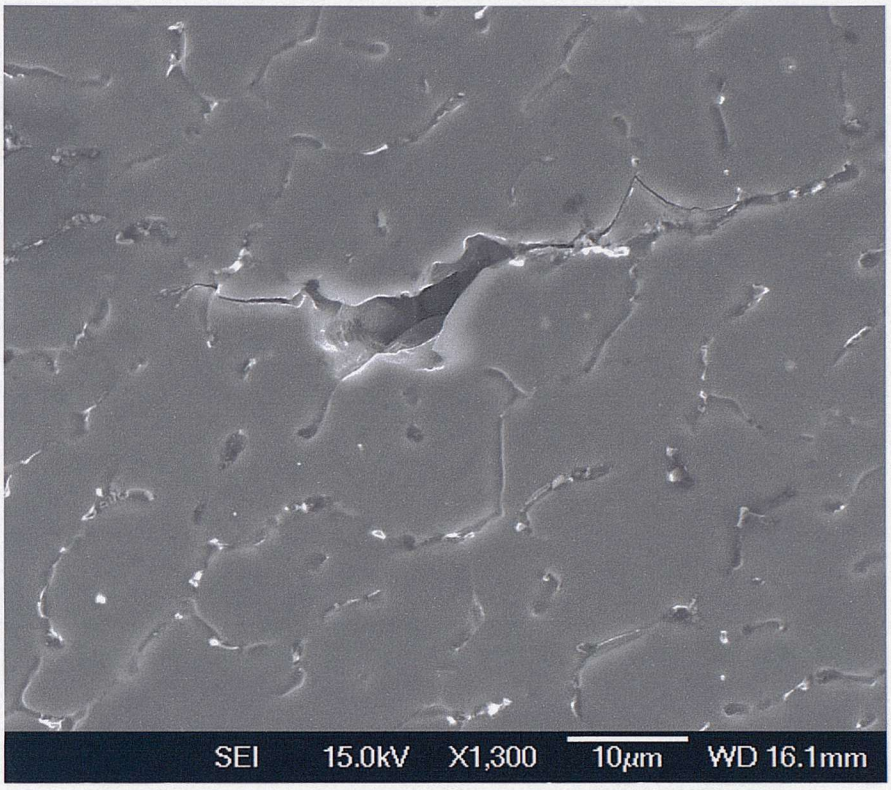

(b)

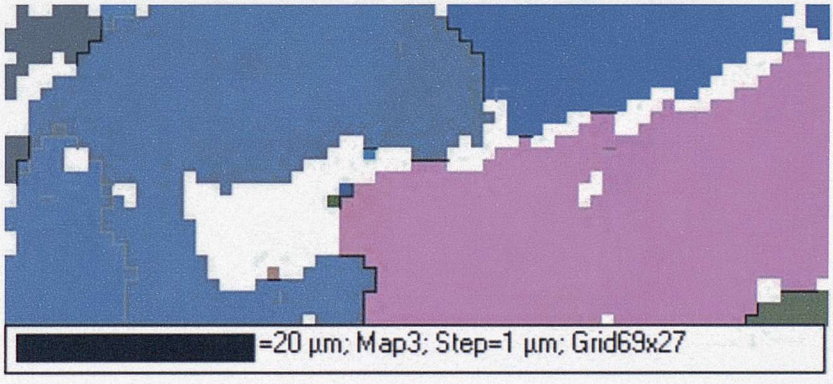

Figure 5.9 SEI macrograph and associated EBSD orientation map of an interdendritic pore and associated cracks with cracks both on and off grain boundaries.

Figure 5.10 EBSD orientation map of MIG fusion and large gas pore highlighting multiple grain boundary interceptions at individual pores.

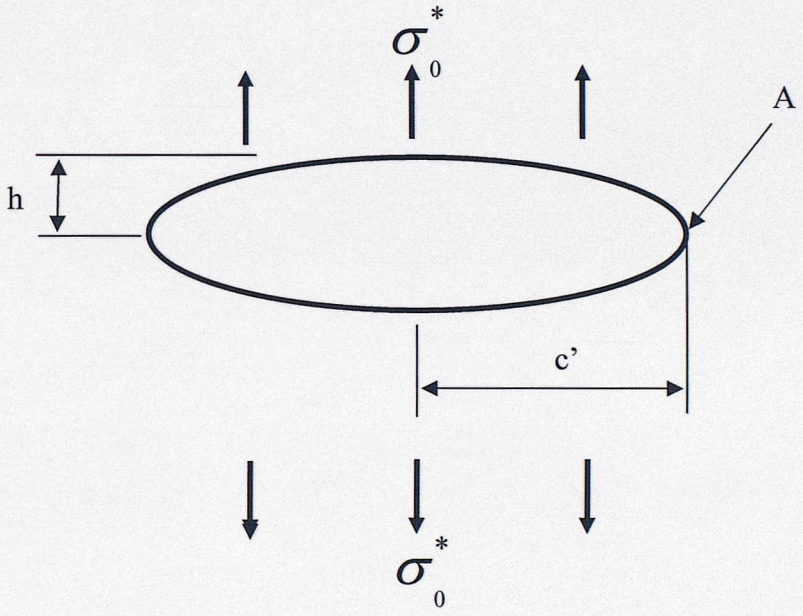

Figure 5.11 Elliptical hole in a flat plate subjected to an uniform uniaxial tensile stress σ_0^*.

Defect	Ellipse 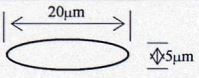			Circle 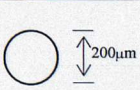		
Crack length	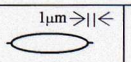	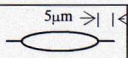	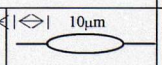	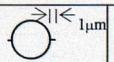	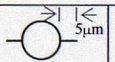	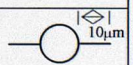
K (MPa√m) (σ=250MPa)	1.50	1.68	1.83	1.69	2.95	3.90

Table 5.2 stress Intensity factor for different crack length (1, 5 and 10μm) and defect shapes (ellipse and circle)

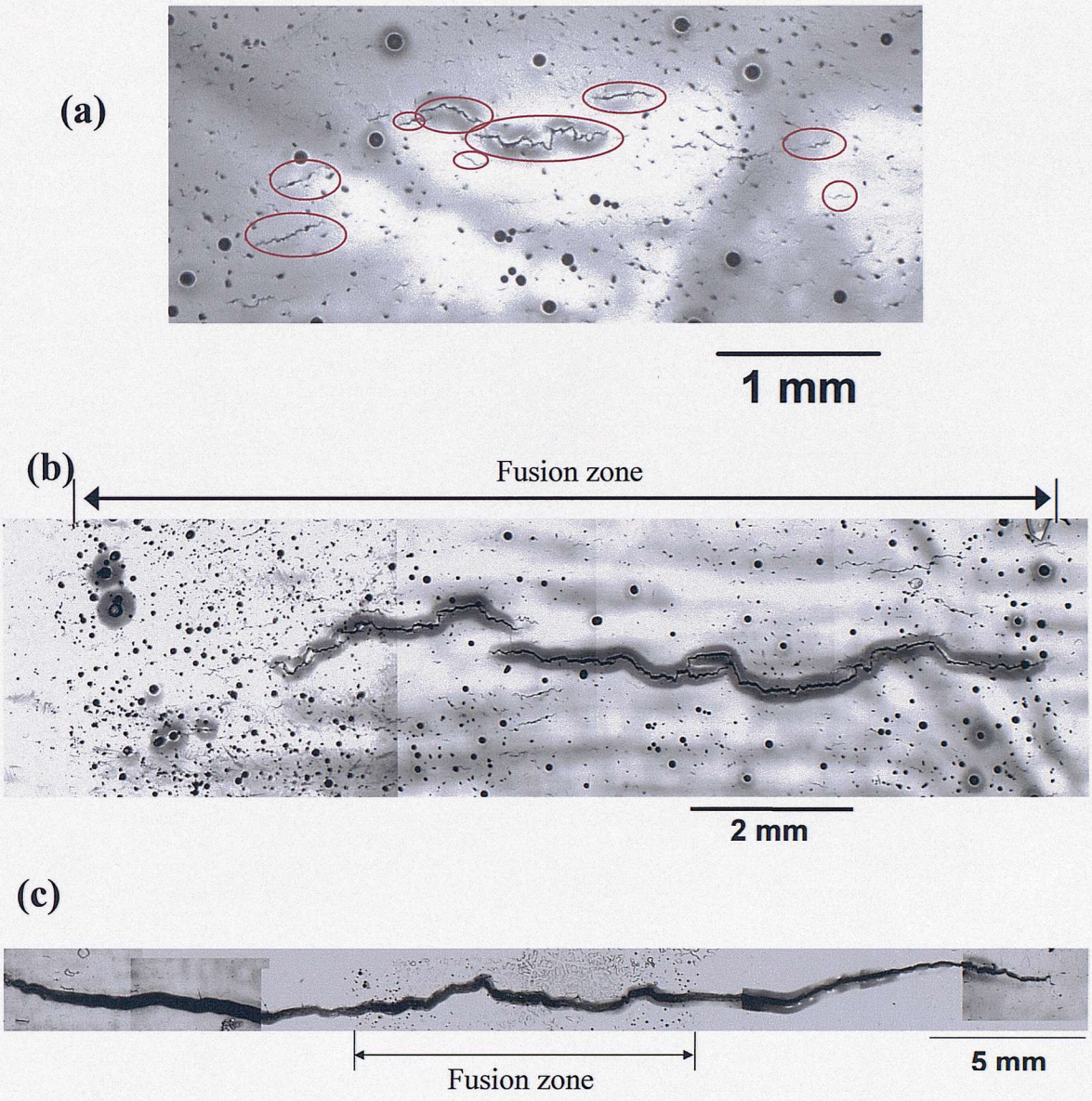

Figure 5.12 Optical macrographs of the MIG fusion zone at stages of crack evolution for a stress level of 307 MPa: (a) $N/N_f = 0.3$ (b) $N/N_f = 0.6$ (c) $N/N_f = 0.99$

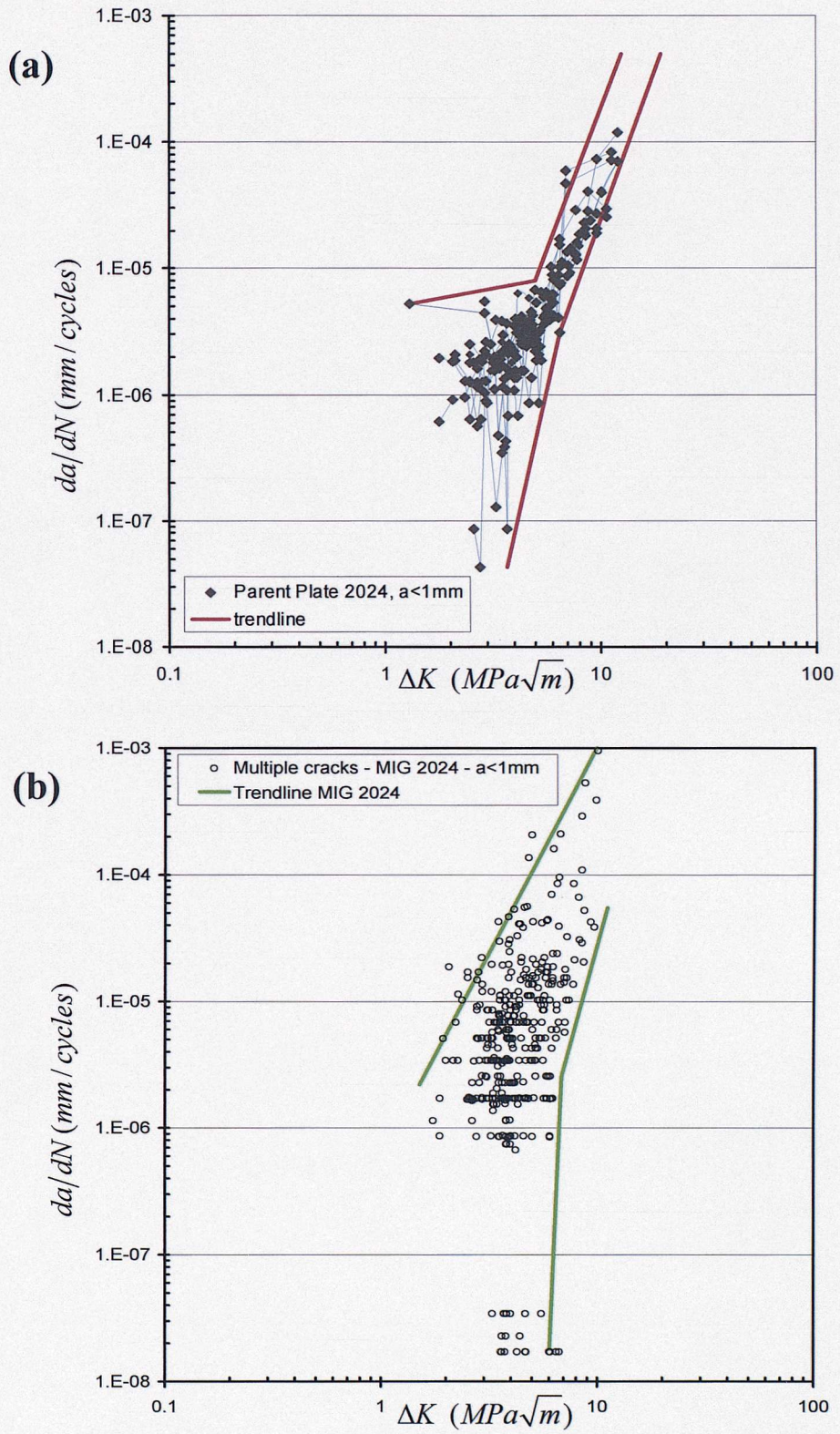

Figure 5.13 Short crack growth data for (a) the parent plate 2024 and (b) the MIG weld fusion zone

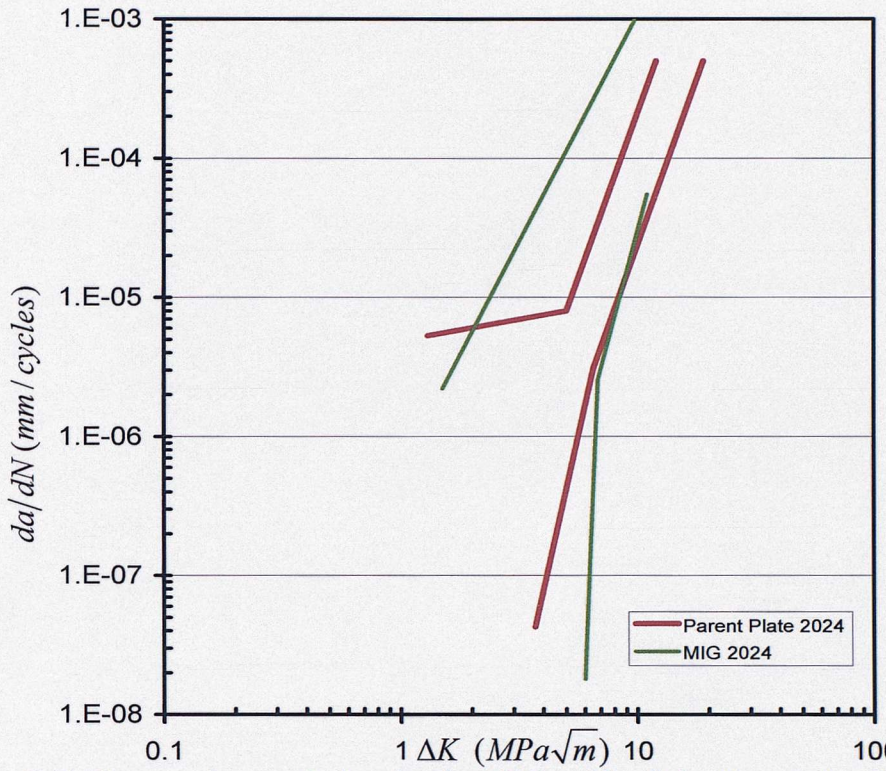

Figure 5.14 Short crack growth data for the MIG weld and the Parent plate 2024.

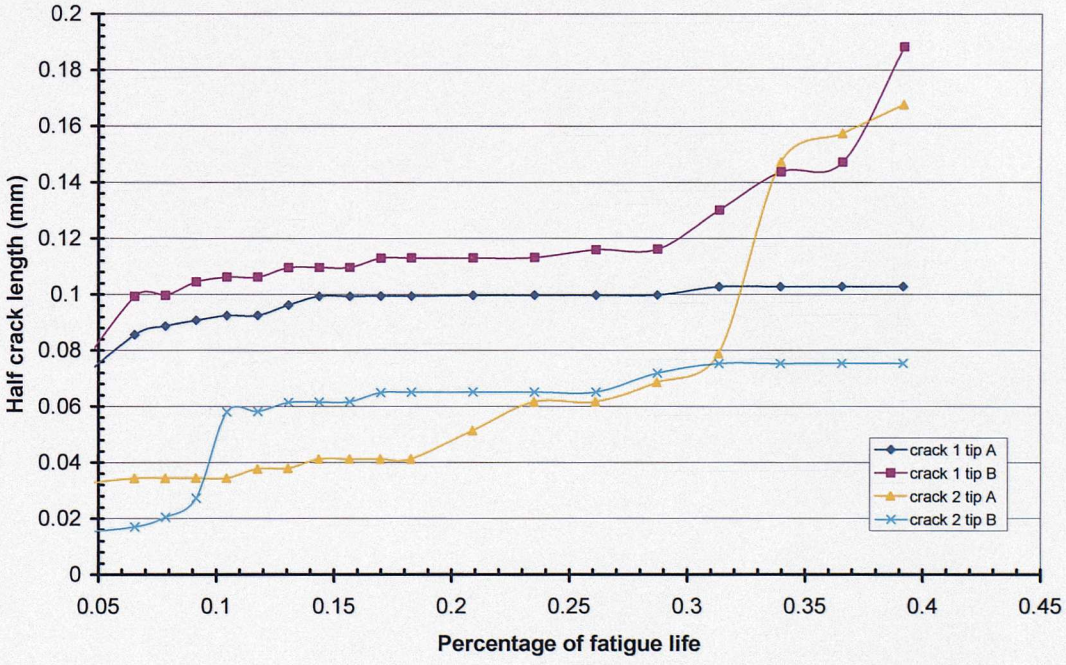

Figure 5.15 Crack lengths versus number of cycles highlighting crack-crack interactions in relation with Figure 5.16.

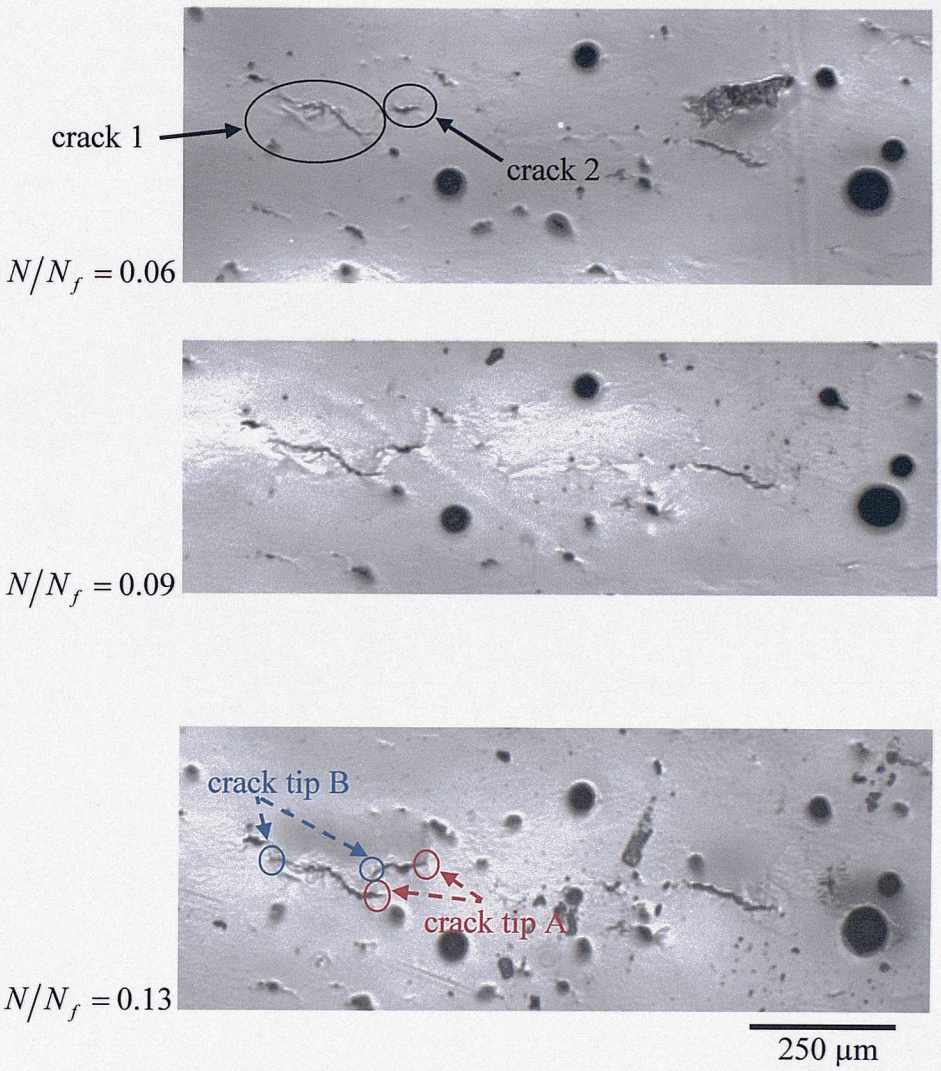

Figure 5.16 (a) Sequence of multiple cracks growth with crack interaction phenomena (shielding, coalescence events) from $N/N_f = 0.06$ to $N/N_f = 0.13$

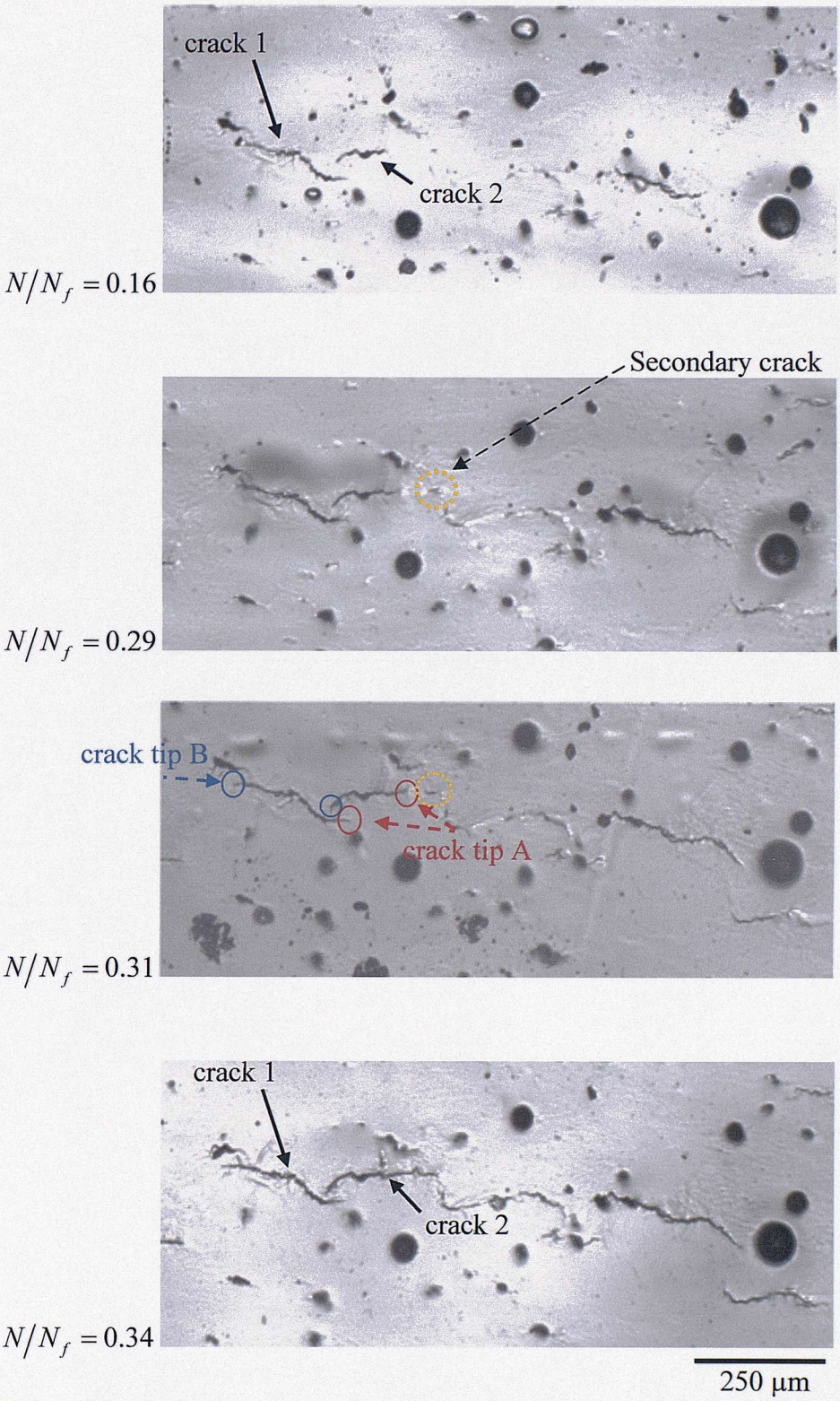

Figure 5.16 (b) Sequence of multiple cracks growth with crack interaction phenomena (shielding, coalescence events) from $N/N_f = 0.16$ to $N/N_f = 0.34$

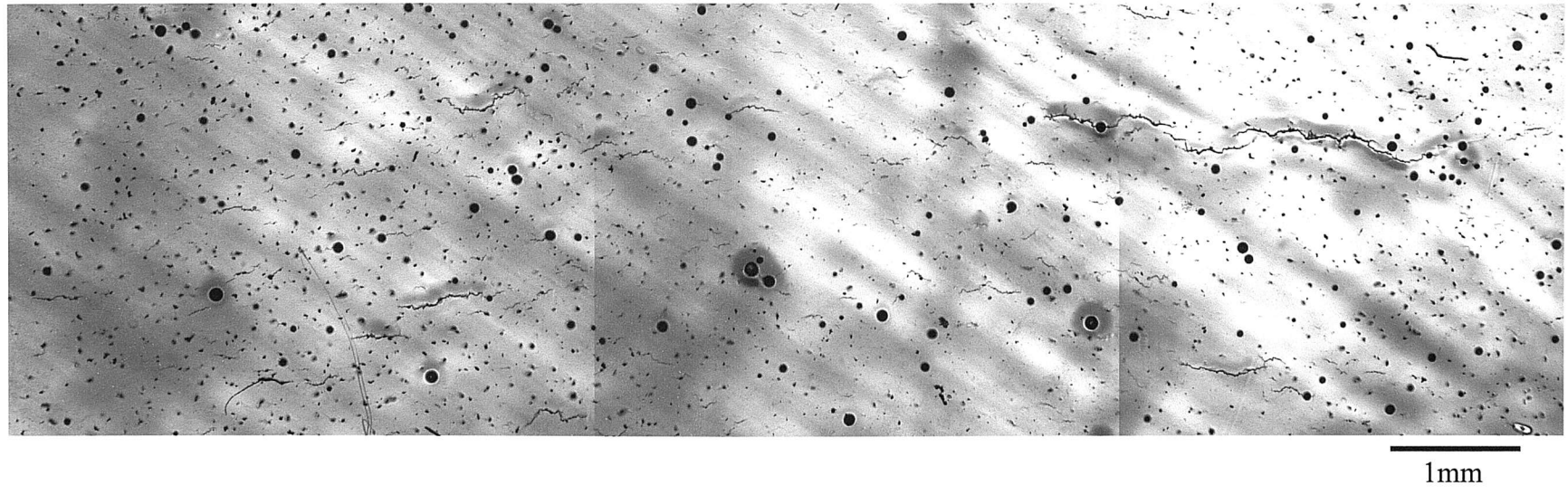

Figure 5.17 Optical macrograph of the MIG fusion zone at for a stress level of 270MPa at 50% of the fatigue life

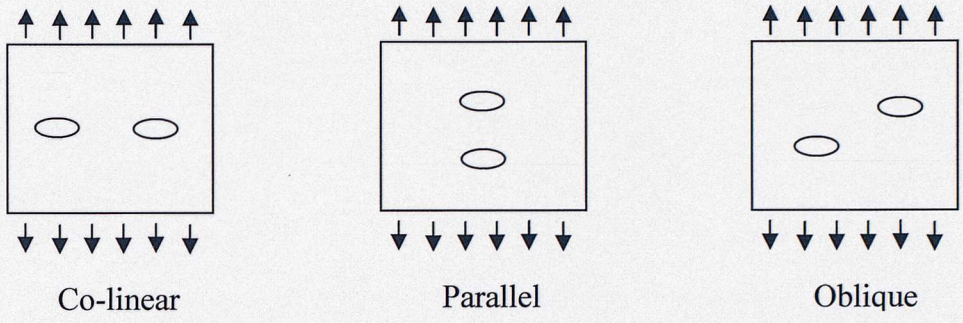

Figure 5.18 Two dimensional representations of two interacting cracks used for FE modelling by Joyce (Joyce, 2000)

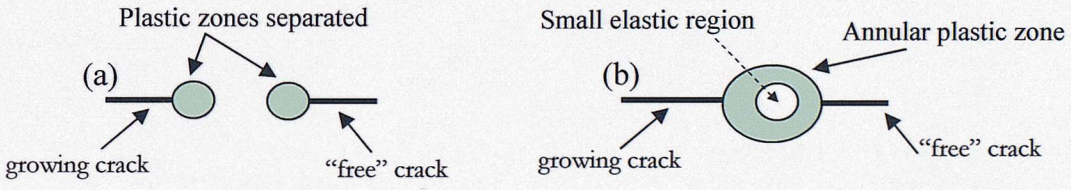

Figure 5.19 Schematic plastic zone development as co-linear cracks coalesce with (a) at the crack initiation, (b) at growing crack length.

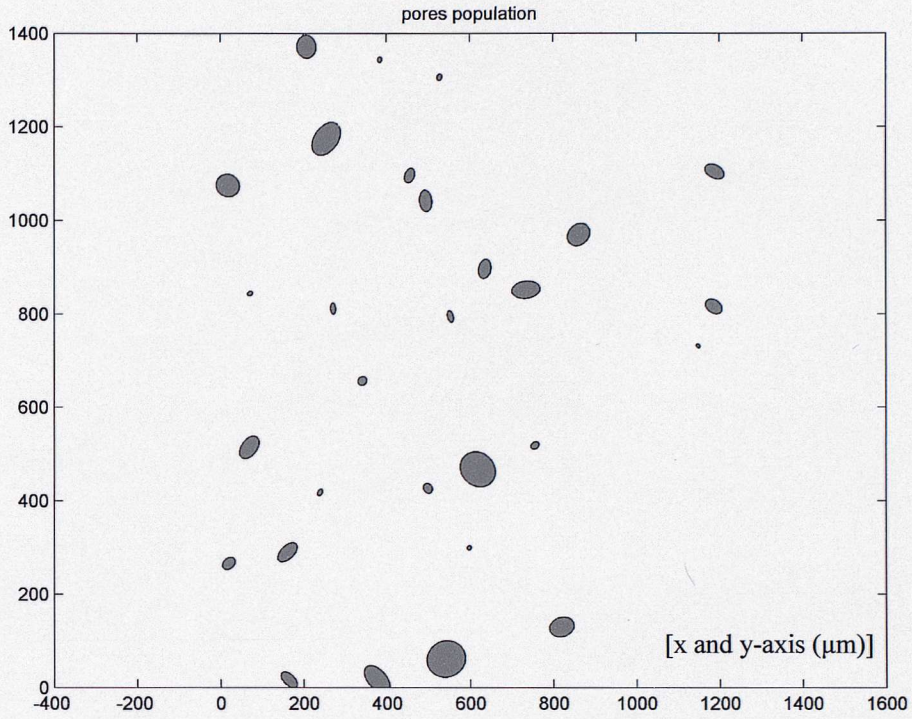

Figure 5.20 Computer generated pore distribution with random spatial distribution and random size and shape ranges in a section of 1.2mm x 1.4mm.

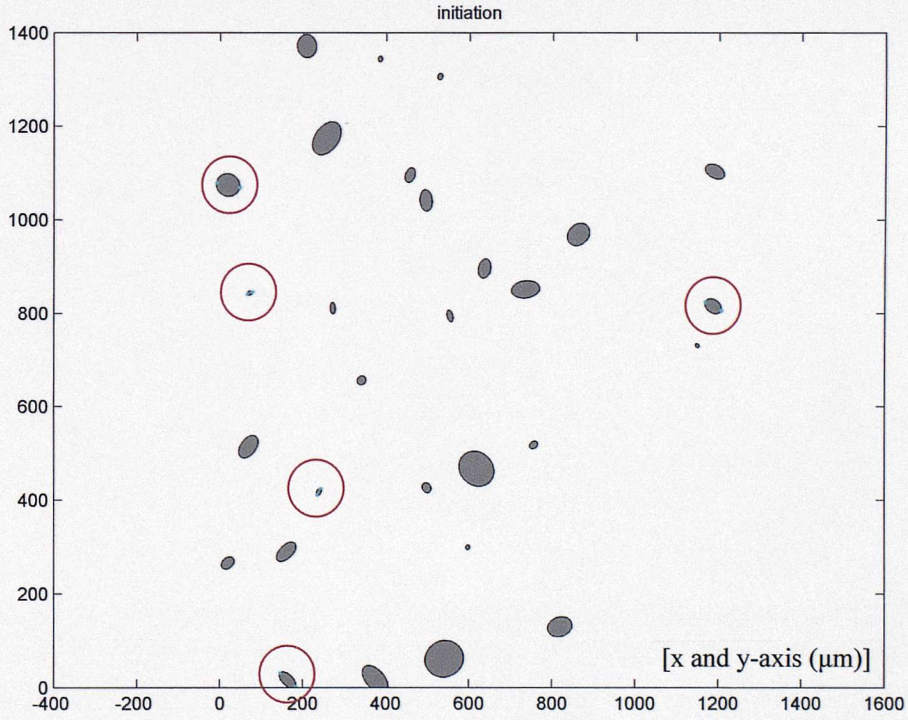

Figure 5.21 Distribution of initiated cracks in the same section (as Figure 5.19). The circles highlight the initiation sites.

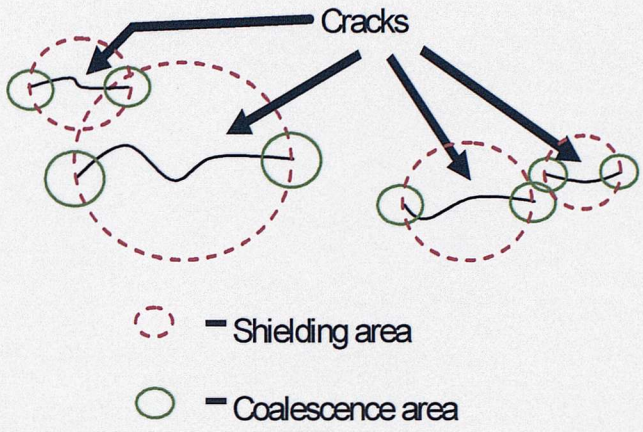

Figure 5.22 Schematic illustration of crack interactions

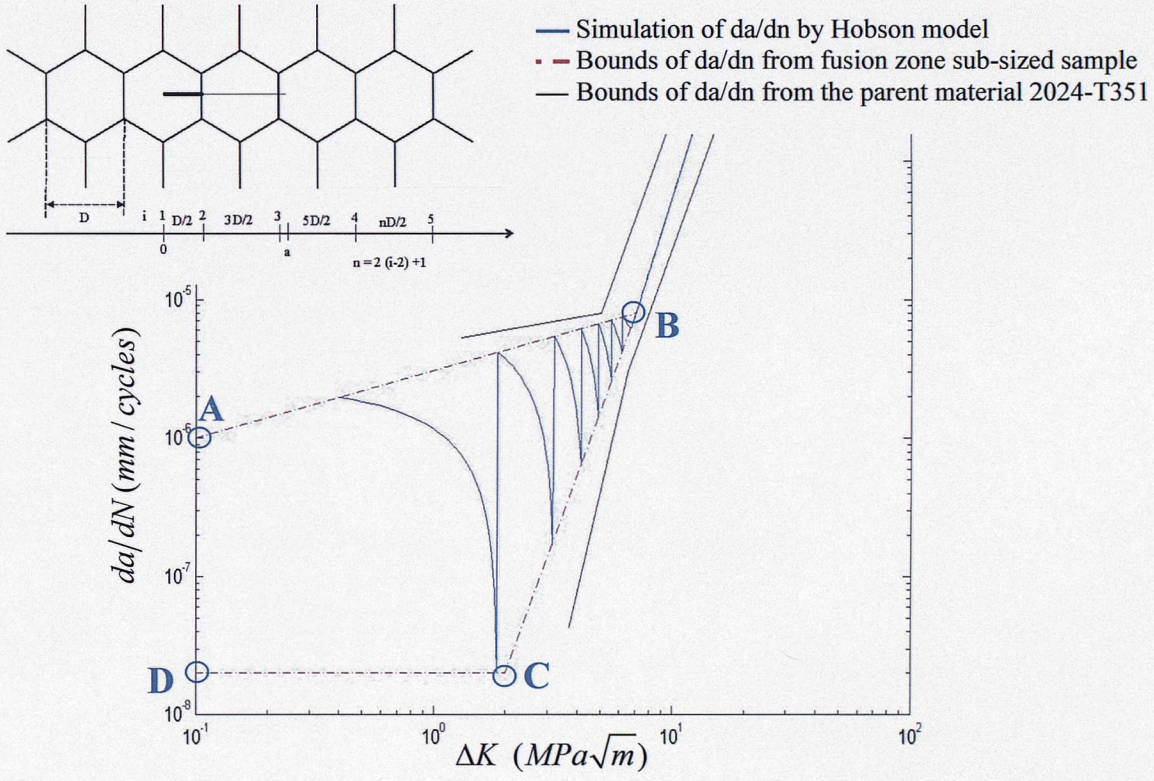

Figure 5.23 Bounds used for short crack growth rate modelling (at a stress level of 270MPa) (Hobson-type model formulation) based on filled VPPA fusion zone sub-sized samples (defined via points A, B, C and D). A schematic illustration of crack and grain structure is also shown, identifying a regular grain boundary spacing, D, and successive growth steps through each grain

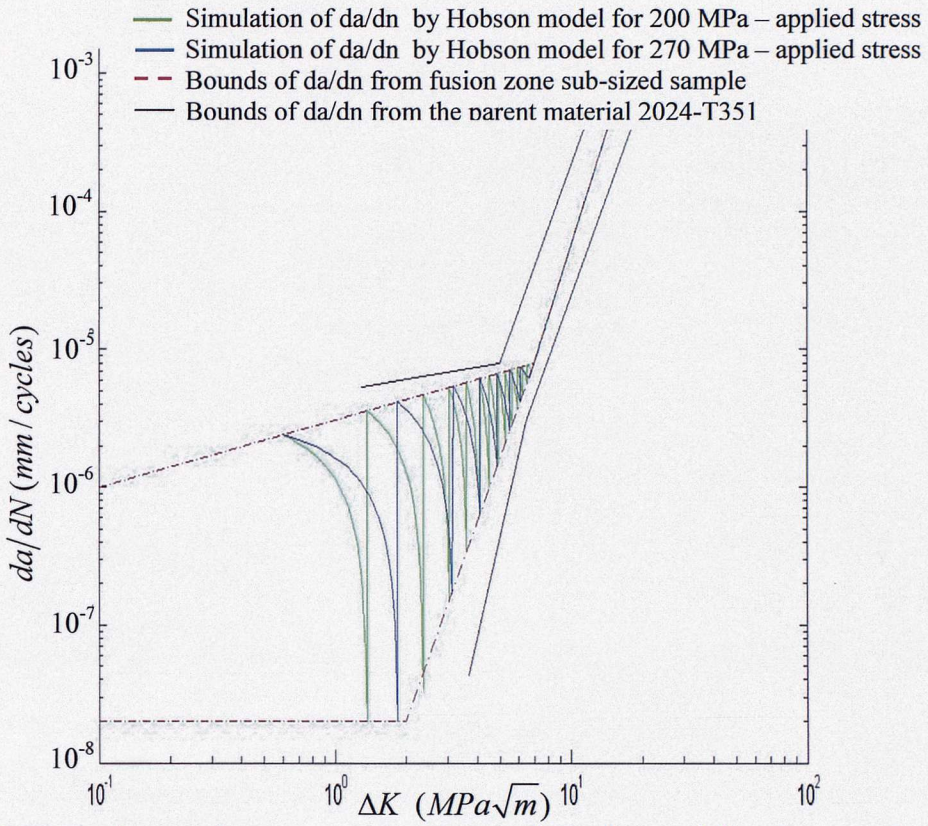

Figure 5.24 Crack growth rate approximation used for the modelling (at stress level of 200MPa and 270MPa) (Hobson-type model formulation) with bounds based on fusion zone sub-sized sample.

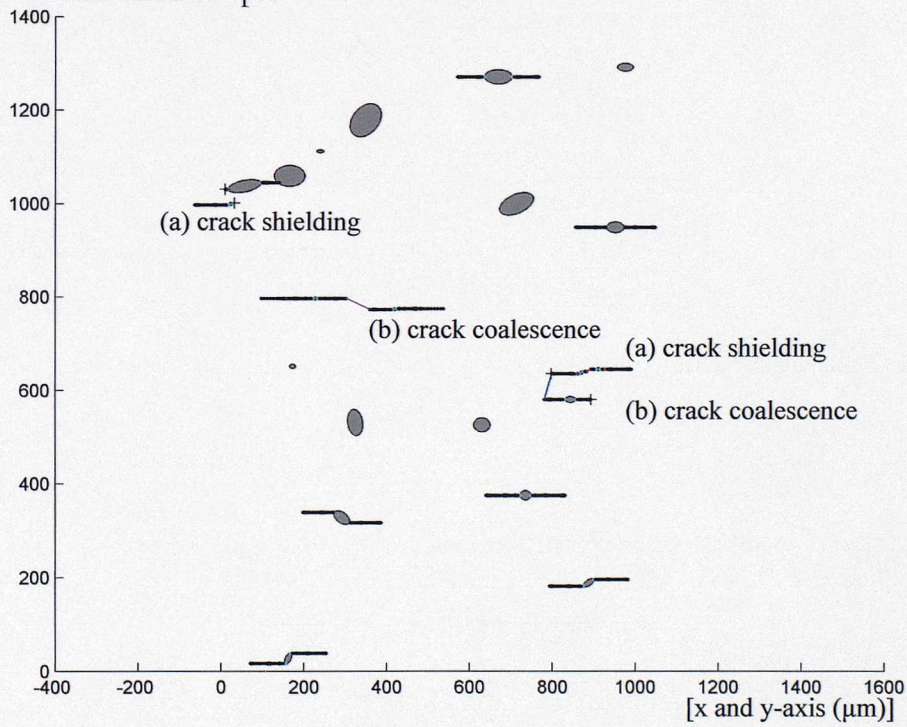

Figure 5.25 Pore distribution with the associated crack initiation and growth for a stress level of 270MPa after 79000 cycles. Crack interaction may be seen at: (a) crack shielding and (b) crack coalescence.

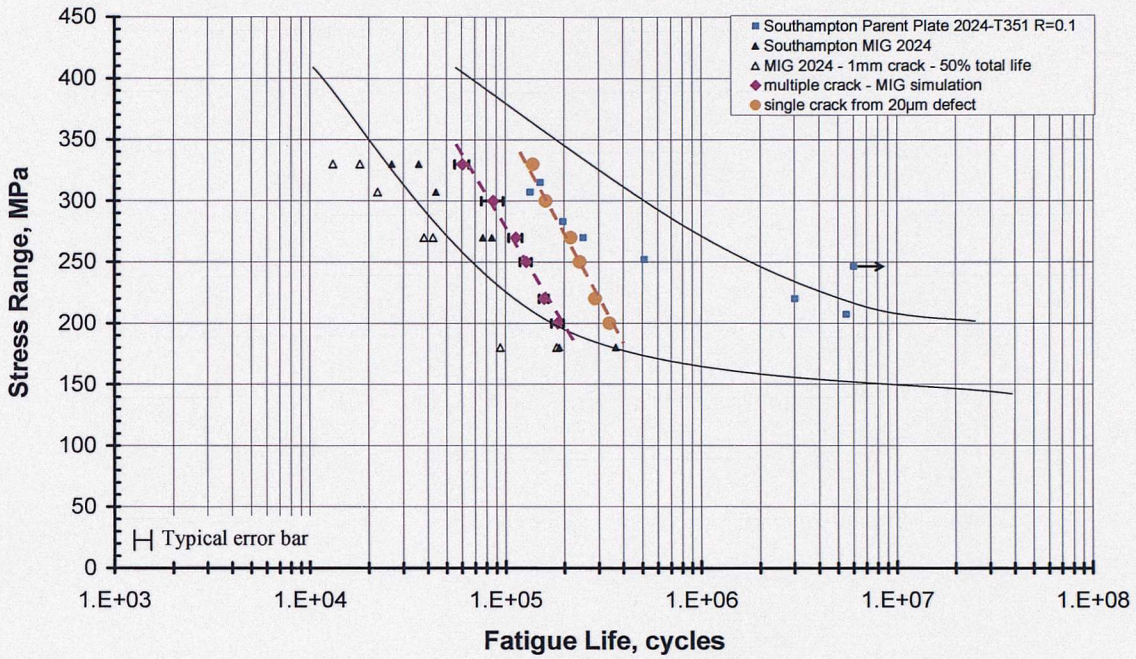

Figure 5.26 Prediction of MIG fusion zone fatigue life based on single crack simulation and MIG Fusion Zone simulation based on ~1.2 x 1.4 mm area micrograph.

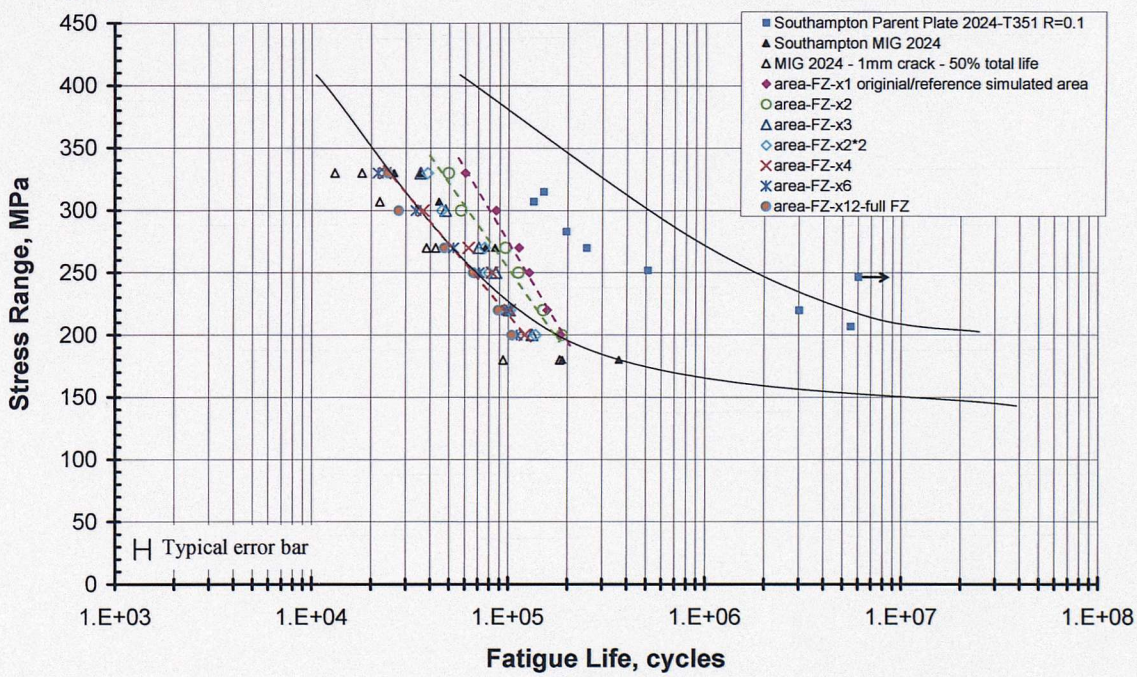

Figure 5.27 Prediction of MIG fusion zone fatigue life for different simulated area sizes: original/reference simulated area (1.2x1.4mm), x2, x3, x4, x6, x12 (fusion zone width), x2*2 (2.4x2.8mm)

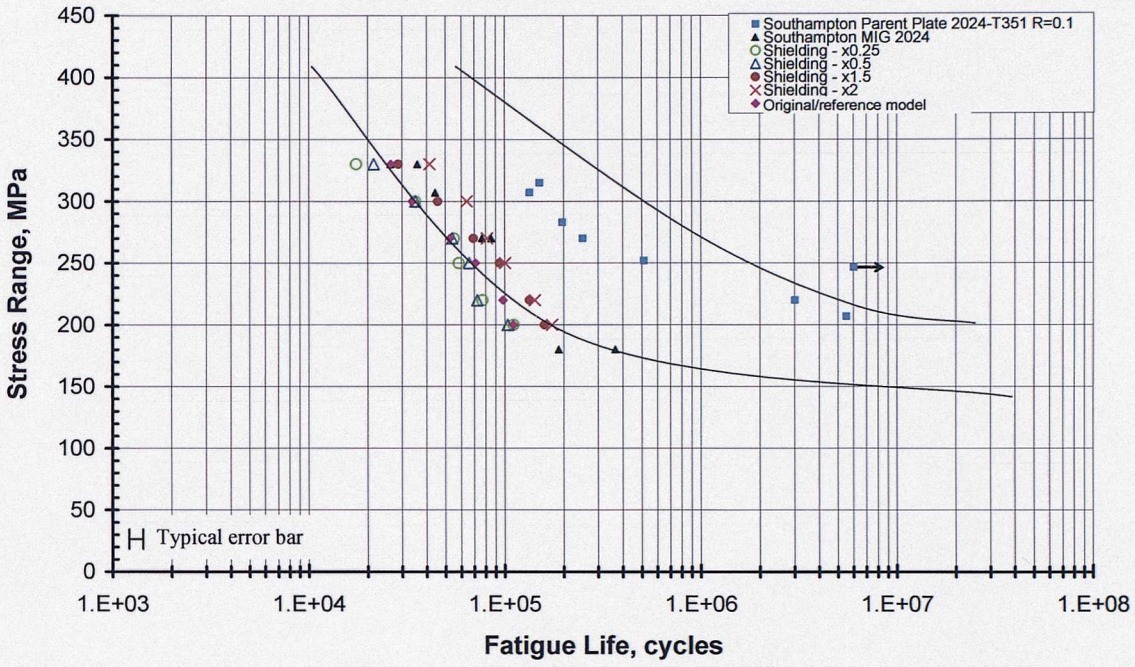

Figure 5.28 Prediction of fatigue life for different shielding area sizes (pore simulated area x6 – half fusion zone)

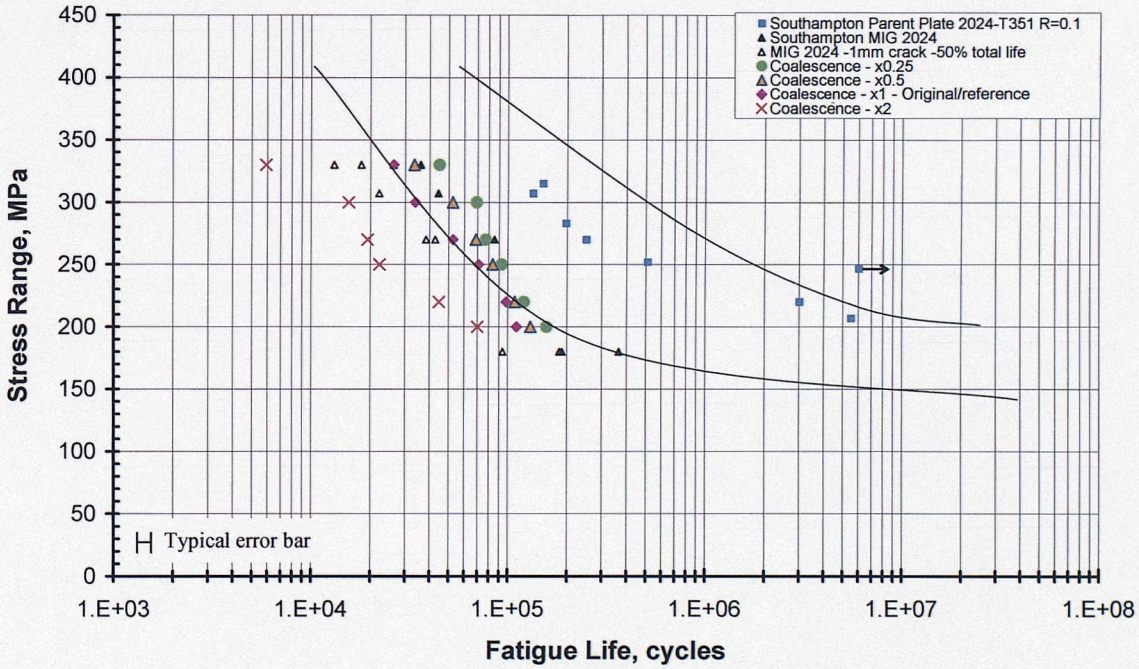

Figure 5.29 Prediction of fatigue life for different coalescence area sizes (pore simulated area x6 – half fusion zone)

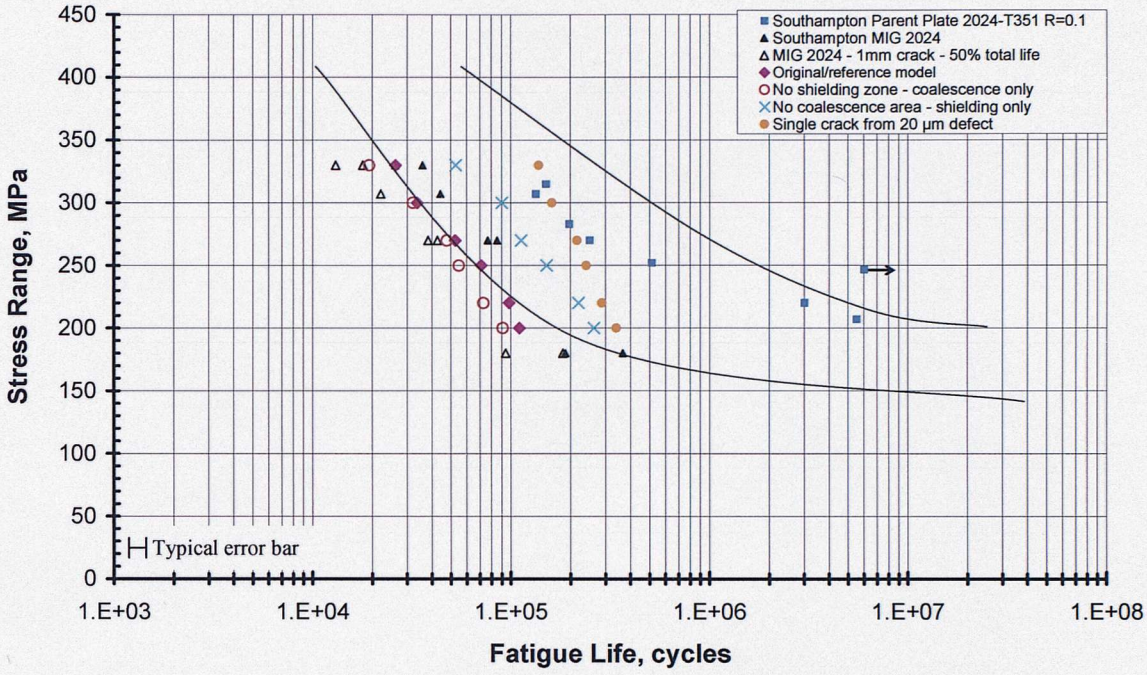

Figure 5.30 Prediction of fatigue life (pore simulated area x6 – half fusion zone) for three simulations: (i) no change, (ii) No shielding area, coalescence only (iii) No coalescence area, shielding only (iv) single crack from 20µm defect

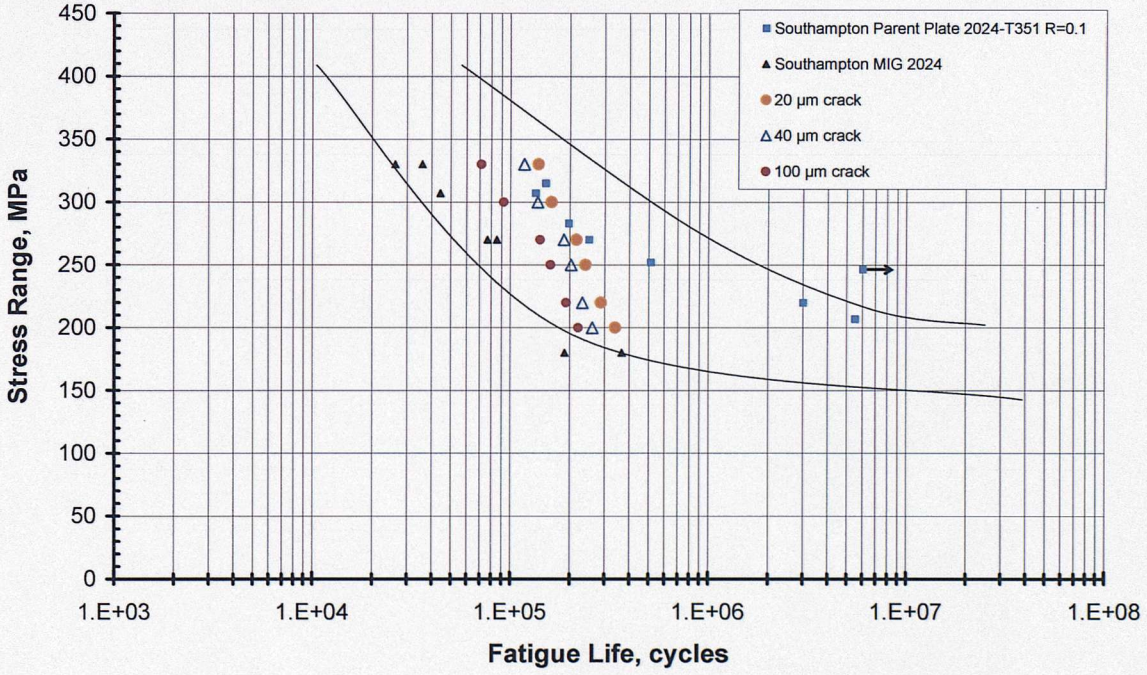

Figure 5.31 Prediction of fatigue life for different single crack lengths (20, 40 and 100µm)

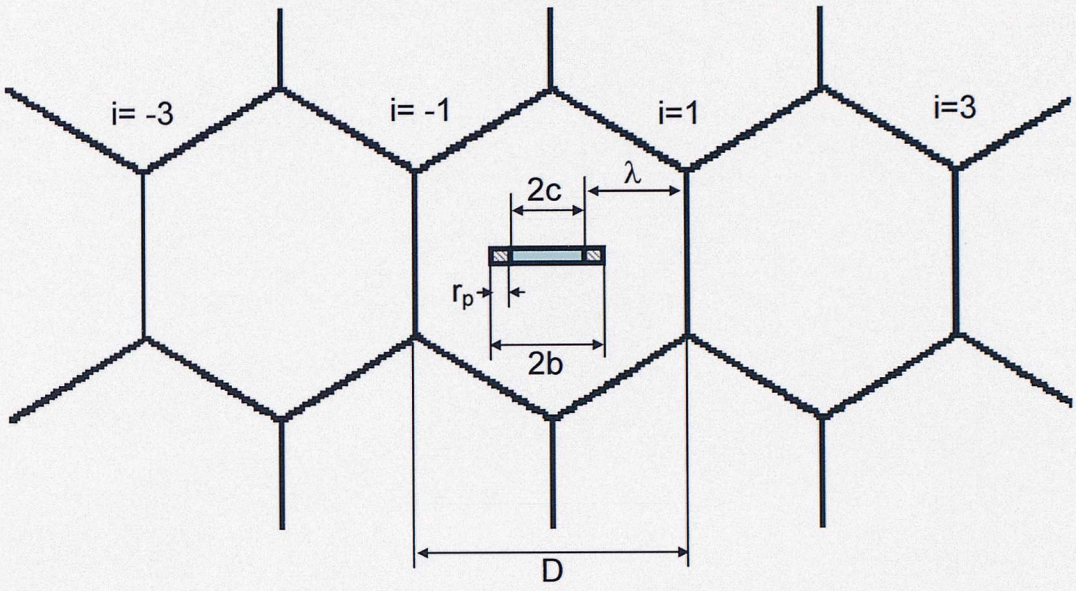

Figure 5.32 Schematic illustration of a crack within a grain and parameters associated with microstructural modelling of short crack growth.

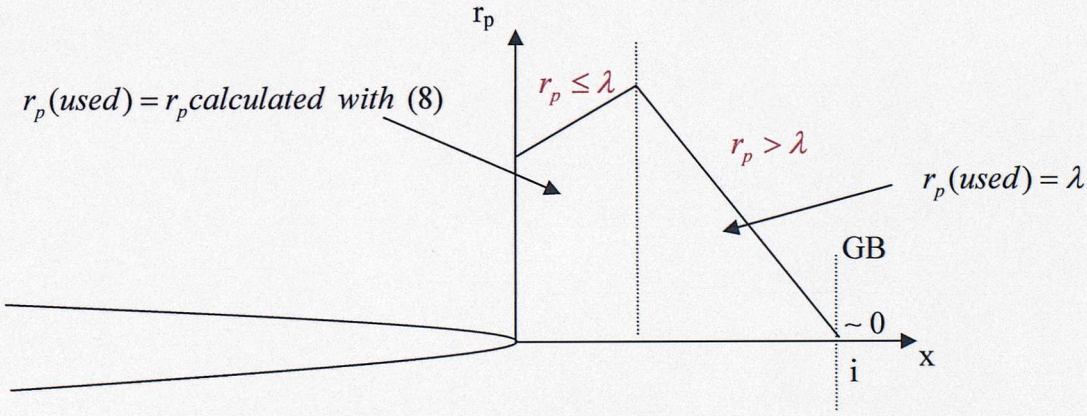

Figure 5.33 Schematic illustration of the plastic zone size as a function of crack tip position (on the x-axis) and relative proximity to a grain boundary (GB)

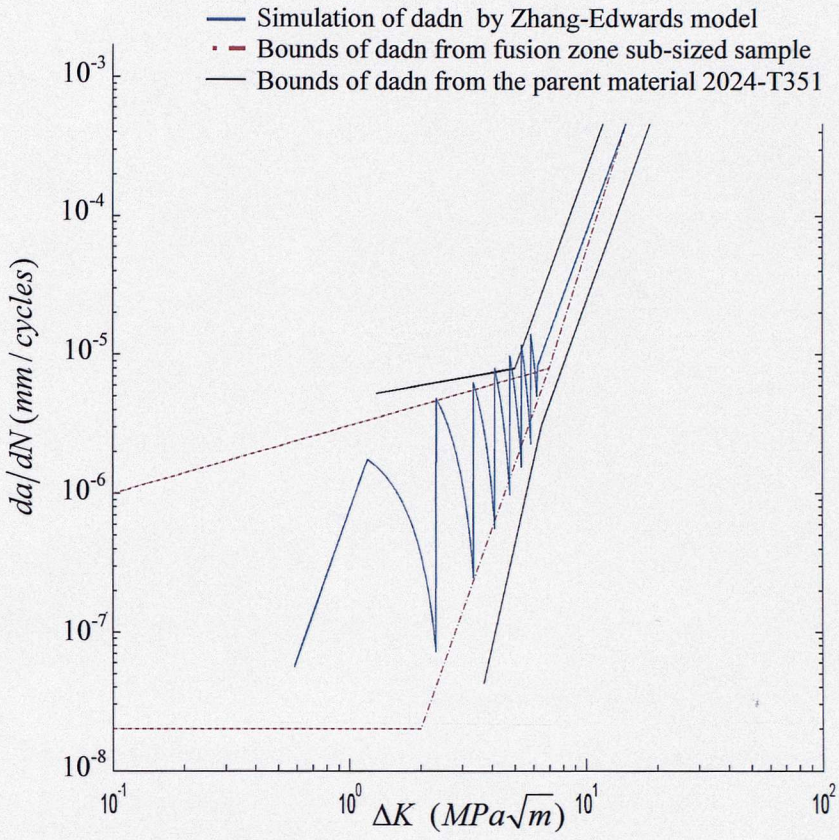

Figure 5.34 Crack growth rate approximation used for the modelling (at stress level of 270MPa) (Zhang and Edwards type formulation) with bounds based on fusion zone sub-sized sample.

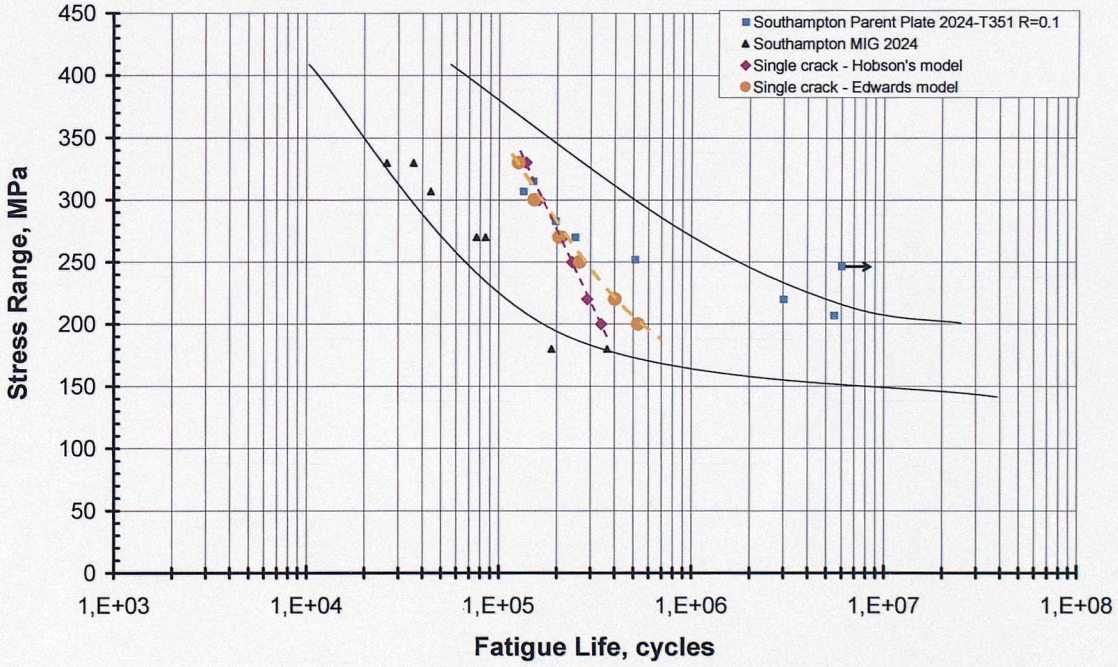

Figure 5.35 Comparison of fatigue life simulations between Hobson model and Edwards model for a single crack from 20μm defect.

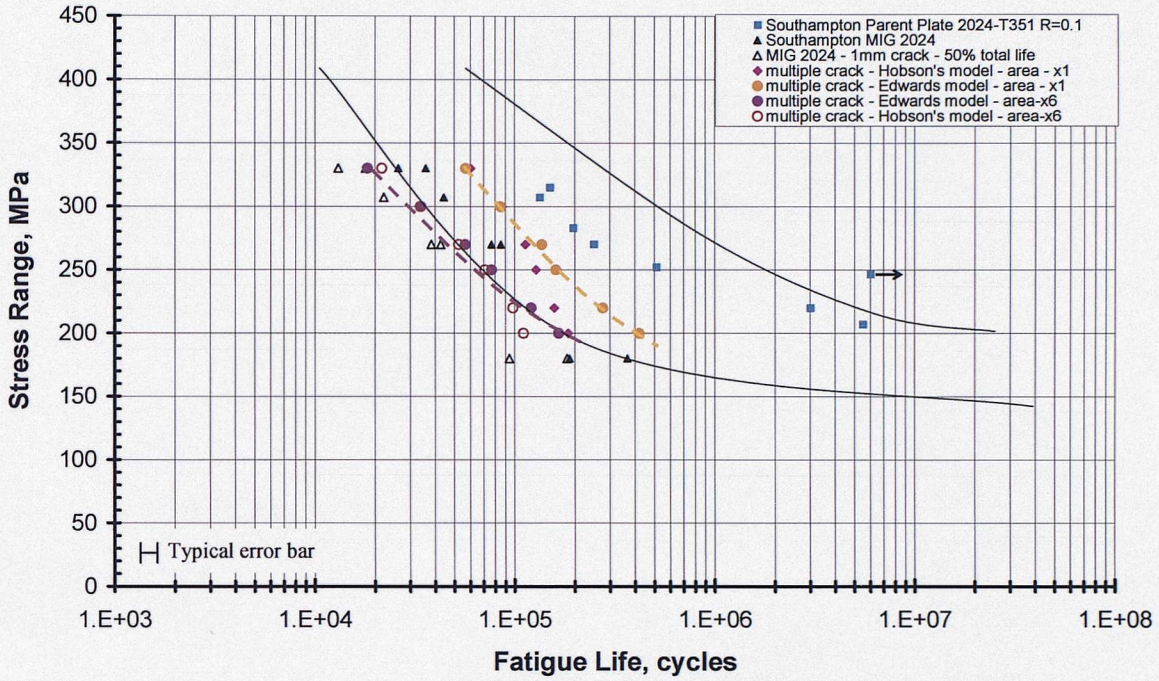

Figure 5.36 Comparison of fatigue lives between Hobson model and Edwards' model for the multiple cracks interaction simulation for two pore simulated areas (the original/reference simulated area (1.2x1.4mm) and the simulated area (x6) representing half fusion zone).

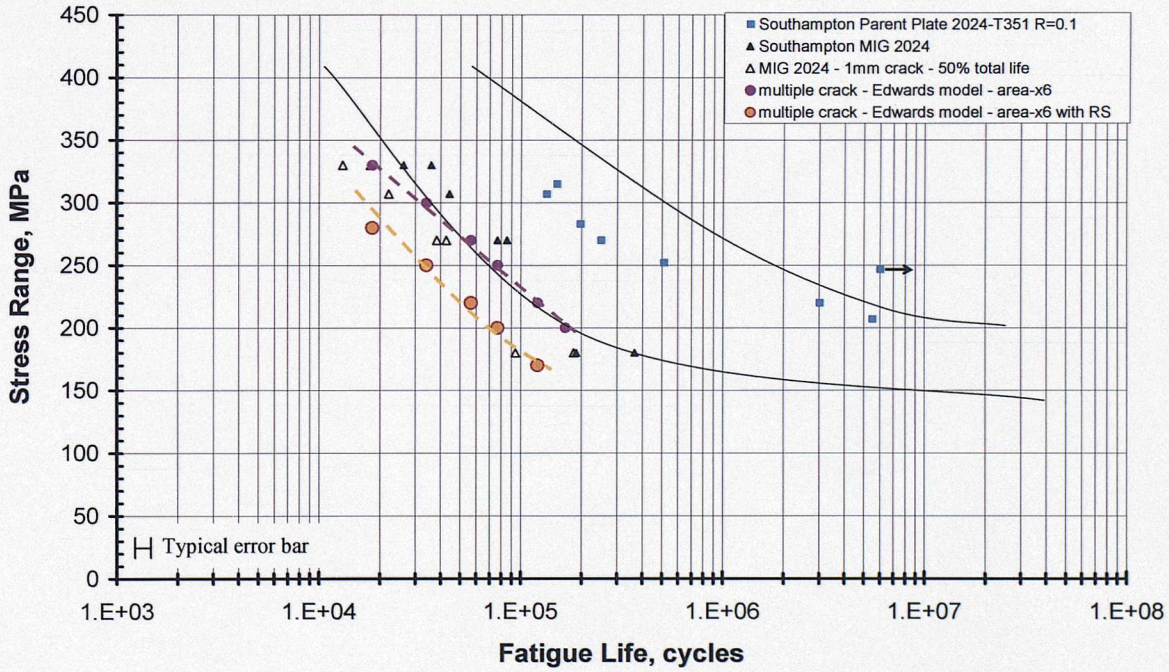

Figure 5.37 Prediction of fatigue life for the multiple cracks interaction simulation including the residual stress effect by simple stress superposition (RS=50MPa) for a simulated area (x6) representing half fusion zone.

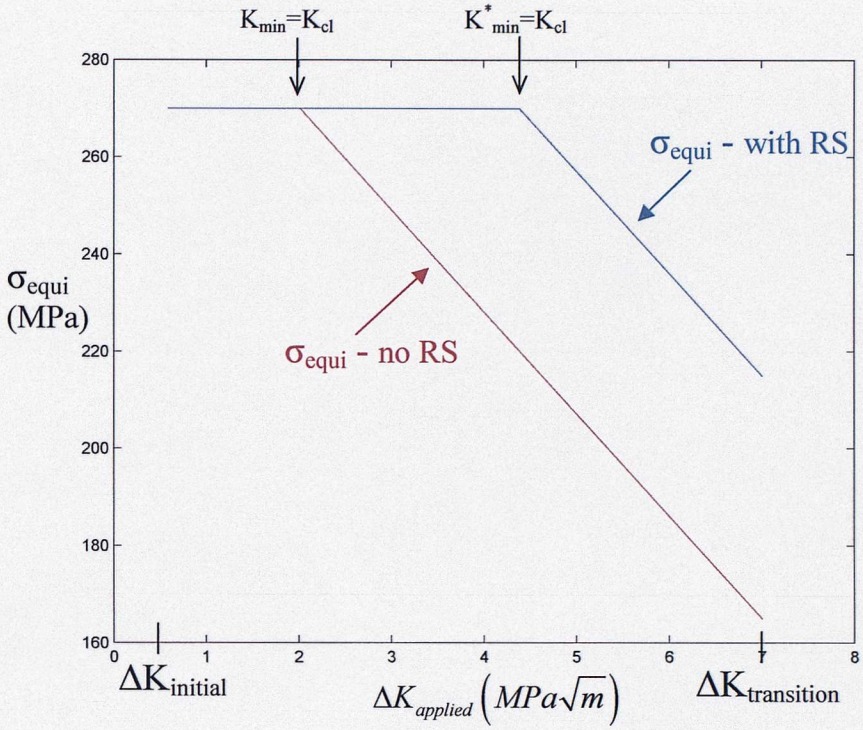

Figure 5.38 Evolution of the stress equivalent considering (a) the closure effect and (b) closure effect and residual stress.

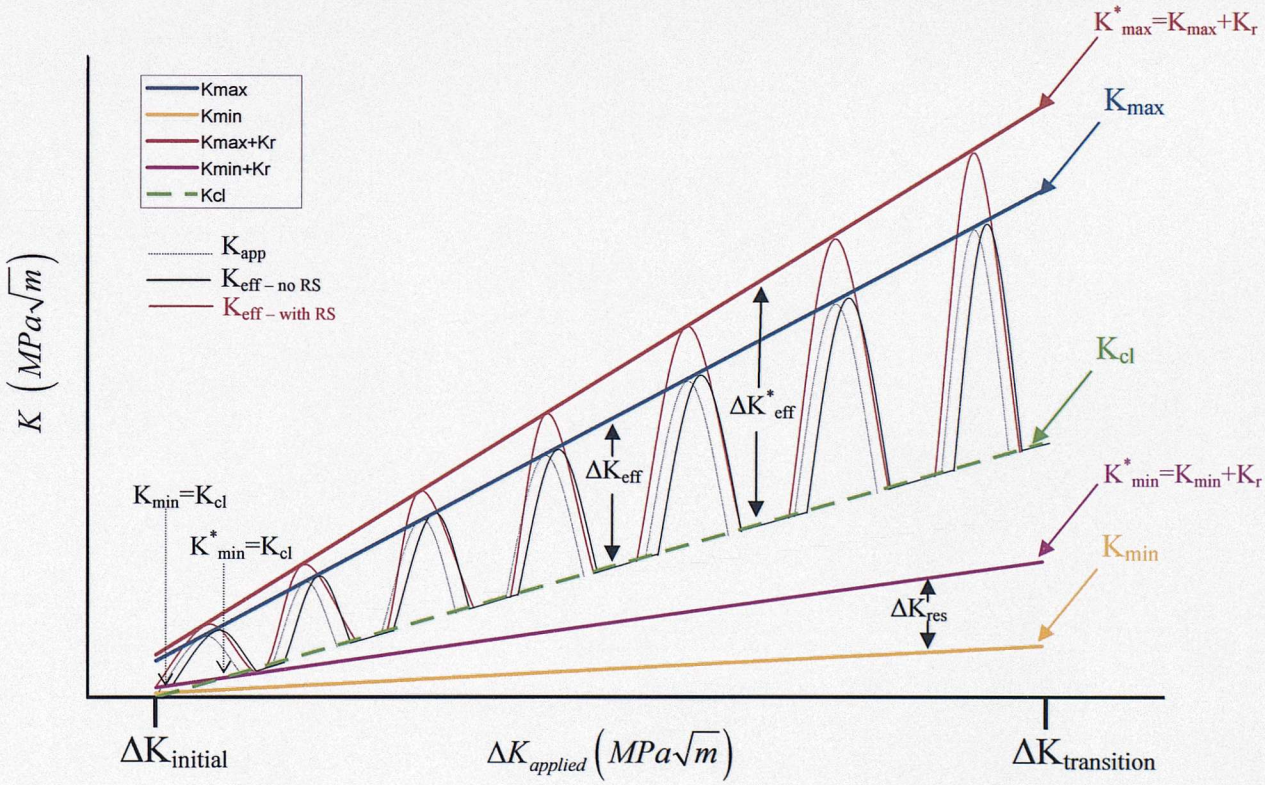

Figure 5.39 Schematic diagram of the stress intensity factor evolution with and without a residual stress field, with closure effects.

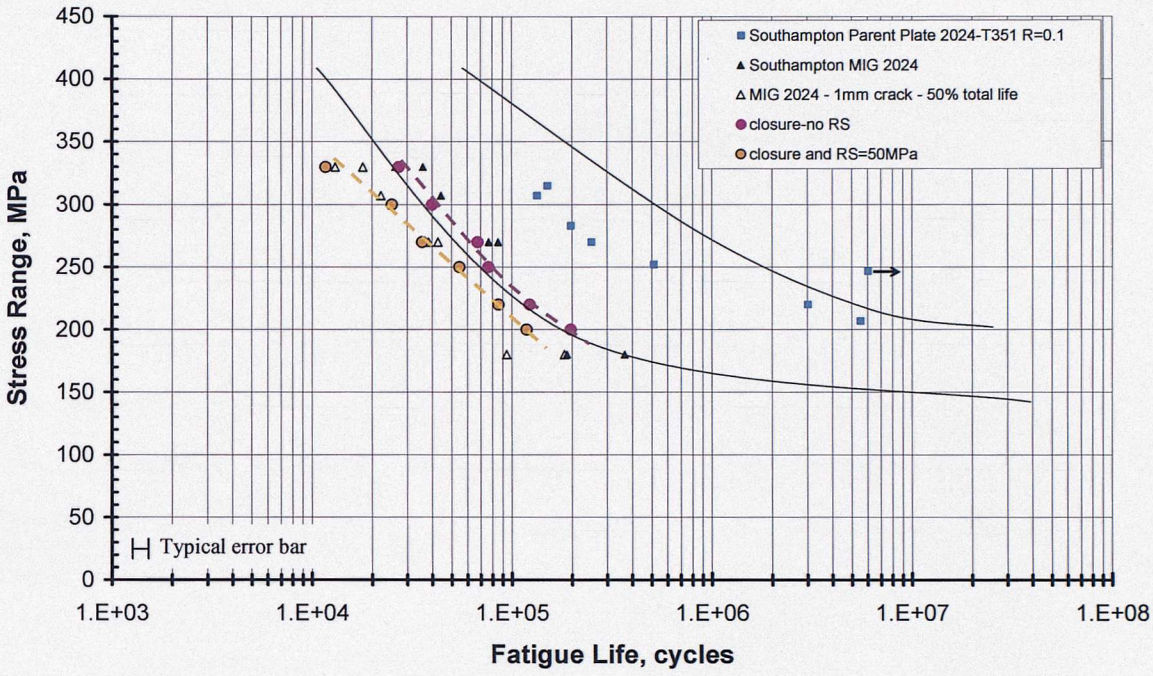

Figure 5.40 Prediction of fatigue life for the multiple cracks interaction simulation including the residual stress effect with closure effect (RS=50MPa) for a simulated area corresponding of half fusion zone (area x6).

Chapter 6

Fatigue behaviour of the filled & autogeneous VPPA welds

6.1 Fatigue life results : S-N curves

As noted in chapter 3, fatigue performance of VPPA welds, in both filled and autogeneous forms, has been tested. Fatigue life results are illustrated in Figure 6.1, along with results for the parent plate tested with the same surface preparation and load geometry. A scatter band of fatigue results for 2024-T351-T4 sheet and plate is also shown, as identified in Chapter 5 (Parry, 2001). Trendlines have been added for the sake of clarity. Whilst material supply severally limited the number of tests of the filled weld in particular, the fatigue performance shown by both welds appears to be similar, with both sets of results falling within a factor of approximately two of the parent data. As such, the fatigue performance of the welds may be seen as relatively good with the two VPPA welds showing only a limited stress penalty over the parent (<50MPa). Figure 6.2 shows S-N curves for the MIG welds, both VPPA welds and parent plate: it may be seen that the VPPA weld process exhibits consistently better behaviour than the MIG. A difference in slope of the weld SN curves may be also noted, with the MIG curve appearing more consistently steeper than the corresponding VPPA and parent plate data.

6.2 Crack initiation

In both VPPA weld samples, crack initiation was identified to occur both within the heat-affected zone and the fusion zone. Both initiation types were seen within a few hundred cycles of loading, however it was clear that the HAZ cracks contributed most significantly to final failure.

- ***Filled welds:***

Figure 6.3(a) and 6.3(b) present optical macrographs of cracks in the heat-affected zone and fusion zone at $N/N_f = 0.4$. In the HAZ (Figure 6.3(a)), two cracks are highlighted with, in particular, the crack being seen to be the largest at final failure marked as the 'main' initiation site, corresponding to a distance of some 18mm from the weld centre. As such main initiation is identifiable with the 'far' HAZ region, close to the outer peak in hardness levels (see Figure 4.20) It may be noticed that the three cracks highlighted in the heat-affected zone and the fusion zone present lengths of the same order (between 70 and 100μm) at 40% of the fatigue life. Figure 6.3(c) shows the crack path evolution after 80% of the life: three coalescence events may be identified, where the main crack has joined with two secondary cracks in the heat affected zone. It is noted that when the main crack achieves 1mm length at ~75% of the fatigue life (in the heat affected zone), cracks seen in the fusion zone exhibit maximum lengths of the order of 300μm.

Having identified where cracks initiate across the weld, it is interesting to clarify the nature of crack initiation sites. Figure 6.4 and Figure 6.5 show SEI and BEI images of crack initiation in the heat-affected zone and fusion zone for the filled VPPA weld. HAZ crack initiation was clearly identified with large intermetallic particles (~20-30μm) in Figure 6.4 (b) where river lines may be seen starting from the particle, as widely reported for conventional parent plate behaviour (Sinclair & Gregson, 1998). In the weld fusion zones, cracks were seen to initiate from interdendritic defects and/or gas porosity although it may be noted that the gas bubble porosity levels were very low in the VPPA welds (see Chapter 4), with the majority of fusion zone cracks clearly coming from interdendritic defects (see Figure 6.5 (a) and (b)). Observations of final fracture surfaces and crack replication show that whilst cracks initiated across the whole weld (heat affected zone and fusion zone), cracks that had initiated in the heat affected zone from intermetallic particles dominated the final failure (consistent with the observations noted above for 75% of life).

- ***Autogeneous welds:***

Similar to the filled welds, crack initiation was seen across all of the weld regions, although overall failure was clearly dominated by growth of HAZ cracks. Figure 6.6 (a) shows the fracture surface of a fatigue sample highlighting the main HAZ crack and the collocation of secondary HAZ and fusion zone initiation sites. The transition between fatigue and final rapid fracture is highlighted in Figure 6.6 (a) by the dashed line on the macrograph. Figure 6.6(b) shows an optical observation at 1000 cycles (less than 1% of fatigue life at a stress level of 270MPa) of HAZ crack initiation from a cracked intermetallic particle. Figure 6.6(c) presents a (BEI) image of the fracture surface at the main HAZ crack site where an intermetallic particle is clearly seen as the initiation site. In the fusion zone, cracks initiate particularly from interdendritic defects, as highlighted in Figure 6.7 by (a) and (b) optical macrographs and (c) BEI micrograph (where interdendritic defects are highlighted by dashed circles). At 75% of the fatigue life, fusion zone cracks are seen to be less than 100μm long, whilst HAZ cracks are of the order of 1mm. Cracks in the heat-affected zone and the fusion zone present lengths between 50 and 100μm at 40% of the fatigue life.

Appreciable multiple crack initiation across the weld/HAZ was particularly noted for the autogeneous VPPA weld (but not as dense as the MIG weld fusion zone, see below). Figure 6.8 presents an optical macrograph of the autogeneous VPPA weld taken in the HAZ where multiple cracks may be seen. To compare both VPPA weld types in terms of crack initiation distribution, the number of initiated cracks located in the HAZ in the region of the main crack (cracks leading to final failure) at a stress level of 307MPa at $N/N_f = 0.7$ was of the order of ~1 crack per mm^2 for the filled weld, whilst the autogeneous weld exhibited crack densities up to ~3 cracks per mm^2. In the MIG fusion zone, crack density was of the order of 8-9 cracks per mm^2 at 270MPa.
A further survey of crack density has been carried out on four of the VPPA autogeneous samples for two different stress levels (270 and 307MPa) at 70% of the fatigue life. For each load, the two samples considered came from different plates (welded under nominally identical conditions) identified here as Plates 1 and 2. Figure 6.9 shows histograms representing crack density values across the welds for the two

stress levels (Plate 1 in Figure 6.9(a) and Plate 2 in Figure 6.9(b)). A complex crack density profile may be identified. In both plates, the pattern is approximately similar for both loading conditions, however the high load case tends to show higher crack densities. Two peaks in crack density may be clearly seen: one in the HAZ and the other in the fusion zone. Considering in the first instance the HAZ region, similar peak crack densities may be seen at 307MPa for both plates (~2.3 cracks per mm^2 for Plate 1 and ~2.8 cracks per mm^2 for Plate 2). The difference in peak densities between plates is more significant at 270MPa (2.3 cracks per mm^2 for Plate 1 compared to 1.4 cracks per mm^2 for Plate 2). Approaching the fusion zone, the crack density drops below 1 crack per mm^2 for both plates and both loading conditions. In the fusion zone, a distinct difference in crack density may be observed between plates. As presented in Section 4.2.1, it may be considered that there are two main parts to the autogeneous weld fusion zone: the centre of the fusion zone, corresponding to an axial columnar dendritic structure, and the edge of the fusion zone, corresponding to a columnar dendritic structure perpendicular to the weld line. For both plates, the crack density is high at the edge of the fusion zone but not to the same levels: Plate 1 has a crack density at the edge of the fusion zone of the order of 2.5 cracks per mm^2 at 307MPa and 1.25 cracks per mm^2 at 270MPa, whilst Plate 2 has a crack density around 5 cracks per mm^2 for both loading conditions. In the middle of the fusion zone, the crack density drops for Plate 1, with a value of 1.2 cracks per mm^2 at 307MPa and 0.3 crack per mm^2 at 270MPa, whilst for Plate 2 the crack density increases to around 5.8 cracks per mm^2 for both loading conditions. Knowing crack density variations appear across the weld, it is clearly of interest to consider possible correlations with strength (via hardness) or residual stress in the welds. The same bar diagrams presented in Figure 6.9 have been plotted again in Figure 6.10 with the superposition of hardness profiles and residual stress traces obtained for equivalent welds before and after the first fatigue load cycle (via Synchrotron X-ray measurements). Starting from the outer edge of the HAZ for both plates, the crack density profile appears to closely follow the residual stress pattern, with the peak in crack density corresponding to the tensile peak in residual stress after loading. From this tensile peak, the residual stress drops to around zero: at this position the crack density is low and the material is very soft/overaged (see

the hardness trace). The minimum of crack density is however seen to coincide with the narrow residual tensile stress and hardness peak close to the fusion zone interface. In the fusion zone, as explained previously, the crack density profile varies depending on which plate is considered, however it may be seen that there is a high crack density at the edge of the fusion zone for both plates and both loading conditions. No residual stress data are available within the fusion zone.

For both filled and autogeneous VPPA welds, whilst the crack densities in the HAZ are different (higher crack density for the autogeneous weld), limited differences are evident in fatigue lives, as presented in section 6.1. No reliable residual stress data for the filled VPPA welds are however available to allow a full comparison between filled and autogeneous welds. It may be noted the crack density in the HAZ at the tensile residual stress peak in the autogeneous welds is consistent with a simple stress contribution to crack initiation (El-Soudani & Pelloux, 1975). Just outside the fusion zone however, crack density was seen to be very low at a location where residual stress and hardness profiles present a peak. As such it may be seen that crack density levels in the HAZ are not singly linked to residual stress or hardness levels, suggesting a combined influence of both stress and microstructure on initiation behaviour. In the region immediately adjacent to the fusion zone grain boundary decoration and intragranular precipitates are in fact identifiable which may be seen as potential microstructural contributions to crack formation. Here it may be interesting to consider alternative potential crack initiation processes, where firstly cracks may be considered to initiate in an essentially static manner in the first load cycle, or, secondly, initiate in an essentially cyclic manner, after the first load cycle and associated relaxation of residual stresses. In terms of static cracking processes, two interactions with residual stress condition may be identified: (a) initial residual stresses provide a simple additional driving force for cracking, and/or (b) plastic strains associated with relaxation of residual stresses provide a driving force for cracking. It has however already been identified that the present crack densities do not follow either of the residual stress patterns on Figure 6.10 (i.e. those before and after first loading) in a simple manner. Based on the location of greatest stress relaxation in the first load cycle it may be estimated that the region of most plastic deformation in the HAZ occurs

around +/-12mm from the weld centre line (consistent with this being the softest part of the HAZ), which again shows no simple relationship with the crack density patterns. As such, a combination of influences on crack initiation again seems likely. Considering residual stress and hardness/ageing effects together, a simple qualitative description of crack behaviour may be identified as follows: moving towards the weld centreline from the far HAZ, crack densities peak under the particular influence of the (post-initial loading) residual stress in a region where parent material is essentially overaged (between 10 and 25mm from the centreline). Between 10 and 6mm from the weld centreline residual stress levels are again high, however, the increased damage tolerance of the locally reverted microstructure (i.e. essentially underaged/zone strengthened) and associated strength increase limits initiation. Within the fusion zone cracks densities rise again due to the change in defect density and the presence of a re-cast structure.

Overall it may be seen that a variety of interactions may exist across the VPPA welds in terms of crack initiation with more detailed separation of HAZ thermal history and residual stress states clearly being of interest for example. It is clear however that, contrary to the MIG welds, overall failure is not strongly influenced by multiple crack initiation phenomena, with the propagation of reasonably isolated defects in the far HAZ region (far from the fusion zone interface) controlling fatigue performance, at least for the simple tests conditions of interest here.

In the fusion zone for both VPPA welds types, it has been observed that crack initiation mainly occurs from interdendritic defects. For the autogeneous VPPA welds exhibiting variable crack densities in the fusion zone, it is clearly interesting to consider original defect density in the fusion zone of the two plates. In the first instance, densities have been measured without considering defect sizes. The Plate 2 fusion zone has been measured to have ~30% more defects overall than the Plate 1 fusion zone: in the centre of the fusion zone (where the weld has an axial dendritic structure). The defect density increase is of the order of 50%. Such differences are of course qualitatively consistent with the higher crack densities identified in the fusion zone of

Plate 2 (especially in the centre of the fusion zone) but do not offer a simple quantitative explanation for plate differences.

A further potential factor in the variability of autogeneous VPPA weld behaviour may be seen in the coarse grain 'bundles' making up the fusion zone centre, see Figure 6.11 (the EBSD orientation maps for Plate 1 and 2) and Chapter 4. As such variations in initiation behaviour from one sample to another may be linked to favourable or adverse dendrite and/or crystal orientation conditions in the peak stress region of a given test sample. Such an effect may be expected to contribute to sample-to-sample variations from any one weld rather than the consistent effect that is seen between the two Plate 1 samples and two Plate 2 samples, however a coincidental correlation with weld plate number cannot be ruled out.

6.3 Crack propagation

In terms of crack propagation, growth rate data for the filled VPPA weld samples are shown in Figure 6.12 for: (a) cracks initiated in the HAZ where the main crack (crack dominating failure) is located, and (b) cracks initiated in the fusion zone. The crack lengths are considered up to or equal to 1mm. In the first instance it may be seen that the cracks initiated in the HAZ show reasonably conventional short crack behaviour, with a broad scatter band of data. In the fusion zone it may also be seen that there is scatter in crack growth rates, with average growth rates for the fusion zone cracks being found to be significantly lower than those for the HAZ cracks, i.e. fusion zone initiated cracks have a negligible influence on final failure in the VPPA samples.

The autogeneous VPPA weld data also exhibits scatter in crack growth rates, as shown in Figure 6.13 (a) and (b). Figure 6.13 (a) represents HAZ growth rates for cracks located in the region where the main crack (crack dominating failure) is located. Scatter may be seen and corresponding trendlines may be defined. In the fusion zone, crack growth rate data have been plotted for Plate 1 and Plate 2 tests. Scatter is again evident and no significant difference may be observed in the crack growth rates for the two plates. Whilst crack density and microstructure in the fusion zone may indeed be

slightly different for the different autogeneous VPPA welds, this variability does not appear to significantly affect growth rate bounds.

Figure 6.14 (a) presents crack growth rate trendlines plotted for both VPPA welds for cracks formed in the HAZ (i.e. in the region leading to final failure) in relation to the parent plate 2024 results. In the overall trends, limited differences may be identified in the data of the three materials, however it may be noticed that at higher stress intensity factor ranges, the upper bound of the crack growth rate band is slightly greater for both VPPA welds compared to the parent plate material. It may be noted that tensile residual stress would be expected to have more effect at greater crack lengths as cracks must tend towards long crack growth conditions for closure to be important. At this location in the HAZ, the VPPA autogeneous presents a (relaxed) tensile residual stress of ~100MPa which may then be expected to accelerate crack propagation. Such behaviour is considered further in Section 6.4.

Figure 6.14 (b) presents fusion zone crack growth rate trendlines plotted for three different welds: the filled VPPA weld, the autogeneous VPPA weld and the MIG weld. Compared to the HAZ crack propagation behaviour, the fusion zones clearly present significant differences in growth rates. The upper bound of the MIG fusion zone crack growth may be particularly identified as higher than those for the VPPA fusion zones. In terms of comparison of the two VPPA fusion zone types (i.e. filled and autogeneous), crack growth rates are similar at high stress intensity factor ranges but at low stress intensity factor ranges the VPPA autogeneous crack growth rates seem higher. Various factors may be identified with these growth rate differences: in particular the crack density which may cause early coalescence events and hence higher growth rates (especially for the MIG weld where high upper bound rates have been identified previously), along with differences in microstructure and residual stresses between the three weld types. In terms of grain structure, it has been seen (see Chapter 4), that the MIG weld has a fairly uniform and equiaxed grain structure with grain size of the order of 50 to 100μm for at least 80% of the fusion zone width, whilst the filled VPPA welds presents a predominantly equiaxed grain structure with a gradual decrease in grain size from the centre towards the edge going from approximately 60 to 30μm. The autogeneous weld exhibits a relative coarse columnar structure although the actual

high angle grain boundary separation distances within the axial columnar central region of the welds clearly becomes very small where the narrow "bundles" of twin-related grains exist (boundary separation distances of 20-40μm). Furthermore differences in fusion zone materials compositions exist, with the filled welds clearly being influenced by the use of a high Cu content wire. Overall it may be seen that, a range of microstructural and micromechanical factors may influence growth rate characteristics within the different fusion zones. The obvious incidence of crack-crack interactions in the MIG fusion zone may of course be identified with the wider scatter band of the corresponding growth rate data. In the absence of comparable residual stress data it is difficult to separate other contributions to the growth rate data in Figure 6.14: indirect evidence of residual effects is considered further in the following section.

6.4 Modelling

6.4.1 Sub-size samples:

As presented in chapter 3, fatigue tests were carried out on small scale ("or sub-sized") samples with a view to characterise intrinsic properties of individual regions of the welds in samples that are essentially residual stress free due to being cut to a scale smaller than the wave-length of the stress variations in the weld. The study has been carried out on filled VPPA weld.

From the hardness profile and locations of crack initiation of the filled VPPA welds, two fatigue tests were carried out: (i) from samples located in the fusion zone and (ii) from samples located in the HAZ where the main cracks where initiated (see Figure 6.15). Figure 6.16 illustrates the short crack growth rates obtained for the VPPA fusion zone sample, where reasonably distinct single crack growth behaviour could be monitored within a dendritic microstructure. From the experimental crack propagation data, crack growth rate bounds may be defined. As noted previously in Chapter 5, growth rate bounds for the residual stress-free fusion zone material actually appear quite similar to those for the parent plate. It is significant to note that growth rate bounds in Figure 6.16 are distinctly increased over corresponding results for the *in-situ* fusion zone material (i.e. as part of the weld coupons, illustrated by the dashed lines in Figure 6.14). Figure 6.17 shows the short crack growth rates obtained in the small scale

HAZ samples. The growth data are within the bounds defined by the crack growth trendlines of the filled VPPA welds or parent plate 2024, i.e. microstructural effects on short crack growth rate bounds appear to be limited.

As noted earlier, the data obtained experimentally from the fusion zone (Figure 6.16) has been used as an estimate of individual short crack behaviour in the MIG fusion zone on the basis of being a similar microstructure to that in the MIG (i.e. being a re-cast structure with the same filler wire). The corresponding bounds are then used to estimate the bounds of the Hobson-growth rate model and the material constants used in the microstructure sensitive model (Zhang and Edwards model). On the premise that HAZ microstructural conditions in the two VPPA welds will be reasonably similar for the same general region of the HAZ hardness trendline (specifically, the overaged region, just within the outer HAZ hardness peak), it may be seen that, with the availability of residual stress data for this region of the autogeneous VPPA, then the growth rate bounds identified in Figure 6.17 may be used in the modelling framework of Chapter 5 to predict fatigue life in the autogeneous VPPA welds.

6.4.2 Modelling

In chapter 5, modelling has been developed to predict fatigue life of the MIG weld based on multiple crack interactions and defect population. The multiple crack initiations coming from interdendritic defects seen in the MIG fusion zone may be linked to the multiple crack initiation coming from intermetallic particles seen in the autogeneous VPPA weld heat affected zones. So in this context, a new model has been considered by simulating intermetallic particles as defects of 20μm in size.

In first instance, the crack growth prediction model had to be modified with new material parameters. The average grain size in the HAZ has been defined experimentally by EBSD mapping as being of the order of 100μm and yield strength are scaled in direct proportion with hardness levels. The material constants C and m have been modified to allow the predicted da/dN data to fit with the experimental crack growth data of the parent material. It has been chosen to use the parent material crack growth data because it has been seen that the sub-size samples of the VPPA

filled weld for the HAZ locations presented crack growth rates approximately similar to the parent plate results (see Figure 6.17). Figure 6.18 illustrates the da/dN behaviour used in the simulation at a stress level of 270MPa without closure effect and residual stress influence. C and m are respectively 10^{-7} and 2.3. When the closure approach (section 5.4.2) is included in the model to take into account the residual stress influence, the material parameters become $5x10^{-7}$ and 2.2 for C and m respectively. In chapter 4, the residual stress profile of the VPPA autogeneous welds has been presented. It may be said that a tensile residual stress of the order of 100MPa exists in the HAZ region where the main crack grows. As such the influence of this tensile residual stress has been added into the calculation of the crack propagation prediction using the closure approach.

Having the growth rate prediction data for different stress levels with closure effects and considering the presence or the absence of residual stress, two fatigue life prediction models may be considered; one with a notional single crack growing from a pre-defined 20μm which could be defined as a single crack coming from intermetallic particle growing in the heat-affected zone (filled VPPA behaviour) and another one with multiple cracks growing from an intermetallic particles population with a probability of random initiation of the order of 2.5 cracks/mm^2 as found in the HAZ of the VPPA autogeneous weld (i.e. the second model uses the crack-crack interaction approach developed in Chapter 5). As presented for the MIG modelling, it has been assumed cracks only initiate at the start (in the first cycle) of the fatigue simulation. A total crack length of 1mm has been simulated. In the overall VPPA weld fatigue results, achieving 1mm crack length or a 1mm coalesced group of cracks was seen to correspond to a fatigue life of approximately 75% of the total fatigue life of the welds.

Figure 6.19 presents the life prediction of a single crack without and with the tensile residual stress influence. The real total fatigue life results are plotted on this macrograph including the 1mm crack length at 75% of the total life. It may be noted that the single crack simulation without residual stress influence provides an over-estimate of life in the VPPA welds whilst the predictions considering the residual stress influence give reasonable estimates of fatigue life. Considering the multiple crack initiation in the HAZ for the VPPA welds, Figure 6.20 shows the fatigue life prediction

for multiple cracking with and without residual stress influence. Without the residual stress influence, it may be noticed an over-estimate of the simulated results at high stress level; at low stress level the results are conservative. Considering the residual stress influence, the results show an accelerative effect and appear to estimate reasonably well the VPPA results at high stress level, with conservative estimates seen at low stress level. In keeping with the low crack density of the conditions simulated, it may be seen that predicted multiple-crack interaction effects are actually quite limited (comparing Figure 6.19 & 6.20).

6.4.3 Competition between fusion zone and heat affected zone failure processes:

In the absence of a fully comparable set of synchrotron residual stress measurements for all welds an element of uncertainty must remain in comparing all weld performances. However a number of points may be identified:

In terms of fusion zone behaviour, it is clear that there are important differences between the VPPA and MIG welds (viz, primary failure arising from the fusion zone in the MIG welds, as opposed to the HAZ in the VPPA welds). In Chapter 5, modelling suggested that fatigue performance in the fusion zone region of the MIG welds could be rationalised in terms of multiple crack interactions (particularly crack coalescence), critical initiation defect size, and residual stresses (reducing crack closure effects). Given the measured residual stress levels for the HAZ of the MIG welds are lower than those of the autogeneous VPPA, it may be seen that fatigue life to 1mm crack length for the HAZ region of the MIG should indeed be longer than for the MIG fusion zone failure as such HAZ life predictions for the autogeneous VPPA weld are longer than those of the MIG fusion zone (assuming that the residual stress-free crack growth characteristics for the MIG HAZ are essentially comparable to those of the autogeneous VPPA HAZ, which clearly represents a degree of simplification).

In the VPPA welds fusion zone crack initiation densities were significantly lower than in the MIG case, reducing/limiting multi-crack interactions. In terms of crack initiation density it may be particularly identified that (a) gas bubble densities are considerably lower in the VPPA welds (by a factor of more than 10), and (b) interdendritic defects

are consistently smaller in the VPPA case. In terms of the interdendritic defects (the most critical in the MIG welds), assessment in relation to Figure 5.5 shows that typical VPPA interdendritic defect size fall somewhat below the peak initiating defect size in the MIG welds (VPPA interdendritic defect areas predominantly falling below $50\mu m^2$), consistent with the difference between the weld types.

In terms of crack growth in the VPPA weld fusion zone, it is interesting to consider the model predictions of Chapter 5 (Figure 5.37) for single crack growth from a 20μm defect with no residual stress. Whilst fusion zone residual stresses are not available for the VPPA welds, results shown in Figure 6.10 for the autogeneous VPPA show a value of less than 20MPa at the fusion zone/HAZ interface after initial loading. Examining the residual stress trends in the MIG welds in Figure 4.11 and extrapolating similar behaviour to the VPPA welds, relatively low fusion zone residual stresses may be anticipated. It may also be noted from the Section 6.4.1 where growth rate bounds of the filled VPPA fusion zone were lower compared to growth rate bounds of sub-size fusion zone samples that residual stresses in the fusion zone of the filled VPPA weld are likely to be in compression. Assuming an effective zero fusion zone residual stress, then the fatigue life results plotted in Figure 5.35 represent an approximate fusion zone life prediction for the VPPA fusion zone (at least for the filled weld microstructure), which is seen to be longer than the HAZ life prediction in Figure 6.20. Key assumptions in this comparison are: (a) using the filled VPPA stress-free growth rate trends, and (b) estimating residual stresses within the fusion zone from results just outside the fusion zone/HAZ interface: within these limitations it may still be seen that the critical failure locations of the two weld types are broadly consistent with the present modelling results. In both welds, crack propagation is clearly the main controlling factor in the present fatigue test conditions, with the combination of fusion zone defects and HAZ residual stresses appearing to provide the critical balance in determining primary failure locations.

6.5 Conclusion

2024-T351-based material was studied in conjunction with two VPPA weld types: filled and autogeneous. Fatigue tests were carried out on both welds and similar fatigue performances were observed within the range bounded by the literature. In both fatigue weld samples, crack initiations were identified to occur early in life, within the heat-affected zone and fusion zone however it has been identified that the HAZ cracks lead to the final failure. In the heat-affected zone, cracks initiate from intermetallic particles. In the fusion zone, cracks initiate from interdendritic defects. Larger crack density has been observed in the fatigue samples of the autogeneous weld compared to the filled weld. It has been identified that a combination of residual stress profile, microstructural aspect and strength of the material may control the crack initiation. In the fusion zone, defect population (that is to say the defect density or defect shape), may also be a factor influencing crack initiation. Variability in crack density has been observed in different autogeneous welded plates. In terms of fatigue crack propagation, similar crack growth rates in the HAZ may be seen for both welds. Sub-size fatigue samples have been used to estimate material fatigue behaviour in residual stress free conditions. Using the principles developed for the MIG weld, fatigue life prediction for the VPPA weld has been made considering the intermetallic particles as crack initiators and changing the material parameters. The results show relatively good fatigue life prediction, highlighting a transition to residual stress control of weld performance when fusion zone defect densities are low.

References

El-Soudani, S. M. and R. M. Pelloux (1975). "Anisotropy of fatigue crack propagation in aluminium alloy butt welded joints." Welding Journal: 144s-153s.

Parry, M. R. (2001). Private communication, Plain specimen S-N data for 2024-T3-T4 Aluminium alloy, Airbus, Filton, UK.

Sinclair, I. and P. J. Gregson (1998). Microstructural Control of Fatigue in High Strength Al-alloys. The 6th International Conference on Aluminium Alloys, ICCA-6, Toyohashi, Japan, The Japan Institute of Light Metals, 4, 2091-2104.

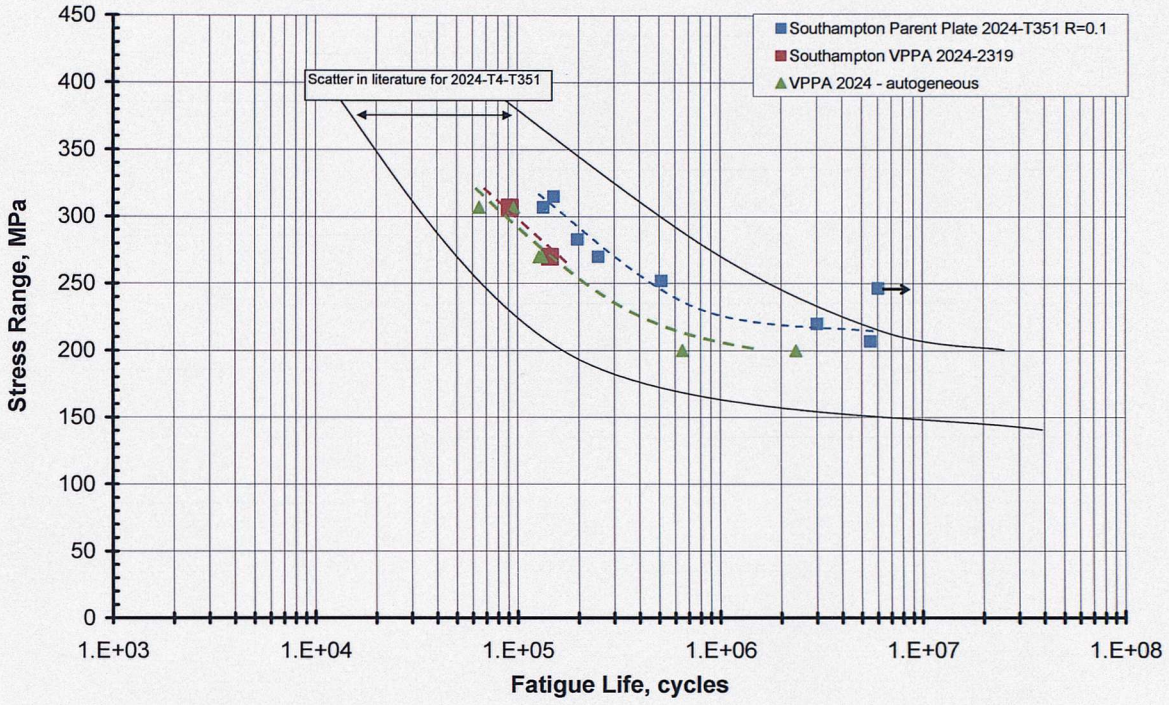

Figure 6.1 SN-curves, Fatigue life versus stress range for the 2024 parent plate and both VPPA welds filled and autogeneous. Lines indicate scatter band for a variety of sources on 2024-T4-T351 plate and sheet at R=0.1.

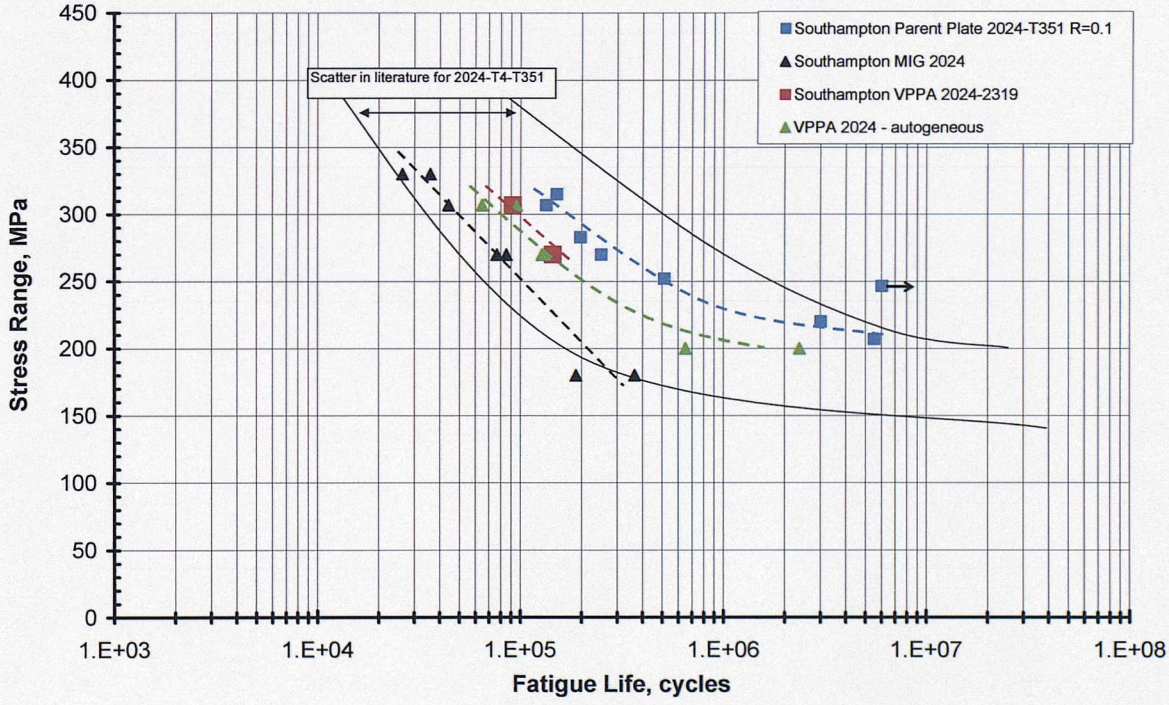

Figure 6.2 Fatigue life versus stress range for the 2024 parent plate and both VPPA welds filled and MIG weld including the scatter band from the literature.

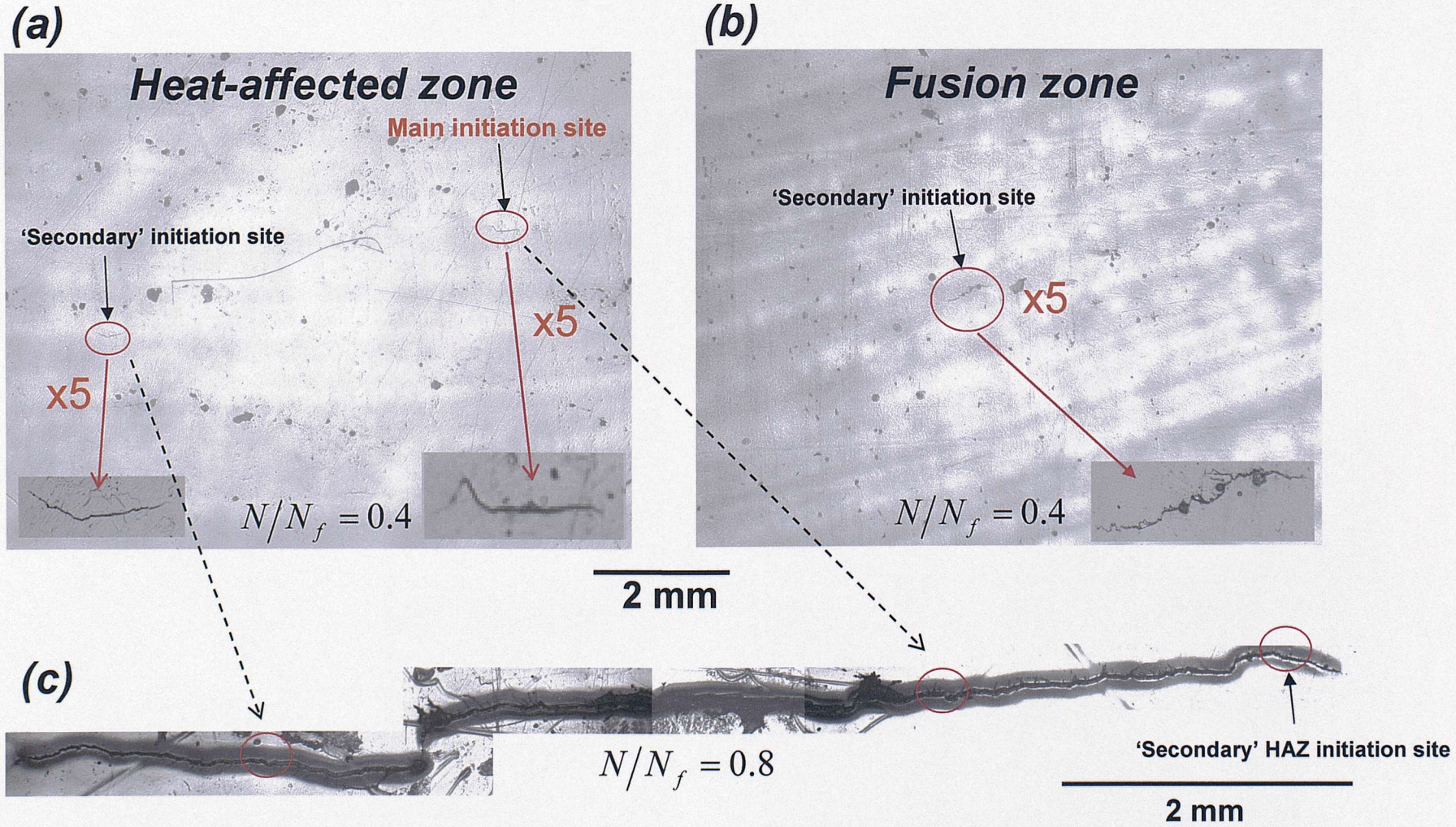

Figure 6.3 Optical macrographs of a filled VPPA fatigue sample; (a) Heat-affected zone and (b) fusion zone at 40% of fatigue life and (c) crack path after 80% of fatigue life. N.B. at the scale of Fig.(c) the location of Fig.(b) is some centimetres beyond the available page area.

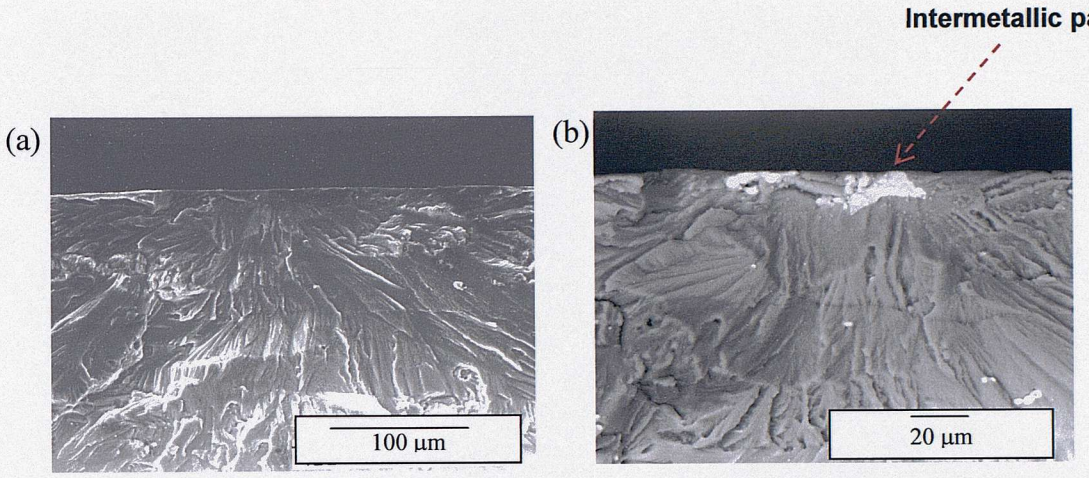

Figure 6.4 Filled VPPA weld: SEM images of 'primary' crack initiation in HAZ: (a) general view, and (b) BEI mode of initiating intermetallic particle.

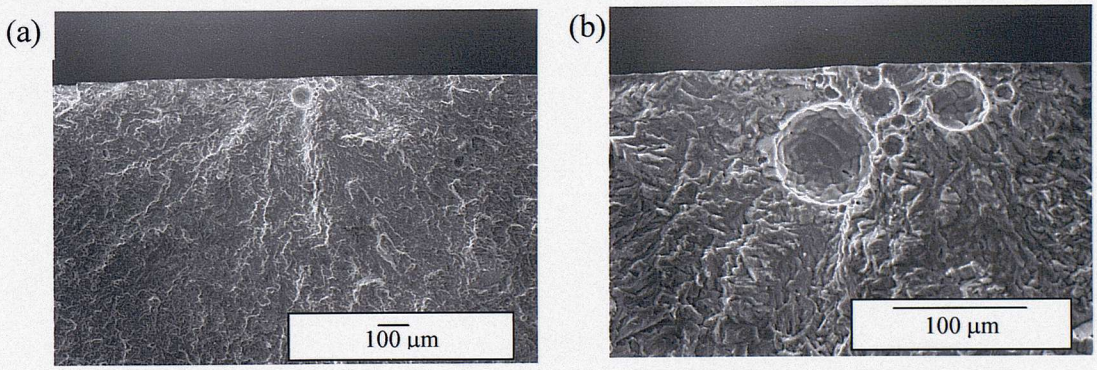

Figure 6.5 Filled VPPA filled weld: SEM images of 'secondary' crack initiation in fusion zone: (a) general view, and (b) detail of initiation site.

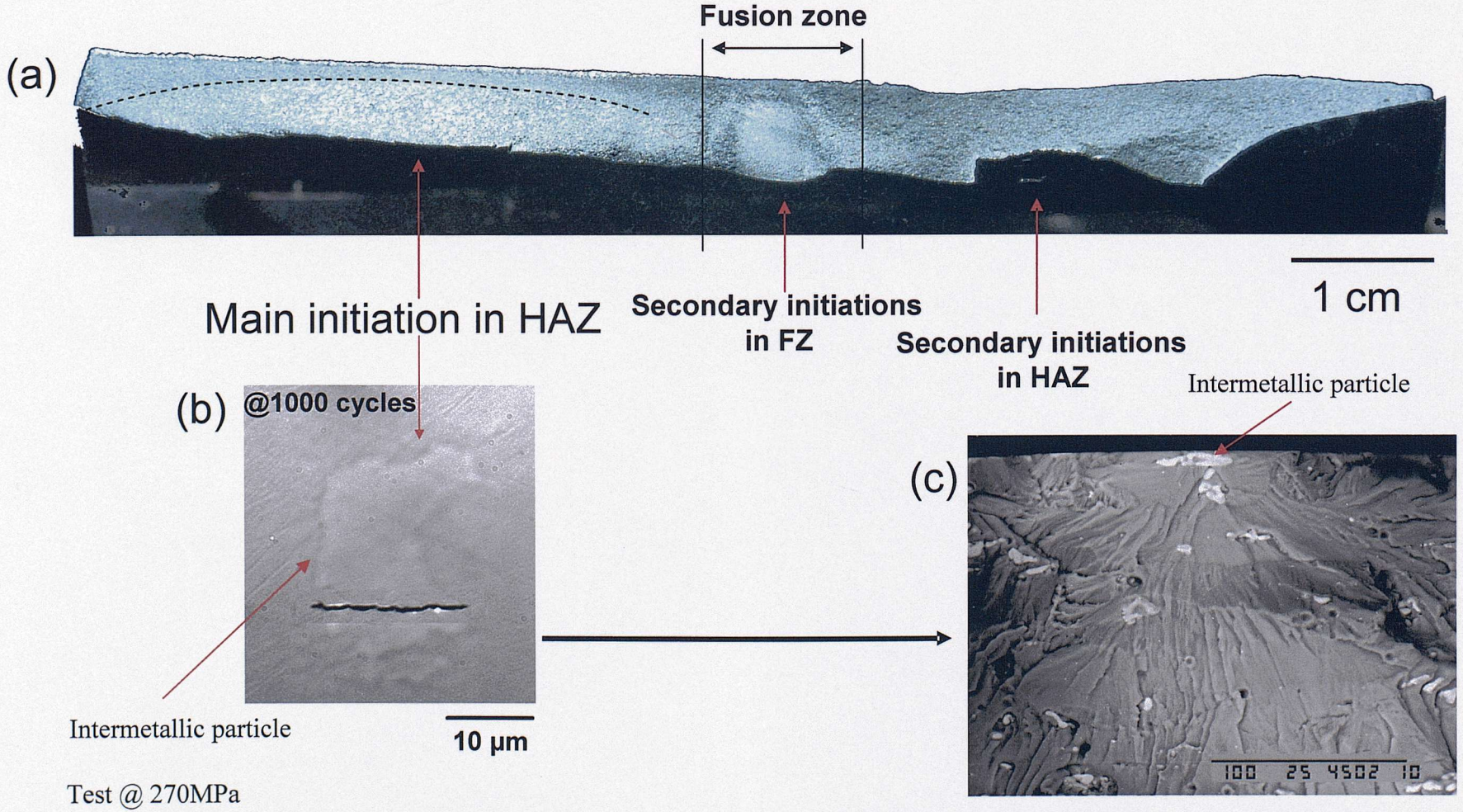

Figure 6.6 VPPA autogeneous fatigue sample: (a) fracture surface, (b) main crack initiation in HAZ, intermetallic particle (optical observation) (c) main crack initiation in HAZ (BEI image), intermetallic particle.

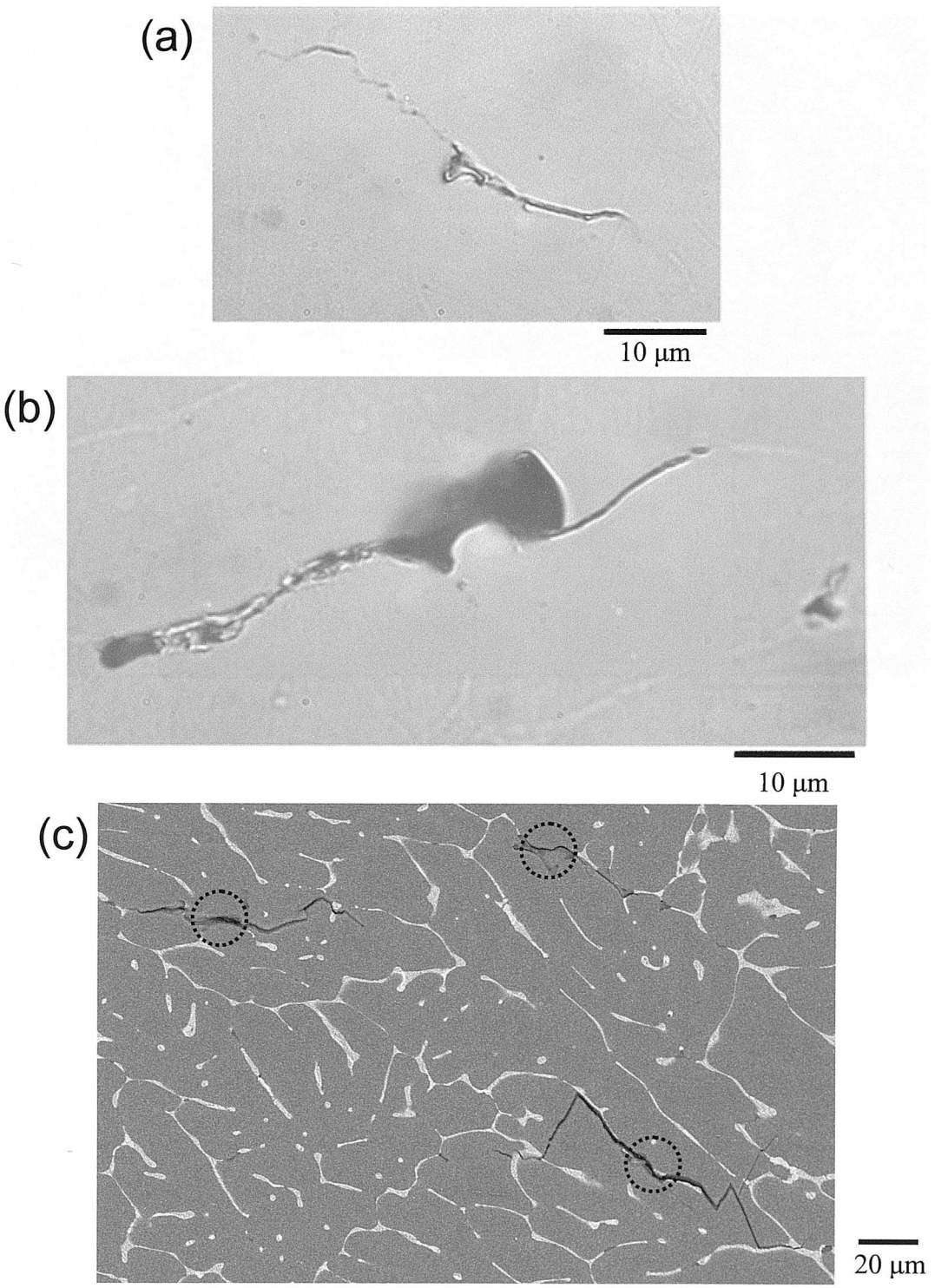

Figure 6.7 Cracks coming from interdendritic defects in the fusion zone for a stress level of 270MPa: (a) and (b) optical macrographs at $N/N_f = 0.75$, and (c) BEI micrograph after failure.

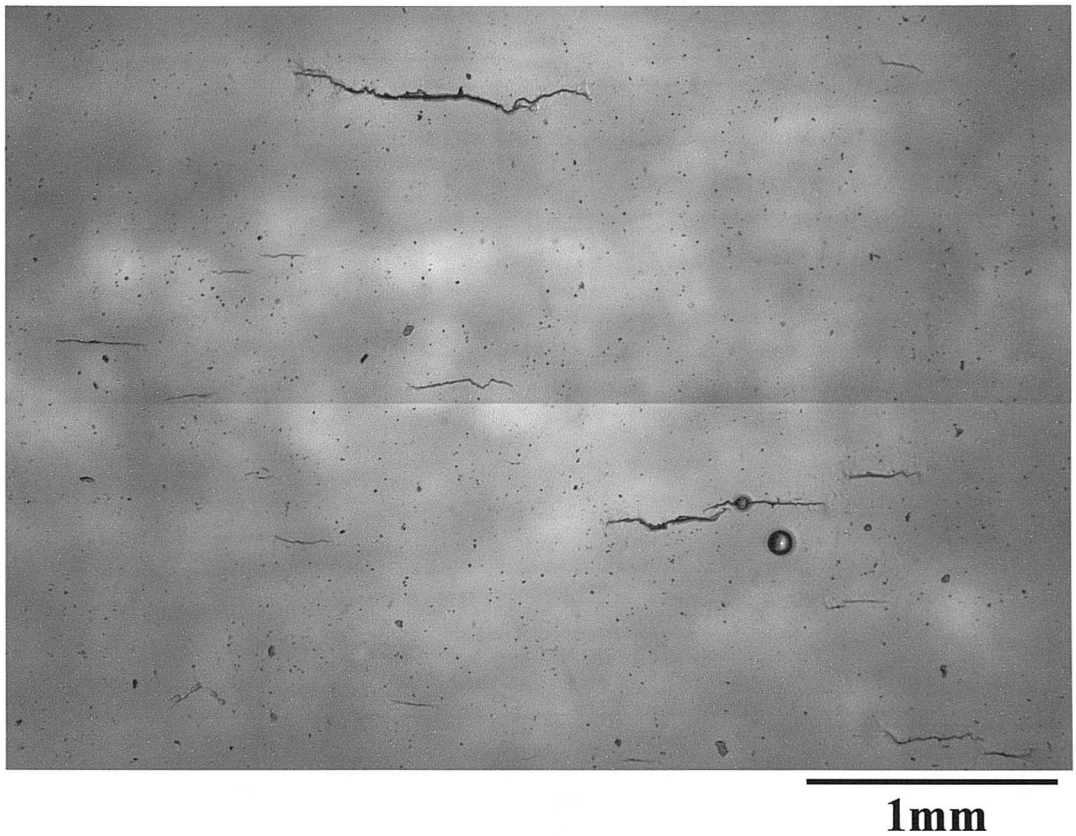

Figure 6.8 Optical macrograph of multiple crack initiation in the HAZ of the autogeneous VPPA weld at a stress level of 270MPa and at $N/N_f = 0.7$.

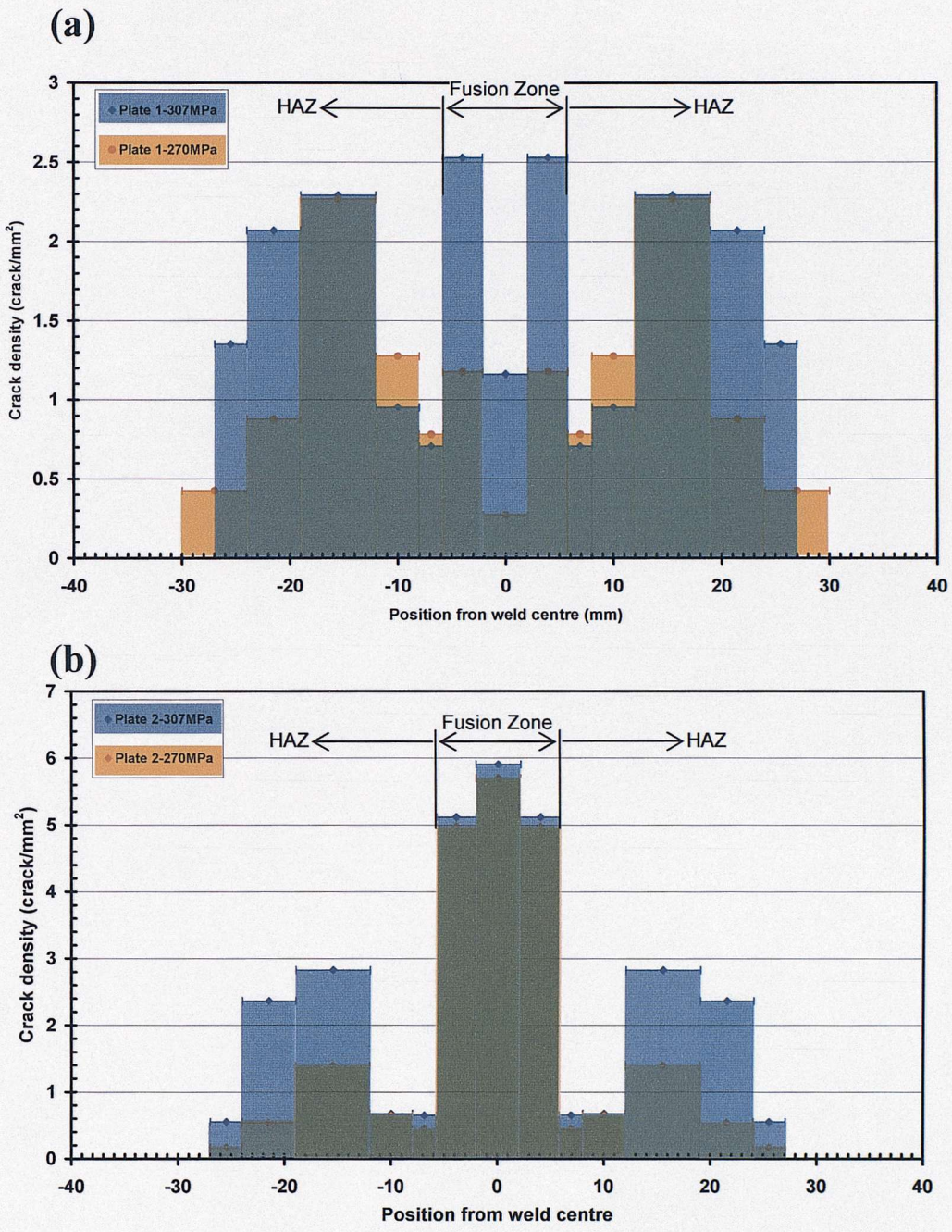

Figure 6.9 Crack density distribution across the VPPA autogeneous welds for two stress levels (270 and 307 MPa) for Plate 1 (a) and Plate 2 (b).

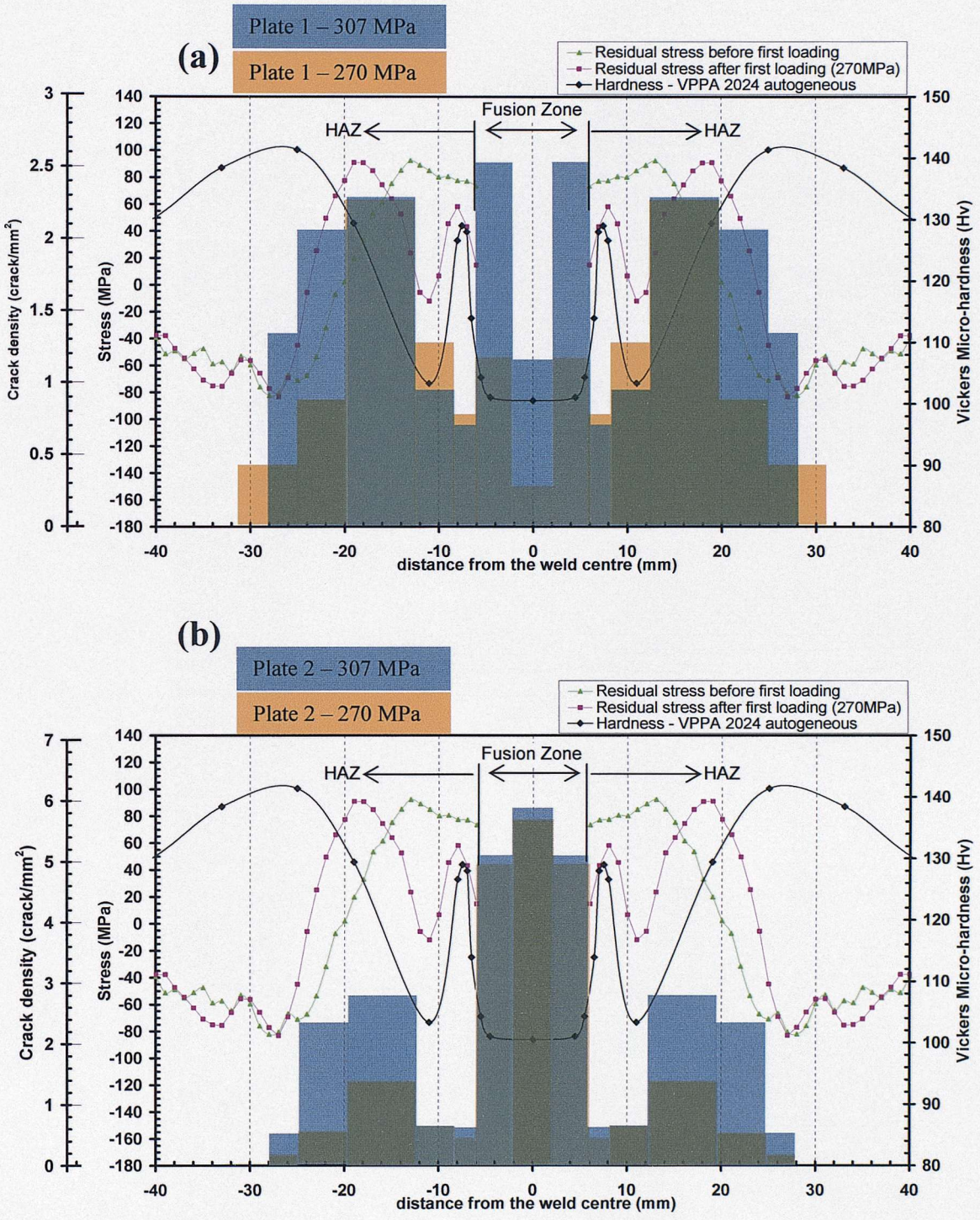

Figure 6.10 Crack density distribution across the VPPA autogeneous welds for two stress levels (270 and 307 MPa) with in superposition the hardness trace and the residual stress field for plate 1 (a) and plate 2 (b)

Plate 1

Plate 2

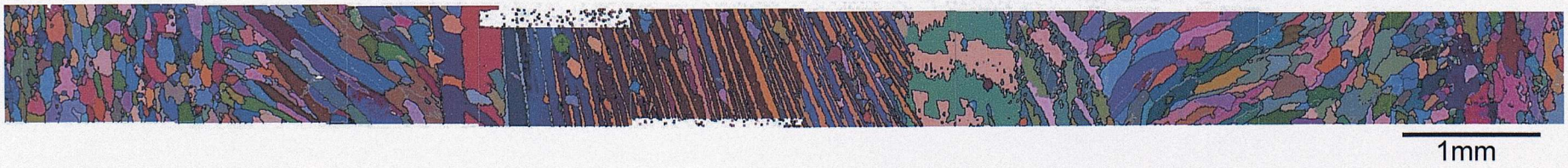

Figure 6.11 EBSD orientation maps of the fusion zones of Plate 1 and Plate 2 with axial columnar grain structure in the middle and coarse columnar structure at the edge.

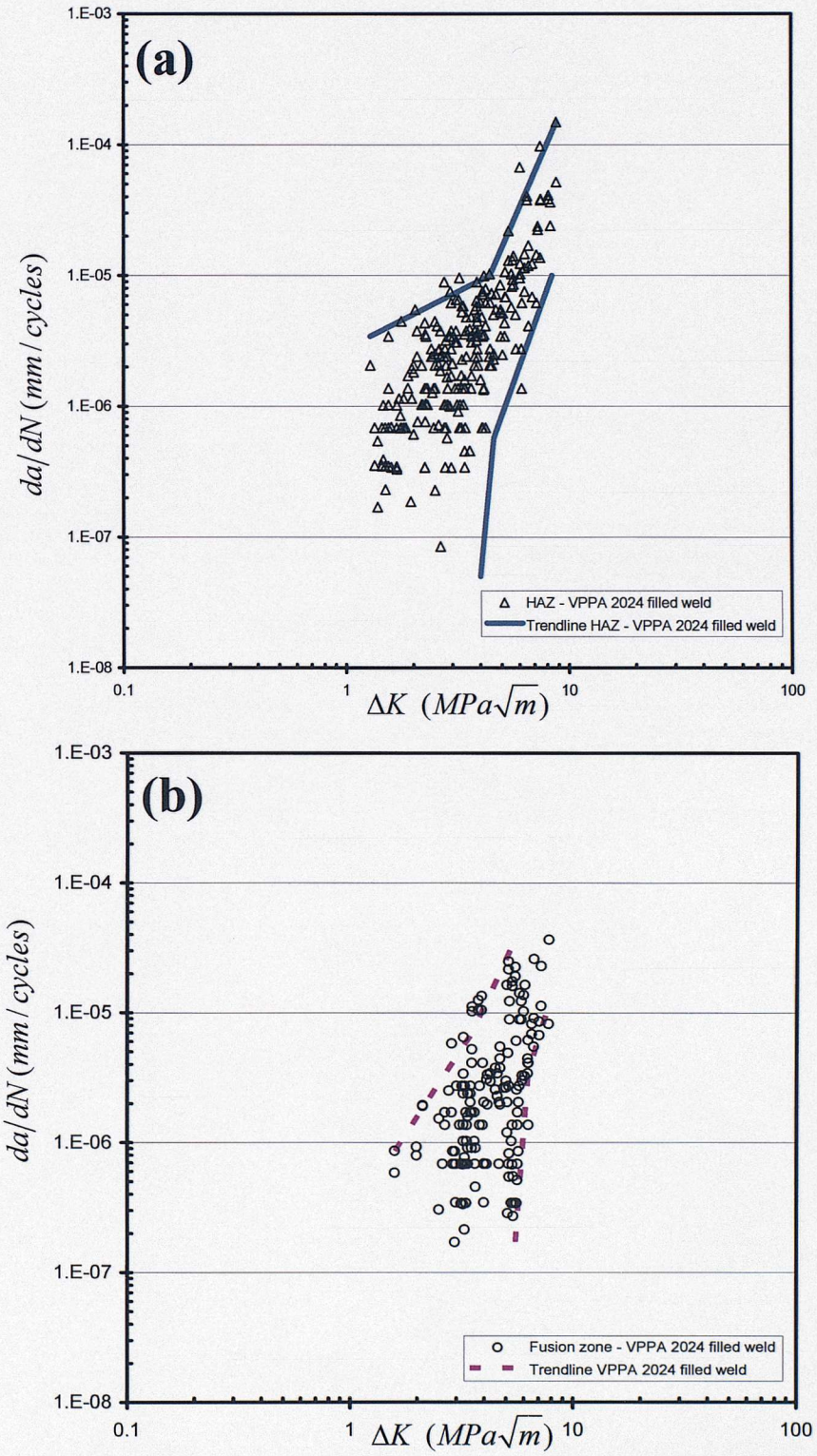

Figure 6.12 Crack growth rate data for the VPPA filled welds: (a) HAZ short cracks and (b) fusion zone short cracks

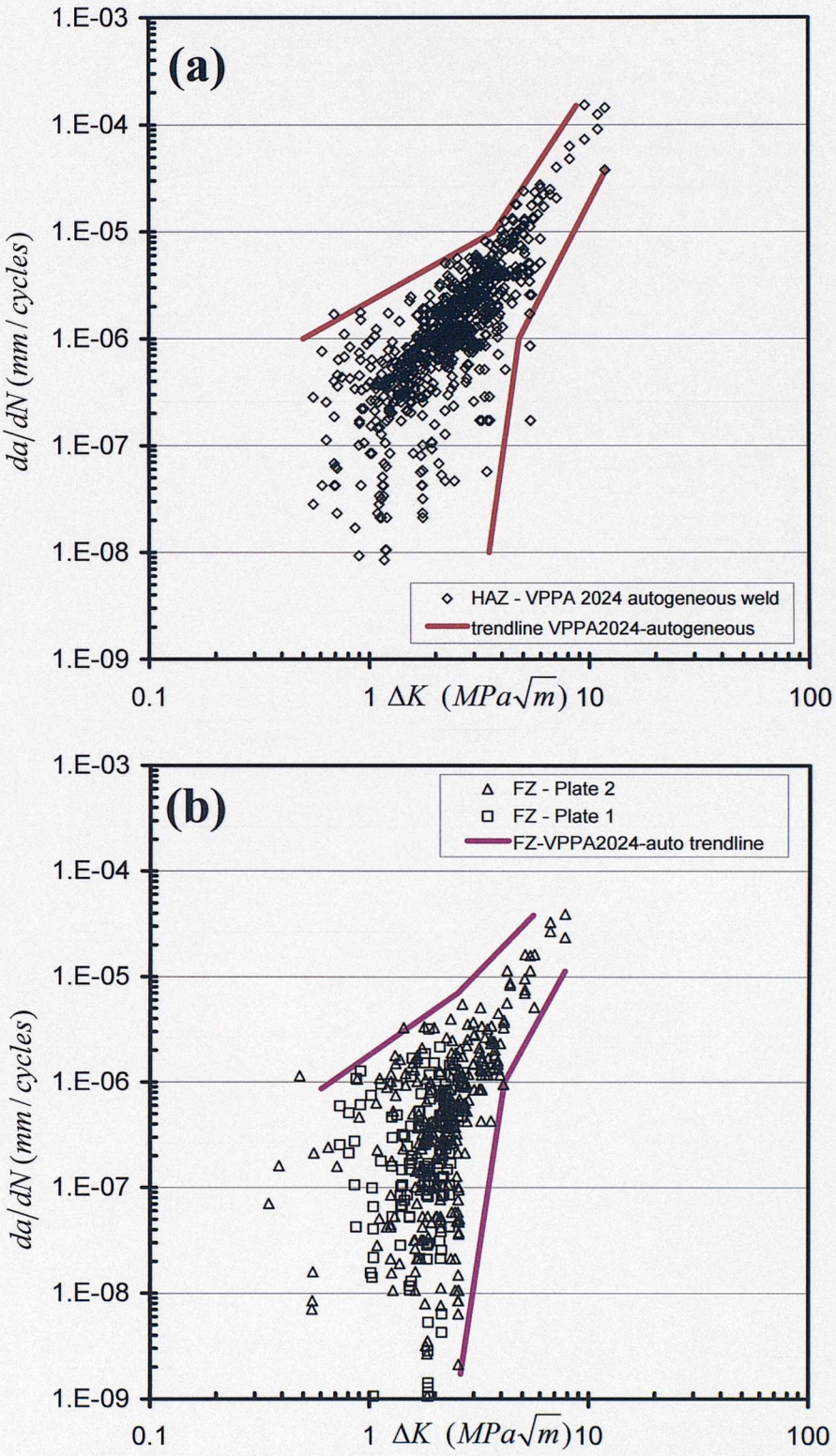

Figure 6.13 Crack growth rate data for the VPPA autogeneous weld: (a) HAZ short cracks and (b) fusion zone short cracks.

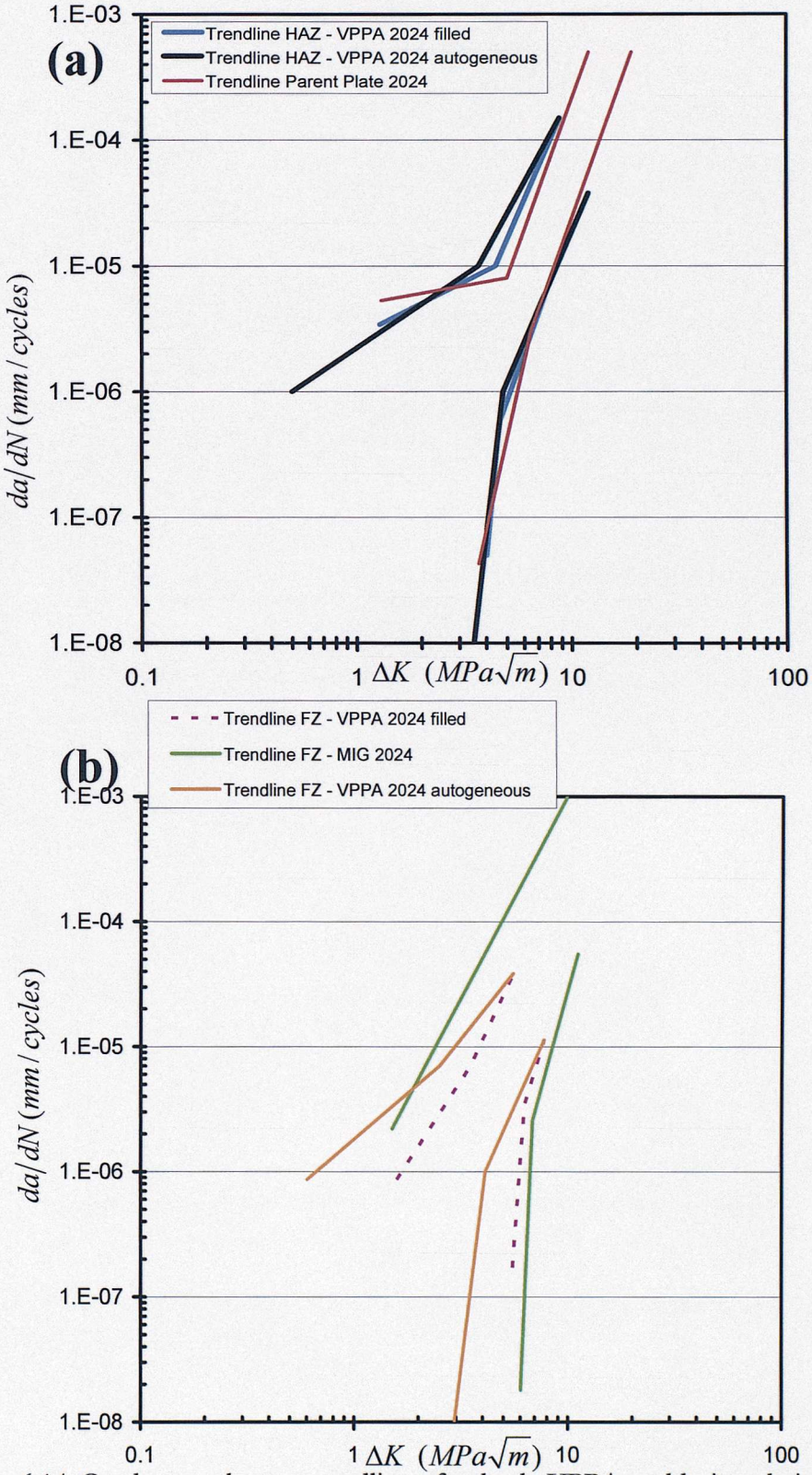

Figure 6.14 Crack growth rate trendlines for both VPPA welds in relation to the parent plate material for HAZ short cracks (a) and to the MIG weld for the fusion zone short cracks (b).

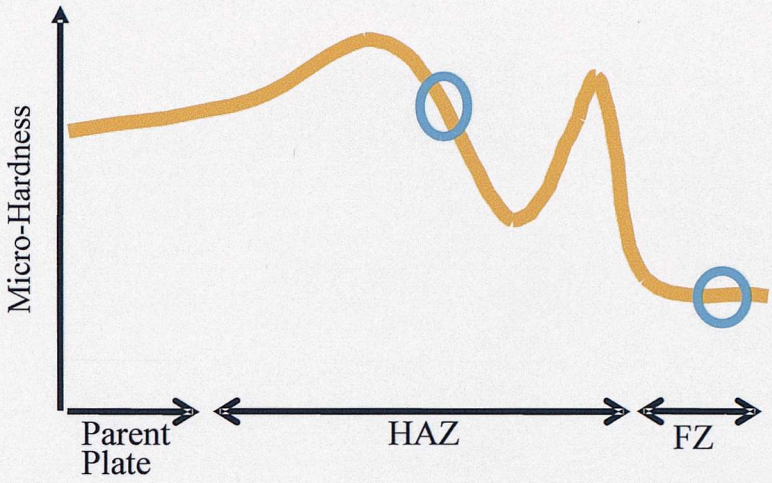

Figure 6.15 Two key locations across the filled VPPA weld function of the hardness profile: fusion zone and HAZ.

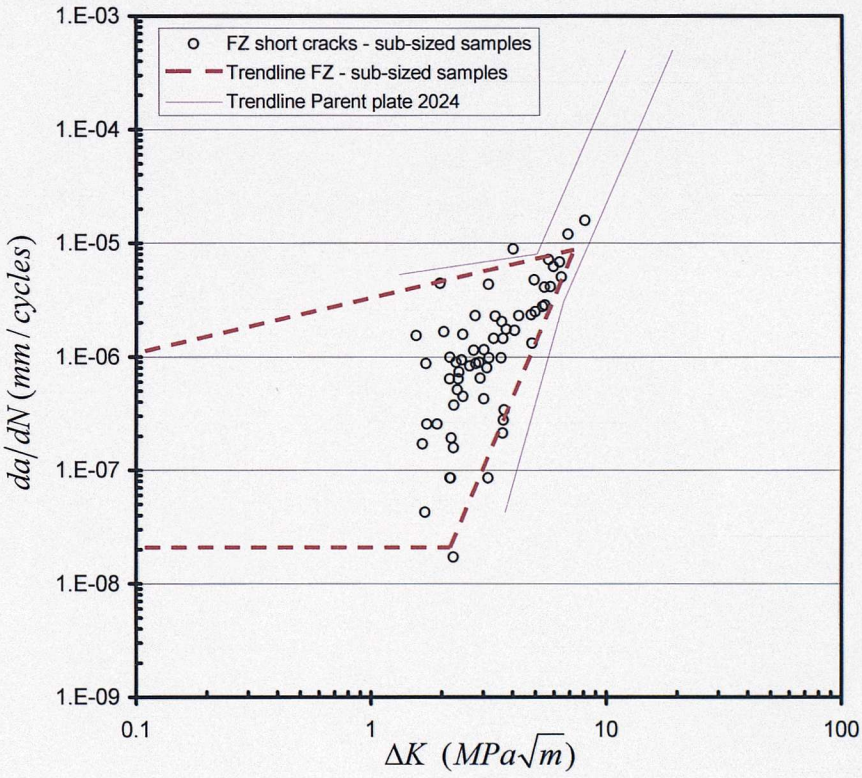

Figure 6.16 FZ crack growth data with the trendlines used as bounds for the crack growth prediction (see chapter 5)

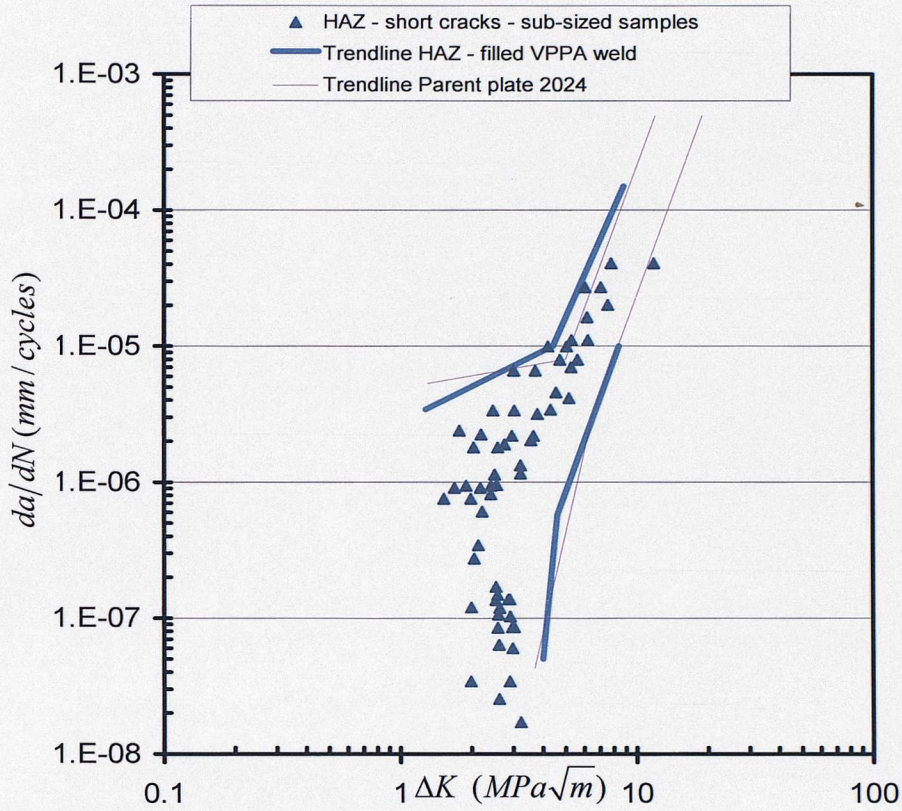

Figure 6.17 Crack growth rate data of cracks located in the HAZ of the filled VPPA weld.

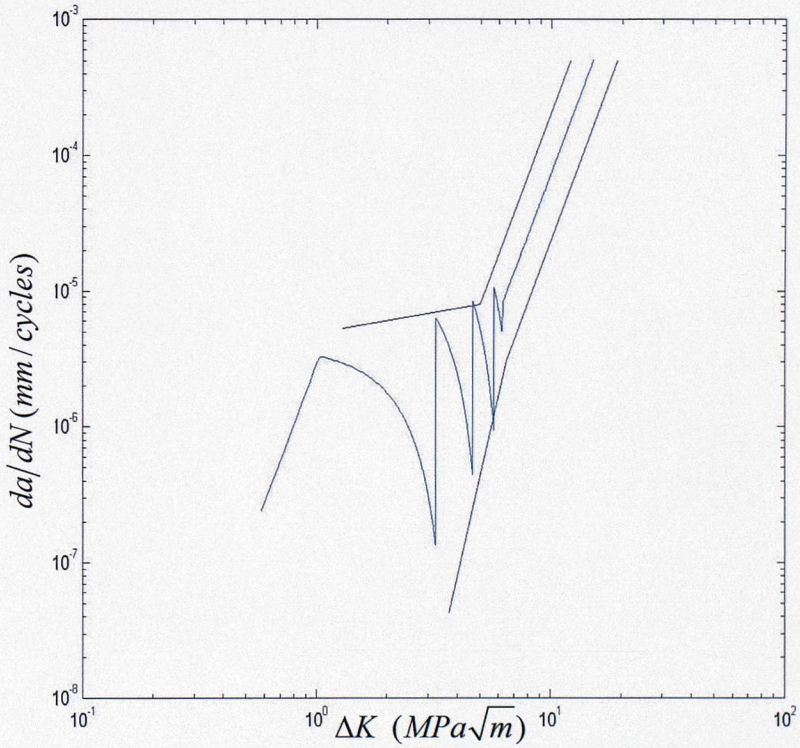

Figure 6.18 Crack growth rate prediction used for the modelling for a stress level of 270MPa

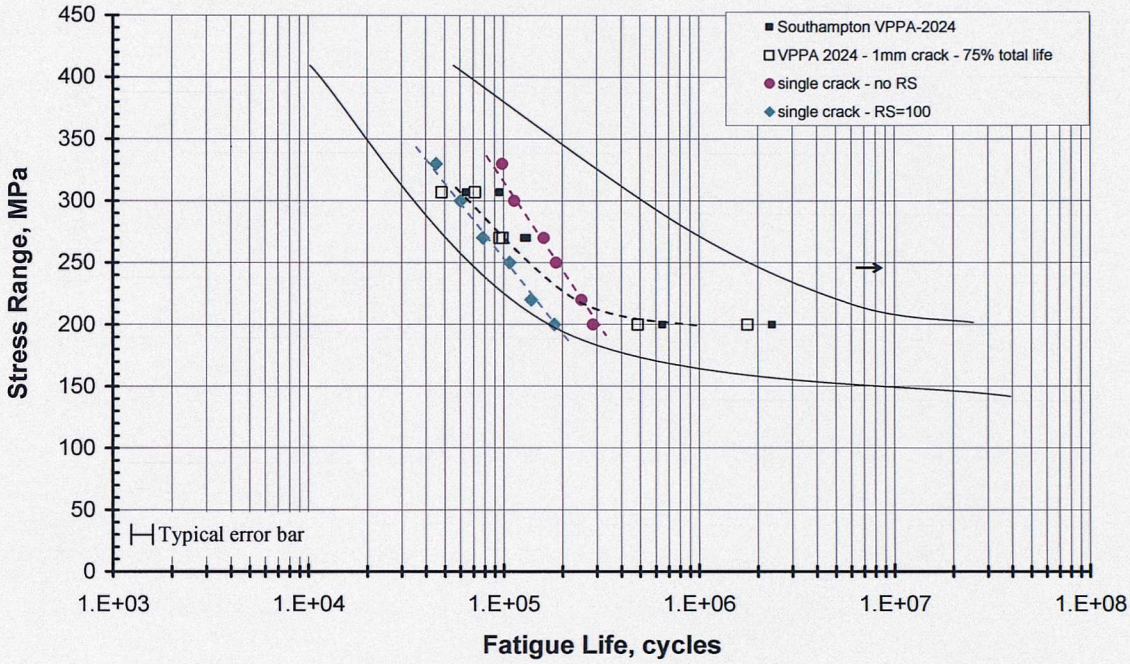

Figure 6.19 Fatigue life predictions for one crack initiated from a 20 μm intermetallic particle with/ without residual stress influences.

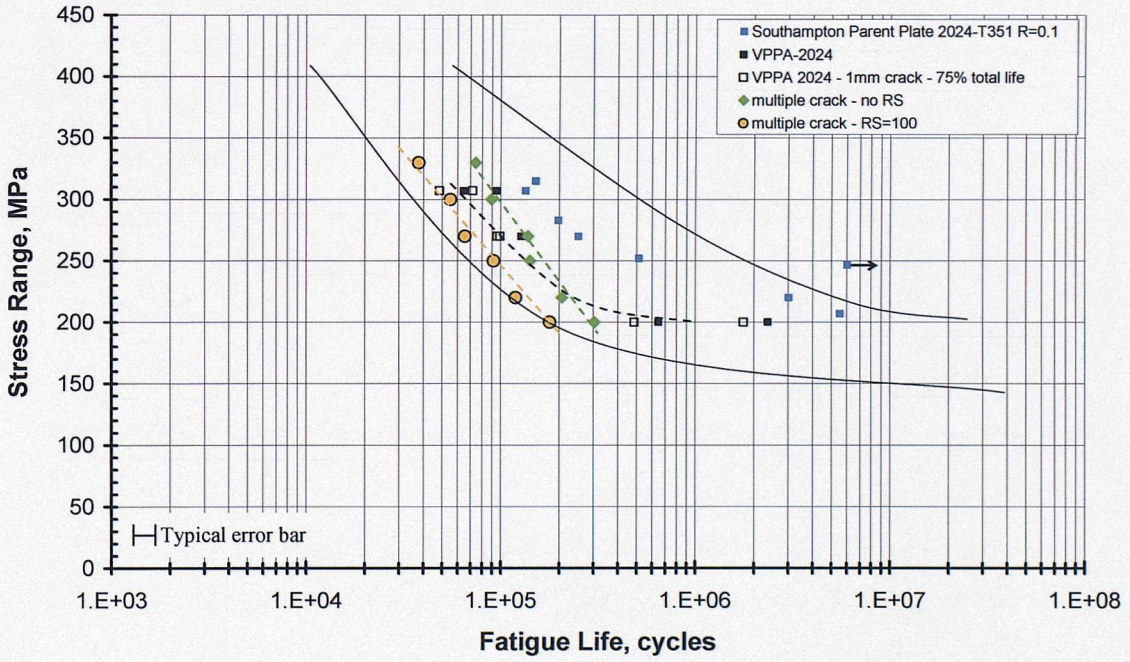

Figure 6.20 Fatigue life predictions for multiple cracks initiated from intermetallic particles with a size inferior to 20 μm with/ without residual stress influences.

Chapter 7

Conclusions

The main aim of this work was to develop a micro-mechanical understanding of fatigue behaviour occurring in fusion welded airframe alloys and develop a basic modelling approach to early fatigue life (life at 1mm crack lengths). This was achieved by characterising the different microstructures of three welds, by analysing their crack initiation and early growth mechanisms, and by predicting short crack growth life in welded structures using a synthesis of several modelling approaches.

Two welding techniques have been selected, with three specific weld types being studied in conjunction with the 2024-T351 based material: filled Metal Inert Gas welding, filled and autogeneous Variable Polarity Plasma Arc welding.

- Whilst columnar dendritic structures at the edge of the fusion zone have been seen in all the welds, equiaxed dendritic structures have been seen in the centre for the MIG and filled VPPA welds and an axial columnar dendritic structure is identified in the autogeneous VPPA welds. Local strengthening and precipitate conditions have been assessed using a combination of differential scanning calorimetry (DSC), transmission electron microscopy (TEM) and micro-hardness measurements. The influences of aging, re-solutionising and re-precipitation were noted across the HAZ, along with the presence incidence of the Ω (Al_2Cu) phase for the VPPA welds. Defect population characterisation has also been carried out, showing a high density of large and circular gas porosity, and more acicular interdendritic defects, in the MIG welds, and a predominance finer interdendritic defect in the VPPA welds.

- In terms of fatigue behaviour, it has been found that both types of welding may perform reasonably well, with the VPPA process particularly providing fatigue llves within a factor of ~2 of parent plate. Several crack initiation and growth processes have been seen to contribute to failure, highlighting a balance of local features that must be considered in understanding and predicting the performance of such welds. In the MIG welds, multiple crack initiations have been observed in the fusion zone coming mostly from interdendritic defects, and leading to significant crack-crack interactions. In the VPPA welds, cracks are again seen to initiate across the whole weld structure but the main cracks leading to failure initiate in the HAZ. In the autogeneous VPPA weld, multiple initiations coming from intermetallic particles could be identified in this region of the HAZ corresponding to the maximum tensile residual stress peak. Whilst variability in the autogeneous welds could be seen, especially in terms of crack density in the fusion zone, the overall fatigue performances were similar between welds consistent with HAZ dominated failure. Microstructures, strength and residual stress profiles of the three welds have been identified to influence crack initiation and crack evolution with crack initiation site density in the autogeneous VPPA welds for example being identified to be a complex function of residual stresses and heat treatment condition in the HAZ.
- A model has initially been developed to predict fatigue life of the MIG fusion zone based on measured defect distributions and multiple crack interaction concepts. To initiate a crack a Monte-Carlo method has been used based on the probability of initiation derived from the experimental observations (pore size and shape). Based on experimental observations it has been considered reasonable to initiate cracks only at the start (in the first cycle) of the fatigue simulations. In the first instance, the propagation model has been based on a linear Hobson approach (Hobson, 1982) and then on a microstructure sensitive approach based on the work of Zhang and Edwards model (Edwards & Zhang, 1994). In terms of crack interaction, based on the work of Hünecke and co-workers (Hünecke & Schöne, 2002), crack shielding or crack coalescence have been defined by a geometrical approach. It has been found that the fatigue simulation provides a good estimate of

early fatigue life in the real MIG welds (life to 1mm crack lengths). Knowing that residual stress is present in welded material, the modelling has been developed to incorporate residual stress influence by using the principle of stress superposition and a first order estimate of short crack closure behaviour. Having developed a model based on crack-crack interaction due to defect populations, a modified version of the model has been developed to predict the autogeneous VPPA welds fatigue life replacing pore defects by parent alloy intermetallic particles. In first approximation, the modelling results show relatively good fatigue life predictions.

Whilst not all relevant data has been available for a full comparative predictions of fatigue performance across all of the regions of the different welds (for example in terms of residual stress data), it is noted that in terms of competition between HAZ and fusion zone failure in the MIG and autogeneous VPPA welds, the current modelling approach is generally consistent with the test observations: the fusion zone controlled fatigue life of the MIG samples is then a combined function of interdendritic defect sizes, crack coalescence, and, to a lesser degree, residual stresses. In the VPPA case, the fusion zone presents a much finer, lower density of crack initiating defects, and although crack initiation is indeed clearly seen in the fusion zone, fatigue life then becomes limited by the high peak residual stress levels of the VPPA HAZ and the 'naturally occurring' defect population of the parent material.

References

Edwards, L. and Y. H. Zhang (1994). "Investigation of Small Fatigue Cracks .2. A Plasticity Based Model of Small Fatigue-Crack Growth." Acta Metallurgica Et Materialia 42(4): 1423-1431.

Hobson, P. D. (1982). "The formulation of a crack growth equation for short cracks." Fatigue of Engineering Materials and Structures 5(4): 323-327.

Hünecke, J. and D. Schöne (2002). Life prediction by observation and Simulation of short crack behaviour in a low carbon steel. Symposium of fatigue testing and analysis under variable amplitude loading, Tour (France), ASTM, 34, 1-3.

Chapter 8

Suggestions for further work

Whilst micromechanical assessment of fatigue in different fusion welds of real airframe aluminium alloys has been carried out, further investigations may be worth to consider in increasing the understanding of the fusion welds behaviour and optimising the fatigue life prediction of these welds.

In future work, microstructural characterisation of the VPPA welds could be extended to obtain detail defect population characterisation as those for the MIG welds. It may be also interesting to use the 3D computed tomography technique to investigate in three dimensions the real pore size and shape and associations with grain boundaries. Residual stress profiles for filled VPPA and MIG welds could be carried out by synchrotron X-ray technique to allow a direct comparison with the autogeneous VPPA welds. To obtain a deeper insight on thermal changes which may occur during the welding process, it would be valuable to supervise the welding process by using thermal gauges and thermocouples to obtain more specific information of the thermal changes and allow more quantitative correlation with the results for the various welds and weld regions.

In terms of fatigue, acoustic emission fatigue testing could be carried out to monitor crack initiation which means to evaluate the exact number of cycles necessary to initiate a crack. Additional sub-size samples of the MIG and autogeneous fusion zone could be machined and tested in fatigue to fit more accurately the crack propagation model. More detailed experimental study of residual stress and short crack closure would be also valuable.

In terms of modelling, good fatigue llfe predictions have been obtained, however it could be interesting to include the angle influences in the probability of initiation and move to a more micro-mechanically based initiation description. Modification of the crack propagation model could be made to include more accurately the residual stress influence.

Appendix 1

Residual stress evaluation

X-ray and synchrotron stress evaluation methods are based on the same principle; the use of the lattice spacing as a strain gauge. To perform strain measurements, the specimen is placed in an X-ray diffractometer, and it is exposed to an X-ray beam that diffracts from the underlying crystal lattice. The strain ε within the surface of the material may be measured by comparing the unstressed lattice inter-planar spacing d_0 with the strained inter-planar spacing d; the strain which is measured may then be defined as $\varepsilon_{\phi\psi}$ by equation (A1.1):

$$\varepsilon_{\phi\psi} = \frac{d - d_0}{d_0} \quad \text{(A1.1)}$$

Figure 3.5 shows the co-ordinate system used for calculating strain and stresses. The distance d is linked directly to the diffraction angle θ according to Bragg's law:

$$\lambda = 2d \sin\theta \quad \text{(A1.2)}$$

where θ is diffraction angle, and λ is the wave length of incident beam.

Combining equation (A1.1) and (A1.2) the formula for strain ε may be written as

$$\varepsilon_{\phi\psi} = \frac{\sin\theta_0 - \sin\theta}{\sin\theta} \quad \text{(A1.3)}$$

Based on the $\sin^2\psi$ law, the relation between the strain ε_n and the stress components is determined using the equilibrium conditions of the free surface.

$$\varepsilon_{\phi\psi} = \frac{1+\nu}{E}(\sigma_1 \cos^2\phi + \sigma_2 \sin^2\phi)\sin^2\psi - \frac{\nu}{E}(\sigma_1 + \sigma_2) \quad \text{(A1.4)}$$

where E and ν are the usual elastic constants, σ_1, σ_2 are principal stresses.
Having the strains in terms of inter-planar spacing, and using the strains calculated in equation (4) the stress can be evaluated by:

$$\sigma_\phi = \frac{E}{(1+\upsilon)\sin^2\psi}\left(\frac{d_\psi - d_n}{d_n}\right) \quad \text{(A1.5)}$$

This equation allows calculation of the stress in any chosen direction from the inter-planar spacings determined from two measurements, made in a plane normal to the surface and containing the direction of the stress to be measured. The $\sin^2\psi$ method is the most commonly used for stress determination.

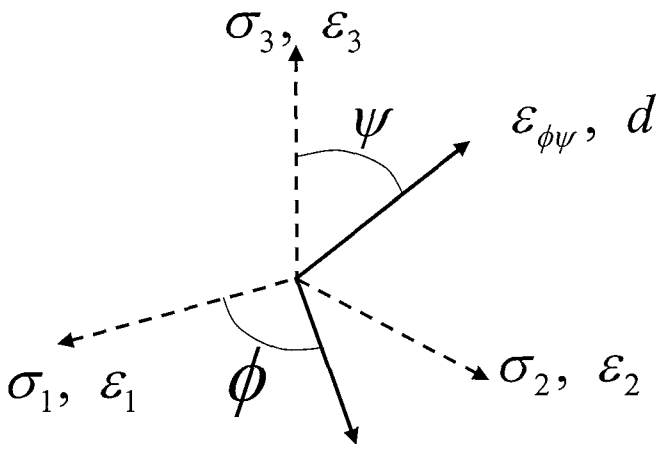

Figure 3.5 Co-ordinate system used for calculating surface strain and stresses.

Appendix 2

Fatigue life predictions: Average and error values

A2.1 Average and error values of fatigue life predictions for the MIG weld:

Table A.1 - Hobson-based fatigue life prediction

Average and error values of fatigue life predictions for different stress levels and different conditions of simulation: (i) original/reference, (ii) different area sizes, (iii) different shielding area sizes and (iv) different coalescence area sizes as presented in Chapter 5.

(i) original/reference – See Figure 5.26

(i)	Original/reference	
Range Stress (MPa)	Number of cycles	Error range (%)
200	184700	14.4
220	157500	10.9
250	127400	13.4
270	113000	15.4
300	86300	25.4
330	60100	16.6

(ii) different area sizes – See Figure 5.27

(ii)	Area X2		Area X3		Area X2*2	
Range Stress (MPa)	Number of cycles	Error range (%)	Number of cycles	Error range (%)	Number of cycles	Error range (%)
200	187000	7.9	131700	15.6	137200	10.9
220	149800	10.5	101100	10.0	101700	6.6
250	112200	6.5	86100	19.7	79300	9.5
270	96200	10.9	70400	19.3	75500	13.1
300	57200	8.7	47700	24.5	45500	17.3
330	49400	17.8	35600	19.4	38600	19.2

(ii)	Area X4		Area X6		Area X12	
Range Stress (MPa)	Number of cycles	Error range (%)	Number of cycles	Error range (%)	Number of cycles	Error range (%)
200	121100	11.6	110400	8.5	103800	8.2
220	101500	13.4	97700	12.7	88500	12.0
250	82500	9.7	70800	15.0	65900	12.2
270	62700	11.2	52300	8.2	47000	19.7
300	36700	11.4	33700	27.0	27500	23.0
330	23500	16.7	21600	23.0	24200	27.0

(v) different shielding area sizes – See Figure 5.28 and Figure 5.30

(v) area x6	Shielding zone x0.25		Shielding zone x0.5		Shielding zone x1.5	
Range Stress (MPa)	Number of cycles	Error range (%)	Number of cycles	Error range (%)	Number of cycles	Error range (%)
200	110400	2.6	103300	9.2	159000	3.4
220	76800	10.7	72400	7.4	133500	8.8
250	58200	11.4	65700	12.7	94200	4.7
270	55000	20.6	53900	22.1	69200	10.5
300	34800	25.0	35000	20.6	45500	8.2
330	17400	19.5	21400	26.8	28600	12.4

(v) area x6	Shielding zone x2		Shielding zone x0	
Range Stress (MPa)	Number of cycles	Error range (%)	Number of cycles	Error range (%)
200	173800	20.2	90800	24.3
220	142200	14.9	72700	27.6
250	100500	14.3	54600	25.2
270	81200	11.1	47500	31.1
300	64100	14.0	32000	31.4
330	41300	14.3	19300	36.2

(v) different coalescence area sizes – See Figure 5.29 and Figure 5.30

(vi) area x6	Coalescence zone x0.25		Coalescence zone x0.5		Coalescence zone x2	
Range Stress (MPa)	Number of cycles	Error range (%)	Number of cycles	Error range (%)	Number of cycles	Error range (%)
200	156800	12.1	129700	6.9	69800	13.4
220	120000	9.9	107900	9.6	44500	13.4
250	92800	12.6	83300	9.7	22200	27.9
270	76800	8.0	68400	7.6	19300	31.7
300	69000	5.3	52200	10.7	15500	40.8
330	44600	1.5	33300	9.3	5900	41.8

(vi) area x6	Coalescence zone x0	
Range Stress (MPa)	Number of cycles	Error range (%)
200	260700	9.4
220	218100	6.1
250	150800	14.6
270	112300	14.1
300	89800	10.5
330	52600	8.2

Table A.2 - Zhang-Edwards based fatigue life prediction

Average and error values of fatigue life predictions for different stress levels without residual stress influence and with closure effect and residual stress influences for two different simulated areas: reference/original area (1.2x1.4mm) and x6 area (half fusion zone).

See Figure 5.36

EDWARDS' MODEL	Without RS (original/reference area)	
Range Stress (MPa)	Number of cycles	Error range (%)
150	418400	9.0
170	275800	13.8
200	160400	13.2
220	136500	18.5
250	84800	12.3
280	56800	15.9
EDWARDS' MODEL	Without RS (areaX6)	
Range Stress (MPa)	Number of cycles	Error range (%)
150	165700	17.8
170	120600	14.0
200	76500	17.1
220	56500	18.1
250	33900	18.6
280	18300	25.2

See Figure 5.37

EDWARDS' MODEL	With stress superposition	
Range Stress (MPa)	Number of cycles	Error range (%)
150	165700	17.8
170	120600	14.0
200	76500	17.1
220	56500	18.1
250	33900	18.6
280	18300	25.2

See Figure 5.40

EDWARDS' MODEL	closure effect & no Residual stress	
Range Stress (MPa)	Number of cycles	Error range (%)
200	196100	11.3
220	122500	9.1
250	76100	14.0
270	67200	11.3
300	39800	13.4
330	27100	11.6

See Figure 5.40

EDWARDS' MODEL	Closure effect & residual stress	
Range Stress (MPa)	Number of cycles	Error range (%)
200	118500	20.3
220	85800	13.1
250	54700	9.9
270	35600	13.1
300	25100	17.5
330	11700	14.0

A2.2 Average and error values of fatigue life predictions for the VPPA weld:

Table A.3 - Zhang-Edwards based fatigue life prediction for the VPPA weld

Average and error range values of fatigue llfe predictions for different stress levels with or without residual stress influence and with closure effect for a simulated intermetallic particles population.

See Figure 6.20

VPPA model	closure effect & no Residual stress	
Range Stress (MPa)	Number of cycles	Error range (%)
200	301700	7.3
220	205400	20.1
250	141100	21.0
270	137600	29.9
300	89200	17.1
330	73700	21.4

VPPA model	Closure effect & residual stress	
Range Stress (MPa)	Number of cycles	Error range (%)
200	178600	10.0
220	119300	13.5
250	91800	16.8
270	65300	14.1
300	55000	26.2
330	37700	12.3

Appendix 3

Crack interaction modelling

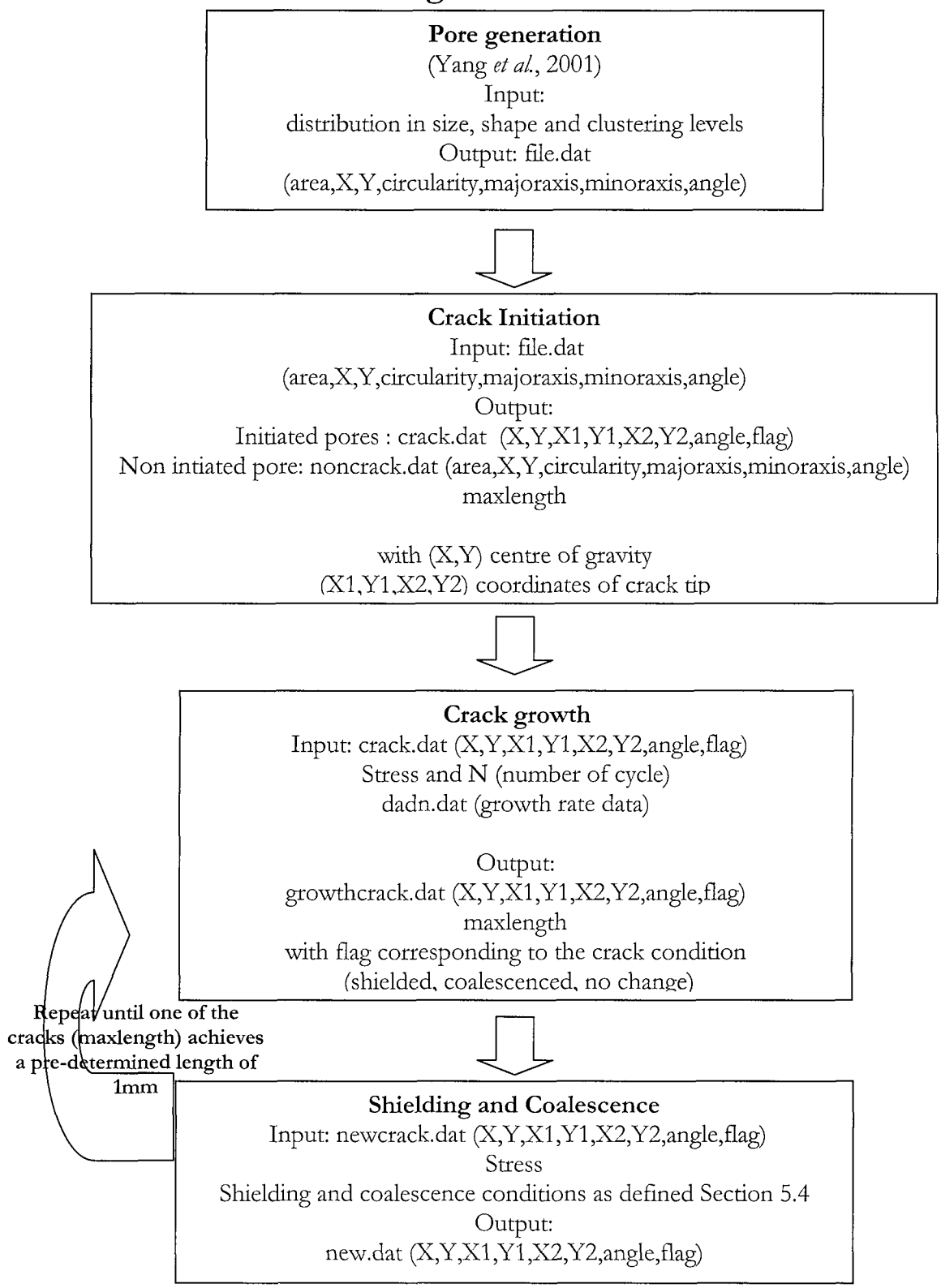

```
% crack initiation
function [crack,noncrack,maxlength]=init(file)
%rand('state',1000)
% Input data
load prob.dat; % area,circularity,angle,cycle,stress,probability
prob(:,6)=prob(:,6)*1;
% Program
b=1;
c=1;
m=size(file,1)
flg=0;
for i=1:m
   k=1;
   h=0;
   while (k <= size(prob,1)) & (h==0)
      if file(i,1)<= prob(k,1),
         if file(i,4)<= prob(k,2),
            p=prob(k,6)/100;
            h=1;
         end
      end
      k=k+1;
   end
   t=0;
   for j=1:m
   X=rand(1);
      if X < p,
         t=t+1;
      end
   end
   if (t/m) < p,
      crack(b,1)=file(i,2);
      crack(b,2)=file(i,3);
      if (file(i,7)<=90)
         crack(b,3)=file(i,2)+file(i,5)*cos(file(i,7)*pi/180);
         crack(b,4)=file(i,3)+file(i,5)*sin(file(i,7)*pi/180);
         crack(b,5)=file(i,2)-file(i,5)*cos(file(i,7)*pi/180);
         crack(b,6)=file(i,3)-file(i,5)*sin(file(i,7)*pi/180);
      else
         crack(b,5)=file(i,2)+file(i,5)*cos(file(i,7)*pi/180);
         crack(b,6)=file(i,3)+file(i,5)*sin(file(i,7)*pi/180);
         crack(b,3)=file(i,2)-file(i,5)*cos(file(i,7)*pi/180);
         crack(b,4)=file(i,3)-file(i,5)*sin(file(i,7)*pi/180);
      end
      crack(b,7)=file(i,7);
      crack(b,8)=0;
      a = sqrt((crack(b,3)-crack(b,5))^2+(crack(b,4)-crack(b,6))^2);
      crack(b,9)=0;
      crack(b,10)=0;
      crack(b,11)=0;
      crack(b,12)=0;
      if (flg <= a),
         flg = (a);
      end
      b=b+1;
   else noncrack(c,:)=file(i,:);
```

```
      c=c+1;
   end
end
maxlength = flg;

% crack growth
function [growthcrack]=growth(crack,N,stress)
%
%clear all

% Parameter To be specified by user

%stress=270; % Stress Range in MPa
W=7.5; %in mm

% Input data
%load crack.dat; % X,Y,X1,Y1,X2,Y2,angle,flag
load dadn.dat; %deltaK,dadn in micron

% Program
m=size(crack,1);
n=size(dadn,1);

for i=1:m
   length=sqrt((crack(i,3)-crack(i,5))^2+(crack(i,4)-crack(i,6))^2); %a1+a2
   X=(length)*(10^-3)/(2*W);
   const= (1.21*(1-0.3*X)*(1-X^12))+(0.394*1.57*X^12*(1/1)^0.5);
   K=const*(stress/1.57)*((3.1415927*((length)*(10^-3)*1/2000))^0.5);
   h=0;
   j=1;
   while (j<=(n-1)) & (h==0)
      if K <= dadn(j+1,1) & K >= dadn(j,1),
         if K == dadn(j,1),
            Y=dadn(j,2);
         elseif K == dadn(j+1,1)
            Y=dadn(j+1,2);
         else Y=(dadn(j,2)+dadn(j+1,2))/2;
         end
         h=1;
      end
      j=j+1;
   end
   growthcrack(i,:)=crack(i,:);
   if (crack(i,8)==0),
   growthcrack(i,3)=growthcrack(i,3)+Y*N;
   growthcrack(i,5)=growthcrack(i,5)-Y*N;
   elseif (crack(i,8)==1)|(crack(i,8)==6),
   growthcrack(i,3)=growthcrack(i,3)+Y*N;
   growthcrack(i,5)=growthcrack(i,5)-Y*N;
   elseif (crack(i,8)==3),
   growthcrack(i,3)=growthcrack(i,3);
   growthcrack(i,5)=growthcrack(i,5)-Y*N;
   elseif (crack(i,8)==4),
   growthcrack(i,3)=growthcrack(i,3)+Y*N;
   growthcrack(i,5)=growthcrack(i,5);
   elseif (crack(i,8)==5),
```

```
   growthcrack(i,3)=growthcrack(i,3);
   growthcrack(i,5)=growthcrack(i,5);
   end
end
%growthcrack

%save growthcrack.dat growthcrack -ascii;

% Shielding and Coalescence
function [new,maxlength]=coal(newcrack,stress)
%
%clear all

% Input data
%load newcrack.dat; % X,Y,X1,Y1,X2,Y2,angle,flag

% Parameter To be specified by user
%stress=300; %  stress Range in MPa
W=7.5; %in mm

% Program
 T=newcrack;
 S=newcrack;
 m=size(T,1);
 for i=1:m
   %a1=sqrt((T(i,3)-T(i,1))^2+(T(i,4)-T(i,2))^2);
   %a2=sqrt((T(i,5)-T(i,1))^2+(T(i,6)-T(i,2))^2);
   length=sqrt((T(i,3)-T(i,5))^2+(T(i,4)-T(i,6))^2); %a1+a2
   tip1(i,1)=T(i,3);
   tip1(i,2)=T(i,4);
   tip2(i,1)=T(i,5);
   tip2(i,2)=T(i,6);
   %radius(i)=(a1+a2)/2;
   radius(i)=length/2*(1);
   X=(length)*10^-3/(2*W);              %plastic zone size calculation
   const= (1.21*(1-0.3*X*(1-X^12)))+(0.394*1.57*X^12*(1/1)^0.5);
   deltaK=const*(stress/(1.57))*((3.1415927*((length)*10^-3*1/2000))^0.5);
   K=deltaK/0.9; %Kmax
   rp(i)=10^6*K^2/(pi*(350)^2); %maximum plastic zone with 350MPa yield stress
 end

%check for shielding
e=1;
f=1;
g=1;
 for i=1:m
    j=1;
    centre(i,1)=(tip1(i,1)+tip2(i,1))/2;
    centre(i,2)=(tip1(i,2)+tip2(i,2))/2;
    while (j<=m)
      if j~=i,
         g1=sqrt((tip1(j,1)-centre(i,1))^2+(tip1(j,2)-centre(i,2))^2);
         g2=sqrt((tip2(j,1)-centre(i,1))^2+(tip2(j,2)-centre(i,2))^2);
         if (g1<=radius(i)),
            if T(j,8)==4 | T(j,8)==5,
              T(j,8)=5;
```

```
          else T(j,8)=3;
           end
        elseif (g2<=radius(i)),
          if T(j,8)==3 | T(j,8)==5,
            T(j,8)=5;
          else T(j,8)=4;
           end
        elseif  (g1<=radius(i))&(g2<=radius(i)),
          T(j,8)= 5;
        end
      end
      j=j+1;
   end
  end
```

%check for coalescence

```
 a=1;
 b=1;
 c=1;
 d=1;
 for i=1:m
    j=i+1;
    while (j<=m-1)
      f11=sqrt((tip1(i,1)-tip1(j,1))^2+(tip1(i,2)-tip1(j,2))^2);
      f12=sqrt((tip1(i,1)-tip2(j,1))^2+(tip1(i,2)-tip2(j,2))^2);
      f21=sqrt((tip2(i,1)-tip1(j,1))^2+(tip2(i,2)-tip1(j,2))^2);
      f22=sqrt((tip2(i,1)-tip2(j,1))^2+(tip2(i,2)-tip2(j,2))^2);
      r=(rp(i)+rp(j))*1;
      if (f11 <= r),
       if (S(j,8)==3 | S(i,8)==3)
        T(i,8)=3;
        T(j,8)=3;
       else
        if (tip1(i,1)<=tip1(j,1))
          coa1(a,3)=tip1(j,1);
          coa1(a,4)=tip1(j,2);
          coa1(a,9)=tip1(i,1);
          coa1(a,10)=tip1(i,2);
        else
          coa1(a,3)=tip1(i,1);
          coa1(a,4)=tip1(i,2);
          coa1(a,9)=tip1(j,1);
          coa1(a,10)=tip1(j,2);
        end
        if (tip2(i,1)<=tip2(j,1))
          coa1(a,5)=tip2(j,1);
          coa1(a,6)=tip2(j,2);
          coa1(a,11)=tip2(i,1);
          coa1(a,12)=tip2(i,2);
        else
          coa1(a,5)=tip2(i,1);
          coa1(a,6)=tip2(i,2);
          coa1(a,11)=tip2(j,1);
          coa1(a,12)=tip2(j,2);
        end
        coa1(a,1)= (coa1(a,3)+coa1(a,5))/2;
```

```
    coa1(a,2)=(coa1(a,4)+coa1(a,6))/2;
    coa1(a,7)=0;
    coa1(a,8)=3;
    hold on
    plot (tip1(i,1),tip1(i,2),'.k');
    hold on
    plot (tip1(j,1),tip1(j,2),'.k');
    hold on
    plot ([tip1(i,1),tip1(j,1)],[tip1(i,2),tip1(j,2)],'g');
    hold on
    plot(coa1(a,5),coa1(a,6),'.g')
    hold on
    plot(coa1(a,3),coa1(a,4),'+g')
    hold on
    T(i,8)=111;
    T(j,8)=211;
    a=a+1;
  end
elseif  (f12 <= r),
  if (S(j,8)==4 | S(i,8)==3)
     T(j,8)=4;
     T(i,8)=3;
  else
    coa2(b,1)= (tip2(i,1)+tip1(j,1))/2;
    coa2(b,2)=(tip2(i,2)+tip1(j,2))/2;
    coa2(b,3)=tip1(j,1);
    coa2(b,4)=tip1(j,2);
    coa2(b,5)=tip2(i,1);
    coa2(b,6)=tip2(i,2);
    coa2(b,7)=0;
    coa2(b,8)=0;
    T(i,8)=112;
    T(j,8)=212;
    coa2(b,9)=tip1(i,1);
    coa2(b,10)=tip1(i,2);
    coa2(b,11)=tip2(j,1);
    coa2(b,12)=tip2(j,2);
    hold on
    plot(coa2(b,9),coa2(b,10),'.k');
    hold on
    plot(coa2(b,11),coa2(b,12),'.k');
    hold on
    plot ([coa2(b,9),coa2(b,11)],[coa2(b,10),coa2(b,12)],'r');
    hold on
    plot(coa2(b,3),coa2(b,4),'.r')
    hold on
    plot(coa2(b,5),coa2(b,6),'.r')
    hold on
    b=b+1;
  end
elseif (f21 <= r),
  if (S(j,8)==3 | S(i,8)==4)
     T(j,8)=3;
     T(i,8)=4;
  else
    coa3(c,1)= (tip1(i,1)+tip2(j,1))/2;
```

```
    coa3(c,2)=(tip1(i,2)+tip2(j,2))/2;
    coa3(c,3)=tip1(i,1);
    coa3(c,4)=tip1(i,2);
    coa3(c,5)=tip2(j,1);
    coa3(c,6)=tip2(j,2);
    coa3(c,7)=0;
    coa3(c,8)=0;
    coa3(c,9)=tip1(j,1);
    coa3(c,10)=tip1(j,2);
    coa3(c,11)=tip2(i,1);
    coa3(c,12)=tip2(i,2);
    T(i,8)=121;
    T(j,8)=221;
    hold on
    plot(coa3(c,9),coa3(c,10),'.k');
    hold on
    plot(coa3(c,11),coa3(c,12),'.k');
    hold on
    plot ([coa3(c,9),coa3(c,11)],[coa3(c,10),coa3(c,12)],'m');
    hold on
    plot(coa3(c,3),coa3(c,4),'.m')
    hold on
    plot(coa3(c,5),coa3(c,6),'.m')
    hold on
    c=c+1;
  end
elseif (f22 <= r),
  if (S(j,8)==4 | S(i,8)==4)
     T(j,8)=4;
     T(i,8)=4;
  else
    if (tip1(i,1)<=tip1(j,1))
       coa4(d,3)=tip1(j,1);
       coa4(d,4)=tip1(j,2);
       coa4(d,9)=tip1(i,1);
       coa4(d,10)=tip1(i,2);
    else
       coa4(d,3)=tip1(i,1);
       coa4(d,4)=tip1(i,2);
       coa4(d,9)=tip1(j,1);
       coa4(d,10)=tip1(j,2);
    end
    if (tip2(i,1)<=tip2(j,1))
       coa4(d,5)=tip2(j,1);
       coa4(d,6)=tip2(j,2);
       coa4(d,11)=tip2(i,1);
       coa4(d,12)=tip2(i,2);
    else
       coa4(d,5)=tip2(i,1);
       coa4(d,6)=tip2(i,2);
       coa4(d,11)=tip2(j,1);
       coa4(d,12)=tip2(j,2);
    end
    coa4(d,1)= (coa4(d,3)+coa4(d,5))/2;
    coa4(d,2)=(coa4(d,4)+coa4(d,6))/2;
    coa4(d,7)=0;
```

```
            coa4(d,8)=4;
            hold on
            plot (tip2(i,1),tip2(i,2),'.k');
            hold on
            plot (tip2(j,1),tip2(j,2),'.k');
            hold on
            plot ([tip2(i,1),tip2(j,1)],[tip2(i,2),tip2(j,2)],'b');
            hold on
            plot(coa4(d,3),coa4(d,4),'.b')
            hold on
            plot(coa4(d,5),coa4(d,6),'+b')
            hold on
            d=d+1;
            T(i,8)=122;
            T(j,8)=222;
          end
        end
      j=j+1;
    end
  end
T
%Recover data from shielding and coalescence
axis([-600 6500 -100 1600]);
h=1;
for i=1:m
   if (T(i,8)<100) ,
        new(h,:)=T(i,:);
        h=h+1;
        hold on
        if (T(i,8)==3)
        plot (T(i,3),T(i,4),'+k')
        plot (T(i,5),T(i,6),'.k');
       elseif (T(i,8)==4)
        plot (T(i,3),T(i,4),'.k')
        plot (T(i,5),T(i,6),'+k');
       elseif (T(i,8)==5)
        plot (T(i,3),T(i,4),'+k')
       plot (T(i,5),T(i,6),'+k');
       else
       plot (T(i,3),T(i,4),'.k')
       plot (T(i,5),T(i,6),'.k');
     end
     hold on
     end
end


h=h-1;
hold on
   if (a>1),
       coa1;
       for j=1:size(coa1,1)
         new((h+j),:)=coa1(j,:);
       end
   end
   if (b>1),
```

```
        coa2;
        for j=1:size(coa2,1)
        new((h+j),:)=coa2(j,:);

       end
    end
    if (c>1),
        coa3;
        for j=1:size(coa3,1)
        new((h+j),:)=coa3(j,:);
        end
    end
    if (d>1),
        coa4;
        for j=1:size(coa4,1)
        new((h+j),:)=coa4(j,:);

       end
    end
new;
maxlength=0;
for p=1:size(new,1)
    alength=sqrt((new(p,3)-new(p,5))^2+(new(p,4)-new(p,6))^2);
    if maxlength < alength
       maxlength=alength;
    end
end
maxlength
%save newcrack.dat new -ascii;


% Main program
%Initiation, growth, interaction and coalescence
%
%clear all
figure
axis([-600 6500 -100 1600]);
hold on
% Program
%initiation
load file.dat; % area,X,Y,circularity,majoraxis,minoraxis,angle
graph1(file);
title ('pores population');
print -djpeg100 -r300 pores;
stress=200
[crack,noncrack,max]=init(file);
max;
crack;
noncrack;
save crack.dat crack -ascii; % X,Y,X1,Y1,X2,Y2,angle,flag
save cr0.dat crack -ascii; % X,Y,X1,Y1,X2,Y2,angle,flag
save noncrack.dat noncrack -ascii;% area,X,Y,circularity,majoraxis,minoraxis,angle
load crack.dat;
graph(crack);
title ('initiation');
%print -djpeg100 -r300 crack0;
```

```
%Propagation after N cycles
Nstep=1000;
N=1000;
%Maxlength=max;
crack;
[growthcrack]=growth(crack,N,stress);
growthcrack;
save growthcrack.dat growthcrack -ascii;

newcrack(:,:)=growthcrack(:,:); %creation of a new file

newcrack(:,8)=0; %after the first Delta N cycles
newcrack; % X,Y,X1,Y1,X2,Y2,angle,flag
[newcrack,maxlength]=coal(newcrack,stress);

save newcrack.dat newcrack -ascii;
filename=[int2str(stress),'-',int2str(Nstep),'cr',int2str(N),'.dat']
%save (filename,'newcrack','-ascii');

name=[int2str(stress),'-',int2str(Nstep),'graph',int2str(N)];
   title([int2str(stress),'-',int2str(N),' cycles']);
%print ('-djpeg100','-r300', name);

while maxlength <(1*10^3)
   N=N+1000;
   [growthcrack]=growth(newcrack,Nstep,stress);
   %save growthcrack.dat growthcrack -ascii;
   newcrack(:,:)=growthcrack(:,:) %creation of a new file

   [newcrack,maxlength]=coal(newcrack,stress);
   %save newcrack.dat newcrack -ascii;

   filename=[int2str(stress),'-',int2str(Nstep),'cr',int2str(N),'.dat'];
   %save (filename,'newcrack','-ascii');
   title([int2str(stress),'-',int2str(N),' cycles']);
   name=[int2str(count),'-',int2str(stress),'-',int2str(Nstep),'graph',int2str(N)];
   %print ('-djpeg100','-r300', name);
end
print ('-djpeg100','-r300', name);
clear crack
clear noncrack
clear growthcrack
clear newcrack
%testprog(N,Nstep,stress);
```

Crack growth simulation: Hobson-type (Hobson, 1982)

```
clear all
%function dadnprog(d,stress)
K11=0.1;
K12=0.008;
K21=7;
K22=K12;
K31=15;
K32=0.5;
```

```
K41=0.1;
K42=2*(10^-5);
K51=3;
K52=K42;

stress=270;
d=5; %grain size in micron

W=7.5;
%half grain size
X0=(d/2)*(10^-3)/(2*W);
const0= (1.21*(1-0.3*X0)*(1-X0^12))+(0.394*1.57*X0^12*(1/1)^0.5);
deltaKd0=const0*(stress/1.57)*((3.1415927*((d/2)*(10^-3)*1/2000))^0.5);
%Grain size
X=(d)*(10^-3)/(2*W);
const= (1.21*(1-0.3*X)*(1-X^12))+(0.394*1.57*X^12*(1/1)^0.5);
deltaKd=const*(stress/1.57)*((3.1415927*((d)*(10^-3)*1/2000))^0.5);

%upper band parameter
   X1=[log(K11) log(K21)];
Y1=[log(K12) log(K22)];
P1=polyfit(X1,Y1,1);
%lower band parameter
   X2=[log(K41) log(K51)];
Y2=[log(K52) log(K52)];
P2=polyfit(X2,Y2,1);
%upper band parameter -long crack
   X3=[log(K21) log(K31)];
Y3=[log(K22) log(K32)];
P3=polyfit(X3,Y3,1);
%lower band parameter -long crack
   X4=[log(K51) log(K21)];
Y4=[log(K52) log(K22)];
P4=polyfit(X4,Y4,1);

A(1,1)=0.1;
A(1,2)=(A(1,1)^P2(1))*exp(P2(2));

B(1,1)=A(1,1);
B(1,2)=(B(1,1)^P1(1))*exp(P1(2));

i=2;

while A(i-1,1) < K21
if (A(i-1,1) < K51)
   A(i,1)= A(i-1,1)+((2*(i-2)+1)^0.5)*deltaKd0;
A(i,2)=(A(i,1)^P2(1))*exp(P2(2));
   else
   A(i,1)= A(i-1,1)+((2*(i-2)+1)^0.5)*deltaKd0;
A(i,2)=A(i,1)^(P4(1))*exp(P4(2));
   end
   B(i,1)=B(i-1,1)+((2*(i-2)+1)^0.5)*deltaKd0;
B(i,2)=(B(i,1)^P1(1))*exp(P1(2));
i=i+1;
end
```

```
k=1

C(1,1)=0;
C(1,2)=0;

for j=1:(i-3)
   X5=[A(j+1,1) B(j,1)];
Y5=[A(j+1,2) B(j,2)];
P5=polyfit(X5,Y5,1)
   X6=[A(j+1,1) B(j+1,1)];
Y6=[A(j+1,2) B(j+1,2)];
P6=polyfit(X6,Y6,1);
   C(k,1)=B(j,1);
   C(k,2)=B(j,2);

   k=k+1;

   const2=(B(j+1,1));
   const1=(A(j+1,1));
   test1=B(j,1);

  while ((test1) < const1)
 C(k,1)=C(k-1,1)+0.05;
 C(k,2)=P5(1)*C(k,1)+P5(2);
    test1=C(k,1);
    k=k+1
   end
   k=k-1;
   C(k,1)=const1;
   C(k,2)=A(j+1,2);
   test2=C(k,1);
   k=k+1;
   while ((test2) <= const2)
 C(k,1)=C(k-1,1)+0.05;
 C(k,2)=P6(1)*(C(k,1))+P6(2);
    test2=C(k,1);
    k=k+1
   end
   k=k-1;
   %C(k,1)=C(k-2,1);
%C(k,2)=C(k-2,2);
   j=j+1;
end
for s=1:(k-1)
   T(s,:)=C(s,:);
end

n=size(T,1);
i=n;
test3=T(i,1);
while test3 <= K31
   T(i+1,1)=T(i,1)+0.05;
   T(i+1,2)=exp(P3(2))*(T(i+1,1))^P3(1);
   test3=T(i+1,1);
   i=i+1;
```

```
end
figure
load dadn.dat;
loglog([1 15 0.0001 0.1],'w');
hold on
%plot(dadn(:,1),dadn(:,2),'k')
ppdadn
hold on

plot (T(:,1),T(:,2),'b');
%plot (A(:,1),A(:,2),'or');
%plot (B(:,1),B(:,2),'og');
save dadn.dat T –ascii
```

Crack growth simulation: Zhang & Edwards-type (Edwards & Zhang, 1994)

```
clear all
%function dadn(d,stress)
deltastress=270 %stress in MPa;
RS=50;
stress=deltastress/0.9; %max stress in MPa;
stressmin=0.1*stress;
stress0=(stress)/10; %intrinsic friction stress
stressy=350; %yield stress= 350MPa
stressc=0.96*stressy;%critical stress
r0=1;
Phi=0.5;
C=5*(10^-7);
m1=2.2;
c1=0.25;
%grain size in micron
D=100;
W=7.5
%program
R=0.1;
%initialisation first crack
i=1;
j=1;
%initial 1/2 crack
alpha(j)=2.5; %initial crack equal to 5 micron
%step increment
step=0.5;


%constant short-long crack
dKinitial=0.5831;
dKtransition=7;
clolevel=0.5; %(closure level at the transition point)
Kdarrest=7;
%Initial crack j=1

 X=2*(alpha(j))*(10^-3)/(2*W);
 const= (1.21*(1-0.3*X)*(1-X^12))+(0.394*1.57*X^12*(1/1)^0.5);
 deltaKd(j)=const*(deltastress/1.57)*((3.1415927*(2*(alpha(j))*(10^-3)*1/2000))^0.5);
 Kmax(j)=const*(stress/1.57)*((3.1415927*(2*(alpha(j))*(10^-3)*1/2000))^0.5);
 Kmin(j)=0.1*Kmax(j);
```

```
  gamma(j)=(deltaKd(j)-dKinitial)/(dKtransition-dKinitial);
  Kcl(j)=clolevel*gamma(j)*deltaKd(j);
  KmaxRS(j)=Kmax(j)*(stress+RS)/stress;
  KminRS(j)=Kmin(j)*(stressmin+RS)/stressmin;
  deltaKeffRS(j)=KmaxRS(j)-Kcl(j);
  if KminRS(j) > Kcl(j)
     U(j)=1;
  else
     U(j)=deltaKeffRS(j)/deltaKd(j);
  end
  stressRS(j)=U(j)*deltastress;

  %misorientation factor for the considered grain (i)
  m(i)=m1+c1*log(i);
  %equivalent friction stress for the considered grain (i)
  stressequ(i)=stressy-m(i)*stressc*sqrt(r0/(i*D));
  %plastic zone size calculation
  n(j)=abs(Phi*cos(pi*stressRS(j)/(2*stressequ(i))));
  rp(j)=alpha(j)/n(i)-alpha(j);
  lenda(j)= i*D/2 + D/2 - alpha(j);

%crack growth
while deltaKd(j) <= Kdarrest

  while (rp(j)<=lenda(j)) && (deltaKd(j) <= Kdarrest)
    j=j+1;
    alpha(j)=alpha(j-1)+step;
    X=2*(alpha(j))*(10^-3)/(2*W);
    const= (1.21*(1-0.3*X)*(1-X^12))+(0.394*1.57*X^12*(1/1)^0.5);
    deltaKd(j)=const*(deltastress/1.57)*((3.1415927*(2*(alpha(j))*(10^-3)*1/2000))^0.5);
    Kmax(j)=const*(stress/1.57)*((3.1415927*(2*(alpha(j))*(10^-3)*1/2000))^0.5);
    Kmin(j)=0.1*Kmax(j);
    gamma(j)=(deltaKd(j)-dKinitial)/(dKtransition-dKinitial);
    Kcl(j)=clolevel*gamma(j)*deltaKd(j);
    KmaxRS(j)=Kmax(j)*(stress+RS)/stress;
    KminRS(j)=Kmin(j)*(stressmin+RS)/stressmin;
    deltaKeffRS(j)=KmaxRS(j)-Kcl(j);
    if KminRS(j)>Kcl(j)
      U(j)=1;
    else
      U(j)=deltaKeffRS(j)/deltaKd(j);
    end
    stressRS(j)=U(j)*deltastress;

    n(j)=abs(Phi*cos(pi*stressRS(j)/(2*stressequ(i))));
    rp(j)=alpha(j)/n(j)-alpha(j);
    lenda(j)= i*D/2 + D/2 -alpha(j);

  end
  if rp(j)> lenda(j)
    %stress on dislocation source in the (i+1) grain for the crack(j) in the (i) grain
    Sd= stressRS(j)/sqrt(2)*sqrt((alpha(j)/(rp(j)+r0)))*(1-(2*stress0/(pi*stressRS(j)*(cos(n(i))))))+stress0;
    %critical stress in the (i+1) grain for the crack(j) in the (i) grain
    Scritical=0.5*m(i)*stressc;
    rp(j)=lenda(j);
    while (Sd < Scritical) && (deltaKd(j) <= Kdarrest)
```

```
      j=j+1;
      alpha(j)=alpha(j-1)+step;
      lenda(j)= i*D/2 +D/2-alpha(j);
      rp(j)=lenda(j);
      X=2*(alpha(j))*(10^-3)/(2*W);
      const= (1.21*(1-0.3*X)*(1-X^12))+(0.394*1.57*X^12*(1/1)^0.5);
      deltaKd(j)=const*(deltastress/1.57)*((3.1415927*(2*(alpha(j))*(10^-3)*1/2000))^0.5);
      Kmax(j)=const*(stress/1.57)*((3.1415927*(2*(alpha(j))*(10^-3)*1/2000))^0.5);
      Kmin(j)=0.1*Kmax(j);
      gamma(j)=(deltaKd(j)-dKinitial)/(dKtransition-dKinitial);
      Kcl(j)=clolevel*gamma(j)*deltaKd(j);
      KmaxRS(j)=Kmax(j)*(stress+RS)/stress;
      KminRS(j)=Kmin(j)*(stressmin+RS)/stressmin;
      deltaKeffRS(j)=KmaxRS(j)-Kcl(j);
      if KminRS(j)>Kcl(j)
         U(j)=1;
       else
         U(j)=deltaKeffRS(j)/deltaKd(j);
       end
      stressRS(j)=U(j)*deltastress;
      Sd= stressRS(j)/sqrt(2)*sqrt((alpha(j)/(rp(j)+r0)))*(1-
(2*stress0/(pi*stressRS(j)*(cos(n(i))))))+stress0;
    end
  end
  i=i+2;
  X=2*(alpha(j))*(10^-3)/(2*W);
  const= (1.21*(1-0.3*X)*(1-X^12))+(0.394*1.57*X^12*(1/1)^0.5);
  deltaKd(j)=const*(deltastress/1.57)*((3.1415927*(2*(alpha(j))*(10^-3)*1/2000))^0.5);
  Kmax(j)=const*(stress/1.57)*((3.1415927*(2*(alpha(j))*(10^-3)*1/2000))^0.5);
  Kmin(j)=0.1*Kmax(j);
  gamma(j)=(deltaKd(j)-dKinitial)/(dKtransition-dKinitial);
  Kcl(j)=clolevel*gamma(j)*deltaKd(j);
  KmaxRS(j)=Kmax(j)*(stress+RS)/stress;
  KminRS(j)=Kmin(j)*(stressmin+RS)/stressmin;
  deltaKeffRS(j)=KmaxRS(j)-Kcl(j);
    if KminRS(j)>Kcl(j)
      U(j)=1;
    else
      U(j)=deltaKeffRS(j)/deltaKd(j);
    end
  stressRS(j)=U(j)*deltastress;
    %misorientation factor for the considered grain (i)
  m(i)=m1+c1*log(i);
  %equivalent friction stress for the considered grain (i)
  stressequ(i)=stressy-m(i)*stressc*sqrt(r0/(i*D));
    n(j)=abs(Phi*cos(pi*stressRS(j)/(2*stressequ(i))));
  rp(j)=alpha(j)/n(j)-alpha(j);
  lenda(j)= i*D/2 +D/2- alpha(j);
end
p=1;
while p <=(size(rp,2))
    growthrate(p)=(C*((rp(p)))^m1); %growth rate in micron per cycles
    p=p+1;
end
%upper band parameter -long crack
%condition short-long crack
```

```
K21=7;
K22=growthrate(p-2);
K31=15;
K32=0.5;
X3=[log(K21) log(K31)];
Y3=[log(K22) log(K32)];
P3=polyfit(X3,Y3,1);
h=size(growthrate,2);
h=h-1;
s=h
dK=deltaKd;
test3=deltaKd(h);
while test3 <= K31
   deltaKd(h+1)=deltaKd(h)+0.05;
   growthrate(h+1)=exp(P3(2))*(deltaKd(h+1))^P3(1);
  test3=deltaKd(h+1);
   h=h+1;
end
%DeltaK effective
R=0.1;
for i=1:(p-2)
   if deltaKd(i)<=Kdarrest
   deltaKdeff(i)=U(i)*deltaKd(i);
   rate(i)=growthrate(i);
   end
end
figure
loglog([1 15 0.0001 0.1],'w');
hold on
ppdadn;
hold on
RSfreedadn1;
hold on
plot (deltaKdeff,rate,'b');
   title([int2str(deltastress),' MPa']);
   name=['dadnclRS-D=100-',int2str(deltastress),];
   print ('-djpeg100','-r300', name);
%T(:,1)=alpha(:);
h=size(growthrate,2);
for i=1:h
   T(i,1)=deltaKd(i);
   T(i,2)=growthrate(i);
end
%T((size(rp,2)),2)
filename=['dadnclRS-D=100-',int2str(deltastress),'.dat'];
   save (filename,'T','-ascii');
%save dadnedw.dat T –ascii
```


Edwards, L. and Y. H. Zhang (1994). "Investigation of Small Fatigue Cracks .2. A Plasticity Based Model of Small Fatigue-Crack Growth." Acta Metallurgica Et Materialia 42(4): 1423-1431.

Hobson, P. D. (1982). "The formulation of a crack growth equation for short cracks." Fatigue of Engineering Materials and Structures 5(4): 323-327.

Yang, N., J. Boselli and I. Sinclair (2001). "Simulation and quantitative assessment of homogeneous and inhomogeneous particle distributions in particulate metal matrix composites." Journal of Microscopy - Oxford 201(Part 2): 189-200.